Efficient models for bipartite open quantum systems

Angela Riva

Sorbonne Université

Doctoral Thesis

Efficient models of bipartite open quantum systems

Author:
Angela RIVA

Supervisor:
Alain SARLETTE

Cosupervisor:
Alexandru PETRESCU

Thesis defense committee:

Thomas CHAMBRION	Université de Bourgogne	*Reviewer*
Marco SCHIRÒ	Collège de France	*Reviewer, President*
Jonathan KEELING	University of St Andrews	*Examiner*
Lorenza VIOLA	Dartmouth College	*Examiner*
Alain SARLETTE	INRIA Paris	*Director*
Alexandru PETRESCU	Mines Paris – PSL	*Invited*

Paris, 2 February 2026

Abstract

This thesis develops model reduction methods for open quantum system dynamics, yielding efficient models for bipartite systems, with direct application to circuit QED and broader applicability beyond this platform.

First, we consider dissipative dynamics characterized by timescale separation, which translates to a gap on the real axis of the spectrum of the Liouvillian generating it. This allows to compute the reduced evolution for a target subsystem by adiabatically eliminating fast-decaying degrees of freedom. A Sylvester equation integral representation yields closed forms for the reduced generators and explicit reconstruction maps to arbitrary order without a preliminary interaction-picture averaging step, providing a linear center manifold description that separates long-lived from fast-decaying modes by the real parts of the spectrum. The reduced dynamics takes place on the center manifold, that is, the spectral subspace associated with eigenvalues whose real parts are small (long-lived modes), while placing no restriction on imaginary parts, thus allowing for fast unitary dynamics on the target subsystem. We further demonstrate the equivalence of such a geometric approach to adiabatic elimination with the time-convolutionless master equation framework, by showing that the maps defining the reduced model satisfy the same invariance equation in both frameworks. The time-convolutionless formulation of adiabatic elimination extends to cases where the target system undergoes fast unitary dynamics and retains explicit time dependence in the reduced model, hence capturing initial transients that are neglected in time-independent geometric reductions.

Second, we apply a unitary chain mapping of microscopic system–environment Hamiltonians to a nearest-neighbor form, enabling efficient time evolution exploiting tensor network time evolution algorithms based on the time dependent variational principle. Accuracy of the tensor network representation, and thus the size of the reduced model, is controlled by entanglement entropy growth, which we quantify numerically. While the methods are general and apply beyond the specific platform considered, we focus on dispersive readout in circuit QED (a qubit dipolarly coupled to a driven, lossy cavity). We quantify the dependence of the relaxation time T_1 of the qubit on intracavity photon number $\bar{n}$ (and thus on the drive amplitude) and on the spectral structure of the environment, and compute the emission spectrum directly from environmental observables. Simulations including a Purcell notch filter predict a decrease of T_1 with increasing drive power, a qualitatively different behavior with respect to Born–Markov–secular GKSL predictions but consistent with experimental trends, indicating that explicit filter modeling is required in this case. Together, the results specify when reduced Liouvillian models under a dissipative gap are reliable and when microscopic, non-perturbative simulations are required.

Acknowledgements

[Acknowledgments will be added!]

Notation

Conventions

Operators on Hilbert space are bold ($\mathbf{H}, \boldsymbol{\rho}, \mathbf{L}_k$).

Superoperators are calligraphic ($\mathcal{L}, \mathcal{E}, \mathcal{P}, \mathcal{Q}$). We may write $\mathcal{L}(\bullet)$, or, in some cases, we may omit the parenthesis to ease the notation $\mathcal{L}\bullet$.

Vectorized operators use double kets/bras ($|A\rangle\rangle, \langle\langle A|$).

Vectorized superoperators carry hats ($\hat{\mathcal{L}}, \hat{\mathcal{P}}, \hat{\mathcal{Q}}$); e.g. $\frac{d}{dt}|\rho\rangle\rangle = \hat{\mathcal{L}}\,|\rho\rangle\rangle$.

Commutator superoperator denoted $\boldsymbol{H}^{\times}(\bullet) \coloneqq [\boldsymbol{H}, \bullet]$, with $[\boldsymbol{H}, \bullet] = \boldsymbol{H}\bullet - \bullet\boldsymbol{H}$.

Anti commutator superoperator is defined as $\{\boldsymbol{O}, \bullet\} = \boldsymbol{O}\bullet + \bullet\boldsymbol{O}$.

Dissipators are defined as $\mathcal{D}[\boldsymbol{L}](\bullet) = \boldsymbol{L}\bullet\boldsymbol{L}^\dagger - \frac{1}{2}\{\bullet, \boldsymbol{L}^\dagger\boldsymbol{L}\}$.

List of acronyms

1TDVP one-site TDVP.

2TDVP two-sites TDVP.

DMRG density matrix renormalization group.

DTDVP adaptive TDVP.

DUST drive-activated unwanted state transitions.

GKSL Gorini, Kossakowski, Sudarshan, Lindblad.

MPO matrix product operator.

MPS matrix product state.

PEPS projected entangled pair state.

QED quantum electrodynamics.

QND quantum non-demolition.

RWA rotating-wave approximation.

SVD singular value decomposition.

T-TEDOPA temperature dependent TEDOPA.

TDVP time dependent variational principle.

TEBD time evolving block decimation.

TEDOPA time evolving density matrix using orthogonal polynomials algorithm.

TN tensor network.

TTN tree-tensor network.

List of symbols

$\boldsymbol{\sigma}_z$ Pauli Z operator; eigenstates $|g\rangle, |e\rangle$ with eigenvalues $+1$ and -1, respectively.

$\boldsymbol{\sigma}_+$ Raising (ladder) operator: $\boldsymbol{\sigma}_+ = \frac{1}{2}(\boldsymbol{\sigma}_x + i\boldsymbol{\sigma}_y) = |e\rangle\langle g|$.

$\boldsymbol{\sigma}_-$ Lowering (ladder) operator: $\boldsymbol{\sigma}_- = \frac{1}{2}(\boldsymbol{\sigma}_x - i\boldsymbol{\sigma}_y) = |g\rangle\langle e|$.

χ Bond dimension for a MPS.

$\langle\langle A|$ Hermitian conjugate of $|A\rangle\rangle$.

$|A\rangle\rangle$ Column vector representation of an operator $\boldsymbol{A}$.

$\hbar = 1$ Reduced Planck constant, set to 1 throughout this work.

$|\psi\rangle$ Pure quantum state. Ray in a Hilbert space.

$\mathcal{H}$ Hilbert space.

$\mathscr{M}^{(0)}$ Invariant subspace for $\epsilon = 0$.

$\mathscr{M}^{(\epsilon)}$ Invariant subspace for $\epsilon > 0$.

d Local Hilbert space dimension for a MPS.

Contents

Chapter 1

Introduction

Contents

Model reduction is a central procedure in physics. Complexity is reduced by exploiting the structure of a problem to define a prescription for the computation of the effective evolution on a smaller state space. In this thesis we consider two kinds of structures to achieve model reduction of open quantum systems. (i) Exploiting real-axis, or dissipative, spectral gaps, we derive closed-form effective Liouvillians describing the reduced evolution of a target system via adiabatic elimination of the rapidly-decaying degrees of freedom; furthermore, we show the equivalence of such a geometric approach to adiabatic elimination with the time-convolutionless master equation framework, which can be straightforwardly applied to regimes with fast unitary motion and initial relaxation with an impact on the subsequent reduced dynamics. (ii) We employ matrix-product state compression to compute the unitary time evolution generated by a microscopic Hamiltonian modeling experimentally relevant driven-dissipative systems. The microscopic model is mapped by a unitary transformation to a Hamiltonian with

only nearest-neighbor interactions, well adapted for matrix product state time-evolution algorithms. We study in particular the problem of dispersive readout in circuit and cavity quantum electrodynamics, where an indirect measurement of the qubit is obtained by measuring the frequency of the cavity, which is shifted depending on the state of the qubit. We analyze how the qubit energy relaxation time $T_1(\bar{n})$ depends on the cavity photon number $\bar{n}$ and on spectral properties of the environment, and we compute emission spectra directly from environmental observables. This provides a non-perturbative method for the modeling of driven-dissipative quantum systems that goes beyond the Born–Markov–secular master equations used in (i).

1.1 Contributions of this thesis

The development of experimental platforms to store and control quantum information–such as for example trapped ions [1], neutral atoms [2], spin qubits [3, 4] and superconducting circuits [5]–is paving the way towards achieving coherence-enabled quantum technologies [6, 7]. Despite rapid progress, the scalability [8, 3] of these platforms is limited by unavoidable couplings to external degrees of freedom. Practical devices are intrinsically open [9]: they interact both unintentionally, through noise causing relaxation and dephasing [10, 11, 12, 13, 14], and intentionally, through the control and measurement apparatus – drive and readout lines – which enable fast operations [15, 16, 17] and readout [18, 19, 20] but introduce additional leakage channels [21, 22, 23, 24]. Achieving fast and high-fidelity quantum control therefore requires suppressing uncontrolled couplings [25] while maintaining strong, precisely engineered interactions for operations. Open quantum systems theory [26, 27] provides the framework to model such driven-dissipative effective dynamics.

Realistic models of the open quantum systems routinely stabilized and manipulated in laboratories need to track the dynamics of many coupled degrees of freedom, representing, for instance, in the case of circuit quantum electrodynamics (QED) [28, 29, 10], the various on-chip components: non-linear Josephson-junction based qubits [30], readout resonators [31, 32], couplers [33], filters [19, 34, 35], or even undesired impurities [36]. In general, the task is therefore to model a many body system of N modes, where the Hilbert space size of each mode can itself be very large–or even infinite, as in the case of harmonic oscillators. The exponential growth with N of the number of parameters needed to describe a quantum system is ubiquitous in many-body physics, and has motivated efforts in condensed matter physics to compute effective dynamics for a smaller number of degrees of freedom than in the original problem; it is also one of the main problems that quantum computing could potentially solve [37], by simulating quantum systems with quantum systems [38].

Moreover, open systems should model the evolution of composite systems, in which a controlled subsystem preserves coherence, while the remaining degrees of freedom are ignored. Modeling such a situation, as we will detail, requires working with density matrices (of dimension d^2) instead of vectors (of dimension d), making the problem even more sensitive to the Hilbert space size d. Furthermore, precise modeling of the reduced evolution of a subsystem of a larger open quantum system is crucial in reservoir engineering [1, 39, 40, 41, 42], where dissipation on the subsystem of interest

is engineered by carefully designing the coupling within the open quantum system to achieve stabilization towards a target state [43, 44, 45, 46, 47, 48]. The specific setups engineered in this context are often composed of several components, whose dimensions multiply and span several timescales. The "useful quantum information" represents only a small, ideally non-decaying part of this system. Fast decaying degrees of freedom are thus associated to auxiliary control signals [49]. Model reduction techniques would thus seek to summarize the effect of these fast stabilizing degrees of freedom on the dynamics of the target variables, preferably with operational principles and analytic expressions to guide system design.

The need of dealing with a tractable number of degrees of freedom, and of computing the induced dissipation on a subsystem of interest, motivates model reduction methods for open quantum systems [50, 51, 52, 53]. In this thesis we develop two complementary routes to model reduction for open quantum systems, exploiting spectral gaps (time-scale separation) to achieve model reduction through adiabatic elimination and entanglement constraints to simulate driven-dissipative circuit QED problems with tensor networks.

Adiabatic elimination of the fast-decaying degrees of freedom

Firstly, we exploit timescale separation of the dynamics to adiabatically eliminate the fast-relaxing degrees of freedom [54, 9]. Specific approaches [55, 56, 57] enable the computation of long-time effective time evolution, but lack generality. We follow here the systematic formulation of adiabatic elimination introduced in [58, 59], valid for those open quantum systems described by Liouvillians whose spectrum has a gap on the real axis. The gap encodes the characteristic timescale separation for the dissipation happening during the evolution, and defines the basis for the modes spanning a lower-dimensional subspace where the reduced evolution of slowly decaying modes, associated to eigenvalues with a small real part, takes place. Adiabatic elimination gives a prescription on how to derive the effective linear reduced dynamics on this subspace and how to map linearly the reduced parametrization back to the full state as series expansions in the time-scale separation parameter.

We contribute to the development of adiabatic elimination in two ways. (i) We consider the case when the reduced degrees of freedom undergo fast unitary dynamics, associated to large imaginary parts, instead of just being slow (eigenvalues close to the origin). Such a case was first treated in [60, 61], establishing the abstract expressions up to second-order expansion in the timescale separation parameter, under assumptions on the fast unitary dynamics. Here we develop a formulation of adiabatic elimination that, exploiting stable Sylvester's equation and adjoint dynamics, leads to systematic, explicit expressions at high orders, without additional conditions on the fast unitary dynamics [62]. This covers circuit QED settings [63] where the stabilized state rotates unitarily at characteristic frequencies, allowing for in/out of resonance control, and yields interpretable explicit expressions for the long-term dynamics on the invariant manifold, which we discuss in several examples. (ii) We show the equivalence of adiabatic elimination with the time-convolutionless (TCL) framework [26]. In this formulation [64] the analytical treatment in the presence of fast unitary dynamics is straightforward. Moreover, the TCL formulation explicitly deals with cases where short-time dynamics preceding the decay of fast degrees of freedom influence the long-term dynamics. With

examples we demonstrate a practical methodology to perform calculations and we discuss how the initial relaxation phase relates to the properties of the reduced dynamics.

Compression of unitary dynamics applied to driven-dissipative problems

Secondly, we consider model reduction guided by entanglement constraints, efficiently captured by tensor networks [65, 66]. Here the dynamics is compressed onto a *nonlinear* low-entanglement manifold enabling efficient simulation when entanglement remains limited [67]. Starting from the full unitary evolution of an open quantum system interacting with a continuum of bosonic modes, as in the Caldeira-Leggett model [68], we exploit chain mapping methods [69, 70, 71] to unitarily map the problem on a Hamiltonian with only nearest-neighbor interactions. This yields a one-dimensional Hamiltonian suitable for matrix product state [72] time evolution with the time-dependent variational principle [73], where the accuracy of the reduced model can be controlled by a convergence parameter that defines the manifold on which time evolution is constrained, and thus the size of the reduced model.

In this thesis we build on tensor network [72, 65, 73] and chain mapping tools [69, 70, 74, 75] to treat realistic, structured environments and explicit time dependence in circuit QED, and apply them to simulate the superconducting qubit readout [76] (T_1-under-pump setting [77]): a two-level system coupled to a driven harmonic mode (readout resonator) that in turn couples to a bosonic environment [78]. We quantify how the qubit relaxation time $T_1(\bar{n})$ depends on the cavity photon number $\bar{n}$ and on environmental characteristics (e.g., frequency-dependence, filtering), and we compute emission spectra directly from environmental observables. This provides a non-perturbative benchmark against Born–Markov–secular master equations used earlier in the manuscript. Keeping the environment explicit (via the chain) preserves system–environment correlations that master equations remove by construction, enables direct access to environmental observables, and remains accurate in regimes with strong drives or long bath memory where Markovian assumptions may fail. The price is entanglement growth; we monitor it and report convergence criteria alongside results.

1.1.1 Publications

During the preparation of this thesis, I worked on the following publications:

- Angela Riva, Alain Sarlette, and Pierre Rouchon. "Explicit formulas for adiabatic elimination with fast unitary dynamics". In: *2024 IEEE 63rd Conference on Decision and Control (CDC)*. 2024, pp. 755–760. DOI: 10.1109/CDC56724.2024.10886784, presented in Chap. 2.

- Masaaki Tokieda and Angela Riva. "Time-convolutionless master equation applied to adiabatic elimination". In: *Physical Review A* 111.5 (May 2025). ISSN: 2469-9934. DOI: 10.1103/physreva.111.052206. URL: http://dx.doi.org/10.1103/PhysRevA.111.052206, presented in Chap. 3.

- Thibaut Lacroix, Brieuc Le Dé, Angela Riva, Angus J. Dunnett, and Alex W. Chin. "MPSDynamics.jl: Tensor network simulations for finite-temperature (non-

Markovian) open quantum system dynamics". In: *The Journal of Chemical Physics* 161.8 (Aug. 2024), p. 084116. ISSN: 0021-9606. DOI: 10.1063/5.0223107. URL: https://doi.org/10.1063/5.0223107, the software paper companion to the open-source Julia package `MPSDynamics.jl` (Github: https://github.com/shareloqs/MPSDynamics.jl), to which I contributed; `MPSDynamics.jl` implements the methods presented in Chap. 4.

- *Tensor network study of drive-induced relaxation in circuit QED*, work in preparation based on the results presented in Chap. 5.

Additionally, I contributed with minor theoretical support to the experimental paper by B.-L. Najera-Santos *et al.* [63], from the group of Samuel Deléglise at Laboratoire Kastler Brossel. This collaboration provided experimental motivation for the developments reported in Chap. 2.

1.1.2 Outline of this chapter

In the rest of this introduction we specify the open quantum system models to which the model reduction methods developed in this thesis will be applied. In Sec. 1.2 we recall the postulates of quantum mechanics for composite systems, leading to the notion of complete positivity and its characterization. As we will see in Chap. 2 and Chap. 3, the reduced models obtained from adiabatic elimination do not always conserve this property. In Sec. 1.3, via the theory of quantum dynamical semigroups, we characterize the Gorini–Kossakowski–Sudarshan–Lindblad (GKSL) equation—the starting point for the reduction based on adiabatic elimination developed in Chap. 2. In Sec. 1.4 we reproduce a microscopic derivation of quantum master equations using the time-convolutionless projection-operator formalism, which will be crucial in Chap. 3 for developing model reduction of those same master equations. Finally, in Sec. 1.5 we introduce the full time-dependent microscopic model whose dynamics we compress with tensor-network methods described in Chap. 4. We will apply these methods to study the readout problem in circuit QED setting in Chap. 5. We present the outline of the remainder of this manuscript in Sec. 1.6.

1.2 Composite quantum systems

To specify the models to be reduced and the structure of their dynamics, we first recall the basic postulates of quantum mechanics for an isolated system, then move on to composite systems, and finally describe the most general state-to-state evolution. This path naturally leads to the notion of complete positivity and to a first effective model of open quantum system dynamics.

1.2.1 Postulates of quantum mechanics for closed systems

Quantum mechanics for *closed* systems is summarized by the Dirac–von Neumann postulates [79].

(i) Quantum states are described by rays in a Hilbert space, $|\psi\rangle \in \mathcal{H}$. If $|\psi_1\rangle$ and $|\psi_2\rangle$ are quantum states, then also their linear superposition

$$|\psi\rangle = \alpha\,|\psi_1\rangle + \beta\,|\psi_2\rangle\,, \quad \text{with } \alpha,\, \beta \in \mathbb{C},\, |\psi|^2 = 1 \tag{1.1}$$

is a quantum state (superposition principle). For a composite system made of S_1 and S_2, the state space is the tensor product of the individual Hilbert spaces $\mathcal{H} = \mathcal{H}_1 \otimes \mathcal{H}_2$.

(ii) Unitary time evolution is generated by the Hermitian operator $\boldsymbol{H}(t)$ appearing in the Schrödinger equation[1]

$$i\,\frac{d}{dt}\,|\psi(t)\rangle = \boldsymbol{H}(t)\;|\psi(t)\rangle\,. \tag{1.2}$$

(iii) Projective measurements are represented by a projection–valued measure (PVM) $\{\boldsymbol{\Pi}_\alpha\}$ with $\boldsymbol{\Pi}_\alpha^\dagger = \boldsymbol{\Pi}_\alpha$, $\boldsymbol{\Pi}_\alpha\boldsymbol{\Pi}_\beta = \delta_{\alpha\beta}\boldsymbol{\Pi}_\alpha$, and $\sum_\alpha \boldsymbol{\Pi}_\alpha = \boldsymbol{I}$. An observable $\boldsymbol{O}$ has the spectral decomposition $\boldsymbol{O} = \sum_\alpha \lambda_\alpha \boldsymbol{\Pi}_\alpha$, where each λ_α may be degenerate. For a pure state $|\psi\rangle$, the probability of obtaining outcome λ_α is

$$P(\alpha) = \langle\psi|\,\boldsymbol{\Pi}_\alpha\,|\psi\rangle\,,$$

and, conditional on that outcome, the post-measurement state (Lüders rule) is

$$|\psi\rangle \;\mapsto\; \frac{\boldsymbol{\Pi}_\alpha\,|\psi\rangle}{\sqrt{\langle\psi|\,\boldsymbol{\Pi}_\alpha\,|\psi\rangle}}.$$

1.2.2 Composite systems and reduced quantum states

The postulates of Sec. 1.2.1 suffice to describe isolated systems. But to model control, measurement, and dissipation, we must include couplings to additional degrees of freedom—whether engineered (measurement apparatus, ancillas) or uncontrolled (environment). Let S be a system of interest, and E an arbitrary extension, with Hilbert spaces $\mathcal{H}_S$ and $\mathcal{H}_E$. The composite Hilbert space is the tensor product $\mathcal{H}_{SE} = \mathcal{H}_S \otimes \mathcal{H}_E$ [26, 80, 79, 27].

Entangled states. With orthonormal bases $\{|i\rangle_S\}$ and $\{|j\rangle_E\}$, the most general form of a state in $|\psi\rangle \in \mathcal{H}_{SE}$ is

$$|\psi\rangle = \sum_{ij} c_{ij}\,|i\rangle_S \otimes |j\rangle_E\,. \tag{1.3}$$

The singular value decomposition (SVD) decomposition of the coefficients matrix $C = (c_{ij})$ yields the Schmidt decomposition [79]

$$|\psi\rangle = \sum_{k=1}^{r} \sqrt{\lambda_k}\,|u_k\rangle_S \otimes |v_k\rangle_E\,, \tag{1.4}$$

[1] Here and in the rest of the manuscript $\hbar = 1$.

where $\{|u_k\rangle_S\}$ and $\{|v_k\rangle_E\}$ are orthonormal sets, $r \leq \min(\dim \mathcal{H}_S, \dim \mathcal{H}_E)$ is the Schmidt rank, the positive coefficients $\lambda_k \in \mathbb{R}^+$ are the Schmidt coefficients. The state is *separable* (factorized) iff $r = 1$, i.e., $\psi = |u\rangle_S \otimes |v\rangle_E$; otherwise it is *entangled*. By partial trace on the auxiliary system E, we obtain the reduced states, diagonal in the Schmidt bases

$$\boldsymbol{\rho}_S = \mathrm{Tr}_E\, |\psi\rangle\langle\psi| = \sum_{k=1}^{r} \lambda_k\ |u_k\rangle\langle u_k|\,, \qquad \boldsymbol{\rho}_E = \mathrm{Tr}_S\, |\psi\rangle\langle\psi| = \sum_{k=1}^{r} \lambda_k\ |v_k\rangle\langle v_k|\,, \tag{1.5}$$

so $\mathrm{spec}(\boldsymbol{\rho}_S) = \mathrm{spec}(\boldsymbol{\rho}_E) = \{\lambda_k\}$. A standard entanglement quantifier is the von Neumann entanglement entropy,

$$S(\boldsymbol{\rho}_S) = -\,\mathrm{Tr}[\boldsymbol{\rho}_S \log \boldsymbol{\rho}_S] = -\sum_k \lambda_k \log \lambda_k = S(\boldsymbol{\rho}_E) \tag{1.6}$$

which vanishes iff $r = 1$ and increases with the spread of the spectrum.

Density operators. When $r > 1$ in Eq. 1.5, no *ray* in $\mathcal{H}_S$ represents the local state[2], that is, the state of the system S alone without conditioning on E. We must update the postulates of Sec. 1.2.1 to work instead with density operators, starting with (i). Let $\mathcal{T}(\mathcal{H})$ denote the trace-class operators with trace norm $\|\boldsymbol{A}\|_1 = \mathrm{Tr}\sqrt{\boldsymbol{A}^\dagger \boldsymbol{A}}$.[3] States are described by density operators in the convex set of operators with non negative eigenvalues

$$\mathcal{S}(\mathcal{H}) = \{\boldsymbol{\rho} \in \mathcal{T}(\mathcal{H}) \mid \boldsymbol{\rho} \geq 0,\ \mathrm{Tr}\,\boldsymbol{\rho} = 1\}\,. \tag{1.7}$$

Every $\boldsymbol{\rho} \in \mathcal{S}(\mathcal{H})$ admits a spectral decomposition

$$\boldsymbol{\rho} = \sum_k \lambda_k\, |\psi_k\rangle\langle\psi_k|\,, \tag{1.8}$$

interpretable as a statistical ensemble (the convex decomposition need not be unique). The state is *pure* iff $\mathrm{Tr}(\boldsymbol{\rho}^2) = 1$ (equivalently, there exists one and only one $\bar{k}$ such that $\lambda_{\bar{k}} = 1$ and $\lambda_{k\neq\bar{k}} = 0$); otherwise it is *mixed*. Any observable on S is represented as $\boldsymbol{O}_S \otimes \boldsymbol{I}_E$, where $\boldsymbol{O}_S$ is a Hermitian operator. Hence

$$\langle \boldsymbol{O}_S \rangle = \mathrm{Tr}_S(\boldsymbol{\rho}_S \boldsymbol{O}_S) = \mathrm{Tr}_{SE}(\boldsymbol{\rho}_{SE} \boldsymbol{O}_S \otimes \boldsymbol{I}_E) = \langle\psi|\, \boldsymbol{O}_S \otimes \boldsymbol{I}_E\, |\psi\rangle\,, \tag{1.9}$$

where $\boldsymbol{\rho}_{SE} = |\psi\rangle\langle\psi|$: the reduced state ρ_S reproduces the local measurement statistics on S, as it will be detailed below.

Time evolution. Replacing the state vector $|\psi\rangle$ by a density operator $\boldsymbol{\rho}$ in Eq. 1.2 of the postulate (ii), we obtain the Liouville-von Neumann equation

$$\frac{d}{dt}\boldsymbol{\rho}(t) = -\,i\,[\boldsymbol{H}(t), \boldsymbol{\rho}(t)], \qquad \boldsymbol{\rho}(t) = \boldsymbol{U}(t)\boldsymbol{\rho}(0)\boldsymbol{U}^\dagger(t), \tag{1.10}$$

where $\boldsymbol{U}(t) = \mathcal{T}\, e^{-i\int_0^t \boldsymbol{H}(\tau)\, d\tau}$ is the time-ordered propagator of the time dependent Hamiltonian $H(t)$.

[2] When $r > 1$, the state $|\psi\rangle$ of Eq. 1.4 is a purification of the mixed state $\boldsymbol{\rho}_S$ (or, equivalently, of $\boldsymbol{\rho}_E$).

[3] $(\mathcal{T}(\mathcal{H}), \|\cdot\|_1)$ is a Banach space. The trace distance is $D(\boldsymbol{\rho}, \boldsymbol{\sigma}) = \frac{1}{2}\|\boldsymbol{\rho} - \boldsymbol{\sigma}\|_1$. Its Banach dual is $\mathcal{B}(\mathcal{H})$, the space of bounded operators with operator norm $\|X\|_\infty = \sup_{\|\psi\|=1} \|X\psi\|$, via the pairing $\langle \rho, X\rangle = \mathrm{Tr}(\rho X)$ and Hölder's inequality $|\,\mathrm{Tr}(\rho X)| \leq \|\rho\|_1\, \|X\|_\infty$.

Measurements. Finally, we can update the measurement postulate (iii). We consider the measurement of an observable $\boldsymbol{O}_S$ acting on $\mathcal{H}_S$. By application of the Born rule on a purification of a composite state $|\psi\rangle \in \mathcal{H}_S \otimes \mathcal{H}_E$ the probability of measuring λ_i is

$$p_i = \langle\psi|\, \boldsymbol{\Pi}_i \otimes \boldsymbol{I}_E \,|\psi\rangle = \mathrm{Tr}_{SE}\Big[\, |\psi\rangle\langle\psi|\, \boldsymbol{\Pi}_i \otimes \boldsymbol{I}_E\Big] = \mathrm{Tr}_S\Big[\boldsymbol{\Pi}_i \boldsymbol{\rho}_S \boldsymbol{\Pi}_i\Big] = \mathrm{Tr}_S\Big[\boldsymbol{\Pi}_i \boldsymbol{\rho}_S\Big]. \tag{1.11}$$

Similarly, the post-measurement state becomes

$$\boldsymbol{\rho}_S^{(i)} = \frac{1}{p_i} \boldsymbol{\Pi}_i \boldsymbol{\rho}_S \boldsymbol{\Pi}_i. \tag{1.12}$$

If a measurement is made, but the result is not recorded, then the post-measurement state is given by the proper mixture [81] $\boldsymbol{\rho}_S = \sum_i p_i \boldsymbol{\rho}_S^{(i)} = \sum_i \boldsymbol{\Pi}_i \boldsymbol{\rho}_S \boldsymbol{\Pi}_i$.[4] Consistently, for a projective measurement, $\boldsymbol{O}_S = \sum_i \lambda_i \boldsymbol{\Pi}_i$, $p_i = \mathrm{Tr}(\boldsymbol{\Pi}_i \boldsymbol{\rho}_S)$.

1.2.3 Completely positive maps

We now restrict our attention to the evolution in time of the subsystem S. The relevant object for prediction and control is the time-dependent reduced state

$$\boldsymbol{\rho}_S(t) = \mathrm{Tr}_E\Big[\boldsymbol{\rho}_{SE}(t)\Big], \qquad \boldsymbol{\rho}_{SE}(t) = \boldsymbol{U}(t)\, \boldsymbol{\rho}_{SE}(0)\, \boldsymbol{U}^\dagger(t). \tag{1.13}$$

If correlations between S and E build up during the joint unitary evolution generated by $\boldsymbol{H}(t)$, then the map dictating the evolution $\boldsymbol{\rho}_S(0) \mapsto \boldsymbol{\rho}_S(t)$ is, in general, non-unitary [26]. This motivates representing the reduced dynamics by a *state-to-state* map[5] $\mathcal{E} : \mathcal{S}(\mathcal{H}_S) \to \mathcal{S}(\mathcal{H}_S)$ that is linear, positive and trace-preserving (TP), without imposing unitarity. To ensure physicality even when S is entangled with an arbitrary auxiliary system E, the stronger notion of complete positivity [27, 80] can be introduced and characterized via Kraus's theorem, built on Stinespring's 1955 dilation result [27].

Definition 1.2.1 (Complete positivity). *A linear map $\mathcal{E} : \mathcal{T}(\mathcal{H}_S) \to \mathcal{T}(\mathcal{H}_S)$ is* positive *if $\boldsymbol{X} \geq 0 \Rightarrow \mathcal{E}(\boldsymbol{X}) \geq 0$. It is* completely positive (CP) *if the dilation*

$$\mathcal{E} \otimes \mathcal{I}_E : \mathcal{T}(\mathcal{H}_S \otimes \mathcal{H}_E) \to \mathcal{T}(\mathcal{H}_S \otimes \mathcal{H}_E)$$

acting on the extended Hilbert space $\mathcal{H}_S \otimes \mathcal{H}_E$ is also positive.

Remark 1.2.1 (Heisenberg adjoint). *For any linear map $\mathcal{E} : \mathcal{T}(\mathcal{H}) \to \mathcal{T}(\mathcal{H})$, the* Heisenberg adjoint *$\mathcal{E}^\dagger : \mathcal{B}(\mathcal{H}) \to \mathcal{B}(\mathcal{H})$ is defined by $\mathrm{Tr}(\mathcal{E}(\boldsymbol{\rho})\, \boldsymbol{X}) = \mathrm{Tr}\Big(\boldsymbol{\rho}\, \mathcal{E}^\dagger(\boldsymbol{X})\Big)$; thus $\mathcal{E}$ is trace-preserving iff $\mathcal{E}^\dagger$ is unital, i.e. it preserves identity.*

[4] This holds in general, i.e. even for $\boldsymbol{\rho} = |\psi\rangle\langle\psi| \in \mathcal{T}(\mathcal{H})$, and gives another physical motivation for the introduction of density operators: describing proper mixtures of possible state preparations. Projective measurements can be generalized by relaxing orthogonality and idempotence. A measurement is specified by a collection of positive semidefinite operators $\{E_i\}$ ("effects") with $\sum_i E_i = I$, called a *positive operator-valued measure* (POVM) [80]. Outcome probabilities are $p_i = \mathrm{Tr}(E_i\, \rho)$. If a measurement instrument $\{M_i\}$ is specified with $E_i = M_i^\dagger M_i$, then the (selective) post-measurement state is $\rho^{(i)} = M_i \rho M_i^\dagger / p_i$. See the Naimark's dilation theorem [79].

[5] We denote superoperators with calligraphic characters.

Theorem 1.2.1 (Kraus, 1971). *Given a linear trace preserving map $\mathcal{E} : \mathcal{T}(\mathcal{H}_S) \to \mathcal{T}(\mathcal{H}_S)$, the following statements are equivalent:*

1. *$\mathcal{E}$ is CP.*

2. *$\mathcal{E}$ admits Kraus representation*

$$\mathcal{E}(\boldsymbol{\rho}_S) = \sum_k \boldsymbol{M}_k \boldsymbol{\rho}_S \boldsymbol{M}_k^\dagger, \qquad \textit{with} \qquad \sum_k \boldsymbol{M}_k^\dagger \boldsymbol{M}_k = \boldsymbol{I}. \tag{1.14}$$

3. *$\mathcal{E}$ can be expressed as*

$$\mathcal{E}(\boldsymbol{\rho}_S) = \mathrm{Tr}_E \left[\boldsymbol{U}(\boldsymbol{\rho}_S \otimes \boldsymbol{\rho}_E)\boldsymbol{U}^\dagger \right], \tag{1.15}$$

where $\boldsymbol{\rho}_E \in \mathcal{T}(\mathcal{H}_E)$ is an arbitrary state, and $\boldsymbol{U} \in \mathcal{B}(\mathcal{H}_S \otimes \mathcal{H}_E)$

Point (3) of Kraus theorem ensures us that a linear map is CPTP if and only if it can be obtained as the partial trace of a unitary acting on a larger Hilbert space, consistent with the composite-system viewpoint. In other words, CPTP maps describing reduced dynamics are precisely those reduced evolutions obtained by unitary dynamics on a larger space with a *fixed* auxiliary state $\boldsymbol{\rho}_E$, independent of the input state $\boldsymbol{\rho}_S$. Point (2) provides a practical representation of such maps. Eq. 1.15 should be read as a single-step dilation. If correlations build between S and E, then it is not possible to iterate the evolution of $\mathcal{E}$. This motivates asking for more stringent properties for maps to model open quantum system evolution, as we will see in Sec. 1.3.

To conclude this section, we report an important result by Choi, which gives a useful criterion for testing complete positivity in finite dimension [27].

Theorem 1.2.2 (Choi, 1972). *Consider the linear map $\mathcal{E} : \mathcal{M}_{n\times n}(\mathbb{C}) \to \mathcal{M}_{d\times d}(\mathbb{C})$[6]. Given the orthonormal basis $\{e_i\}$ of $\mathbb{C}^n$, $\mathcal{E}$ is completely positive iff the Choi matrix $C_\mathcal{E}$ is positive semidefinite*

$$C_\mathcal{E} \;=\; \sum_{i,j=1}^{n} \mathcal{E}(|e_i\rangle\langle e_j|) \otimes |e_i\rangle\langle e_j| \;\in\; \mathcal{M}_{nd\times nd}(\mathbb{C}). \tag{1.16}$$

From the Choi matrix $C_\mathcal{E}$ it is possible to recover the Kraus representation of Theorem 1.2.1: given that the Choi matrix is positive semidefinite, then it is possible to write its spectral decomposition as

$$C_\mathcal{E} = \sum_k \lambda_k \, |W_k\rangle\!\rangle\langle\!\langle W_k| \,, \tag{1.17}$$

where $\langle\!\langle W_k|$ is a vectorized operator[7], related to the Kraus operators as $|M_k\rangle\!\rangle = \sqrt{\lambda_k}\,|W_k\rangle\!\rangle$. Recovering their operator form yields Eq. 1.14.

[6] In this thesis we mostly consider $d = n$.

[7] $\langle\!\langle A|$, $|B\rangle\!\rangle$ are row/column vectorized representations of operators, with inner product $\langle\!\langle A|B\rangle\!\rangle = \mathrm{Tr}(\boldsymbol{A}^\dagger \boldsymbol{B})$

1.3 Quantum dynamical semigroup evolution

In Sec. 1.2 we motivated nonunitary reduced dynamics for composite systems and required that the reduced map remain positive under arbitrary extensions. This led to CPTP maps as the correct notion of physical reduced evolutions. Kraus's theorem gives equivalent operator-sum and unitary-dilation characterizations, while Choi's criterion tests complete positivity in finite dimensions. The next step is to identify generators of continuous one-parameter families of CPTP maps (quantum dynamical semigroups). The Gorini, Kossakowski, Sudarshan, Lindblad (GKSL) theorem provides the canonical Lindblad form for open quantum system dynamics [27]. This will serve as our starting point for model reduction with adiabatic elimination in Chap. 2.

Definition 1.3.1. *A time-homogeneous* quantum dynamical semigroup *on* $\mathcal{T}(\mathcal{H})$ *is a family* $\{\Phi_t\}_{t\geq 0}$ *of linear maps such that*

- *Semigroup composition holds:* $\Phi(t+s) = \Phi(t) \circ \Phi(s)\ \forall t, s > 0,\ \Phi_0 = \mathcal{I}$
- $\Phi(t)$ *is CPTP* $\forall t$
- $\Phi(t) \to \mathcal{I}$ *for* $t \to 0$
- $\Phi(t)$ *is continuous* $\forall t > 0$

The generator $\mathcal{L}$ of $\Phi(t)$ is defined by the strong limit

$$\mathcal{L}(\boldsymbol{\rho}) = \lim_{t\to 0} \frac{\Phi(t)\boldsymbol{\rho} - \boldsymbol{\rho}}{t}, \tag{1.18}$$

and $\Phi(t) = e^{t\mathcal{L}}$ in the semigroup sense. Setting $\boldsymbol{\rho}(t) = \Phi(t)\boldsymbol{\rho}(0)$, we have the following master equation for the density operator $\boldsymbol{\rho}_S \in \mathcal{T}(\mathcal{H}_S)$

$$\frac{d}{dt}\boldsymbol{\rho}(t) = \mathcal{L}(\boldsymbol{\rho}(t)). \tag{1.19}$$

The generator of the semigroup dynamics can be characterized by the following theorem (which can be extended to the infinite dimensional case).

Theorem 1.3.1 (Gorini, Kossakowski, Sudarshan, 1976. Lindblad, 1976)**.** *Let* $n = \dim(\mathcal{H}_S)$. *A linear operator* $\mathcal{L} : \mathcal{T}(\mathcal{H}_S) \to \mathcal{T}(\mathcal{H}_S)$ *is the generator of a quantum dynamical semigroup iff it is of the form*

$$\mathcal{L}(\boldsymbol{\rho}(t)) = -i[\boldsymbol{H}_S, \boldsymbol{\rho}(t)] + \sum_{i=1}^{n^2-1} \kappa_i \left(\boldsymbol{L}_i \boldsymbol{\rho}(t) \boldsymbol{L}_i^\dagger - \frac{1}{2} \left\{ \boldsymbol{\rho}(t),\, \boldsymbol{L}_i^\dagger \boldsymbol{L}_i \right\} \right), \tag{1.20}$$

with $\kappa_i \geq 0$, $\boldsymbol{L}_i \in \mathcal{B}(\mathcal{H}_S)$ *are bounded operators not necessarily Hermitian, and* $\boldsymbol{H}_S = \boldsymbol{H}_S^\dagger$.

The super operators defined as $\mathcal{D}[\boldsymbol{L}](\bullet) = \boldsymbol{L} \bullet \boldsymbol{L}^\dagger - \frac{1}{2}\{\bullet, \boldsymbol{L}^\dagger \boldsymbol{L}\}$ are called *dissipators*. We will call the operators $\boldsymbol{L}_i$ *jump operators* [26, 27]. We note that it is also possible to encounter the Lindblad equation in the non-diagonal Kossakowski form

$$\mathcal{L}(\boldsymbol{\rho}(t)) = -i[\boldsymbol{H}_S, \boldsymbol{\rho}(t)] + \sum_{i,j} h_{ij} \left(\boldsymbol{L}_i \boldsymbol{\rho}(t) \boldsymbol{L}_j^\dagger - \frac{1}{2} \left\{ \boldsymbol{\rho}(t),\, \boldsymbol{L}_j^\dagger \boldsymbol{L}_i \right\} \right), \tag{1.21}$$

where the matrix $H = (h_{ij})$ is positive semi-definite. Diagonalization of H yields the diagonal form of Eq. 1.20. A time dependent GKSL form (with Hamiltonian $\boldsymbol{H}_S(t)$, operators $\boldsymbol{L}_\mu(t)$ and non-negative rates $\gamma_\mu(t) \geq 0$ in Eq. 1.20) exists only for CP-divisible evolutions, see [82].

Adiabatic elimination based model reduction. The GKSL equation is the starting point for the adiabatic elimination model reduction technique, which will be studied in Chap. 2 and Chap. 3. The reduced model resulting from adiabatic elimination is a linear superoperator, which, when trace-preserving and Hermiticity-preserving, can be put in the form given by Eq. 1.21. Not necessarily in GKSL form: checking the positivity of the matrix $H = (h_{ij})$ of Eq. 1.21 allows to check if the reduced evolution can be put in GKSL form, and thus if it is CPTP. As it was shown in [83], and as we will see in Chap. 2, 3, this is not always the case.

1.4 Microscopic derivation of the GKSL equation

In Sec. 1.3 we have retraced the steps that led to the GKSL Eq. 1.20 as an effective model of open quantum system dynamics from a priori considerations on quantum mechanics. This axiomatic derivation however does not give a precise prescription on how to write the jump operators L_i and rates κ_i. In practice, what is usually done is to take an *a posteriori* path, that is, to write the Hamiltonian for the system S and to add some realistic dissipators. The parameters of the time evolution, such as the rates, are usually fitted. Two natural questions follow: (i) can κ_i and $\boldsymbol{L}_i$ be derived from first principles? and (ii) how should one treat time dependence (most notably, in the context of circuit QED introduced by control drives), given that the semigroup picture is time-homogeneous? (iii) When S interacts at discrete times t_1 and t_2 with E, system–environment correlations build up, so that the evolution map from t_1 to t_2 for the system S alone is not in general CPTP, unless the state of the environment E is reinitialized after each interaction with the system. How then can we obtain a closed continuous time equation for $\boldsymbol{\rho}_S(t)$, depending (approximately) only on $\boldsymbol{\rho}_S(t)$, and consistent with the exact unitary dynamics on SE?

To this end, it is instructive to recall the historical development of the GKLS equation [84]. Master equations were first obtained microscopically by modeling the full Hamiltonian on $\mathcal{H}_{SE} = \mathcal{H}_S \otimes \mathcal{H}_E$ and deriving a reduced evolution for S via projection methods [85, 86, 87], with the GKSL characterization coming later. The microscopic route remains essential to address (i)–(ii). Microscopic derivations can be viewed as model reduction by projection: the effective dynamics of the relevant degrees of freedom is obtained by eliminating the irrelevant ones via a projection superoperator. This comes

with a cost: namely, as we will see, one has to compute a memory kernel entering a convolution integral, or, equivalently a time dependent generator, rather than a simpler time-homogeneous linear superoperator. Through the Nakajima–Zwanzig framework this yields the time-convolutionless master equation, an exact representation that holds in general settings with only weak assumptions [88, 26]. At weak coupling, the time-convolutionless master equation kernel is determined by the environmental two-time correlation functions; these are the same correlators that enter Kubo linear-response theory [89]. We then show how the second order expansion of the time-convolutionless generator, under the Markov limit and secular approximation, reduces to the GKSL form (1.20), with jump operators and rates fixed microscopically by bath spectra.

1.4.1 Time-convolutionless master equation

We now rederive the weak-coupling Bloch–Redfield equation [26, 27] and, after secularization, the GKSL master equation in the Schrödinger picture using the time-convolutionless projection operator formalism. We include this derivation both as a worked example, that illustrates the assumptions required to obtain a master equation, and as an introduction to the formalism we later apply in Chap. 3 to reduce these very master equations.

Let

$$\boldsymbol{H} = \boldsymbol{H}_S \otimes \boldsymbol{I}_E + \boldsymbol{I}_S \otimes \boldsymbol{H}_E + \epsilon \boldsymbol{H}_I \tag{1.22}$$

be the Hamiltonian for the total evolution of a composite system in $\mathcal{T}(\mathcal{H})$, where $\mathcal{H} = \mathcal{H}_S \otimes \mathcal{H}_E$. Typically, the subsystem E is identified as the *environment* interacting through $\epsilon \boldsymbol{H}_I$ (where ϵ is a dimensionless coupling parameter) with the system S, constituted by the relevant degrees of freedom. The Liouvillian (Eq. 1.10) decomposes as

$$\frac{d}{dt}\boldsymbol{\rho}(t) = (\mathcal{L}_0 + \epsilon \mathcal{L}_1)\,\boldsymbol{\rho}(t), \quad \mathcal{L}_0 \bullet \equiv -i\,[\boldsymbol{H}_S \otimes \boldsymbol{I}_E + \boldsymbol{I}_S \otimes \boldsymbol{H}_E, \bullet\,], \quad \mathcal{L}_1 \bullet \equiv -i\,[\boldsymbol{H}_I, \bullet\,]. \tag{1.23}$$

We then decompose the total Hilbert space using two projection super-operators, which for now we keep general without specifying their action, acting from $\mathcal{T}(\mathcal{H})$ to $\mathcal{T}(\mathcal{H})$. Let $\mathcal{P}$ be a projection superoperator satisfying $\mathcal{P}^2 = \mathcal{P}$. The superoperator projecting onto the complementary subspace is given by $\mathcal{Q} = \mathcal{I} - \mathcal{P}$. From its construction, it is evident that $\mathcal{Q}$ satisfies $\mathcal{Q}^2 = \mathcal{Q}$ and $\mathcal{P}\mathcal{Q} = \mathcal{Q}\mathcal{P} = 0$.

Projected dynamics. The TCL master equation is an evolution equation for $\mathcal{P}\rho(t)$–our reduced model, obtained by elimination of $\mathcal{Q}\rho(t)$. From Eq. 1.23, the coupled equations for $\mathcal{P}\rho(t)$ and $\mathcal{Q}\rho(t)$ can be written as

$$\begin{aligned} \frac{d}{dt}\mathcal{P}\boldsymbol{\rho}(t) &= \mathcal{P}\mathcal{L}(\mathcal{P}+\mathcal{Q})\boldsymbol{\rho}(t), \\ \frac{d}{dt}\mathcal{Q}\boldsymbol{\rho}(t) &= \mathcal{Q}\mathcal{L}(\mathcal{P}+\mathcal{Q})\boldsymbol{\rho}(t). \end{aligned} \tag{1.24}$$

Solving the equation for $\mathcal{Q}\boldsymbol{\rho}(t)$ formally (with initial time set to 0) gives

$$\mathcal{Q}\boldsymbol{\rho}(t) = e^{\mathcal{Q}\mathcal{L}\mathcal{Q}t}\mathcal{Q}\boldsymbol{\rho}(0) + \int_0^t ds\, e^{\mathcal{Q}\mathcal{L}\mathcal{Q}(t-s)}\mathcal{Q}\mathcal{L}\mathcal{P}\boldsymbol{\rho}(s), \tag{1.25}$$

To obtain a *time-local* equation, we write $\boldsymbol{\rho}(s) = e^{\mathcal{L}(s-t)}\boldsymbol{\rho}(t)$ and substitute into Eq. 1.25:

$$[\mathcal{I} - \Sigma(t)]\mathcal{Q}\boldsymbol{\rho}(t) = e^{\mathcal{Q}\mathcal{L}\mathcal{Q}t}\mathcal{Q}\boldsymbol{\rho}(0) + \Sigma(t)\mathcal{P}\boldsymbol{\rho}(t). \tag{1.26}$$

The expression of Eq. 1.26 links $\mathcal{P}\boldsymbol{\rho}(t)$, $\mathcal{Q}\boldsymbol{\rho}(t)$ and $\mathcal{Q}\boldsymbol{\rho}(0)$, and implicitly carries memory via

$$\Sigma(t) = \int_0^t d\tau\, e^{\mathcal{Q}\mathcal{L}\mathcal{Q}\tau}\mathcal{Q}\mathcal{L}\mathcal{P}e^{-\mathcal{L}\tau}. \tag{1.27}$$

The usefulness of this will become clear in the next paragraphs.

Canonical projection and factorized initial state. So far the TCL construction held for an arbitrary projector $\mathcal{P}$. From here on we specify the action of $\mathcal{P}$ as the canonical system–environment projection

$$\boldsymbol{\rho} \mapsto \mathcal{P}\boldsymbol{\rho} = \mathrm{Tr}_E[\boldsymbol{\rho}] \otimes \boldsymbol{\rho}_E \equiv \boldsymbol{\rho}_S \otimes \boldsymbol{\rho}_E, \tag{1.28}$$

where we choose the environmental state defined by the projection $\mathcal{P}$ as a stationary fixed environment state $\boldsymbol{\rho}_E$ (e.g. the thermal state for $\boldsymbol{H}_E$) such that $[\boldsymbol{H}_E, \boldsymbol{\rho}_E] = 0$, which implies $[\mathcal{L}_0, \mathcal{P}] = 0$ and $e^{\mathcal{L}_0 t}\mathcal{P}\boldsymbol{\rho}(t) = e^{-i\boldsymbol{H}_S t}\boldsymbol{\rho}_S e^{+i\boldsymbol{H}_S t} \otimes \boldsymbol{\rho}_E$. We can then replace $\mathcal{Q}\mathcal{L}\mathcal{P}$ by $\mathcal{Q}\mathcal{L}_1\mathcal{P}$ in Eq. 1.25 due to $\mathcal{Q}\mathcal{P} = 0$:

$$\Sigma(t) = \epsilon \int_0^t d\tau\, e^{\mathcal{Q}\mathcal{L}\mathcal{Q}\tau}\mathcal{Q}\mathcal{L}_1\mathcal{P}e^{-\mathcal{L}\tau}. \tag{1.29}$$

We assume a *factorized initial state* $\boldsymbol{\rho}(0) = \boldsymbol{\rho}_S \otimes \boldsymbol{\rho}_E$ we have $\mathcal{P}\boldsymbol{\rho}(0) = \boldsymbol{\rho}(0)$ and hence $\mathcal{Q}\boldsymbol{\rho}(0) = 0$, so the inhomogeneous term in Eq. 1.26 vanishes.

Born approximation. Since $\Sigma(t) = \mathcal{O}(\epsilon)$, the inverse $[\mathcal{I} - \Sigma(t)]^{-1}$ exists provided its Neumann series $\sum_k \Sigma(t)^k$ converges, which is guaranteed for small ϵ and short times t [26]. With $\mathcal{Q}\boldsymbol{\rho}(0) = 0$, Eq. 1.26 yields

$$\mathcal{Q}\boldsymbol{\rho}(t) = \Big([\mathcal{I} - \Sigma(t)]^{-1} - \mathcal{I}\Big)\,\mathcal{P}\boldsymbol{\rho}(t), \qquad \boldsymbol{\rho}(t) = [\mathcal{I} - \Sigma(t)]^{-1}\,\mathcal{P}\boldsymbol{\rho}(t). \tag{1.30}$$

Truncating to second order (Born) gives

$$\boldsymbol{\rho}(t) = \Big[\mathcal{I} + \Sigma_1(t)\Big]\mathcal{P}\boldsymbol{\rho}(t) + \mathcal{O}(\epsilon^2), \qquad \Sigma_1(t) = \epsilon \int_0^t d\tau\, e^{\mathcal{L}_0\tau}\,\mathcal{Q}\mathcal{L}_1\mathcal{P}\,e^{-\mathcal{L}_0\tau}. \tag{1.31}$$

Substituting into $\frac{d}{dt}(\mathcal{P}\boldsymbol{\rho}) = \mathcal{P}\mathcal{L}\,\boldsymbol{\rho}$ gives the TCL equation up to $\mathcal{O}(\epsilon^2)$:

$$\frac{d}{dt}\,\mathcal{P}\boldsymbol{\rho}(t) = \mathcal{P}\mathcal{L}\Big[\mathcal{I} + \Sigma_1(t)\Big]\mathcal{P}\boldsymbol{\rho}(t) = \mathcal{P}\mathcal{L}\mathcal{P}\,\boldsymbol{\rho}(t) + \epsilon\,\mathcal{P}\mathcal{L}_1\int_0^t d\tau\, e^{\mathcal{L}_0\tau}\,\mathcal{Q}\mathcal{L}_1\mathcal{P}\,e^{-\mathcal{L}_0\tau}\,\mathcal{P}\boldsymbol{\rho}(t), \tag{1.32}$$

where again, since $[\mathcal{L}_0, \mathcal{P}] = 0$, we have $\mathcal{P}\mathcal{L}_0\mathcal{Q} = 0$, so $\mathcal{P}\mathcal{L}\Big[\mathcal{I} + \Sigma_1(t)\Big]\mathcal{P} = \mathcal{P}\mathcal{L}_0\mathcal{P} + \epsilon\,\mathcal{P}\mathcal{L}_1\Big[\mathcal{I} + \Sigma_1(t)\Big]\mathcal{P}$ with $\mathcal{P}\mathcal{L}_0\,\Sigma_1(t)\,\mathcal{P} = 0$.

Bloch-Redfield. We now consider a system-environment interaction of the kind

$$\epsilon \boldsymbol{H}_I = \sum_\alpha \boldsymbol{A}_\alpha \otimes \boldsymbol{B}_\alpha, \tag{1.33}$$

where we assume for simplicity that $\mathrm{Tr}_E[\boldsymbol{B}_\alpha \boldsymbol{\rho}_E] = 0$. It follows that $\mathcal{P}\mathcal{L}_1\mathcal{P} = 0$ and $\mathcal{Q}\mathcal{L}_1\mathcal{P} = \mathcal{L}_1\mathcal{P}$. We can write Eq. 1.32 explicitly, using Eq. 1.28, where the commutators are given by the action of $\mathcal{L}_1$

$$\frac{d}{dt}\boldsymbol{\rho}_S(t) \otimes \boldsymbol{\rho}_E = -i[\boldsymbol{H}_S, \boldsymbol{\rho}_S(t)] \otimes \boldsymbol{\rho}_E - \epsilon^2 \int_0^t d\tau \, \mathrm{Tr}_E \left\{[\boldsymbol{H}_I, [\boldsymbol{H}_I(-\tau), \boldsymbol{\rho}_S(t) \otimes \boldsymbol{\rho}_E]]\right\} \otimes \boldsymbol{\rho}_E. \tag{1.34}$$

We remark that

$$e^{\mathcal{L}_0 \tau} \, \mathcal{L}_1 \, e^{-\mathcal{L}_0 \tau} \bullet = -i[\, \boldsymbol{H}_I(-\tau), \bullet \,], \quad \text{with} \quad \boldsymbol{H}_I(\tau) = e^{+i(\boldsymbol{H}_S + \boldsymbol{H}_E)\tau} \boldsymbol{H}_I e^{-i(\boldsymbol{H}_S + \boldsymbol{H}_E)\tau}, \tag{1.35}$$

while the state remains at the current Schrödinger time $\rho_S(t)$. Expanding the commutators, and introducing environmental correlation function

$$C_{\alpha\beta}(\tau) = \mathrm{Tr}_E(\boldsymbol{B}_\alpha(\tau)\boldsymbol{B}_\beta(0)\boldsymbol{\rho}_E), \tag{1.36}$$

with $\boldsymbol{A}_\beta(-\tau) = e^{-i\boldsymbol{H}_S\tau}\boldsymbol{A}_\beta e^{+i\boldsymbol{H}_S\tau}$, and $\boldsymbol{B}_\alpha(\tau) = e^{+i\boldsymbol{H}_E\tau}\boldsymbol{B}_\alpha e^{-i\boldsymbol{H}_E\tau}$, we get the Bloch-Redfield equation

$$\begin{aligned} \frac{d}{dt}\boldsymbol{\rho}_S(t) &= -i[\boldsymbol{H}_S, \boldsymbol{\rho}_S(t)] \\ + \sum_{\alpha,\beta} \int_0^t d\tau \, &\left[C_{\alpha\beta}(\tau)[\boldsymbol{A}_\beta(-\tau)\boldsymbol{\rho}_S(t), \, \boldsymbol{A}_\alpha] + C_{\beta\alpha}(-\tau)[\boldsymbol{A}_\alpha, \, \boldsymbol{\rho}_S(t)\boldsymbol{A}_\beta(-\tau)]\right]. \end{aligned} \tag{1.37}$$

Markov approximation. We now assume that the contribution of $C_{\alpha\beta}(\tau)$ is negligible for times larger than τ_E, so that we can extend the integral support $\int_0^t \to \int_0^\infty$, which yields a time-independent generator in the TCL equation [26, 27] (see Sec. 1.5 for explicit timescales in a concrete model). This assumption reflects physically [26, 27] the fact that the environmental correlation functions $C_{\alpha\beta}$ decay on a short time compared to the relaxation time of the system $\tau_E \ll \tau_S$. By taking the eigen-decomposition of the system operators $\boldsymbol{A}_\alpha = \sum_\omega \boldsymbol{A}_\alpha(\omega)$ with respect to the transition frequencies ω (the eigenvalues of the commutator superoperator $-[\boldsymbol{H}_S, \bullet]$, $[\boldsymbol{H}_S, \boldsymbol{A}_\alpha(\omega)] = -\omega \boldsymbol{A}_\alpha(\omega)$) and by defining

$$\Gamma_{\alpha\beta}(\omega) = \int_0^{+\infty} d\tau e^{i\omega\tau} C_{\alpha\beta}(\tau) = \frac{1}{2}\gamma_{\alpha\beta}(\omega) + iS_{\alpha\beta}(\omega), \tag{1.38}$$

where $\gamma_{\alpha\beta}$ and $S_{\alpha\beta}$ are respectively the real and imaginary part of $\Gamma_{\alpha\beta}(\omega)$ we can write the Bloch-Redfield master equation

$$\begin{aligned} \frac{d}{dt}\boldsymbol{\rho}_S(t) &= -i[\boldsymbol{H}_S + \boldsymbol{H}_{LS}, \, \boldsymbol{\rho}_S(t)] \\ + \sum_{\omega,\omega'} \sum_{\alpha,\beta} \gamma_{\alpha\beta}(\omega) &\left[\boldsymbol{A}_\beta(\omega)\boldsymbol{\rho}_S(t)\boldsymbol{A}_\alpha^\dagger(\omega') - \frac{1}{2}\{\boldsymbol{A}_\alpha^\dagger(\omega')\boldsymbol{A}_\beta(\omega), \, \boldsymbol{\rho}_S(t)\}\right], \end{aligned} \tag{1.39}$$

where $\boldsymbol{H}_{LS} = \sum_{\omega,\alpha,\beta} S_{\alpha\beta}(\omega)\boldsymbol{A}_\alpha^\dagger(\omega)\boldsymbol{A}_\beta(\omega)$ is the Lamb-shift term. We quantify the system relaxation time by the inverse dissipative gap [27],

$$\tau_S \simeq \left[\min_{\alpha,\beta,\omega} \mathrm{spect}\{\gamma_{\alpha\beta}(\omega)\}\right]^{-1}. \tag{1.40}$$

Secular approximation. We retain only terms with $\omega = \omega'$, since cross terms carry phases $e^{i(\omega'-\omega)t}$ in the interaction picture with respect to $\boldsymbol{H}_S$, where $\boldsymbol{A}_\alpha(\omega)$ is replaced by $\boldsymbol{A}_\alpha(\omega)e^{-i\omega t}$, and average out over any coarse-graining window Δt with $|\omega - \omega'|\,\Delta t \gg 1$. Equivalently, introduce the rate scale

$$\Gamma = \max_{\omega,\,\alpha,\,\beta} \gamma_{\alpha\beta}(\omega), \tag{1.41}$$

and require

$$\min_{\omega \neq \omega'} |\omega - \omega'| \;\gg\; \Gamma. \tag{1.42}$$

After secular approximation we obtain the GKSL form, guaranteed by the fact that the matrix $G = (\gamma_{\alpha\beta})$ is positive semi-definite for each fixed ω [27] and can be diagonalized, yielding

$$\begin{aligned} \frac{d}{dt}\boldsymbol{\rho}_S(t) &= -i[\boldsymbol{H}_S + \boldsymbol{H}_{LS},\, \boldsymbol{\rho}_S(t)] \\ &+ \sum_{\omega,\mu} \gamma_\mu(\omega) \left[\boldsymbol{L}_\mu(\omega)\boldsymbol{\rho}_S(t)\boldsymbol{L}_\mu^\dagger(\omega) - \frac{1}{2}\left\{ \boldsymbol{L}_\mu^\dagger(\omega)\boldsymbol{L}_\mu(\omega),\, \boldsymbol{\rho}_S(t) \right\} \right]. \end{aligned} \tag{1.43}$$

1.4.2 Time dependence and partial secularization

Some remarks about this derivation are in order.

- There are textbook cases where microscopic derivations collapse to a single, physically transparent jump operator (e.g., a driven damped harmonic oscillator with single-photon loss dissipator $\mathcal{D}[\boldsymbol{a}]$ [26]). In general, one obtains a sum of dissipators over the transition frequencies $\mathcal{D}[\boldsymbol{L}_\mu(\omega)]$ weighted by rates $\gamma_\mu(\omega)$ determined by bath spectra.

- The autonomous Bloch-Redfield equation 1.39 for $\boldsymbol{\rho}_S$ is not in GKSL form due to the presence of cross-terms $\omega \neq \omega'$. The associated Kossakovski matrix is not in general positive semidefinite, and thus complete positivity is not guaranteed, although often holding. Complete positivity can be recovered in practice by either (i) retaining the finite-time upper limit in the time-convolutionless kernel (Eq. 1.37) [90], (ii) dynamical coarse graining, which averages the generator over a window and yields a GKSL form [91, 92], (iii) *partial secularization*, which clusters transition frequencies into blocks and discards inter-block terms, restoring complete positivity [93, 94, 95] (iv) full secularization.

TCL approach to model reduction. The TCL master equations derived in this section serve as the starting point for the time-convolutionless formulation of adiabatic elimination, presented in Chap. 3, which enables model reduction of master equations, not necessarily in GKSL form, characterized by a timescale separation by discarding rapidly decaying degrees of freedom. We note that the results of Chap.2 as well apply directly to Bloch–Redfield–type equations such as Eq. (1.39). In fact, complete positivity is not a prerequisite for performing model reduction. Adiabatic elimination itself can alter CP properties of the reduced dynamics, and care is required when interpreting the resulting generator [83].

1.5 Time-dependent unitary linear system-boson model

In Sec. 1.4 we have seen how effective master equations can be derived from a time-independent microscopic model by application of successive approximations. The treatment of driven-dissipative systems in full generality is, however, more challenging. Adding time-dependence to the system Hamiltonian, such as in the case of a control drive acting on the system, complicates the writing of the propagators. Additionally, in realistic devices, the system contains multiple interacting modes that are simultaneously driven and dissipative.

The microscopic derivation of master equations in the presence of time-dependent Hamiltonians requires going to the interaction picture with respect to a time-dependent Hamiltonian $\boldsymbol{H}_0(t) = \boldsymbol{H}_S(t) + \boldsymbol{H}_E$,

$$\boldsymbol{H}_I(t) = \boldsymbol{U}^\dagger(t)\boldsymbol{H}_I\boldsymbol{U}(t) \qquad \boldsymbol{U}(t) = \mathcal{T}e^{-i\int_0^t d\tau \boldsymbol{H}_0(\tau)}, \tag{1.44}$$

so one must compute a time-ordered propagator rather than a simple exponential as in the time independent case. For arbitrary time dependence, microscopic constructions of time-dependent Markovian master equations [82] are available in the adiabatic limit of slow drive frequency compared to the system's timescales [55], and beyond the adiabatic regime, for systems with clear time-scale separation conditions [96, 97]. The approach presented in [98] consists of deriving a completely positive map for the reduced density matrix by Dyson expansion of the propagator.

For periodic Hamiltonians, $\boldsymbol{H}_0(t) = \boldsymbol{H}_0(t+T)$, Floquet-Markov master equations can be derived in the Floquet eigenbasis [99, 100, 101, 26]. However, when computing numerically the propagator for resonantly-driven infinite-dimensional systems (e.g. the closed driven harmonic oscillator, with no dissipation), the finite Hilbert-space truncation leads to spurious avoided crossings, created by the cutoff-dependent level repulsion [102, 103]. Analytically, in the resonant case, small frequency splittings in the denominators make the perturbative expansion of $\boldsymbol{U}(t)$ ill-defined, requiring careful treatment [78, 104]. Introducing a damping at rate κ regularizes these denominators by giving finite linewidths to the frequency transitions, enabling a perturbative expansion of the master equation not plagued by small denominators [105, 106, 107, 108].

Moreover, when the system-environment coupling is strong or characterized by a structured dependence on frequency, the environmental correlation time can be comparable to the system's: $\tau_E \sim \tau_S$. System and environment then evolve and build correlations on the timescales of interest. A faithful description must therefore track in real time the system-environment correlations, pushing beyond Markovian models and posing a substantial computational challenge [109, 110, 82, 111, 112, 113]. A structured dependence on frequency is ubiquitous in circuit QED, as it will be analyzed in detail in the next chapters. Even if the electromagnetic environment of a transmission line can be modeled as Ohmic [29], cavity modes due to buffer modes, readout, or filters induce "Lorentzian" peaks ([114, 29], see also the examples in Sec 2.3, Sec. 3.4). Moreover, it is possible to engineer filters that cut Lorentzian notches in the spectral density of the environment, adding further structure [19]. Under drive, "AC-Stark shifts" and power broadening [29] move and widen system transition frequencies, sweeping them across

these environmental features and potentially bringing them into resonance. Accurately capturing these effects is therefore essential.

These considerations motivate the need for tools that can deal automatically with experimentally relevant driven-dissipative problems in the presence of structured environments. In our contribution, see Chap. 5, instead of reducing the complexity of the time evolution by partitioning the Hilbert space into a relevant set of degrees of freedom (the system S) and an irrelevant one (the environment E), we specify the microscopic model for the full system-environment evolution, and we compress its unitary dynamics using a combination of chain mapping [69, 70] and tensor network methods [72, 73]. Computing the full unitary dynamics with tensor networks thus serves as a non-perturbative benchmark: it flags when approximate master equations break positivity and Markovianity, at the cost of entanglement-limited computational effort. We now introduce the model used throughout.

1.5.1 Unitary evolution in the presence of a bosonic environment

We consider the time-dependent total Hamiltonian on $\mathcal{H} = \mathcal{H}_S \otimes \mathcal{H}_E$ of the linear system-boson Hamiltonian [26, 68]

$$\boldsymbol{H}(t) = \boldsymbol{H}_S \otimes \boldsymbol{I}_E + \boldsymbol{H}_d(t) \otimes \boldsymbol{I}_E + \boldsymbol{I}_S \otimes \boldsymbol{H}_E + \boldsymbol{H}_I, \tag{1.45}$$

where $\boldsymbol{H}_d(t)$ is a time-dependent drive acting on the system, $\boldsymbol{H}_S$ is an arbitrary Hamiltonian for the system. We specify the model of the environment as a continuum of bosonic modes interacting via dipolar coupling with the system, as in the Caldeira-Leggett model [68], which is often used to model a transmission line [29]

$$\boldsymbol{H}_E = \int_0^\infty d\omega \omega \boldsymbol{b}_\omega^\dagger \boldsymbol{b}_\omega, \qquad \boldsymbol{H}_I = \boldsymbol{A}_S \otimes \int_0^\infty d\omega \sqrt{J(\omega)} (\boldsymbol{b}_\omega^\dagger + \boldsymbol{b}_\omega). \tag{1.46}$$

Here $\boldsymbol{A}_S = \boldsymbol{A}_S^\dagger$ is a system operator, $[\boldsymbol{b}_\omega, \boldsymbol{b}_{\omega'}^\dagger] = \delta(\omega - \omega')$, and $J(\omega)$ is the spectral density function, defining the system-environment coupling. A counterterm is often included to absorb the static renormalization term into the system Hamiltonian $\boldsymbol{H}_S$ ([68] see Appendix 7.6 for explicit derivation). At zero temperature, the sum on the environmental correlation functions of Eq. 1.36 can be written as

$$C(t) = \int_0^{+\infty} d\omega J(\omega) e^{-i\omega t}. \tag{1.47}$$

From this, it becomes clear that the Markov approximation performed in Sec. 1.4 can become invalid depending on the frequency bandwidth and structure of the spectral density function $J(\omega)$.

When $[\boldsymbol{H}, \boldsymbol{A}_S] = 0$, the time evolution starting from a pure factorized state of system and environment

$$|\psi(0)\rangle_{SE} = |\psi(0)\rangle_S \otimes |\psi(0)\rangle_E \tag{1.48}$$

can be treated analytically (for the time independent case see [26]). Closed form solutions exist for bosonic Hamiltonians linearly coupled to the oscillators bath, which

are examples treated in [115], . Otherwise, an analytical treatment becomes more involved. Possible strategies are the formalism of Feynman-Vernon influence functional [116]. Here, we resort to numerics. The numerical treatment has to be handled carefully: the open quantum system problem is now formulated as a many-body problem, and a series of approximations have to be introduced to enable converged numerical simulations.

We note that, in contrast to master-equation based methods, computing the full unitary time evolution leaves the environmental degrees of freedom open to inspection, allowing for direct evaluation of environmental observables. Moreover, the full-unitary approach is non-perturbative, making these methods interesting for benchmarking of master equations. In other words, the same Born-Markov-secular approximations applied in Sec. 1.4 can be applied specifically to Eq. 1.46, and the resulting master equations can be quantitatively compared to the exact numerics. We also remark that the full unitary evolution leads by construction to CPTP dynamics from the point of view of the system; the reduced map from 0 to t obtained by tracing the chain is therefore CPTP up to numerical error.

By choosing to keep the environmental degrees of freedom, the compression of the unitary evolution generated by Eq. 1.46 will happen on a non-linear variational manifold with dimension significantly larger than $\mathcal{H}_S$ (as in Sec. 1.4), but significantly smaller than the dimension of the total Hilbert space $\mathcal{H}$. This manifold captures the entanglement structure of the many body state: the lower the entanglement, the more efficient the compression, and thus the lower the dimension of the reduced model, as we will detail in Chap 4. As we will see in Chap. 4, the accuracy of this reduced model is controlled by entanglement: when entanglement is modest the compression is faithful, whereas growing entanglement degrades the approximation unless the nonlinear manifold is enlarged.

Open quantum systems as many-body problems. The Hamiltonian of Eq. 1.46 couples the (driven) system to *all* of the environmental degrees of freedom, creating $S-E$ correlations during the dynamics. The cost of the simulation depends on the growth of the system-environment correlations during the time evolution. If such growth is moderate, it is then possible to constrain the time evolution on a lower dimensional manifold of the Hilbert space characterized by limited entanglement. To this end, it is convenient to map instead the problem on a chain with only nearest-neighbors interactions [70, 69, 71]. Such a one dimensional problem can be efficiently treated with matrix product states algorithms [72, 117]. We present a short introduction to the chain mapping and tensor network simulation methods in Chapter 4. We present their application in Chapter 5, where we use them to investigate how a qubit's relaxation rate dependence on the drive amplitude can be influenced by environmental characteristics. We exploit the access to the environmental degrees of freedom to simulate the emission spectrum of the driven dissipative system.

1.6 Outline of this manuscript

The rest of this manuscript is organized as follows.

In Chapter 2 we present a formulation of the adiabatic elimination of fast decaying degrees of freedom in open quantum systems which can be performed with a series expansion in the timescale separation. Exploiting Sylvester's equation and adjoint dynamics, we obtain systematic, explicit expressions at high orders.

In Chapter 3 we present the time-convolutionless master equation formulation of adiabatic elimination. We show that the TCL formulation yields results equivalent to those obtained from the standard formulation of adiabatic elimination. By applying the TCL master equation formulation to typical examples, we demonstrate a practical methodology for performing adiabatic elimination calculation.

In Chapter 4 we present a self-contained introduction to time evolving density matrix using orthogonal polynomials algorithm (TEDOPA)/matrix product state (MPS) methods for open quantum systems. After a brief overview of tensor networks formalism (Sec. 4.1), we introduce the star-to-chain mapping and discretization (Sec. 4.2) for the linear system-boson model, and extend it to finite temperature via T-TEDOPA. The emphasis is on the concepts needed for reliable simulations. Implementation details, practical convergence diagnostics, and a typical workflow are summarized in Sec. 4.3.

In Chapter 5 we apply the TEDOPA/MPS methods to simulate the dynamics of a two-level system (qubit) coupled to a driven cavity, itself coupled to a bath with structured frequency dependence. This setup allows for investigation of the role of environmental degrees of freedom in the T_1 vs $\bar{n}$ problem, that is, how the relaxation rate of the qubit depends on the strength of the drive on the cavity, as well as the computation of the emission spectrum of the driven qubit-cavity system into the environment.

In Chapter 6 we summarize the results and discuss future work.

Chapter 2

Adiabatic elimination with fast unitary dynamics

Contents

Contributions. This chapter is based on joint work with my supervisor Alain Sarlette and Pierre Rouchon, both permanent members at the Quantic team and early contributors to the geometric approach to adiabatic elimination [58, 59, 118]. The main motivation came from a collaboration with the experimental team of Samuel Deléglise at Laboratoire Kastler Brossel. In their experiment, a heavy Fluxonium qubit in the few-MHz range is dipolarly coupled to a readout cavity in the GHz-range [63]. The large detuning suggests eliminating the cavity mode while allowing potentially fast unitary dynamics on the qubit. Adiabatic elimination has been developed via a series-expansion formula, whose practical bottleneck is the inversion of the fast Lindbladian; closed-form results in the presence of fast unitary dynamics on the target system remain scarce. I initially derived the reduced dynamics by postulating an ansatz to solve the equations defining them, following [60]. Later, P. Rouchon recognized that these equations can be recast as Sylvester equations, which removes the inversion bottleneck and yields general, explicit expressions. This reformulation also clarifies how adiabatic elimination can be performed while avoiding a rotating-wave approximation. The propositions and examples presented here synthesize these developments. Our work appears in: Angela Riva, Alain Sarlette, and Pierre Rouchon. "Explicit formulas for adiabatic elimination

with fast unitary dynamics". In: *2024 IEEE 63rd Conference on Decision and Control (CDC)*. 2024, pp. 755–760. DOI: 10.1109/CDC56724.2024.10886784.

2.1 Model reduction for master equations

This chapter develops adiabatic elimination for bipartite open quantum systems with fast unitary center dynamics. We begin with a concise overview of adiabatic elimination for open quantum systems, and specify the bipartite setting in Sec. 2.1.1.

Using coherence-enabled quantum effects in practical platforms means balancing two competing requirements: isolation (to protect coherences) and rapid control (to implement operations). Modern devices are therefore composite, high-dimensional, and multi-timescale. The useful quantum information represents only a small, ideally non-decaying part of this system, while engineered auxiliary sectors provide fast stabilization and control. Model reduction via adiabatic elimination aims to summarize the effect of these fast, stabilizing degrees of freedom on the target dynamics, ideally with interpretable formulas to guide system design [39, 40, 41, 48].

There are multiple formulations of adiabatic elimination for open quantum systems described by master equations. One approach extends techniques from Hamiltonian closed systems, applying the Born-Markov approximation [119, 120, 121, 57, 55], Laplace-transform methods on projected master equations [122, 56, 108], and the Schrieffer-Wolff transformation [123, 124]. Another approach exploits the linearity of master equations for open quantum systems, which allows, in principle, a spectral decomposition of the vectorized Liouvillian generator of the dynamics, very much like Hamiltonian (block-)diagonalization, defining a lower-dimensional subspace to which trajectories are attracted in the long-time domain [125, 126]. Such a geometric picture led to a general and systematic formulation of adiabatic elimination for GKSL dynamics, rooted in singular perturbation theory for dynamical systems [127]: identifying, via series expansion, the variables and dynamics corresponding to a lower-dimensional invariant subspace where dynamics is at the slowest timescale. The approach was applied to perform model reduction inside a single system (Cartesian product, [58]) and in more general composite systems (tensor product, [59]). Because the GKSL master equation is linear, one can mirror the reduction in Heisenberg picture, which often simplifies multi-partite settings and numerics [118, 128]. As demonstrated in [83], the reduced dynamics is not guaranteed to be in GKSL form.

All previously mentioned studies address scenarios where a rapid relaxation, characterized by eigenvalues with large negative real parts $\mathrm{Re}\lambda_i$, surrounds a slower evolution on a slow invariant subspace associated with eigenvalues close to the origin of the complex plane. However, like in the center manifold theory [129], the same model reduction technique should also admit a rapid relaxation towards an invariant subspace featuring large, almost purely imaginary eigenvalues, with magnitude in principle comparable to $\mathrm{Im}\lambda_i$ (unitary dynamics). This would fit practical situations where e.g. the stabilized system rotates unitarily at characteristic frequencies comparable to $\mathrm{Re}\lambda_i$, allowing for both *in resonance* and *out of resonance* control [63]. When the system frequencies are in resonance, a unitary change of frame at the resonant frequency nearly cancels the fast unitary dynamics, justifying a secular approximation; when out of resonance, in any

rotating frame, a large frequency detuning survives, preventing such an approximation. We illustrate both cases in Sec. 2.3 with Example 1 (in resonance) and Example 2 (out of resonance).

A first study of adiabatic elimination in presence of fast unitary dynamics was carried out in [60, 61], leading to abstract expressions up to second-order expansion, where second-order expressions were obtained under explicit assumptions on the spectrum of the Hamiltonian generating the fast unitary dynamics. In this chapter we provide integral formulas for high order adiabatic elimination in the presence of fast unitary dynamics on the target system, without any condition on it, other than being associated to eigenvalues with real part close to zero (Section 2.2). We then highlight how, for typical systems of interest, namely, eliminating a rapidly decaying harmonic oscillator environment, these integral formulas also lead more easily to interpretable explicit expressions for the long-term dynamics on the invariant manifold, where the integrals can be computed in analytic form (see the physical examples of section 2.3). The two key technical ingredients are the use of stable Sylvester equation solutions (Proposition 1) and the treatment of the typical dynamics on the adjoint state (Proposition 2). Our key assumption, in contrast to [60, 61], is to be able to explicitly write the Heisenberg dynamics of the fast system.

2.1.1 Adiabatic elimination for bipartite systems

This section recalls the setting and adiabatic elimination approach for bipartite Hilbert spaces as used e.g. in [59, 60, 83]. To go beyond the case of bipartite systems see e.g. [58, 118].

We consider a density operator $\boldsymbol{\rho}(t)$ at time t, defined over a bipartite Hilbert space $\mathcal{H} = \mathcal{H}_A \otimes \mathcal{H}_B$. The time evolution of this operator is described by the linear dynamics:

$$\frac{d}{dt}\boldsymbol{\rho}(t) = \mathcal{L}(\boldsymbol{\rho}(t)) = -i(\boldsymbol{H}_A \otimes \boldsymbol{I}_B)^{\times}(\boldsymbol{\rho}(t)) + \mathcal{I}_A \otimes \mathcal{L}_B(\boldsymbol{\rho}(t)) - ig\boldsymbol{H}_I^{\times}(\boldsymbol{\rho}(t)). \tag{2.1}$$

Here $\boldsymbol{I}_M$ is the identity operator and $\mathcal{I}_M$ the identity superoperator, associated to the Hilbert space $\mathcal{H}_M$, and we use the notation $\boldsymbol{H}^{\times}(\bullet) \equiv [\boldsymbol{H}, \bullet]$ to represent the commutator with operator H, i.e. $[\boldsymbol{H}, \bullet] = \boldsymbol{H}\bullet - \bullet\boldsymbol{H}$. The GKSL term for the mode B takes the general form:

$$\mathcal{L}_B(\bullet) = -i\boldsymbol{H}_B^{\times}(\bullet) + \kappa \sum_k \mathcal{D}[\boldsymbol{L}_k](\bullet)\ , \tag{2.2}$$

with κ the damping rate and $\mathcal{D}[\boldsymbol{L}](\bullet) \equiv \boldsymbol{L}\bullet\boldsymbol{L}^{\dagger} - \frac{1}{2}(\boldsymbol{L}^{\dagger}\boldsymbol{L}\bullet + \bullet\boldsymbol{L}^{\dagger}\boldsymbol{L})$ the dissipation channel associated to operator $\boldsymbol{L}$. The coupling between $\mathcal{H}_A$ and $\mathcal{H}_B$ is weak and Hamiltonian:

$$g\boldsymbol{H}_I = g\sum_k \boldsymbol{A}_k \otimes \boldsymbol{B}_k \tag{2.3}$$

with A_k and B_k operators on $\mathcal{H}_A$ and $\mathcal{H}_B$ respectively and g a small positive parameter.

The adiabatic elimination procedure is based on the assumption that the system exhibits a clear separation of timescales, allowing for a perturbative expansion in the small parameter $\epsilon = g/\kappa \ll 1$. The dynamics for $g = \epsilon = 0$ is assumed "relatively

easy to compute", with $\mathcal{L}_B$ converging exponentially towards a unique equilibrium state $\bar{\boldsymbol{\rho}}_B$ and subsystem A independently rotating with a Hamiltonian $\boldsymbol{H}_A$; thus, $\mathcal{L}\boldsymbol{\rho}$ then features a subspace $\mathscr{M}^{(0)}$ spanned by $\{\boldsymbol{\rho} = \boldsymbol{\rho}_s \otimes \bar{\boldsymbol{\rho}}_B$, for any ρ_s on $\mathcal{H}_A\}$, which is invariant under the operation of $\mathcal{L}_0$, that is, $\mathcal{L}(\mathscr{M}^{(0)}) \subseteq \mathscr{M}^{(0)}$. All eigenvalues of $\mathcal{L}_0$ on $\mathscr{M}^{(0)}$ are purely imaginary (center manifold [129]). For $\epsilon \neq 0$, the interaction Hamiltonian H_I only acts as a perturbation on this situation. Classical results [127] from the theory of dynamical systems guarantee the existence of $\mathscr{M}^{(\epsilon)}$, a subspace ϵ-close to $\mathscr{M}^{(0)}$, invariant under the full dynamics $\mathcal{L}$. The goal is then to efficiently compute the long-term dynamics, taking place on $\mathscr{M}^{(\epsilon)}$. Such dynamics happens on the subspace spanned by the eigenoperators of $\mathcal{L}$ associated to eigenvalues with real part close to zero, while relaxation is slow (small real part), fast unitary dynamics is allowed.

When $\epsilon \neq 0$, the interaction Hamiltonian creates correlations between the two subsystems A and B. As a result, the invariant subspace $\mathscr{M}^{(\epsilon)}$ does not take the same form as $\mathscr{M}^{(0)}$ anymore. Still, it is convenient to parameterize states on $\mathscr{M}^{(\epsilon)}$ by using $\boldsymbol{\rho}_s \otimes \bar{\boldsymbol{\rho}}_B \in \mathscr{M}^{(0)}$ as coordinates. Indeed, the dynamics are then reduced to $\boldsymbol{\rho}_s$ whose evolution can be interpreted in comparison to the case $\epsilon = 0$. In order to characterize the long-term behavior of the system, we then aim to find two linear, time independent maps: $\mathcal{L}_s$, describing the dynamics of the reduced system via its coordinates $\frac{d}{dt}\boldsymbol{\rho}_s = \mathcal{L}_s(\boldsymbol{\rho}_s)$; and $\mathcal{K}$, mapping $\boldsymbol{\rho}_s$ to the solution $\boldsymbol{\rho} = \mathcal{K}(\boldsymbol{\rho}_s) \in \mathscr{M}^{(\epsilon)}$ of the complete dynamics 2.1. Expressing that the evolution of $\boldsymbol{\rho}_s$ must mirror the one of $\mathcal{K}(\boldsymbol{\rho}_s)$ leads to the condition:

$$\mathcal{K}(\mathcal{L}_s(\boldsymbol{\rho}_s)) = \mathcal{L}(\mathcal{K}(\boldsymbol{\rho}_s)). \tag{2.4}$$

Following approximation theory, well-justified when the function to be found is analytic, we solve 2.4 by expanding the maps $\mathcal{L}_s$ and $\mathcal{K}$ in powers of $\epsilon \ll 1$,

$$\mathcal{L}_s(\boldsymbol{\rho}_s) = \sum_{j=0}^{\infty} \epsilon^j \mathcal{L}_{s,j}(\boldsymbol{\rho}_s), \quad \mathcal{K}(\boldsymbol{\rho}_s) = \sum_{j=0}^{\infty} \epsilon^j \mathcal{K}_j(\boldsymbol{\rho}_s)\ , \tag{2.5}$$

and requiring to satisfy the condition 2.4 separately at each order ϵ^j. Since the lowest-order contributions are the dominant ones, usually only the solutions $\mathcal{L}_{s,j}$,$\mathcal{K}_j$ for the first few orders are computed explicitly, e.g. $j \leq 2$. The solution to 2.4 is certainly not unique, as it involves a coordinate choice on $\mathscr{M}^{(\epsilon)}$, expressed via $\mathcal{K}$.

The most natural solution to 2.4 at order ϵ^0, is the one corresponding to $\epsilon = 0$, thus

$$\mathcal{L}_{s,0}(\boldsymbol{\rho}_s) = -i\boldsymbol{H}_A^{\times}(\boldsymbol{\rho}_s), \quad \mathcal{K}_0(\boldsymbol{\rho}_s) = \boldsymbol{\rho}_s \otimes \bar{\boldsymbol{\rho}}_B\,. \tag{2.6}$$

In this chapter, we further specify the coordinate choice by imposing the *partial trace gauge*, namely $\boldsymbol{\rho}_s = \mathrm{Tr}_B(\boldsymbol{\rho}) = \mathrm{Tr}_B(\mathcal{K}(\boldsymbol{\rho}_s))$ at all orders of approximation, where Tr_B denotes the partial trace over $\mathcal{H}_B$. This choice implies that $\mathrm{Tr}_B\,\mathcal{K}_1 = \mathrm{Tr}_B\,\mathcal{K}_2 = ... = 0$.

Note that when $\boldsymbol{H}_A = 0$, we get $\mathcal{L}_{s,0} = 0$ and this simplifies all further orders (see e.g. [59]). Our contributions are meant to address the difficulties appearing in solving 2.4, 2.5 at orders ϵ^1, ϵ^2 for $\boldsymbol{H}_A \neq 0$.

2.2 Explicit formulas for adiabatic elimination with fast unitary dynamics

Given the elements $\mathcal{L}_{s,0}, \mathcal{K}_0$ specified in Eq. 2.6, we can solve the invariance equation 2.4 at higher orders by expanding Eq. 2.5. The computation of the first order contribution to the reduced dynamics $\mathcal{L}_{s,1}$ poses no particular problem, and yields

$$\epsilon\mathcal{L}_{s,1}(\boldsymbol{\rho}_s) = -ig \sum_k \mathrm{Tr}(\boldsymbol{B}_k\bar{\boldsymbol{\rho}}_B)[\boldsymbol{A}_k, \boldsymbol{\rho}_s]. \tag{2.7}$$

We give the details of the derivation of Eq. 2.7 in the proof of Proposition 1 below. Our results concern the next order. Proposition 1 derives a new integral closed form for the map $\mathcal{K}_1$ by solving a Sylvester equation. In Proposition 2, the second-order reduced dynamics $\mathcal{L}_{s,2}$, involving the commutator between H_I and $\mathcal{K}_1$, is re-expressed with this form, putting the integral on a dual operator which is more systematically manageable in typical situations. Examples illustrate the usefulness of these formulas in Section 2.3. We start by defining some simplifying notation.

Definition 2.2.1. *Operator $\boldsymbol{B}_{0,k}$ on $\mathcal{H}_B$ is defined as*

$$\boldsymbol{B}_{0,k} = \boldsymbol{B}_k - \mathrm{Tr}_B(\boldsymbol{B}_k\bar{\boldsymbol{\rho}}_B)\boldsymbol{I}_B. \tag{2.8}$$

Definition 2.2.2. *Operator $\boldsymbol{A}_k^-(t)$ on $\mathcal{H}_A$ is defined as*

$$\boldsymbol{A}_k^-(t) = e^{-it\boldsymbol{H}_A^\times}(\boldsymbol{A}_k) = e^{-it\boldsymbol{H}_A}\boldsymbol{A}_k e^{it\boldsymbol{H}_A}. \tag{2.9}$$

(Note that this is the opposite propagation to the Heisenberg picture evolution under $\boldsymbol{H}_A$, see Remark 2.2.1.)

Proposition 1. *Consider model 2.1 and the adiabatic elimination expansion of Section 2.1.1 with partial trace gauge. The first order map $\mathcal{K}_1$ is given by*

$$\epsilon\mathcal{K}_1(\boldsymbol{\rho}_s) = -ig\sum_k \int_0^{+\infty} \left\{\boldsymbol{A}_k^-(t)\boldsymbol{\rho}_s \otimes e^{t\mathcal{L}_B}(\boldsymbol{B}_{0,k}\bar{\boldsymbol{\rho}}_B) - \boldsymbol{\rho}_s\boldsymbol{A}_k^-(t) \otimes e^{t\mathcal{L}_B}(\bar{\boldsymbol{\rho}}_B\boldsymbol{B}_{0,k})\right\}dt. \tag{2.10}$$

Proof. By inserting 2.5 in the general invariance equation 2.4 and grouping terms of order ϵ, we obtain the first order invariance equation:

$$\begin{aligned} -i[\boldsymbol{H}_A \otimes \boldsymbol{I}_B, \epsilon\mathcal{K}_1(\boldsymbol{\rho}_s)] + \mathcal{I}_A \otimes \mathcal{L}_B(\epsilon\mathcal{K}_1(\boldsymbol{\rho}_s)) - ig[\boldsymbol{H}_I, \mathcal{K}_0(\boldsymbol{\rho}_s)] \\ = \mathcal{K}_0(\epsilon\mathcal{L}_{s,1}(\boldsymbol{\rho}_s)) + \epsilon\mathcal{K}_1(\mathcal{L}_{s,0}(\boldsymbol{\rho}_s)). \end{aligned} \tag{2.11}$$

This equation has two unknowns: $\mathcal{L}_{s1}$ and $\mathcal{K}_1$. Two terms involving $\mathcal{K}_1$ are due to $\boldsymbol{H}_A \neq 0$ and therefore new with respect to [59]. Nevertheless, thanks to the gauge choice with $\mathrm{Tr}_B(\mathcal{K}_1) = 0$, we can much like in [59] apply Tr_B to 2.11 and directly isolate $\mathcal{L}_{s1}$ in the form 2.7. To get this, we further observe that $\mathrm{Tr}_B(\mathcal{L}_B) = 0$ and $\mathrm{Tr}_B(\boldsymbol{H}_A^\times(\bullet)) = \boldsymbol{H}_A^\times(\mathrm{Tr}_B(\bullet))$. Next, inserting 2.7 into 2.11 yields the condition:

$$\begin{aligned} -i[\boldsymbol{H}_A \otimes \boldsymbol{I}_B, \epsilon\mathcal{K}_1(\boldsymbol{\rho}_s)] + \mathcal{I}_A \otimes \mathcal{L}_B(\epsilon\mathcal{K}_1(\boldsymbol{\rho}_s)) \\ + i\epsilon\mathcal{K}_1([\boldsymbol{H}_A, \boldsymbol{\rho}_s]) = ig\textstyle\sum_k [\boldsymbol{A}_k \otimes \boldsymbol{B}_{0,k}, \boldsymbol{\rho}_s \otimes \bar{\boldsymbol{\rho}}_B], \end{aligned} \tag{2.12}$$

to be solved for $\mathcal{K}_1$. At the level of superoperators, 2.12 is in fact a Sylvester equation [130] of the form $AX + XB = C$, where $\epsilon\mathcal{K}_1$ plays the role of the unknown term X. To be explicit: $A \to -i(\boldsymbol{H}_A \otimes \boldsymbol{I}_B)^\times(\bullet) + \mathcal{I}_A \otimes \mathcal{L}_B(\bullet)$, $B \to i\boldsymbol{H}_A^\times(\bullet)$, $C \to ig\sum_k[\boldsymbol{A}_k \otimes \boldsymbol{B}_{0,k}, \bullet \otimes \bar{\boldsymbol{\rho}}_B]$. The solution to this Sylvester equation can be written as

$$X = -\int_0^{+\infty} e^{tA} C e^{tB} dt, \tag{2.13}$$

provided

$$\lim_{t\to+\infty} e^{tA} C e^{tB} = 0\,. \tag{2.14}$$

Using that (super)operators acting on different subsystems commute, as well as $e^{i\boldsymbol{H}^\times}(\boldsymbol{Q}) = e^{i\boldsymbol{H}}\boldsymbol{Q}e^{-i\boldsymbol{H}}$, we obtain:

$$\begin{aligned}
&e^{tA} C e^{tB}(\rho_s)\,/g \\
&= i\sum_k e^{t((-i\boldsymbol{H}_A\otimes\boldsymbol{I}_B)^\times + \mathcal{I}_A\otimes\mathcal{L}_B)}\left[\boldsymbol{A}_k \otimes \boldsymbol{B}_{0,k}, e^{it\boldsymbol{H}_A^\times}(\boldsymbol{\rho}_s) \otimes \bar{\boldsymbol{\rho}}_B\right] \\
&= i\sum_k \left(e^{-it\boldsymbol{H}_A^\times}(\boldsymbol{A}_k)\boldsymbol{\rho}_s \otimes e^{t\mathcal{L}_B}\left(\boldsymbol{B}_{0,k}\bar{\boldsymbol{\rho}}_B\right) - \boldsymbol{\rho}_s e^{-it\boldsymbol{H}_A^\times}(\boldsymbol{A}_k) \otimes e^{t\mathcal{L}_B}\left(\bar{\boldsymbol{\rho}}_B\boldsymbol{B}_{0,k}\right)\right)\,.
\end{aligned}$$

This last expression corresponds to the proposition statement. Since $\lim_{t\to+\infty} e^{t\mathcal{L}_B}(\bullet) = \mathrm{Tr}(\bullet)\bar{\boldsymbol{\rho}}_B$, we have $\lim_{t\to+\infty} e^{t\mathcal{L}_B}(\boldsymbol{B}_{0,k}\bar{\rho}_B) = \lim_{t\to+\infty} e^{t\mathcal{L}_B}(\bar{\boldsymbol{\rho}}_B\boldsymbol{B}_{0,k}) = 0$, such that condition 2.14 is satisfied. □

Remark 2.2.1. *Note that $\boldsymbol{A}_k^-(t)$ in the statement of Proposition 1 follows the opposite dynamics to the Heisenberg evolution under $\boldsymbol{H}_A$. We can understand this as follows. According to $\mathcal{L}_{s,0}$, $\boldsymbol{\rho}_s$ already rotates with $\boldsymbol{H}_A$. Inside the integral of 2.10, we must replace it by $(A_k\rho_s)$ rotating with $\boldsymbol{H}_A$, much like the second tensor factor takes $(\boldsymbol{B}_{0,k}\bar{\boldsymbol{\rho}}_B)$ evolving under $\mathcal{L}_B$.*

Compared to previous work [60, 61], the proposition 1 avoids any technical conditions and the need to solve several equations by treating the components of $\boldsymbol{H}_A$ individually. In turn, it does not guarantee positivity — whose importance has anyway been re-evaluated since [83] — and it leaves a propagator equation to solve, for all t and separately for each subsystem. Instead of computing a large joint propagation on $\mathcal{H}_A \otimes \mathcal{H}_B$, one can compute two lower-dimensional ones acting separately in A and B, substantially easing the computations. In fact, without this formula Eq. 2.10, one is left to solve Eq. 2.11 by positing ansätze for both $\mathcal{K}_1$ and $\mathcal{L}_{s1}$ and then solving additional consistency equations, as in [60], provided that the certain commutation relations are satisfied by the fast unitary dynamics Hamiltonian $\boldsymbol{H}_A$. Propagation on subsystem A, with a fixed Hamiltonian $\boldsymbol{H}_A$, is usually easily computable. Often, $\boldsymbol{H}_A$ can be diagonalized efficiently or commuted through typical operators to compute $\boldsymbol{A}_k^-(t)$. Propagation on subsystem B, requiring diagonalization of a GKSL superoperator, is computationally less convenient. Indeed, even for simple steady-state cases like convergence towards a thermally broadened vacuum, it is not trivial to express the state at any time along the trajectory starting from rather arbitrary initial states like $\boldsymbol{B}_{0,k}\bar{\boldsymbol{\rho}}_B$ [131]. The following result mitigates this difficulty.

Definition 2.2.3. *The operator $\boldsymbol{B}_k(t)$ on $\mathcal{H}_B$, evolving under the action of $\mathcal{L}_B$ in the Heisenberg picture, is defined as:*

$$\boldsymbol{B}_k(t) = e^{t\mathcal{L}_B^*}(\boldsymbol{B}_k), \tag{2.15}$$

with the adjoint $\mathcal{L}^*$ of the GKSL defined as

$$\mathcal{L}^*(\bullet) = +i[\boldsymbol{H}, \bullet] + \kappa \sum_k \left(\boldsymbol{L}_k^\dagger \bullet \boldsymbol{L}_k - \frac{1}{2}(\boldsymbol{L}_k^\dagger \boldsymbol{L}_k \bullet + \bullet \boldsymbol{L}_k^\dagger \boldsymbol{L}_k) \right)$$

.

Proposition 2. *Consider model 2.1 and the adiabatic elimination expansion of Section 2.1.1 with partial trace gauge. The second order reduced dynamics is given by:*

$$\begin{aligned} \epsilon^2 \mathcal{L}_{s,2} = -\frac{g^2}{\kappa} \sum_{k,l} \int_0^{+\infty} \Big\{ & \operatorname{Tr}\{\boldsymbol{B}_l(t)\boldsymbol{B}_{0,k}\bar{\boldsymbol{\rho}}_B\}\big[\boldsymbol{A}_l,\ \boldsymbol{A}_k^-(t)\boldsymbol{\rho}_s\big] \\ & - \operatorname{Tr}\{\boldsymbol{B}_l(t)\bar{\boldsymbol{\rho}}_B\boldsymbol{B}_{0,k}\}\big[\boldsymbol{A}_l,\ \boldsymbol{\rho}_s\boldsymbol{A}_k^-(t)\big]\Big\}\, dt. \end{aligned} \tag{2.16}$$

Proof. In the second order invariance condition:

$$\begin{aligned} -i[\boldsymbol{H}_A \otimes \boldsymbol{I}_B, \epsilon^2\mathcal{K}_2(\boldsymbol{\rho}_s)] + \mathcal{I}_A \otimes \mathcal{L}_B(\epsilon^2\mathcal{K}_2(\boldsymbol{\rho}_s)) - i[g\boldsymbol{H}_I, \epsilon\mathcal{K}_1(\boldsymbol{\rho}_s)] \\ = \mathcal{K}_0(\epsilon^2\mathcal{L}_{s,2}(\boldsymbol{\rho}_s)) + \epsilon^2\mathcal{K}_1(\mathcal{L}_{s,1}(\boldsymbol{\rho}_s)) + \epsilon^2\mathcal{K}_2(\mathcal{L}_{s,0}(\boldsymbol{\rho}_s)), \end{aligned} \tag{2.17}$$

take the partial trace over subsystem B, like we did before Proposition 1 towards getting $\mathcal{L}_{s,1}$, in order to obtain:

$$\epsilon^2\mathcal{L}_{s,2}(\boldsymbol{\rho}_s) = -i\ \operatorname{Tr}_B\{[g\boldsymbol{H}_I, \epsilon\mathcal{K}_1(\boldsymbol{\rho}_s)]\}.$$

Substituting $\boldsymbol{H}_I$, and $\mathcal{K}_1$ from Proposition 1, yields:

$$\begin{aligned} \epsilon^2\mathcal{L}_{s,2}(\boldsymbol{\rho}_s) = (-ig)^2 \sum_{l,k} \Big\{ & \Big[\boldsymbol{A}_l,\ \int_0^{+\infty} c_{k,l}(t)\boldsymbol{A}_k^-(t)\, dt\, \boldsymbol{\rho}_s\Big] \\ & - \Big[\boldsymbol{A}_l,\ \boldsymbol{\rho}_s \int_0^{+\infty} \tilde{c}_{k,l}(t)\boldsymbol{A}_k^-(t)\, dt\Big]\Big\}, \end{aligned} \tag{2.18}$$

where

$$\begin{aligned} c_{k,l}(t) &= \operatorname{Tr}\Big(\boldsymbol{B}_l e^{t\mathcal{L}_B}(\boldsymbol{B}_{0,k}\bar{\boldsymbol{\rho}}_B)\Big) = \operatorname{Tr}\Big(e^{t\mathcal{L}_B^*}(\boldsymbol{B}_l)\boldsymbol{B}_{0,k}\bar{\boldsymbol{\rho}}_B\Big) \\ \tilde{c}_{k,l}(t) &= \operatorname{Tr}\Big(\boldsymbol{B}_l e^{t\mathcal{L}_B}(\bar{\boldsymbol{\rho}}_B\boldsymbol{B}_{0,k})\Big) = \operatorname{Tr}\Big(e^{t\mathcal{L}_B^*}(\boldsymbol{B}_l)\bar{\boldsymbol{\rho}}_B B_{0,k}\Big). \end{aligned} \tag{2.19}$$

On the right-hand side of Eqs. 2.19, we have transferred the GKSL dynamics to the adjoint, in other words evolving the partner operator inside the trace in Heisenberg picture. Recalling Definition 2.2.3, this corresponds to the statement. □

Remark 2.2.2. *Proposition 2 does not claim that the resulting reduced dynamics preserves positivity — thus taking the typical GKSL form with positive dissipation rates. This property is proven in [59] for $\boldsymbol{H}_A = 0$, and in [61] under more technical conditions; it was demonstrated in [83] that there are examples of dynamics where no choice of parametrization can restore complete positivity.*

The essential part of Proposition 2 is to replace, when computing $\mathcal{L}_{s,2}$, the GKSL trajectory starting at $(\boldsymbol{B}_{0,k}\bar{\boldsymbol{\rho}}_B)$ by an adjoint GKSL trajectory on $\boldsymbol{B}_l$. As already noted in [132], the latter is often much easier to compute in typical situations. For instance, the operator propagation can be computed with little more effort than a classical system, when both $\mathcal{L}_B$ and $\boldsymbol{B}_l$ on subsystem B correspond to a so-called linear quantum system [133].

The strategy followed by these two Propositions addresses the same major issue in resolving the series expansion 2.4, 2.5, namely the inversion (in matrix inverse sense) of the generator of the fast dynamics. When pursuing the expansion at higher orders, the main computational issue remains the same, and we can reiterate the same procedure to obtain explicit expressions.

Proposition 3. *Consider model 2.1 and the adiabatic elimination expansion of Section 2.1.1 with partial trace gauge. Assume that the terms of the series expansion have been computed up to $n-1$. Then, for all $n \geq 1$,*

$$\epsilon\mathcal{L}_{s,n}(\boldsymbol{\rho}_s) = -ig\sum_k \left[\boldsymbol{A}_k\,,\,\mathrm{Tr}_B\left((\boldsymbol{I}_A\otimes\boldsymbol{B}_k)\mathcal{K}_{n-1}(\boldsymbol{\rho}_s)\right)\right] \tag{2.20}$$

and $\epsilon\mathcal{K}_n$ can be computed with an integral formula similar to 2.10.

Proof. The invariance condition at order ϵ^n writes:

$$\begin{aligned}\epsilon\mathcal{K}_0(\mathcal{L}_{s,n}(\boldsymbol{\rho}_s)) = \epsilon\left(-i(\boldsymbol{H}_A\otimes\boldsymbol{I}_B)^\times + \mathcal{I}_A\otimes\mathcal{L}_B\right)(\mathcal{K}_n(\boldsymbol{\rho}_s)) - \epsilon\mathcal{K}_n\left(\mathcal{L}_{s,0}(\boldsymbol{\rho}_s)\right)\\ - \epsilon\sum_{m=1}^{n-1}\mathcal{K}_m\left(\mathcal{L}_{s,n-m}(\boldsymbol{\rho}_s)\right) - ig(\boldsymbol{H}_I^\times)(\mathcal{K}_{n-1}(\boldsymbol{\rho}_s))\,.\end{aligned} \tag{2.21}$$

The last line contains only known terms at stage n. Like in Proposition 1, by taking the partial trace over subsystem B, all the terms involving $\mathcal{K}_n$ vanish with the gauge choice $\rho_s = \mathrm{Tr}_B(\rho)$, while $\mathrm{Tr}_B\,\mathcal{K}_0 = \mathcal{I}_s$. The terms in $\mathcal{K}_m$ also vanish by partial trace. We thereby obtain the explicit expression 2.20 for $\mathcal{L}_{s,n}$, assuming all previous orders were known.

After this, the left-hand side of 2.21 is also known and the equation takes the Sylvester form $AX + XB = C$ like in the proof of Prop.1, with A and B unchanged, $\epsilon\mathcal{K}_n$ playing the role of X, and C containing all known terms. There remains to show that the integral form solution 2.13 converges at this order. Like in the proof of Prop.1, this is ensured thanks to $\lim_{t\to+\infty} e^{tA}(\bullet) = \mathcal{U}_{t,A}(\mathrm{Tr}_B(\bullet))\otimes\bar{\boldsymbol{\rho}}_B$ with $\mathcal{U}_{t,A}$ a unitary evolution, and the annihilation of terms under Tr_B. □

When one is only interested in the dynamics $\mathcal{L}_{s,n}$, it is possible to also apply the Heisenberg evolution trick of Proposition 2 iteratively at all orders. This simplifies computations significantly, compared to computing each $\mathcal{K}_m$ explicitly. Investigating this possibility is part of ongoing work.

2.3 Examples

In this section, we give some practical demonstrations of the results presented in Section 2.2. The starting point is a harmonic oscillator B subsystem undergoing so-called

quantum linear dynamics [133]:

$$\mathcal{L}_B(\bullet) = -i\omega_B[\boldsymbol{b}^\dagger\boldsymbol{b}, \bullet] + \kappa_\phi\mathcal{D}[\boldsymbol{b}^\dagger\boldsymbol{b}](\bullet) + \kappa(1+n_{\text{th}})\mathcal{D}[\boldsymbol{b}](\bullet) + \kappa n_{\text{th}}\mathcal{D}[\boldsymbol{b}^\dagger](\bullet), \tag{2.22}$$

with $\boldsymbol{b}$ ($\boldsymbol{b}^\dagger$) the bosonic annihilation (creation) operator, $\boldsymbol{b}^\dagger\boldsymbol{b}$ the number operator, ω_B the undamped harmonic oscillator frequency, κ the damping rate for the dissipator $\mathcal{D}$, and n_{th} the residual thermal excitation. We note that the unique steady state such that $\mathcal{L}_B(\boldsymbol{\rho}) = 0$ is the thermal state,

$$\bar{\boldsymbol{\rho}}_B = \sum_{n=0}^{+\infty} \frac{n_{\text{th}}^n}{(n_{\text{th}}+1)^{n+1}} |n\rangle\langle n| \tag{2.23}$$

in the number-basis $|n\rangle$, i.e. where $\boldsymbol{b}^\dagger\boldsymbol{b} = \sum_{n=0}^{+\infty} n\,|n\rangle\langle n|$.

We couple this system to an arbitrary A subsystem, using a standard dipolar coupling which is also linear:

$$g\tilde{\boldsymbol{H}}_I = g\tilde{\boldsymbol{A}} \otimes (\boldsymbol{b} + \boldsymbol{b}^\dagger)\ . \tag{2.24}$$

In the vast majority of cases [134], the timescale separation between ω_B and g is so large that significant coupling effects on A only happen when $\boldsymbol{H}_A$ contains frequencies close to ω_B. This is what lies behind resonance conditions invoked in high-level descriptions in cavity quantum electrodynamics [134], where fast-rotating terms are discarded and energy-conserving arguments are invoked to simplify Hamiltonian evolutions, as we will detail in Sec. 2.3.1. More precisely, going to a rotating frame with ω_B and averaging the resulting time-dependent dynamics singles out the relevant dominant long-term behavior [135]. Note that this is mathematically justified only if $\omega_B \gg \kappa$ as well. In physics terms [134], the resonance has a width of order κ, thus frequency selection only works for $\kappa \ll \omega_B$.

With the framework developed here, we are able to compare the results of adiabatic elimination in both cases:

- **Example 1**: the physics traditional way, i.e. first averaging out the large part of $\boldsymbol{H}_A$ in a rotating frame, solved in Sec 2.3.1;
- **Example 2**: maintaining all terms in so-called "inertial frame", with thus ω_B and $\boldsymbol{H}_A$ of the same order and non-negligible compared to κ. The results should match those of Section 2.3.1 when ω_B and $\boldsymbol{H}_A$ are close and large compared to κ; otherwise they are new, and discussed in Sec. 2.3.2. The same example is also treated within the time-convolutionless framework in Chap. 3.

2.3.1 Jaynes-Cummings interaction

We now take the model introduced in Sec. 2.3, and specify the subsystem A as a qubit linearly coupled to the subsystem B. In the lab frame we have

$$\tilde{\boldsymbol{H}}_A = -\frac{\omega_{eg}}{2}\boldsymbol{\sigma}_z, \qquad \tilde{\boldsymbol{H}}_I = (\boldsymbol{\sigma}_+ + \boldsymbol{\sigma}_-) \otimes (\boldsymbol{b} + \boldsymbol{b}^\dagger), \tag{2.25}$$

where $\mathcal{H}_A = \text{span}\{|g\rangle, |e\rangle\}$ and $\boldsymbol{\sigma}_- = (\boldsymbol{\sigma}_+)^\dagger = |g\rangle\langle e|$ the qubit lowering operator (from excited to ground state), while the subsystem B evolves according to Eq. 2.22, where we define

$$\tilde{\boldsymbol{H}}_B = \omega_B\boldsymbol{b}^\dagger\boldsymbol{b}. \tag{2.26}$$

Derivation of Jaynes-Cummings Hamiltonian

The Jaynes-Cummings interaction is obtained by only keeping near resonant Hamiltonian terms, see e.g. [134, Chap. 3.4], and corresponds to the canonical theoretical and practical case of coupling subsystem B with a (quasi-)resonant qubit A. We make a change of frame of the GKSL master equation so that $\boldsymbol{\rho}^I(t) = \boldsymbol{U}(t)\,\tilde{\boldsymbol{\rho}}(t)\,\boldsymbol{U}^\dagger(t)$, and the unitary transformation $\boldsymbol{U}(t)$ is given by

$$\boldsymbol{U}(t) = e^{+i\omega_{eg}\left(-\frac{\boldsymbol{\sigma}_z}{2}\otimes\boldsymbol{I}_B+\boldsymbol{I}_A\otimes\boldsymbol{b}^\dagger\boldsymbol{b}\right)t}, \tag{2.27}$$

so that, by inserting $\boldsymbol{\rho}^I(t)$ in the Liouville equation 1.10 we have

$$\boldsymbol{H}^I(t) = \boldsymbol{U}(t)\tilde{\boldsymbol{H}}\boldsymbol{U}^\dagger(t) + i\dot{\boldsymbol{U}}(t)\boldsymbol{U}^\dagger(t), \quad \boldsymbol{L}_k^I(t) = \boldsymbol{U}(t)\tilde{\boldsymbol{L}}_k\boldsymbol{U}^\dagger(t). \tag{2.28}$$

In particular, the jump operators $\tilde{\boldsymbol{L}}_1 = \boldsymbol{n}$, $\tilde{\boldsymbol{L}}_2 = \boldsymbol{b}$ and $\tilde{\boldsymbol{L}}_3 = \boldsymbol{b}^\dagger$ in the lab frame transform as $\boldsymbol{L}_k(t) = e^{i\phi t}\tilde{\boldsymbol{L}}_k$,

$$\boldsymbol{L}_1^I(t) = \boldsymbol{n}, \quad \boldsymbol{L}_2^I(t) = e^{-i\omega_{eg}t}\boldsymbol{b}, \quad \boldsymbol{L}_3^I(t) = e^{+i\omega_{eg}t}\boldsymbol{b}^\dagger, \tag{2.29}$$

so that the associated dissipators are unchanged: $\mathcal{D}[\tilde{\boldsymbol{L}}_k] = \mathcal{D}[\boldsymbol{L}_k^I(t)]$ (invariance under global phase), yielding

$$\begin{aligned}
\boldsymbol{H}_A^I(t) &= 0 \\
\boldsymbol{H}_I^I(t) &= \boldsymbol{\sigma}_+\boldsymbol{b} + \boldsymbol{\sigma}_-\boldsymbol{b}^\dagger + \boldsymbol{\sigma}_+\boldsymbol{b}^\dagger e^{+2i\omega_{eg}t} + \boldsymbol{\sigma}_-\boldsymbol{b}e^{-2i\omega_{eg}t}, \\
\boldsymbol{H}_B^I(t) &= \Delta\boldsymbol{b}^\dagger\boldsymbol{b},
\end{aligned} \tag{2.30}$$

where we introduced the detuning $\Delta = \omega_B - \omega_{eg}$. The terms rotating at $2\omega_{eg}$ in $\boldsymbol{H}_I^I(t)$ can be discarded by first-order averaging [131], provided that

$$g,\ \Delta,\ \kappa,\ \kappa n_{\mathrm{th}},\ \kappa_\phi \ll \omega_{eg}, \tag{2.31}$$

leaving the Jaynes-Cummings interaction

$$\boldsymbol{H}_I = \boldsymbol{\sigma}_+\boldsymbol{b} + \boldsymbol{\sigma}_-\boldsymbol{b}^\dagger. \tag{2.32}$$

This is the effective model on which we perform adiabatic elimination in Example 1.

Adiabatic elimination of the cavity mode

Example 1. *Consider the bipartite system composed of a harmonic oscillator and a two-level system (qubit), whose dynamics is described by*

$$\begin{aligned}
\mathcal{L}_B(\bullet) &= -i\Delta[\boldsymbol{b}^\dagger\boldsymbol{b}, \bullet] + \kappa(1+n_{th})\mathcal{D}[\boldsymbol{b}](\bullet) + \kappa n_{th}\mathcal{D}[\boldsymbol{b}^\dagger](\bullet) + \kappa_\phi\mathcal{D}[\boldsymbol{b}^\dagger\boldsymbol{b}](\bullet)\ , \\
\boldsymbol{H}_A &= 0\ , \\
\boldsymbol{H}_I &= \boldsymbol{\sigma}_+ \otimes \boldsymbol{b} + \boldsymbol{\sigma}_- \otimes \boldsymbol{b}^\dagger,
\end{aligned} \tag{2.33}$$

with $\mathcal{H}_A = span\{|g\rangle, |e\rangle\}$ *and* $\boldsymbol{\sigma}_- = (\boldsymbol{\sigma}_+)^\dagger = |g\rangle\langle e|$ *the qubit lowering operator (from excited to ground state). With Proposition 2, assuming* $\kappa \gg g$*, the second order reduced dynamics is given by*

$$\begin{aligned}\frac{d}{dt}\boldsymbol{\rho}_s = \epsilon^2 \mathcal{L}_{s,2}(\boldsymbol{\rho}_s) = &- i(1+2n_{th})\frac{4\Delta g^2}{|\gamma|^2}\left[\frac{\boldsymbol{\sigma}_z}{2}, \boldsymbol{\rho}_s\right] \\ &+ (1+n_{th})(\kappa+\kappa_\phi)\frac{4g^2}{|\gamma|^2}\mathcal{D}[\boldsymbol{\sigma}_-](\boldsymbol{\rho}_s) \\ &+ n_{th}(\kappa+\kappa_\phi)\frac{4g^2}{|\gamma|^2}\mathcal{D}[\boldsymbol{\sigma}_+](\boldsymbol{\rho}_s),\end{aligned} \tag{2.34}$$

where $\boldsymbol{\sigma}_z = |g\rangle\langle g| - |e\rangle\langle e|$ *and* $\gamma = \kappa + \kappa_\phi + 2i\Delta$.

Solution. The coupling corresponds to our general setting with $\boldsymbol{B}_1 = \boldsymbol{b}$, $\boldsymbol{B}_2 = \boldsymbol{b}^\dagger$, $\boldsymbol{A}_1 = \boldsymbol{\sigma}_+$, $\boldsymbol{A}_2 = \boldsymbol{\sigma}_-$. The zeroth-order dynamics $\mathcal{L}_{s,0}$ vanishes since $\boldsymbol{H}_A = 0$. Note that $\mathcal{L}_B$ in 2.33 still features the unique steady state 2.23, and since $\langle n|\,\boldsymbol{b}\,|n\rangle = 0$ for all n we also have $\mathcal{L}_{s,1} = 0$. To recover the second order reduced dynamics, we start by computing the Heisenberg representation of the coupling operators (Definition 2.2.3):

$$\frac{d}{dt}\boldsymbol{b}^H(t) = \mathcal{L}_B^*(\boldsymbol{b}^H(t)) = -\tfrac{\gamma}{2}\boldsymbol{b}^H(t), \quad \text{thus} \quad \boldsymbol{b}^H(t) = e^{-\frac{\gamma}{2}t}\boldsymbol{b}^H(0), \quad \text{with} \quad \boldsymbol{b}^H(0) = \boldsymbol{b} \tag{2.35}$$

and γ defined as in the statement. By the same calculation,

$$(\boldsymbol{b}^\dagger)^H(t) = e^{-\frac{\gamma^*}{2}t}\,\boldsymbol{b}^\dagger, \quad \text{with} \quad (\boldsymbol{b}^\dagger)^H(0) = \boldsymbol{b}^\dagger. \tag{2.36}$$

In our notation, we keep $\boldsymbol{b}, \boldsymbol{b}^\dagger$ as fixed (time-independent) operators; only their Heisenberg-evolved copies $\boldsymbol{b}^H(t), (\boldsymbol{b}^\dagger)^H(t)$ carry the time dependence. In this step, we highly benefit from assuming a linear quantum system [133] on B in order to obtain such easy closed-form solution. Indeed, for a general quantum system B, the computation of 2.15 in Definition 2.2.3 can be a significant bottleneck.

Exploiting the geometric series introduced by the thermal state $\bar{\boldsymbol{\rho}}_B$, $\sum_{k=0}^{+\infty} q^k = 1/(1-q)$, with $0 < q = n_{\text{th}}/(n_{\text{th}}+1) < 1$, we obtain the coefficients of the second order reduced dynamics $c_{k,l}(t)$ and $\tilde{c}_{k,l}(t)$ mentioned in 2.19 as

$$\begin{aligned}
c_{1,1}(t) &= \mathrm{Tr}\Big(\boldsymbol{b}^H(t)\boldsymbol{b}\bar{\boldsymbol{\rho}}_B\Big) = 0 \\
\tilde{c}_{1,1}(t) &= \mathrm{Tr}\Big(\boldsymbol{b}^H(t)\bar{\boldsymbol{\rho}}_B\boldsymbol{b}\Big) = 0 \\
c_{2,1}(t) &= \mathrm{Tr}\Big(\boldsymbol{b}^H(t)\boldsymbol{b}^\dagger\bar{\boldsymbol{\rho}}_B\Big) = (1+n_{\text{th}})e^{-\frac{\gamma}{2}t} \\
\tilde{c}_{2,1}(t) &= \mathrm{Tr}\Big(\boldsymbol{b}^H(t)\bar{\boldsymbol{\rho}}_B\boldsymbol{b}^\dagger\Big) = n_{\text{th}}e^{-\frac{\gamma}{2}t} \\
c_{1,2}(t) &= \mathrm{Tr}\Big((\boldsymbol{b}^\dagger)^H(t)\boldsymbol{b}\bar{\boldsymbol{\rho}}_B\Big) = n_{\text{th}}e^{-\frac{\gamma^*}{2}t} \\
\tilde{c}_{1,2}(t) &= \mathrm{Tr}\Big((\boldsymbol{b}^\dagger)^H(t)\bar{\boldsymbol{\rho}}_B\boldsymbol{b}\Big) = (n_{\text{th}}+1)e^{-\frac{\gamma^*}{2}t} \\
c_{2,2}(t) &= \mathrm{Tr}\Big((\boldsymbol{b}^\dagger)^H(t)\boldsymbol{b}^\dagger\bar{\boldsymbol{\rho}}_B\Big) = 0 \\
\tilde{c}_{2,2}(t) &= \mathrm{Tr}\Big((\boldsymbol{b}^\dagger)^H(t)\bar{\boldsymbol{\rho}}_B\boldsymbol{b}^\dagger\Big) = 0.
\end{aligned} \tag{2.37}$$

Since $\boldsymbol{H}_A = 0$, the operators $\boldsymbol{A}_k^-(t) = \boldsymbol{A}_k$ are time independent so that we write

$$\epsilon^2 \mathcal{L}_{s2}(\boldsymbol{\rho}_s) = (-ig)^2 \sum_{k,l=1}^{2} \left\{ \int_0^{+\infty} c_{k,l}(t)dt \, [\boldsymbol{A}_l, \, \boldsymbol{A}_k \, \boldsymbol{\rho}_s] - \int_0^{+\infty} \tilde{c}_{k,l}(t)dt \, [\boldsymbol{A}_l, \, \boldsymbol{\rho}_s \boldsymbol{A}_k] \right\}. \tag{2.38}$$

By inserting the coefficients of Eqs. 2.37 in Eq. 2.38, we notice that the integrals to be solved are simply.

$$\int_0^{+\infty} e^{-s\frac{\gamma}{2}} ds = \tfrac{2}{\gamma} = \tfrac{2\gamma^*}{|\gamma|^2} \qquad \int_0^{+\infty} e^{-s\frac{\gamma^*}{2}} ds = \tfrac{2}{\gamma^*} = \tfrac{2\gamma}{|\gamma|^2} \tag{2.39}$$

We can thus define

$$\begin{aligned} \int_0^{+\infty} c_{1,2}(t)dt &= \frac{2n_{\text{th}}}{\gamma} \equiv \alpha, \qquad & \int_0^{+\infty} \tilde{c}_{1,2}(t)dt &= \frac{2(n_{\text{th}}+1)}{\gamma} \equiv \beta, \\ \int_0^{+\infty} \tilde{c}_{2,1}(t)dt &= \frac{2n_{\text{th}}}{\gamma^*} \equiv \alpha^*, \qquad & \int_0^{+\infty} c_{2,1}(t)dt &= \frac{2(n_{\text{th}}+1)}{\gamma^*} \equiv \beta^*. \end{aligned} \tag{2.40}$$

With this we obtain

$$\begin{aligned} \epsilon^2 \mathcal{L}_{s2}(\boldsymbol{\rho}_s) = -g^2 \Big\{ & \alpha \left[\boldsymbol{\sigma}^-\boldsymbol{\sigma}^+ \boldsymbol{\rho}_s - \boldsymbol{\sigma}^+ \boldsymbol{\rho}_s \boldsymbol{\sigma}^-\right] + \alpha^* \left[\boldsymbol{\sigma}^+\boldsymbol{\sigma}^- \boldsymbol{\rho}_s - \boldsymbol{\sigma}^- \boldsymbol{\rho}_s \boldsymbol{\sigma}^+\right] \\ & -\beta \left[\boldsymbol{\sigma}^- \boldsymbol{\rho}_s \boldsymbol{\sigma}^+ - \boldsymbol{\rho}_s \boldsymbol{\sigma}^+ \boldsymbol{\sigma}^-\right] - \beta^* \left[\boldsymbol{\sigma}^+ \boldsymbol{\rho}_s \boldsymbol{\sigma}^- - \boldsymbol{\rho}_s \boldsymbol{\sigma}^- \boldsymbol{\sigma}^+\right] \Big\}, \end{aligned} \tag{2.41}$$

which gives, rearranging the terms,

$$\begin{aligned} \epsilon^2 \mathcal{L}_{s2}(\boldsymbol{\rho}_s) = {} & 2g^2 \text{Re}\beta \left[\boldsymbol{\sigma}^- \boldsymbol{\rho}_s \boldsymbol{\sigma}^+ - \frac{1}{2}\{\boldsymbol{\rho}_s, \boldsymbol{\sigma}^+\boldsymbol{\sigma}^-\}\right] + 2ig^2 \text{Im}\beta[\boldsymbol{\sigma}^+\boldsymbol{\sigma}^-, \boldsymbol{\rho}_s] \\ & + 2g^2 \text{Re}\alpha \left[\boldsymbol{\sigma}^+ \boldsymbol{\rho}_s \boldsymbol{\sigma}^- - \frac{1}{2}\{\boldsymbol{\rho}_s, \boldsymbol{\sigma}^-\boldsymbol{\sigma}^+\}\right] - 2ig^2 \text{Im}\alpha[\boldsymbol{\sigma}^-\boldsymbol{\sigma}^+, \boldsymbol{\rho}_s]. \end{aligned} \tag{2.42}$$

We note that $\boldsymbol{\sigma}^-\boldsymbol{\sigma}^+ = |g\rangle\langle g| = \frac{\boldsymbol{I}+\boldsymbol{\sigma}_z}{2}$, $\boldsymbol{\sigma}^+\boldsymbol{\sigma}^- = |e\rangle\langle e| = \frac{\boldsymbol{I}-\boldsymbol{\sigma}_z}{2}$, and $\boldsymbol{\sigma}_z = |g\rangle\langle g| - |e\rangle\langle e|$, we have

$$\text{Im}\beta[\boldsymbol{\sigma}^+\boldsymbol{\sigma}^-, \boldsymbol{\rho}_s] - \text{Im}\alpha[\boldsymbol{\sigma}^-\boldsymbol{\sigma}^+, \boldsymbol{\rho}_s] = -(\text{Im}\beta + \text{Im}\alpha)\left[\frac{\boldsymbol{\sigma}_z}{2}, \boldsymbol{\rho}_s\right]. \tag{2.43}$$

Inserting the definitions of Eq. 2.40 in Eq. 2.42, and remembering that $(\boldsymbol{\sigma}^-)^\dagger = \boldsymbol{\sigma}^+$, leads to Eq. 2.34. □

General subsystem A. The reduced model 2.34 thus contains a unitary shift with B pulling on the frequency of A (Hamiltonian in $\boldsymbol{\sigma}_z$); and it translates thermal dissipations on B into corresponding dissipations in $\boldsymbol{\sigma}_-$ and $\boldsymbol{\sigma}_+$ on A, yet with decreasing effect as κ increases. This result is well-known [59]. It readily generalizes to a subsystem A of higher dimension. One just replaces, in the model and in the resulting dissipator, $\boldsymbol{\sigma}_-$ by $\boldsymbol{A}$ and $\boldsymbol{\sigma}_+$ by $\boldsymbol{A}^\dagger$; in the resulting slow Hamiltonian, one replaces $(1+2n_{th})\frac{\boldsymbol{\sigma}_z}{2}$ by $(n_{th}\boldsymbol{A}\boldsymbol{A}^\dagger - (1+n_{th})\boldsymbol{A}^\dagger\boldsymbol{A})$.

2.3.2 Treatment with fast unitary dynamics in inertial frame

We now consider the same setting *in inertial frame*, i.e. without going to rotating frame and averaging, but thus with Hamiltonian $\tilde{\boldsymbol{H}}_A$ (and $\omega_B\, \boldsymbol{b}^\dagger \boldsymbol{b}$) not small compared to κ. The model corresponds to fast GKSL dynamics on the mode B generated by 2.22, and the interaction Hamiltonian of Eq. 2.24 with, for a qubit, $\tilde{\boldsymbol{A}} = (\sigma_- + \sigma_+) = \boldsymbol{\sigma}_x$ and $\boldsymbol{H}_A$ proportional to $\boldsymbol{\sigma}_z$.

Example 2. *Consider the bipartite system described by:*

$$\begin{aligned} \mathcal{L}_B(\bullet) &= -i\omega_B[\boldsymbol{b}^\dagger \boldsymbol{b}, \bullet] + \kappa(1+n_{th})\mathcal{D}[\boldsymbol{b}](\bullet) + \kappa n_{th}\mathcal{D}[\boldsymbol{b}^\dagger](\bullet) + \kappa_\phi \mathcal{D}[\boldsymbol{n}](\bullet)\ , \\ \boldsymbol{H}_A &= -\omega_{\mathrm{eg}} \tfrac{\boldsymbol{\sigma}_z}{2}, \\ \boldsymbol{H}_I &= \boldsymbol{\sigma}_x \otimes (\boldsymbol{b} + \boldsymbol{b}^\dagger), \end{aligned} \tag{2.44}$$

with the energy gap $\omega_{\mathrm{eg}} = \omega_e - \omega_g$, $\boldsymbol{\sigma}_x = |e\rangle\langle g| + |g\rangle\langle e|$, $\boldsymbol{\sigma}_z = |g\rangle\langle g| - |e\rangle\langle e|$. *With Proposition 2, assuming* $\kappa \gg g$, *the second order reduced dynamics is given by*

$$\begin{aligned} \tfrac{d}{dt}\rho_s = \mathcal{L}_{s,0}(\boldsymbol{\rho}_s) + \epsilon^2 \mathcal{L}_{s,2}(\boldsymbol{\rho}_s) &= -i[-\omega_{\mathrm{eg}} \tfrac{\boldsymbol{\sigma}_z}{2}, \boldsymbol{\rho}_s] - ig^2 Y \left[\frac{\boldsymbol{\sigma}_z}{2}, \boldsymbol{\rho}_s\right] \\ &\quad + g^2 \sum_{\ell,\ell' \in \{+,-\}} X_{\ell\ell'} \left(\boldsymbol{\sigma}_{\ell'} \boldsymbol{\rho}_s \boldsymbol{\sigma}_\ell^\dagger - \frac{\boldsymbol{\rho}_s \boldsymbol{\sigma}_\ell^\dagger \boldsymbol{\sigma}_{\ell'} + \boldsymbol{\sigma}_\ell^\dagger \boldsymbol{\sigma}_{\ell'} \boldsymbol{\rho}_s}{2} \right)\ , \end{aligned} \tag{2.45}$$

with the hermitian matrix X *and coefficient* Y *defined by:*

$$\begin{aligned} X_{\ell\ell'} &= r_{\ell'} + r_\ell^* + e_{\ell'} + e_\ell^* \\ Y &= \tfrac{1}{2i}(r_+ + e_+ - r_+^* - e_+^* - r_- - e_- + r_-^* + e_-^*), \end{aligned} \tag{2.46}$$

and the coefficients r_ℓ *and* e_ℓ, $\ell \in \{+,-\}$*:*

$$r_\pm = \frac{2(1+n_{\mathrm{th}})}{\gamma_\pm}, \quad e_\pm = \frac{2n_{\mathrm{th}}}{\gamma_\mp{}^*}, \tag{2.47}$$

where $\gamma_\pm = \kappa + \kappa_\phi + 2i(\omega_B \pm \omega_{\mathrm{eg}})$.

Solution. The coupling corresponds to the general setting of Sec. 2.1.1 with the operators in the interaction Hamiltonian of Eq. 2.3 $\boldsymbol{A}_1 = \boldsymbol{\sigma}_x$, $\boldsymbol{B}_1 = \boldsymbol{b} + \boldsymbol{b}^\dagger$, and GKSL evolution on the mode B given by Eq. 2.22. The zero order, given by Eq. 2.6, is

$$\mathcal{L}_{s,0}(\boldsymbol{\rho}_s) = +i\frac{\omega_{eg}}{2}\boldsymbol{\sigma}_z^\times(\boldsymbol{\rho}_s). \tag{2.48}$$

As in Example 1, $\mathcal{L}_B$ in 2.33 still features the unique steady state 2.23, and since $\langle n|\, \boldsymbol{b}\, |n\rangle = 0$ for all n, in this case as well we have $\mathcal{L}_{s,1} = 0$.

To obtain the second order reduced dynamics, we proceed as follows. Via Definition 2.2.3, the time dependence for $\boldsymbol{b}^H(t)$ is the same as in 2.35, except with ω_B replacing Δ in the definition of γ, and hence

$$\boldsymbol{b}^H(t) = e^{-\frac{\gamma}{2}t}\boldsymbol{b}, \qquad (\boldsymbol{b}^\dagger)^H(t) = e^{-\frac{\gamma^*}{2}t}\boldsymbol{b}^\dagger, \qquad \gamma = \kappa + \kappa_\phi + 2i\omega_B \tag{2.49}$$

where again we keep the operators $\boldsymbol{b}$, $\boldsymbol{b}^\dagger$ fixed; only their Heisenberg-evolved copies carry t. We notice that $\boldsymbol{b}^H(t)+(\boldsymbol{b}^\dagger)^H(t) = (\boldsymbol{b}+\boldsymbol{b}^\dagger)^H(t)$. With this one can easily obtain according to Eq. 2.19 the sole coefficients

$$\begin{aligned} c_{11}(t) &= \mathrm{Tr}\Big[((\boldsymbol{b}^H(t)+(\boldsymbol{b}^\dagger)^H(t))(\boldsymbol{b}+\boldsymbol{b}^\dagger)\bar{\boldsymbol{\rho}}_B\Big] = (n_{th}+1)e^{-\frac{\gamma t}{2}} + n_{th}e^{-\frac{\gamma^* t}{2}} \\ \tilde{c}_{11}(t) &= \mathrm{Tr}\Big[((\boldsymbol{b}^H(t)+(\boldsymbol{b}^\dagger)^H(t))\bar{\boldsymbol{\rho}}_B(\boldsymbol{b}+\boldsymbol{b}^\dagger)\Big] = c_{11}(t)^*. \end{aligned} \tag{2.50}$$

Contrary to the case of Example 1, the operator $\boldsymbol{A}_1^-(t)$ conserves some time dependence, due to the fast unitary dynamics $\boldsymbol{H}_A$ on A,

$$\boldsymbol{A}_1^-(t) = e^{-it\boldsymbol{H}_A^\times}(\boldsymbol{\sigma}_x) = \boldsymbol{\sigma}_+ e^{-i\omega_{\mathrm{eg}}t} + \boldsymbol{\sigma}_- e^{+i\omega_{\mathrm{eg}}t}, \tag{2.51}$$

which we can insert in Eq. 2.16 from Proposition 2,

$$\begin{aligned} \epsilon^2\mathcal{L}_{s2}(\boldsymbol{\rho}_s) = -g^2\Big\{ &\int_0^{+\infty} c_{1,1}(t)\boldsymbol{A}_1^-(t)dt\, \boldsymbol{A}_1\,\boldsymbol{\rho}_s - \boldsymbol{A}_1\,\boldsymbol{\rho}_s \int_0^{+\infty} c_{1,1}(t)\boldsymbol{A}_1^-(t)dt \\ &- \int_0^{+\infty} \tilde{c}_{1,1}(t)\boldsymbol{A}_1^-(t)dt\,\boldsymbol{\rho}_s\boldsymbol{A}_1\Big\} + \boldsymbol{\rho}_s\boldsymbol{A}_1\int_0^{+\infty}\tilde{c}_{1,1}(t)\boldsymbol{A}_1^-(t)dt\Big\}, \end{aligned} \tag{2.52}$$

yielding, with Eq. 2.50, the following time integrals to compute:

$$\begin{aligned} \int_0^{+\infty} e^{-\frac{\gamma}{2}t-i\omega_{eg}t}dt &= \frac{2}{\gamma_+}, \qquad \int_0^{+\infty} e^{-\frac{\gamma}{2}t+i\omega_{eg}t}dt = \frac{2}{\gamma_-} \\ \int_0^{+\infty} e^{-\frac{\gamma^*}{2}t-i\omega_{eg}t}dt &= \frac{2}{\gamma_+^*}, \qquad \int_0^{+\infty} e^{-\frac{\gamma^*}{2}t+i\omega_{eg}t}dt = \frac{2}{\gamma_-^*}. \end{aligned} \tag{2.53}$$

Therefore, by inserting Eq. 2.53 in Eq. 2.52, with $\boldsymbol{A}_1^-(t)$ expressed in terms of Pauli matrices $\boldsymbol{\sigma}^+ = (\boldsymbol{\sigma}^-)^\dagger$

$$\begin{aligned} \int_0^{+\infty} c_{11}(t)\boldsymbol{A}_1^-(t)dt &= \sum_{\ell\in\{+,-\}} (r_\ell + e_\ell)\boldsymbol{\sigma}_\ell, \\ \int_0^{+\infty} \tilde{c}_{11}(t)\boldsymbol{A}_1^-(t)dt &= \sum_{\ell\in\{+,-\}} (r_\ell^* + e_\ell^*)\boldsymbol{\sigma}_\ell^\dagger. \end{aligned} \tag{2.54}$$

The statement then follows after plugging Eq. 2.54 in Eq. 2.52, collecting terms proportional to $\boldsymbol{\sigma}_{\ell'}\boldsymbol{\rho}_s\boldsymbol{\sigma}_\ell^\dagger$, $\boldsymbol{\rho}_s\boldsymbol{\sigma}_\ell^\dagger\boldsymbol{\sigma}_{\ell'}$, $\boldsymbol{\sigma}_\ell^\dagger\boldsymbol{\sigma}_{\ell'}\boldsymbol{\rho}_s$, and adding the zero order contribution of Eq.2.48 □

General subsystem A. The result generalizes to higher-dimensional subsystems A without much difficulties. Replace $\boldsymbol{\sigma}_x$ by $(\boldsymbol{A}+\boldsymbol{A}^\dagger)$ and $\boldsymbol{H}_A = \sum_{s=1}^{d_A}\omega_s\,|s\rangle\langle s|$ in the problem statement. The computations of $c_{11}(t)$ and $\tilde{c}_{11}(t)$ involving exponentials remain unchanged. The time evolution of the operators $\boldsymbol{A}_k^-(t)$ will be given by

$$\boldsymbol{A}_k^-(t) = \sum_{n,m=1}^{d_A} e^{-i(\omega_n-\omega_m)t}\,\langle n|\,\boldsymbol{A}_k\,|m\rangle\,|n\rangle\langle m|\ . \tag{2.55}$$

With these expressions, we can compute the integrals

$$\int_0^{+\infty} c_{k,l}(t)\boldsymbol{A}_k^-(t)dt \quad \text{and} \quad \int_0^{+\infty}\tilde{c}_{k,l}(t)\boldsymbol{A}_k^-(t)dt, \tag{2.56}$$

and easily obtain the second order reduced dynamics.

Interpretation. The following observations are in order about the result in 2.45.

- One checks that for $\omega_{eg} = \omega_B$ large, averaging the reduced system in a frame rotating with $\boldsymbol{U}(t) = e^{i\omega_{eg} t \boldsymbol{\sigma}_z/2}$, yields back the result of Example 1 as expected. Without averaging, terms in X_{+-} and X_{-+} remain.

- Note though that the averaging condition now relaxes to $\omega_B, \omega_{eg} \gg \epsilon^2\kappa$, thanks to confining ourselves to a manifold with slow dissipative dynamics, while without adiabatic elimination the averaging condition was $\omega_B, \omega_{eg} \gg \kappa$. Adiabatic elimination thus makes us win a factor ϵ^2.

- For $\omega_{eg} = 0$ instead, we have $r_+ = r_-$ and $e_+ = e_-$ such that $Y = 0$ and X is proportional to the all-ones matrix. This singularity implies a single dissipation channel, in $\boldsymbol{\sigma}_x$ i.e. proportional to the coupling operator, in agreement with the result of [59] when $\boldsymbol{H}_A = 0$.

- The formula 2.45 thus allows us to capture all intermediate scaling cases, where the averaging approximation is less justified.

- To have a completely positive GKSL form, interpretable as a standalone open quantum system, the matrix X in 2.45 should be positive. Here, X has a positive trace, but its *determinant is independent of* n_{th} *and negative as soon as* $\omega_{eg} \neq 0$. Then such interpretation fails, as also happened in [83] for the partial trace gauge ($\boldsymbol{\rho}_s = \mathrm{Tr}_B(\boldsymbol{\rho})$). This raises the natural question of whether an alternative gauge choice could restore a positive X, as seen in [58] for the second-order case with $\boldsymbol{H}_A = 0$, and in [61] for $\boldsymbol{H}_A \neq 0$ under specific conditions. More recently, [83] demonstrated that for $\boldsymbol{H}_A = 0$ at 4th order and for a class of parameters, no gauge choice can restore positivity. Further investigation into gauge choices and the preservation of positivity is left for future work. See also next items.

- The corresponding Bloch equations for $\boldsymbol{\rho} = \frac{\boldsymbol{I} + x\boldsymbol{\sigma}_x + y\boldsymbol{\sigma}_y + z\boldsymbol{\sigma}_z}{2}$ are:

$$\begin{aligned}
\dot{x} &= \left(\omega_{eg} - g^2 Y \frac{2n_{th}}{1+2n_{th}}\right) y \\
\dot{y} &= \left(-\omega_{eg} + g^2 Y \frac{2+2n_{th}}{1+2n_{th}}\right) x \; - g^2(1+2n_{th})\, r_z\, y \\
\dot{z} &= -g^2(1+2n_{th}) r_z\, (z - \bar{z})
\end{aligned} \tag{2.57}$$

  where

$$r_z = 4(\kappa + \kappa_\phi)\left(\frac{1}{|\gamma_+^2|} + \frac{1}{|\gamma_-^2|}\right), \quad \bar{z} = \frac{|\gamma_+|^2 - |\gamma_-|^2}{(|\gamma_+|^2 + |\gamma_-|^2)(1+2n_{th})}. \tag{2.58}$$

  For $\omega_{eg} \neq 0$ this system converges to $x = y = 0$, $z = \bar{z}$. For $\omega_{eg} = 0$, the x coordinate remains invariant and the two others converge exponentially to $y = 0$ and $z = 0$.

- The equations 2.57 can thus best be seen as just coordinates, because the evolution can in general be non positive, and thus accurately describing the GKSL form

2.44 when restricted to an invariant subspace inside $\mathcal{H}_A \otimes \mathcal{H}_B$. In [83], a necessary and sufficient inequality on the spectrum of Bloch equations is presented to decide whether another coordinate choice (thus not imposing $\rho_s = \mathrm{Tr}_B(\rho)$) may yield a completely positive reduced model, identifiable with a qubit. Remarkably, for any parameter values, our particular result 2.57 appears to lie on the boundary of these inequalities. Higher orders of the expansion thus have to be examined before concluding on the existence of another gauge restoring the CPTP character of the evolution.

2.4 Concluding remarks

We derived compact adiabatic–elimination formulas from the integral solution of a Sylvester equation, covering gapped Liouvillians even when the modes to be kept carry imaginary parts comparable to the dissipation rates of the variables to be eliminated (fast unitary center dynamics). Formally, this completes the spectral block–decomposition picture by requiring only a separation on the real parts of the spectrum; practically, it avoids switching to an interaction picture and performing a preliminary averaging/RWA.

We postpone a more detailed discussion on future work to Chap. 6. Here, we limit ourselves to remark that it should also be possible to generalize Proposition 1 beyond the bipartite system case, to settings where $\mathcal{L} = \mathcal{L}_0 + \epsilon\mathcal{L}_1$, with the spectrum of $\mathcal{L}_0$ containing eigenvalues with large imaginary part. We also note that the GKSL form is not required for Proposition 1 to hold, which applies also to evolutions where the Kossakowski matrix of Eq. 1.21 is not positive semidefinite.

The time-convolutionless approach to adiabatic elimination presented in Chapter 3 provides a different formalism to perform adiabatic elimination, as we will see. In particular, the TCL formulation does not assume a bipartite structure for the Hilbert space, nor a dynamics generated by a Liouvillian not necessarily in GKSL form. A discussion on the CPTP violation within the partial trace gauge for Example 2 can be found in Chapter 3, where time dependence due to the initial relaxation phase is also taken into account.

Chapter 3

Time-convolutionless master equation applied to adiabatic elimination

Contents

Contributions. This chapter is based on joint work with Masaaki Tokieda (then a postdoctoral researcher at the Quantic team, later at Kyoto University). Early in my PhD, we both studied the geometric approach to adiabatic elimination [83, 62] (see also Chap 2). In our discussions, M. Tokieda suggested an alternative way to compute the reduced dynamics, based on the time-convolutionless master equation. We verified on representative models that the time-convolutionless approach yields the same results as those derived in the examples of Chap. 2, and conjectured the equivalence of the two methods. M. Tokieda subsequently rigorously proved this equivalence. The formal statements and complete proofs appear in: Masaaki Tokieda and Angela Riva. "Time-convolutionless master equation applied to adiabatic elimination". In: *Physical Review A* 111.5 (May 2025). ISSN: 2469-9934. DOI: 10.1103/physreva.111.052206. URL: http://dx.doi.org/10.1103/PhysRevA.111.052206.

3.1 Projection methods for adiabatic elimination

In this chapter we introduce a time-convolutionless (TCL) master equation formulation of adiabatic elimination, as in the geometric approach initiated in Refs. [58, 59, 118] and further developed in Chapter 2 of this manuscript. The TCL master equation [136, 137, 88, 138] is a standard tool in the theory of open quantum systems: given a projection onto degrees of freedom of interest, it yields an exact time-local evolution for the projected state. As recalled in Sec. 1.4, TCL is typically derived for a closed system-environment model. Here we apply the projection-operator technique directly to master equations for open quantum systems with separated time scales (not necessarily in GKSL form nor tied to a bipartite structure), and show that the TCL master equation framework yields the same reduced model as the geometric adiabatic elimination construction, establishing a methodological equivalence.

We demonstrate the equivalence in Sec. 3.3.2 by identifying the TCL projector onto the relevant subspace and showing that it coincides with the geometric projector on the invariant subspace $\mathscr{M}^{(\epsilon)}$ of adiabatic elimination, spanned by the slowly decaying modes. We then construct the TCL counterparts of (i) the reduced generator map $\mathcal{F}^{(\epsilon)}$ and (ii) the reconstruction map from the reduced state to the full state $\mathcal{K}^{(\epsilon)}$, and we prove that they satisfy the invariance equation under the same gauge condition. This gives a geometric interpretation of the TCL formalism, which is usually presented purely analytically, opening the possibility to import analytical techniques from projection-operator methods into geometric model reduction.

The projection techniques in the TCL master equation framework also simplify situations that are challenging to address using only the geometric approach: (i) fast unitary center dynamics (non-negligible imaginary eigenvalues with small real part, thus long surviving) and (ii) short time transients that influence the subsequent reduced evolution. While both have been addressed by extensions of the geometric approach (Chap. 2 for unitary dynamics; Ref. [118] for fast transients), the TCL master equation framework offers a consistent and straightforward solution, as we will demonstrate by analyzing the same model considered in Example 2 of Chap. 2.

In summary, this analysis bridges the two viewpoints: it places model-reduction techniques from singular-perturbation theory and projection methods for reduced master equations within a single framework, with the TCL asymptotic projector identified as the geometric projector onto the slow invariant manifold. Since the main result of this chapter is a proof of equivalence, we spend some time to introduce the formalism of adiabatic elimination within the TCL framework. As a final remark, we note that lot of the developments presented in this Chapter are a rewriting of the formalism presented in Chap. 2 in a different language, in order to prove the equivalence of the time-convolutionless approach with the geometric approach to adiabatic elimination.

3.2 Adiabatic elimination for gapped Liouvillians

In this section we specify the model we consider throughout this chapter. Instead of the bipartite Hilbert space of Chap. 2, we consider a linear master equation on operators

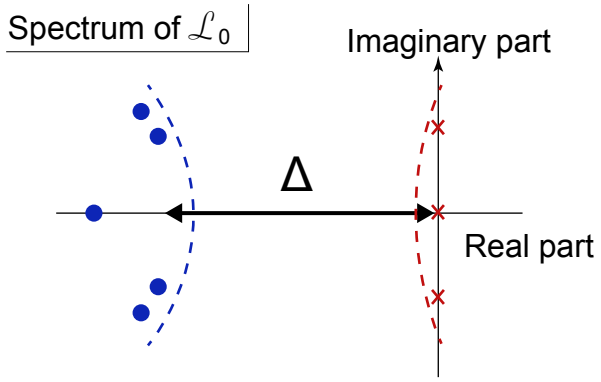

Figure 3.1: Typical spectrum of $\mathcal{L}_0$ [see Eq. 3.1] in adiabatic elimination. The presence of a gap Δ is assumed between surviving modes proximate to the imaginary axis (represented by the red crosses) and fast relaxation modes (represented by the blue circles).

$\boldsymbol{\rho}(t) \in \mathcal{T}(\mathcal{H})$, which was already considered in [58, 118, 139] for the setting of the geometric approach to adiabatic elimination. Specifically, we take

$$\frac{d}{dt}\boldsymbol{\rho}(t) = (\mathcal{L}_0 + \epsilon\mathcal{L}_1)\boldsymbol{\rho}(t) \equiv \mathcal{L}\boldsymbol{\rho}(t), \tag{3.1}$$

with $\epsilon > 0$. $\mathcal{L}_0$ is assumed to be diagonalizable and admitting a gap Δ on the real axis.

Vectorized notation. We use the Hilbert-Schmidt vectorization $|A\rangle\!\rangle$ of an operator $\boldsymbol{A}$, with $\langle\!\langle A|$ as its Hermitian conjugate, and inner product $\langle\!\langle A|B\rangle\!\rangle = \mathrm{Tr}\left(\boldsymbol{A}^\dagger \boldsymbol{B}\right)$. Superoperators are represented as matrices, denoted with a hat ($\hat{}$). The eigenvalue problem of $\mathcal{L}_0$ reads

$$(\hat{\mathcal{L}}_0 - \lambda_i \hat{\mathcal{I}})\,|r_i\rangle\!\rangle = 0, \qquad \langle\!\langle l_i|\,(\hat{\mathcal{L}}_0 - \lambda_i \hat{\mathcal{I}}) = 0, \tag{3.2}$$

where λ_i is the eigenvalue and $|r_i\rangle\!\rangle$ and $\langle\!\langle l_i|$ are the right and left eigenvectors, normalized as $\langle\!\langle l_i|r_j\rangle\!\rangle = \delta_{ij}$.

Surviving vs. fast relaxation modes. We assume the existence of a gap Δ in the real axis of the spectrum of $\mathcal{L}_0$, which allows to divide the eigenvalues in to surviving modes λ_s such that $\mathrm{Re}\lambda_s = 0\ \forall s$, and fast relaxing modes λ_f. As in Chap 2, we make no assumptions on $\mathrm{Im}\lambda_s$ (which was assumed to be of order ϵ in Ref. [118]). The gap Δ can be written as

$$\Delta = \min_f \mathrm{Re}(-\lambda_f). \tag{3.3}$$

As illustrated in Fig. 3.1, we split the eigenvalues $\{\lambda_i\}$ of $\mathcal{L}_0$ into fast-relaxation modes $\{\lambda_f\}$, associated to strictly negative real part and surviving modes $\{\lambda_s\}$, which survive asymptotically. The dynamics of a gapped Liouvillian $\mathcal{L}_0$ begin with a rapid decaying phase described by the fast relaxation modes. This phase is subsequently followed by an evolution dominated by the surviving modes, as in the adiabatic elimination scenarios of Chap. 2.

Invariant subspace $\mathscr{M}^{(\epsilon)}$. Let $\mathscr{M}^{(0)}$ denote the subspace spanned by the surviving modes of $\mathcal{L}_0$; it is exactly invariant under $\mathcal{L}_0$. For $\epsilon > 0$ small compared to the spectral gap Δ (matrix elements of $\epsilon\mathcal{L}_1$ in the eigenbasis of $\mathcal{L}_0$ are small relative to Δ), there exists an ϵ–close invariant subspace $\mathscr{M}^{(\epsilon)}$ for $\mathcal{L}$ [127]. Starting from arbitrary initial conditions, the component orthogonal to $\mathscr{M}^{(\epsilon)}$ decays on the fast timescale set by Δ^{-1}, and trajectories contract onto $\mathscr{M}^{(\epsilon)}$ after an initial relaxation phase. Adiabatic elimination targets the dynamics confined to $\mathscr{M}^{(\epsilon)}$, which involves fewer degrees of freedom than Eq. 3.1.

Parametrization. We parametrize the degrees of freedom in $\mathscr{M}^{(\epsilon)}$ as $\vec{x}$. As in Sec 2.1.1, we need to obtain two linear, time-independent maps, denoted here as $\mathcal{K}^{(\epsilon)}$, which relates the parametrization to the solution to Eq. 3.1,

$$|\rho(t)\rangle\!\rangle = \mathcal{K}^{(\epsilon)}\vec{x}(t), \tag{3.4}$$

and as $\mathcal{F}^{(\epsilon)}$[1], which describes the time evolution of the parameters $\vec{x}$,

$$\frac{d}{dt}\vec{x}(t) = \mathcal{F}^{(\epsilon)}\vec{x}(t). \tag{3.5}$$

When $\epsilon = 0$, a state in $\mathscr{M}^{(\epsilon=0)}$ can be represented by a linear combination of $\{|r_s\rangle\!\rangle\}$. Hence, we fix $\mathcal{K}^{(\epsilon=0)}$ as

$$\mathcal{K}^{(\epsilon=0)}\vec{x} = \sum_s x_s\,|r_s\rangle\!\rangle\,. \tag{3.6}$$

Inserting the definitions of the maps into Eq. 3.1, we obtain the invariance condition,

$$\mathcal{K}^{(\epsilon)}\mathcal{F}^{(\epsilon)} = \hat{\mathcal{L}}\mathcal{K}^{(\epsilon)}. \tag{3.7}$$

Closed form solutions for $\mathcal{K}^{(\epsilon)}$ and $\mathcal{F}^{(\epsilon)}$ exist in special cases [140, 83]. Generally however, one solves Eq. 3.7 order by order in ϵ to find an approximate solution, as shown in Chap 2 for the bipartite system case, and in Appendix 7.1 for the general case.

Gauge degree of freedom. The solution to Eq. 3.7 is not unique. To see this, let $\mathcal{T}$ be an invertible map (not necessarily a unitary map) of the same dimension as $\mathcal{F}^{(\epsilon)}$. If $\mathcal{K}^{(\epsilon)}$ and $\mathcal{F}^{(\epsilon)}$ satisfy Eq. 3.7, then the maps defined by $\mathcal{K}^{(\epsilon)}\mathcal{T} \equiv \bar{\mathcal{K}}^{(\epsilon)}$ and $\mathcal{T}^{-1}\mathcal{F}^{(\epsilon)}\mathcal{T} \equiv \bar{\mathcal{F}}^{(\epsilon)}$ also satisfy the invariance condition ($\bar{\mathcal{K}}^{(\epsilon)}$ is consistent with Eq. 3.6 assuming $\lim_{\epsilon\to 0}\mathcal{T} = \mathcal{I}$). Given the definitions in Eqs. 3.4, 3.5, we can show that $|\rho(t)\rangle\!\rangle = \bar{\mathcal{K}}^{(\epsilon)}\vec{y}(t)$ and $(d/dt)\vec{y}(t) = \bar{\mathcal{F}}^{(\epsilon)}\vec{y}(t)$ with $\vec{y}(t) = \mathcal{T}^{-1}\vec{x}(t)$. These identities indicate that the solutions $\bar{\mathcal{K}}^{(\epsilon)}$ and $\bar{\mathcal{F}}^{(\epsilon)}$ are the maps for the different parametrization $\vec{y}(t)$. Thus, the gauge degree of freedom is associated with the non-uniqueness of the parametrization. In what follows, we consider only a gauge choice such that, with Eq. 3.6,

$$\langle\!\langle l_s|\,(\mathcal{K}^{(\epsilon)} - \mathcal{K}^{(\epsilon=0)})\vec{x} = 0, \tag{3.8}$$

for any s and $\vec{x}$. In the bipartite setting, this corresponds to the partial trace gauge considered in Chap. 2. This choice is equivalent to considering the parametrization given by $x_s(t) = \langle\!\langle l_s|\rho(t)\rangle\!\rangle$. As we discuss later, this is a natural representation in practice [see Eq. 3.37].

[1]The linear map $\mathcal{F}^{(\epsilon)}$ corresponds to the map $\mathcal{L}_s$ of Chap. 2. While $\mathcal{L}_s$ was acting on the reduced density operator $\boldsymbol{\rho}_S$, $\mathcal{F}^{(\epsilon)}$ acts on vectors $\vec{x}$.

3.3 Adiabatic elimination through the TCL master equation framework

In this section, we first review the TCL master equation in Sec. 3.3.1, We then show in Sec. 3.3.2 that the geometric formulation of adiabatic elimination, presented in Sec. 3.2, can be equivalently formulated using the TCL master equation.

3.3.1 TCL master equation

We begin by reviewing the TCL master equation, following [88, 26], which we introduced in Chapter 1. Let $\mathcal{P}$ be a projector ($\mathcal{P}^2 = \mathcal{P}$) and $\mathcal{Q} = \mathcal{I} - \mathcal{P}$. As shown in Eq. (1.26), one has

$$\Big[\mathcal{I} - \Sigma(t)\Big]\,\mathcal{Q}\rho(t) \;=\; e^{\mathcal{Q}\mathcal{L}\mathcal{Q}\,t}\,\mathcal{Q}\rho(0) \;+\; \Sigma(t)\,\mathcal{P}\rho(t),$$

with

$$\Sigma(t) \;=\; \int_0^t d\tau\, e^{\mathcal{Q}\mathcal{L}\mathcal{Q}\,\tau}\,\mathcal{Q}\mathcal{L}\mathcal{P}\,e^{-\mathcal{L}\tau}. \tag{3.9}$$

which lead us to define the two distinct cases we examine in what follows.

Case 1. In the first case, we assume $[\mathcal{P}, \mathcal{L}_0] = 0$. We can then replace $\mathcal{Q}\mathcal{L}\mathcal{P}$ by $\mathcal{Q}\mathcal{L}_1\mathcal{P}$ due to $\mathcal{Q}\mathcal{P} = 0$:

$$\Sigma(t) = \epsilon \int_0^t d\tau\, e^{\mathcal{Q}\mathcal{L}\mathcal{Q}\tau}\mathcal{Q}\mathcal{L}_1\mathcal{P}e^{-\mathcal{L}\tau}. \tag{3.10}$$

We assume the existence of $[\mathcal{I} - \Sigma(t)]^{-1}$, which is valid for small ϵ and short times (the Neumann series has to converge). By inverting $[\mathcal{I} - \Sigma(t)]$ and using $[\mathcal{I} - \Sigma(t)]^{-1}\Sigma(t) = [\mathcal{I} - \Sigma(t)]^{-1} - \mathcal{I}$, we obtain an expression of $\mathcal{Q}\boldsymbol{\rho}(t)$ without the time-convolution integral,

$$\mathcal{Q}\boldsymbol{\rho}(t) = \mathcal{J}(t)\mathcal{Q}\boldsymbol{\rho}(0) + \Big\{[\mathcal{I} - \Sigma(t)]^{-1} - \mathcal{I}\Big\}\mathcal{P}\boldsymbol{\rho}(t),$$

where

$$\mathcal{J}(t) = [\mathcal{I} - \Sigma(t)]^{-1}e^{\mathcal{Q}\mathcal{L}\mathcal{Q}t}\mathcal{Q}. \tag{3.11}$$

This equation indicates

$$\boldsymbol{\rho}(t) = \mathcal{J}(t)\mathcal{Q}\boldsymbol{\rho}(0) + \mathcal{P}(t)\boldsymbol{\rho}(t), \tag{3.12}$$

with

$$\mathcal{P}(t) = [\mathcal{I} - \Sigma(t)]^{-1}\mathcal{P}. \tag{3.13}$$

We can show $[\mathcal{P}(t)]^2 = \mathcal{P}(t)$ from $\mathcal{P}\Sigma(t) = 0$. Hence, $\mathcal{P}(t)$ is also a projection. Inserting Eq. 3.12 into the right hand side of $(d/dt)\mathcal{P}\boldsymbol{\rho}(t) = \mathcal{P}\mathcal{L}\boldsymbol{\rho}(t)$, we obtain the TCL master equation

$$\frac{d}{dt}\mathcal{P}\boldsymbol{\rho}(t) = \mathcal{P}\mathcal{L}\mathcal{J}(t)\mathcal{Q}\boldsymbol{\rho}(0) + \mathcal{P}\mathcal{L}\mathcal{P}(t)\boldsymbol{\rho}(t). \tag{3.14}$$

Note that, in Eqs. 3.12 and 3.14, the terms involving $\mathcal{J}(t)$ explicitly depend on the initial condition in the complementary subspace $\mathcal{Q}\boldsymbol{\rho}(0)$.

Case 2. In the second case we assume $\Sigma(t) = 0$. We obtain

$$\mathcal{Q}\boldsymbol{\rho}(t) = \exp(\mathcal{Q}\mathcal{L}\mathcal{Q}t)\mathcal{Q}\boldsymbol{\rho}(0), \tag{3.15}$$

which yields

$$\boldsymbol{\rho}(t) = e^{\mathcal{Q}\mathcal{L}\mathcal{Q}t}\mathcal{Q}\boldsymbol{\rho}(0) + \mathcal{P}\boldsymbol{\rho}(t), \tag{3.16}$$

and, by inserting it into the right hand side of $(d/dt)\mathcal{P}\boldsymbol{\rho}(t) = \mathcal{P}\mathcal{L}\boldsymbol{\rho}(t)$,

$$\frac{d}{dt}\mathcal{P}\boldsymbol{\rho}(t) = \mathcal{P}\mathcal{L}e^{\mathcal{Q}\mathcal{L}\mathcal{Q}t}\mathcal{Q}\boldsymbol{\rho}(0) + \mathcal{P}\mathcal{L}\mathcal{P}\boldsymbol{\rho}(t). \tag{3.17}$$

3.3.2 Maps $\mathcal{K}^{(\epsilon)}$ and $\mathcal{F}^{(\epsilon)}$ from the TCL master equation

We show that the TCL master equation framework developed above provides an alternative formulation of adiabatic elimination. For this purpose, the main task is to show that the maps $\mathcal{K}^{(\epsilon)}$ and $\mathcal{F}^{(\epsilon)}$ can be computed using quantities in the TCL master equation framework since the goal of adiabatic elimination is to evaluate those maps. In the geometric formulation, those maps are obtained as a solution to the invariance condition 3.7. The invariance condition is solved under two conditions: the boundary condition 3.6 and the gauge fixing condition 3.8. These conditions determine the parametrization of $\mathscr{M}^{(\epsilon)}$. Hence, we need to prove the existence of maps corresponding to $\mathcal{K}^{(\epsilon)}$ and $\mathcal{F}^{(\epsilon)}$ within the framework of the TCL master equation, which we denote as $\mathcal{K}^{(\epsilon)}_{\mathrm{TCL}}$ and $\mathcal{F}^{(\epsilon)}_{\mathrm{TCL}}$, respectively, such that $\mathcal{K}^{(\epsilon)}_{\mathrm{TCL}}$ satisfies the boundary condition and the gauge fixing condition and that $\mathcal{K}^{(\epsilon)}_{\mathrm{TCL}}$ and $\mathcal{F}^{(\epsilon)}_{\mathrm{TCL}}$ satisfy the invariance condition.

Initial states outside the invariant subspace $\mathscr{M}^{(\epsilon)}$

We first consider scenarios with $\boldsymbol{\rho}(0) \notin \mathscr{M}^{(\epsilon)}$, that is, the initial state $\boldsymbol{\rho}(0)$ is outside the invariant subspace with $\epsilon > 0$. The geometric formulation, which assumes that the initial state is in $\mathscr{M}^{(\epsilon)}$, provides an approximate description of the long-time behavior. To provide physical context, one example of this scenario is quench dynamics, where the system evolves under $\mathcal{L}_0$ for $t < 0$, relaxing to the corresponding invariant subspace such that $\boldsymbol{\rho}(0) \in \mathscr{M}^{(\epsilon=0)}$, and the perturbation $\epsilon\mathcal{L}_1$ is abruptly introduced at $t = 0$.

In this case, we adopt $\mathcal{P} = \mathcal{P}_{\mathrm{inv}}$ with

$$\hat{\mathcal{P}}_{\mathrm{inv}} = \sum_s |r_s\rangle\!\rangle\langle\!\langle l_s| \,, \tag{3.18}$$

the operation of which is given by $\mathcal{P}_{\mathrm{inv}}\boldsymbol{\rho} = \sum_s \mathrm{tr}(\boldsymbol{l}_s^\dagger\boldsymbol{\rho})\boldsymbol{r}_s$. This is a projection onto $\mathscr{M}^{(\epsilon=0)}$. In fact, the orthonormality condition of the eigenvectors ensures the property $\mathcal{P}_{\mathrm{inv}}^2 = \mathcal{P}_{\mathrm{inv}}$, which corroborates its nature as a projection. Furthermore, we have the commutation relation $[\mathcal{L}_0, \mathcal{P}_{\mathrm{inv}}] = 0$, as expected from the fact that $\mathcal{P}_{\mathrm{inv}}$ is a projection onto eigenspaces of $\mathcal{L}_0$. This implies that the corresponding $\Sigma(t)$ defined in Eq. 3.9, which we denote as $\Sigma^{(\epsilon)}_{\mathrm{inv}}(t)$, is given by Eq. 3.10 with $\mathcal{P} = \mathcal{P}_{\mathrm{inv}}$ and $\mathcal{Q} = \mathcal{I} - \mathcal{P}_{\mathrm{inv}} \equiv \mathcal{Q}_{\mathrm{inv}}$. The corresponding $\mathcal{J}(t)$ [Eq. 3.11] and $\mathcal{P}(t)$ [Eq. 3.13], which we denote as $\mathcal{J}^{(\epsilon)}_{\mathrm{inv}}(t)$ and $\mathcal{P}^{(\epsilon)}_{\mathrm{inv}}(t)$, respectively, are given by

$$\mathcal{J}^{(\epsilon)}_{\mathrm{inv}}(t) = [\mathcal{I} - \Sigma^{(\epsilon)}_{\mathrm{inv}}(t)]^{-1} e^{\mathcal{Q}_{\mathrm{inv}}\mathcal{L}\mathcal{Q}_{\mathrm{inv}}t}\mathcal{Q}_{\mathrm{inv}}, \tag{3.19}$$

and

$$\mathcal{P}^{(\epsilon)}_{\rm inv}(t) = [\mathcal{I} - \Sigma^{(\epsilon)}_{\rm inv}(t)]^{-1}\mathcal{P}_{\rm inv}. \tag{3.20}$$

With these notations, Eqs. 3.12 and 3.14 read in the vector representation as

$$\begin{aligned} |\rho(t)\rangle\!\rangle &= \hat{\mathcal{J}}^{(\epsilon)}_{\rm inv}(t)\,|\mathcal{Q}_{\rm inv}\rho(0)\rangle\!\rangle + \hat{\mathcal{P}}^{(\epsilon)}_{\rm inv}(t)\,|\rho(t)\rangle\!\rangle\,, \\ \frac{d}{dt}\hat{\mathcal{P}}_{\rm inv}\,|\rho(t)\rangle\!\rangle &= \hat{\mathcal{P}}_{\rm inv}\hat{\mathcal{L}}\hat{\mathcal{J}}^{(\epsilon)}_{\rm inv}(t)\,|\mathcal{Q}_{\rm inv}\rho(0)\rangle\!\rangle + \hat{\mathcal{P}}_{\rm inv}\hat{\mathcal{L}}\hat{\mathcal{P}}^{(\epsilon)}_{\rm inv}(t)\,|\rho(t)\rangle\!\rangle\,. \end{aligned} \tag{3.21}$$

Now we incorporate the gauge fixing condition 3.8. As discussed below Eq. 3.8, it is equivalent to $x_s(t) = \langle\!\langle l_s|\rho(t)\rangle\!\rangle$ for any surviving modes s. For a more compact description, let us introduce

$$\chi_R = [|r_{s=1}\rangle\!\rangle\ |r_{s=2}\rangle\!\rangle\ \cdots]\,,\quad \chi_L^\dagger = \begin{bmatrix} \langle\!\langle l_{s=1}| \\ \langle\!\langle l_{s=2}| \\ \vdots \end{bmatrix}. \tag{3.22}$$

We find $\chi_R\chi_L^\dagger = \hat{\mathcal{P}}_{\rm inv}$, $\chi_L^\dagger\chi_R = I$, and $\vec{x}(t) = \chi_L^\dagger\,|\rho(t)\rangle\!\rangle$. Inserting these into Eqs. 3.21, the equations can be expressed with $\vec{x}(t)$ as

$$\begin{aligned} |\rho(t)\rangle\!\rangle &= \hat{\mathcal{J}}^{(\epsilon)}_{\rm inv}(t)\,|\mathcal{Q}_{\rm inv}\rho(0)\rangle\!\rangle + \hat{\mathcal{P}}^{(\epsilon)}_{\rm inv}(t)\chi_R\vec{x}(t) \\ \frac{d}{dt}\vec{x}(t) &= \chi_L^\dagger\hat{\mathcal{L}}\hat{\mathcal{J}}^{(\epsilon)}_{\rm inv}(t)\,|\mathcal{Q}_{\rm inv}\rho(0)\rangle\!\rangle + \chi_L^\dagger\hat{\mathcal{L}}\hat{\mathcal{P}}^{(\epsilon)}_{\rm inv}(t)\chi_R\,\vec{x}(t). \end{aligned} \tag{3.23}$$

Let us denote $\mathcal{P}^{(\epsilon)}_{\rm inv}(t)$ in the asymptotic time limit as $\mathcal{P}^{(\epsilon)}_{\rm inv} = \lim_{t\to\infty}\mathcal{P}^{(\epsilon)}_{\rm inv}(t)$. To proceed, we note the following two properties of $\mathcal{J}^{(\epsilon)}_{\rm inv}(t)$ and $\mathcal{P}^{(\epsilon)}_{\rm inv}(t) - \mathcal{P}^{(\epsilon)}_{\rm inv}$. First, for small ϵ, these superoperators decay exponentially in time;

Proposition 4 (Tokieda [64]). *It follows that*

$$\|\hat{\mathcal{P}}^{(\epsilon)}_{\rm inv}(t) - \hat{\mathcal{P}}^{(\epsilon)}_{\rm inv}\| = O\left((\epsilon/\Delta)e^{-t\Delta}\right), \tag{3.24}$$

and

$$\|\hat{\mathcal{J}}^{(\epsilon)}_{\rm inv}(t)\| = O\left(e^{-t\Delta}\right), \tag{3.25}$$

as $\epsilon \to 0$, where $\|\bullet\|$ denotes a matrix norm.

For the second property, recall that $\mathcal{P}^{(\epsilon)}_{\rm inv}(t)$ is a projection as shown below Eq. 3.13. In this regard, the projection in the asymptotic time limit $\mathcal{P}^{(\epsilon)}_{\rm inv}$ has a distinct geometric interpretation as follows.

Proposition 5 (Tokieda [64]). *The image of the projection $\mathcal{P}^{(\epsilon)}_{\rm inv}$ is $\mathscr{M}^{(\epsilon)}$, that is, if $|r^{(\epsilon)}_s\rangle\!\rangle$ is the right eigenvector of $\mathcal{L}$ associated with $|r_s\rangle\!\rangle$ in the limit $\epsilon \to 0$, the projection $\mathcal{P}^{(\epsilon)}_{\rm inv}$ can be expressed as*

$$\hat{\mathcal{P}}^{(\epsilon)}_{\rm inv} = \sum_{ss'} |r^{(\epsilon)}_s\rangle\!\rangle\,[N^{-1}]_{ss'}\,\langle\!\langle l_{s'}|\,, \tag{3.26}$$

with $N_{ss'} = \langle\!\langle l_s|r^{(\epsilon)}_{s'}\rangle\!\rangle$. In particular, it satisfies

$$(\mathcal{I} - \mathcal{P}^{(\epsilon)}_{\rm inv})\mathcal{L}\mathcal{P}^{(\epsilon)}_{\rm inv} = 0. \tag{3.27}$$

On the proofs. Proofs of Propositions 4 and 5 are unchanged from [64] and not part of my contribution; the remainder of the chapter builds on these results. The arguments of the proofs apply to finite-dimensional systems. For completeness, I remark that the proof is obtained by assuming small ϵ to maintain the gapped structure of the generator $\mathcal{L} = \mathcal{L}_0 + \epsilon\mathcal{L}_1$, the spectral decomposition of $\mathcal{L}$ is employed to analyze the time-dependence of $\mathcal{P}_{\text{inv}}^{(\epsilon)}(t)$ and $\mathcal{J}_{\text{inv}}^{(\epsilon)}(t)$. The gap ensures decay of the time-dependent terms, thereby establishing Propositions 4 and 5. Notably, the proof does not rely on perturbation expansions and Eq. 3.27 is valid to all orders of ϵ.

Invariance equation. Exploiting the Propositions, we replace $\mathcal{P}_{\text{inv}}^{(\epsilon)}(t)$ by $\mathcal{P}_{\text{inv}}^{(\epsilon)}$ and $\mathcal{J}_{\text{inv}}^{(\epsilon)}(t)$ by zero in Eqs. 3.23. As a result, we obtain

$$\begin{aligned} |\rho(t)\rangle\!\rangle &= \mathcal{K}_{\text{TCL}}^{(\epsilon)}\vec{x}(t) + e_{\mathcal{K}}(t), \\ \frac{d}{dt}\vec{x}(t) &= \mathcal{F}_{\text{TCL}}^{(\epsilon)}\vec{x}(t) + e_{\mathcal{F}}(t), \end{aligned} \tag{3.28}$$

where we have introduced

$$\mathcal{K}_{\text{TCL}}^{(\epsilon)} = \hat{\mathcal{P}}_{\text{inv}}^{(\epsilon)}\chi_R \quad \text{and} \quad \mathcal{F}_{\text{TCL}}^{(\epsilon)} = \chi_L^\dagger\hat{\mathcal{L}}\hat{\mathcal{P}}_{\text{inv}}^{(\epsilon)}\chi_R. \tag{3.29}$$

In Eqs. 3.28, $e_{\mathcal{K}}(t)$ and $e_{\mathcal{F}}(t)$ represent error terms due to the replacements. From the exponential decaying factors in Eqs. 3.24 and 3.25, those are negligibly small in the long-time regime $t \gg \Delta^{-1}$. Without the error terms, Eqs. 3.28 take similar forms to the equations defining $\mathcal{K}^{(\epsilon)}$ (Eq. 3.4) and $\mathcal{F}^{(\epsilon)}$ (Eq. 3.5). This similarity implies that $\mathcal{K}_{\text{TCL}}^{(\epsilon)}$ and $\mathcal{F}_{\text{TCL}}^{(\epsilon)}$ correspond to $\mathcal{K}^{(\epsilon)}$ and $\mathcal{F}^{(\epsilon)}$, respectively. When $\epsilon = 0$, we find $\mathcal{K}_{\text{TCL}}^{(\epsilon=0)} = \chi_R$, which yields $\mathcal{K}_{\text{TCL}}^{(\epsilon=0)}\vec{x} = \sum_s x_s\,|r_s\rangle\!\rangle$. This confirms that $\mathcal{K}_{\text{TCL}}^{(\epsilon=0)}$ adheres to the boundary condition 3.6. As outlined at the beginning, hence, the remaining task is to show the invariance condition 3.7, that is,

$$\mathcal{K}_{\text{TCL}}^{(\epsilon)}\mathcal{F}_{\text{TCL}}^{(\epsilon)} = \hat{\mathcal{L}}\mathcal{K}_{\text{TCL}}^{(\epsilon)}. \tag{3.30}$$

Inserting the definitions of $\mathcal{K}_{\text{TCL}}^{(\epsilon)}$ and $\mathcal{F}_{\text{TCL}}^{(\epsilon)}$, we obtain

$$\begin{aligned} \hat{\mathcal{L}}\mathcal{K}_{\text{TCL}}^{(\epsilon)} - \mathcal{K}_{\text{TCL}}^{(\epsilon)}\mathcal{F}_{\text{TCL}}^{(\epsilon)} &= \hat{\mathcal{L}}\hat{\mathcal{P}}_{\text{inv}}^{(\epsilon)}\chi_R - \hat{\mathcal{P}}_{\text{inv}}^{(\epsilon)}\hat{\mathcal{L}}\hat{\mathcal{P}}_{\text{inv}}^{(\epsilon)}\chi_R \\ &= (\hat{\mathcal{I}} - \hat{\mathcal{P}}_{\text{inv}}^{(\epsilon)})\hat{\mathcal{L}}\hat{\mathcal{P}}_{\text{inv}}^{(\epsilon)}\chi_R = 0, \end{aligned}$$

where we have used $\mathcal{P}_{\text{inv}}^{(\epsilon)}\mathcal{P}_{\text{inv}} = \mathcal{P}_{\text{inv}}^{(\epsilon)}$ in the first equality and Eq. 3.27 in the last equality. Consequently, we confirm the invariance condition 3.30, which ensures that $\mathcal{K}_{\text{TCL}}^{(\epsilon)}$ and $\mathcal{F}_{\text{TCL}}^{(\epsilon)}$ in the TCL master equation formulation agree with $\mathcal{K}^{(\epsilon)}$ and $\mathcal{F}^{(\epsilon)}$ in the geometric formulation.

Initial states in the invariant subspace $\mathscr{M}^{(\epsilon)}$

Next we examine scenarios with $\boldsymbol{\rho}(0) \in \mathscr{M}^{(\epsilon)}$; the initial state $\boldsymbol{\rho}(0)$ is in the invariant subspace with $\epsilon > 0$. These scenarios are addressed in the geometric formulation, where the relations $|\rho(t)\rangle\!\rangle = \mathcal{K}^{(\epsilon)}\vec{x}(t)$ and $(d/dt)\vec{x}(t) = \mathcal{F}^{(\epsilon)}\vec{x}(t)$ hold for all times. We

confirm these relations in the TCL master equation formulation. To this end, we adopt $\mathcal{P} = \mathcal{P}_{\text{inv}}^{(\epsilon)}$. From Proposition 5, $\boldsymbol{\rho}(0)$ in the present discussion satisfies $\boldsymbol{\rho}(0) = \mathcal{P}_{\text{inv}}^{(\epsilon)}\boldsymbol{\rho}(0)$ or, equivalently, $\mathcal{Q}_{\text{inv}}^{(\epsilon)}\boldsymbol{\rho}(0) = 0$ with $\mathcal{Q}_{\text{inv}}^{(\epsilon)} = \mathcal{I} - \mathcal{P}_{\text{inv}}^{(\epsilon)}$. Furthermore, the relation 3.27, which reads $\mathcal{Q}_{\text{inv}}^{(\epsilon)}\mathcal{L}\mathcal{P}_{\text{inv}}^{(\epsilon)} = 0$, ensures that the corresponding $\Sigma(t)$ defined in Eq. 3.9 vanishes. We hence consider Eqs. 3.16 and 3.17, where the terms involving $\mathcal{Q}_{\text{inv}}^{(\epsilon)}\boldsymbol{\rho}(0)$ vanish from the above discussion. Consequently, Eqs. 3.16 and 3.17 in the vector representation simplify to $|\rho(t)\rangle\!\rangle = \hat{\mathcal{P}}_{\text{inv}}^{(\epsilon)}|\rho(t)\rangle\!\rangle$ and

$$\frac{d}{dt}\hat{\mathcal{P}}_{\text{inv}}^{(\epsilon)}|\rho(t)\rangle\!\rangle = \hat{\mathcal{P}}_{\text{inv}}^{(\epsilon)}\hat{\mathcal{L}}\hat{\mathcal{P}}_{\text{inv}}^{(\epsilon)}|\rho(t)\rangle\!\rangle\,,$$

respectively. Applying $\mathcal{P}_{\text{inv}}$ from the left side to the latter equation and using $\mathcal{P}_{\text{inv}}\mathcal{P}_{\text{inv}}^{(\epsilon)} = \mathcal{P}_{\text{inv}}$, we obtain

$$\frac{d}{dt}\hat{\mathcal{P}}_{\text{inv}}|\rho(t)\rangle\!\rangle = \hat{\mathcal{P}}_{\text{inv}}\hat{\mathcal{L}}\hat{\mathcal{P}}_{\text{inv}}^{(\epsilon)}|\rho(t)\rangle\!\rangle\,. \tag{3.31}$$

Expressing with the parameter $\vec{x}(t)$ and inserting the definitions of $\mathcal{K}_{\text{TCL}}^{(\epsilon)}$ and $\mathcal{F}_{\text{TCL}}^{(\epsilon)}$, we obtain

$$|\rho(t)\rangle\!\rangle = \mathcal{K}_{\text{TCL}}^{(\epsilon)}\vec{x}(t), \quad \frac{d}{dt}\vec{x}(t) = \mathcal{F}_{\text{TCL}}^{(\epsilon)}\vec{x}(t). \tag{3.32}$$

In contrast to Eqs. 3.28, Eqs. 3.32 hold true for all times t without error terms. This is due to the absence of the fast relaxation phase when initially placed in $\mathscr{M}^{(\epsilon)}$. This analysis confirms that the TCL master equation formulation offers a consistent description with the geometric formulation.

Remarks. The following remarks are in order.

1. Proposition 4 quantifies the long-time decay of both $\mathcal{P}_{\text{inv}}^{(\epsilon)}(t) - \mathcal{P}_{\text{inv}}^{(\epsilon)}$ and $\mathcal{J}_{\text{inv}}^{(\epsilon)}(t)$. The relaxation of the former is well known in applications; by contrast, the role of $\mathcal{J}_{\text{inv}}^{(\epsilon)}(t)$ has been less emphasized, largely because one often assumes $\mathcal{Q}\boldsymbol{\rho}(0) = 0$. In the geometric picture, trajectories contract exponentially to $\mathscr{M}^{(\epsilon)}$ for any initial condition, so all contributions that depend explicitly on the initial component in the complementary subspace must vanish at long times. Equation 3.25 makes this precise. Proposition 5 further provides a geometric identification of $\mathcal{P}_{\text{inv}}^{(\epsilon)}$ as the projection onto the invariant manifold $\mathscr{M}^{(\epsilon)}$; the exact invariance relation 3.27 is the non-perturbative extension of $\mathcal{Q}_{\text{inv}}\mathcal{L}_0\mathcal{P}_{\text{inv}} = 0$ to $\epsilon > 0$.

2. The geometric formulation, while generally working for arbitrary λ_s with $\text{Im}\lambda_s = 0$, has mostly been applied to the cases with $\lambda_s = 0$, as discussed in Chap. 2, and further detailed in Appendix 7.1. In this thesis (Chap. 2) we explicitly treat fast unitary center dynamics with $\text{Im}\,\lambda_s \neq 0$ and small $\text{Re}\,\lambda_s$, solving the invariance equation via a Sylvester formulation at the superoperator level. On the TCL side, the computation of $\mathcal{K}_{\text{TCL}}^{(\epsilon)}$ and $\mathcal{F}_{\text{TCL}}^{(\epsilon)}$ proceeds unchanged whether $\lambda_s = 0$ or not; the method is agnostic to the presence of center dynamics once the slow spectral subspace is fixed.

3. The geometric approach describes the motion on $\mathscr{M}^{(\epsilon)}$ but does not capture the initial fast relaxation phase. The TCL formulation incorporates this transient exactly through the finite-time projector $\mathcal{P}_{\mathrm{inv}}^{(\epsilon)}(t)$ and the term $\mathcal{J}_{\mathrm{inv}}^{(\epsilon)}(t)$ in Eq. 3.21. Neglecting this short-time phase may lead to artifacts in the effective generator, namely non-CP dynamics. In Sec. 3.4 we use the time-dependent reduced generator $\mathcal{F}_{\mathrm{TCL}}^{(\epsilon)}(t)$ to regularize such issues while remaining consistent with the long-time limit, by analyzing the same model as of Example 2 of Chap. 2, which was yielding non-CP dynamics.

4. To evaluate the maps $\mathcal{F}_{\mathrm{TCL}}^{(\epsilon)}$ and $\mathcal{K}_{\mathrm{TCL}}^{(\epsilon)}$ perturbatively, one has to expand the asymptotic TCL projector $\mathcal{P}_{\mathrm{inv}}^{(\epsilon)}$. Appendix 7.2 provides explicit expressions up to third order in ϵ. Once identified the specific operation of $\mathcal{P}_{\mathrm{inv}}$ for the system under investigation, they can be readily applied, as we detail in the next section.

3.4 Example

3.4.1 Bipartite systems

In the TCL master equation formulation, the basic procedure to obtain a reduced model consists in four steps:

1. Identifying $\mathcal{L}_0$ and $\mathcal{L}_1$ in the dynamics.

2. Identifying the surviving modes by solving the zero order problem.

3. Specifying the operation of the projection $\mathcal{P}_{\mathrm{inv}}$ defined by Eq. 3.18.

4. Computing the maps $\mathcal{F}_{\mathrm{TCL}}^{(\epsilon)}$ and $\mathcal{K}_{\mathrm{TCL}}^{(\epsilon)}$, which define the reduced model.

To demonstrate these steps, we consider adiabatic elimination for a bipartite system, which serves as a prototypical model for reservoir engineering. We show that the projection $\mathcal{P}_{\mathrm{inv}}$ is given by the partial trace over the eliminated subsystem [see Eq. 3.36]. Furthermore, we apply this scheme to the Rabi model and discuss the positivity of the reduced dynamics.

Consider a bipartite system consisting of two subsystems A and B, the dimensions of which are denoted as d_A and d_B, respectively. Suppose that the density operator $\boldsymbol{\rho}$ obeys a master equation of the form

$$\frac{d}{dt}\boldsymbol{\rho}(t) = \mathcal{L}\boldsymbol{\rho}(t), \quad \mathcal{L} = \mathcal{L}_A \otimes \mathcal{I}_B + \mathcal{I}_A \otimes \mathcal{L}_B + \mathcal{L}_{\mathrm{int}}, \tag{3.33}$$

where, for $\xi = A, B$, $\mathcal{I}_\xi$ is the identity superoperator on ξ, $\mathcal{L}_\xi$ describes the internal dynamics on ξ, and $\mathcal{L}_{\mathrm{int}}$ represents the interaction between A and B. In what follows, we assume that $\mathcal{L}_A$ has a unique steady state and $\mathcal{L}_B$ generates unitary dynamics as $\mathcal{L}_B\boldsymbol{\rho} = -i[H_B, \boldsymbol{\rho}]$.

1. Timescale separation. The first step is to identify $\mathcal{L}_0$ and $\epsilon\mathcal{L}_1$ in the dynamics. This procedure depends on the specific physical setting to be investigated. We consider cases where a strongly dissipative subsystem A is weakly coupled to another subsystem B via $\mathcal{L}_{\rm int}$. Owing to the weak coupling assumption, we can treat $\mathcal{L}_{\rm int}$ as perturbation. Therefore, we set $\mathcal{L}_0 = \mathcal{L}_A \otimes \mathcal{I}_B + \mathcal{I}_A \otimes \mathcal{L}_B$ and $\epsilon\mathcal{L}_1 = \mathcal{L}_{\rm int}$.

2. Identification of the surviving modes. The second step is to identify the surviving modes by solving the eigenvalue problem of $\mathcal{L}_0$ for them. Suppose the eigenvalue problem of $\mathcal{L}_A$ is solved as

$$(\hat{\mathcal{L}}_A - \lambda_{A,i}\hat{\mathcal{I}}_A)\,|r_{A,i}\rangle\!\rangle = 0, \quad \langle\!\langle l_{A,i}|\,(\hat{\mathcal{L}}_A - \lambda_{A,i}\hat{\mathcal{I}}_A) = 0, \tag{3.34}$$

for $i = 1, 2, \ldots, d_A^2$. The assumption of a unique steady state, denoted by $\bar{\boldsymbol{\rho}}_A$, then indicates $\lambda_{A,1} = 0$, $\boldsymbol{r}_{A,1} = \bar{\boldsymbol{\rho}}_A$, $\boldsymbol{l}_{A,1} = \boldsymbol{I}_A$ ($\boldsymbol{I}_\xi$ the identity operator on ξ), and $\mathrm{Re}\lambda_{A,i>1} < 0$. The form of the left eigenvector $\boldsymbol{l}_{A,1}$ follows from $\langle\!\langle I_A|\,\hat{\mathcal{L}}_A \to \mathrm{Tr}_A\mathcal{L}_A = 0$, with Tr_A the trace operation over A. Note that the decay rate in A is characterized by $\min_{i>1}|\mathrm{Re}\lambda_{A,i}|$. For the subsystem B, suppose that the eigenvalue problem of H_B is solved as

$$(\boldsymbol{H}_B - \Omega_{B,m}\boldsymbol{I}_B)\,|b_m\rangle = 0,$$

for $m = 1, 2, \ldots, d_B$. The (right and left) eigenvectors of $\mathcal{L}_B$ then read $|b_m\rangle\langle b_n| \equiv E_{B,mn}$ with the eigenvalue $i(\Omega_{B,n} - \Omega_{B,m}) \equiv i\Omega_{B,mn}$. Assuming $\{|b_m\rangle\}_{1\le m\le d_B}$ to be an orthonormal basis on B, we find the orthonormal relation $\langle\!\langle E_{B,mn}|E_{B,pq}\rangle\!\rangle = \delta_{m,p}\delta_{n,q}$ and the resolution of identity $\hat{\mathcal{I}}_B = \sum_{m,n=1}^{d_B} |E_{B,mn}\rangle\!\rangle\langle\!\langle E_{B,mn}|$.

Given these, the eigenvalue problem of $\hat{\mathcal{L}}_0$ can now be solved formally. The right and left eigenvectors are given by $\{|r_{A,i}\rangle\!\rangle \otimes |E_{B,mn}\rangle\!\rangle\}_{1\le m,n\le d_B}^{1\le i\le d_A^2}$ and $\{\langle\!\langle l_{A,i}| \otimes \langle\!\langle E_{B,mn}|\}_{1\le m,n\le d_B}^{1\le i\le d_A^2}$, respectively, and the eigenvalues read $\lambda_{i,m,n} = \lambda_{A,i} + i\Omega_{B,mn}$. Note that $\min_{i>1,m,n}|\mathrm{Re}\lambda_{i,m,n}| = \min_{i>1}|\mathrm{Re}\lambda_{A,i}|$, where $\min_{i>1}|\mathrm{Re}\lambda_{A,i}|$ is the decay rate in A as mentioned above. The strong dissipation assumption on A implies that this decay rate is much faster compared to the typical scale of $\epsilon\mathcal{L}_1$. In this case, we can take the modes $(i = 1, m, n)_{1\le m,n\le d_B}$ as the surviving modes. This is the same identification used in Chap. 2; here it is written in Liouville–vectorized notation to fix the TCL conventions.

3. Operation of the projection. The third step is to specify the operation of the projection $\mathcal{P}_{\rm inv}$. The general definition of $\mathcal{P}_{\rm inv}$ is given by Eq. 3.18. Since the right and left eigenvectors associated with the surviving modes are $\{|r_{A,1}\rangle\!\rangle \otimes |E_{B,mn}\rangle\!\rangle\}_{1\le m,n\le d_B}$ and $\{\langle\!\langle l_{A,1}| \otimes \langle\!\langle E_{B,mn}|\}_{1\le m,n\le d_B}$, respectively, we obtain

$$\begin{aligned}\hat{\mathcal{P}}_{\rm inv} &= \sum_{m,n=1}^{d_B} |r_{A,1}\rangle\!\rangle \otimes |E_{B,mn}\rangle\!\rangle\,\langle\!\langle l_{A,1}| \otimes \langle\!\langle E_{B,mn}| \\ &= |\bar{\boldsymbol{\rho}}_A\rangle\!\rangle\langle\!\langle I_A| \otimes \hat{\mathcal{I}}_B,\end{aligned} \tag{3.35}$$

the operation of which reads

$$\mathcal{P}_{\rm inv}\boldsymbol{\rho} = \bar{\boldsymbol{\rho}}_A \otimes \mathrm{tr}_A(\boldsymbol{\rho}). \tag{3.36}$$

We note that the abstract definition 3.18 naturally yields Eq. 3.36, which is commonly assumed in the study of bipartite systems, and was also used in Chap. 2.

4. Operation of the projection. The last step is to compute the maps $\mathcal{F}^{(\epsilon)}_{\mathrm{TCL}}$ and $\mathcal{K}^{(\epsilon)}_{\mathrm{TCL}}$ by inserting $\hat{\mathcal{P}}_{\mathrm{inv}}$ into Eq. 3.29. This yields the reduced model.

Remarks. Two remarks are in order.

(α) As noted at the end of Sec. 3.2, the invariance condition 3.7 has multiple solutions due to the nonuniqueness of parametrizing the invariant subspace $\mathscr{M}^{(\epsilon)}$. In this chapter, we impose the condition 3.8, which is equivalent to the parameter choice given by $x_s = \langle\langle l_s|\rho\rangle\rangle$. In the current setting, the left eigenvectors associated with the surviving modes are $\{\langle\langle l_{A,1}| \otimes \langle\langle E_{B,mn}|\}_{1\leq m,n\leq d_B}$. Accordingly, the parameters read

$$x_{mn} = \langle\langle E_{B,mn}|\rho_B\rangle\rangle\,,$$

with $\boldsymbol{\rho}_B = \mathrm{tr}_A\boldsymbol{\rho}$ the reduced density operator on B. Using the resolution of identity, we find

$$\boldsymbol{\rho}_B = \sum_{m,n=1}^{d_B} x_{mn} E_{B,mn}. \tag{3.37}$$

Therefore, in bipartite systems, the gauge condition 3.8 naturally yields the parametrization via the reduced density operator, which we used in Chap. 2.

(β) When the internal dynamics of B have a much slower timescale compared to Δ, $\mathcal{L}_B$ can be treated as perturbation. We can then split $\mathcal{L}$ as $\mathcal{L}_0 = \mathcal{L}_A \otimes \mathcal{I}_B$ and $\epsilon\mathcal{L}_1 = \mathcal{I}_A \otimes \mathcal{L}_B + \mathcal{L}_{\mathrm{int}}$. In this case, the right and left eigenvectors are given as above with $\{E_{B,mn}\}_{1\leq m,n\leq d_B}$ being arbitrary orthonormal operator basis. Hence, the operation of $\mathcal{P}_{\mathrm{inv}}$ is similarly given by Eq. 3.36. For systems dictated by a GKSL equation, such cases were investigated in Ref. [59]. In particular, the authors proved that the second-order reduced dynamics of $\boldsymbol{\rho}_B$ are always given in the GKSL form. When $\mathcal{L}_B$ has a comparable timescale to Δ and needs to be incorporated in $\mathcal{L}_0$, however, the GKSL form is no longer guaranteed as we see below.

3.4.2 Solving the Rabi model

We now give an explicit solution for the dipolar coupling case, already analyzed in Example 2 of Chap. 2. Full computations are provided in Appendix 7.3. Once the operation of $\mathcal{P}_{\mathrm{inv}}$ is specified, it is possible to evaluate $\mathcal{F}^{(\epsilon)}_{\mathrm{TCL}}$ and $\mathcal{K}^{(\epsilon)}_{\mathrm{TCL}}$. We present explicit computations for the Rabi model including a damped oscillator mode. The dissipative subsystem A is the system of a harmonic oscillator mode with dynamics dictated by a GKSL equation

$$\mathcal{L}_A\boldsymbol{\rho} = -i\omega_{\mathrm{ph}}[\boldsymbol{a}^\dagger\boldsymbol{a}, \boldsymbol{\rho}] + \kappa\mathcal{D}[\boldsymbol{a}]\boldsymbol{\rho}, \tag{3.38}$$

where ω_{ph} is the frequency of the harmonic oscillator and κ is the single photon loss rate. The subsystem B is a qubit system spanned by the orthonormal basis $\{|g\rangle\,, |e\rangle\}$. The internal Hamiltonian of B is assumed to be

$$\boldsymbol{H}_B = \frac{\omega_{\mathrm{eg}}}{2}\boldsymbol{\sigma}_z,$$

with $\omega_{\rm eg}$ the energy difference between the two levels and $\sigma_z = |e\rangle\langle e| - |g\rangle\langle g|$. Hence, $\mathcal{L}_B$ reads

$$\mathcal{L}_B\boldsymbol{\rho} = -\frac{i\omega_{\rm eg}}{2}\left[\boldsymbol{\sigma}_z, \boldsymbol{\rho}\right]. \tag{3.39}$$

The two subsystems are coupled by the Rabi interaction

$$\mathcal{L}_{\rm int}\boldsymbol{\rho} = -ig\left[\left(\boldsymbol{a}^\dagger + \boldsymbol{a}\right)\otimes\boldsymbol{\sigma}_x, \boldsymbol{\rho}\right], \tag{3.40}$$

with $\sigma_x = \sigma_+ + \sigma_-$ and $\sigma_+ = \sigma_-^\dagger = |e\rangle\langle g|$.

With $\mathcal{L}_A$ given by Eq. 3.38, we find that $\Delta = \min_{i>1}|{\rm Re}\lambda_{A,i}| = \kappa/2$. Accordingly, the assumption of weak coupling reads $g/\kappa \ll 1$. Under this condition, the maps $\mathcal{F}^{(\epsilon)}_{\rm TCL}$ and $\mathcal{K}^{(\epsilon)}_{\rm TCL}$ can be evaluated perturbatively. Detailed calculations are provided in Appendix 7.3. In what follows, we present the results and focus on their physical significance.

For the parametrization $\boldsymbol{\rho}_B$ in Eq. 3.37, the reduced dynamics up to the second-order expansion read $(d/dt)\boldsymbol{\rho}_B(t) = \mathcal{F}^{(\epsilon)}_{\rm TCL}\boldsymbol{\rho}_B(t)$ with [see Eq. 7.21]

$$\begin{aligned}\mathcal{F}^{(\epsilon)}_{\rm TCL}\boldsymbol{\rho}_B = &-\frac{i}{2}\Big\{\omega_{\rm eg} + g^2{\rm Im}(1/\gamma_+ - 1/\gamma_-)\Big\}[\boldsymbol{\sigma}_z, \boldsymbol{\rho}_B]\\ &+g^2\sum_{j,k=\pm}K_{jk}\left[\boldsymbol{\sigma}_j\boldsymbol{\rho}_B\boldsymbol{\sigma}_k^\dagger - \frac{\boldsymbol{\sigma}_k^\dagger\boldsymbol{\sigma}_j\boldsymbol{\rho}_B + \boldsymbol{\rho}_B\boldsymbol{\sigma}_k^\dagger\boldsymbol{\sigma}_j}{2}\right],\end{aligned}$$

with $\gamma_\pm = (\kappa/2) + i(\omega_{\rm ph} \pm \omega_{eg})$ and $K_{jk} = 1/\gamma_j + 1/\gamma_k^*$. This result agrees with the geometric approach, which we applied to solve Example 2 in Chap. 2, and with the Redfield equation derived in Ref. [141].

CP violation of the reduced dynamics. The eigenvalues of the coefficient matrix in front of the dissipator, K, read

$$\frac{{\rm tr}(K)}{2}\left[1 \pm \sqrt{1 + \left(\frac{4\omega_{\rm eg}}{|\gamma_+\gamma_-|\ {\rm tr}(K)}\right)^2}\right], \tag{3.41}$$

with ${\rm tr}(K) = \kappa/|\gamma_+|^2 + \kappa/|\gamma_-|^2 > 0$. If $\omega_{\rm eg} \neq 0$, one of the eigenvalues becomes negative, as in Example 2 of Chap. 2. This implies that the second-order generator is in a non-GKSL form violating complete positivity of the evolution. This issue was pointed out in Ref. [141], where the authors showed that additional approximations on the generator to obtain the GKSL form lead to qualitatively incorrect dynamics. An approach that ensures complete positivity was developed in Ref. [142], where the authors derive an effective master equation in the GKSL form.

Including the initial relaxation phase. Here we propose an alternative way to ensure complete positivity of the reduced dynamics. In Ref. [90, 143], the authors demonstrated, for composite Hamiltonian systems, that taking into account the time dependence of

coefficients maintains the positivity of the density operator even in the short-time regime. Following these insights, we propose to use

$$\mathcal{F}^{(\epsilon)}_{\mathrm{TCL}}(t) \equiv \chi_L^\dagger \hat{\mathcal{L}} \hat{\mathcal{P}}^{(\epsilon)}_{\mathrm{inv}}(t) \chi_R, \tag{3.42}$$

as the generator, rather than the asymptotic one $\mathcal{F}^{(\epsilon)}_{\mathrm{TCL}} = \lim_{t\to\infty} \mathcal{F}^{(\epsilon)}_{\mathrm{TCL}}(t)$, when the positivity violation becomes an issue. Assuming $\mathcal{Q}_{\mathrm{inv}}\boldsymbol{\rho}(0) = 0$ as in previous studies, the modified reduced dynamics are now given by $(d/dt)\boldsymbol{\rho}_B(t) = \mathcal{F}^{(\epsilon)}_{\mathrm{TCL}}(t)\boldsymbol{\rho}_B(t)$. We numerically demonstrate in Appendix 7.3.2 that this evolution is completely positive at all times (see Fig. 7.1), and we expect this to hold generally, as long as the coupling is weak enough so that the second-order approximation is justified. While the time-dependent generator cannot be derived within the geometric approach, it can be straightforwardly evaluated in the TCL master equation formulation.

Once the evolution of the parameter $\boldsymbol{\rho}_B(t)$ is determined, the density operator of the bipartite system can be obtained as $\boldsymbol{\rho}(t) = \mathcal{K}^{(\epsilon)}_{\mathrm{TCL}}\boldsymbol{\rho}_B(t)$ with, up to the order of ϵ^2, the map $\mathcal{K}^{(\epsilon)}_{\mathrm{TCL}}$ given by [see Eq. 7.22]

$$\begin{aligned}\mathcal{K}^{(\epsilon)}_{\mathrm{TCL}}\boldsymbol{\rho}_B = &(\boldsymbol{I}+\boldsymbol{W})(|0\rangle\langle 0|\otimes\boldsymbol{\rho}_B)(\boldsymbol{I}+\boldsymbol{W})^\dagger \\ &- g^2(\boldsymbol{I}_A\otimes\boldsymbol{\sigma}_\gamma)(|0\rangle\langle 0|\otimes\boldsymbol{\rho}_B)(\boldsymbol{I}_A\otimes\boldsymbol{\sigma}_\gamma)^\dagger.\end{aligned}$$

with $\boldsymbol{I}$ the identity operator on the total space, $\boldsymbol{\sigma}_\gamma = \boldsymbol{\sigma}_-/\gamma_- + \boldsymbol{\sigma}_+/\gamma_+$, and

$$\boldsymbol{W} = -ig\boldsymbol{a}^\dagger\otimes\boldsymbol{\sigma}_\gamma - \frac{g^2}{\kappa + 2i\omega_{\mathrm{ph}}}(\boldsymbol{a}^\dagger)^2\otimes\left(\frac{\boldsymbol{\sigma}_-\boldsymbol{\sigma}_+}{\gamma_+} + \frac{\boldsymbol{\sigma}_+\boldsymbol{\sigma}_-}{\gamma_-}\right). \tag{3.43}$$

Note that $\mathcal{K}^{(\epsilon)}_{\mathrm{TCL}}$ is not a Kraus map due to the negative sign in the second line. This can be interpreted as a signature of quantum correlation built up in states in $\mathscr{M}^{(\epsilon)}$ [83].

3.5 Concluding remarks

In this chapter we recast adiabatic elimination in the time-convolutionless framework: we identified the TCL asymptotic projector with the geometric projector onto the slow invariant manifold, built the TCL reduced and reconstruction maps, and showed they satisfy the same invariance equation under the same gauge. We also discussed through an example how complete positivity can be restored by taking into account the initial phase of fast relaxation in the reduced dynamics. Together with Chap. 2, this chapter contributes to the adiabatic elimination approach to model reduction for open quantum systems, by formulating it in a way that is both geometrically transparent and analytically tractable. We postpone a more detailed discussion on future work to Chap. 6.

Chapter 4

Tensor network and chain mapping methods for open quantum systems

Contents

Contributions. This chapter provides a self-contained introduction to the tensor network and chain mapping methods applied in Chapter 5 to the context of circuit QED, and fixes the notation adopted in the thesis. Before my PhD, I worked on finite-temperature chain mappings during an internship supervised by D. Tamascelli and A. W. Chin, resulting in the publication [144]. During my PhD, I had the opportunity to take part in the ongoing development and maintenance of the Julia package `MPSDynamics.jl`, led by Thibaut Lacroix, Brieuc Le Dé, Angus Dunnett, and A. W. Chin. The package implements the methods presented here; see the software paper: Thibaut Lacroix, Brieuc Le Dé, Angela Riva, Angus J. Dunnett, and Alex W. Chin. "MPSDynamics.jl: Tensor network simulations for finite-temperature (non-Markovian) open quantum system dynamics". In: *The Journal of Chemical Physics*

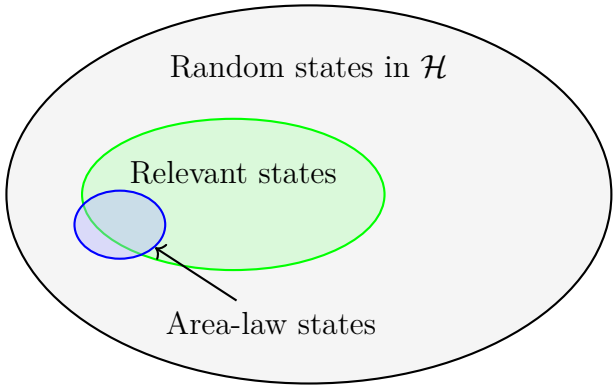

Figure 4.1: The manifold of states that obey the area law of scaling for the entanglement entropy is a (convex, exponentially small) subspace of the total Hilbert space $\mathcal{H}$: arbitrary states exhibit instead a volume law [65].

161.8 (Aug. 2024), p. 084116. ISSN: 0021-9606. DOI: 10.1063/5.0223107. URL: https://doi.org/10.1063/5.0223107.

4.1 Remarks on tensor networks

By promoting the bath modes to relevant degrees of freedom and evolving the combined system–environment state unitarily, an open quantum system is recast as a many-body problem. We use tensor network (TN) to efficiently represent and manipulate many-body states. There are a number of tutorials on the subject [72, 145, 65, 146]. Here, for completeness and to fix notation further used in this thesis, we provide an introduction to the basic notions used throughout.

4.1.1 Quantum many-body states and the area law

A many-body state of N constituents (bosonic or fermionic) describing both the open system and the environmental modes takes the form:

$$|\psi\rangle = \sum_{i_1,i_2,\ldots,i_N} \Psi_{i_1,i_2,\ldots,i_N} |i_1\rangle \otimes |i_2\rangle \otimes \ldots \otimes |i_N\rangle \,. \tag{4.1}$$

Such a state will be represented by a radius in the Hilbert space $\mathcal{H} = \mathcal{H}_1 \otimes \mathcal{H}_2 \otimes \ldots \otimes \mathcal{H}_N$, where each single-particle Hilbert space is spanned by a basis $\{|i_k\rangle\}_{i_k=1}^{d} \in \mathcal{H}_k$, with d being the local dimension, so that $\dim(\mathcal{H}) = d^N$. In the fermionic case, $d = 2$ because of Pauli exclusion principle, whereas in the bosonic case the local Hilbert space is unbounded. This is the so-called *curse of dimensionality* [65].

For large N, exact diagonalisation of the Hamiltonian rapidly becomes infeasible. From its earliest days condensed matter theory has relied on variational methods thank [147]. These approaches rely on the assumption that, even if the whole Hilbert space $\mathcal{H}$ is exponentially big, the set of relevant states–ground states, low-lying excitations, and time-evolved states resulting from the dynamics imposed by a physical Hamiltonian–has some structure that constrains them to a smaller subspace of the Hilbert space $\mathcal{H}$ [148].

Most many-body Hamiltonians couple only nearby degrees of freedom (e.g. nearest- or next-nearest neighbor), and in systems with a spectral gap between ground and first excited states, and with short-range interactions this locality implies an area law for entanglement entropy [145, 67]: when dividing a $D-$dimensional lattice into region A and its complement, the entanglement entropy $S(A)$ scales with the boundary ∂A (growing like N^{D-1}) rather than the volume (growing like N^D). Consequently, low-energy eigenstates of such Hamiltonians lie on an exponentially smaller manifold parameterized by $\mathcal{O}(N)$ degrees of freedom, with accuracy controlled by the entanglement entropy. In one dimension $D = 1$ the entanglement stays constant: an efficient numerical representation of large one-dimensional systems should be possible. Our objective is thus to exploit the entanglement structure of a many-body state by representing it explicitly with tensor networks. The internal tensor ranks bound the bipartite entanglement these states can carry; increasing the ranks systematically improves accuracy, and the truncation error is quantified by the discarded weight in the Schmidt spectrum. This enables efficient representation and dynamics of low-energy states by working directly within the "area law manifold" [67].

4.1.2 Diagrammatic notation for tensor networks

In the following, a tensor is an $n-$dimensional array of complex numbers. The rank of a tensor is the number of indices of the tensor: a scalar is a rank-0 tensor, a vector is a rank-1 tensor, a matrix is a rank-2 tensor, and so forth. Following Penrose's diagrammatic notation [146], a tensor is represented as a geometrical shape, with one "leg" per index

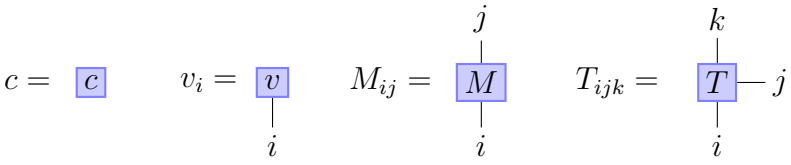

(4.2)

The dimension d of the $k-$th leg is the number of values that the index i_k can take. An index contraction is the sum over all the possible values of the repeated indices of a set of tensors: the two indices must have the same dimension. For example, a contraction is the matrix-vector product

$$u_i = \sum_{j=1}^{d} M_{ij} v_j. \tag{4.3}$$

In the graphical notation, such a contraction of two tensors is represented as

(4.4)

Joining two legs of tensors corresponds to summing over their shared index, which creates a bond. The number of values that index can take is the **bond dimension** χ. Using this convention, arbitrarily complex multi-index contractions can be represented as simple diagrams–so-called tensor networks. A tensor network (TN) is a collection of tensors with a pattern for how to contract their indices. In the graphical notation, a

tensor network is a collection of geometrical shapes (tensors), interconnected by lines (bonds). The legs that do not connect one tensor to the other correspond to the free indices of the tensor network. A simple diagram, for example,

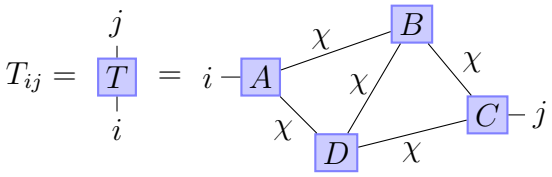

(4.5)

represents the tensor contraction

$$T_{ij} = \sum_{i_2 i_3 i_4 i_5 i_6 = 1}^{\chi} A_{i i_2 i_3} B_{i_3 i_4 i_5} C_{j i_4 i_6} D_{i_2 i_5 i_6}. \tag{4.6}$$

Although any tensor network can in principle be contracted into a single tensor–at an exponential cost $\mathcal{O}(d^N)$, where N is the number of sites and d the dimension of each site–it is often far more efficient not to contract it immediately. Its algebraic structure in fact can be exploited to encode the entanglement structure of a many-body quantum state.

4.1.3 Matrix product states

Several tensor-network architectures have been proposed for representing quantum many-body states [65]. In one dimension, matrix product state (MPS) were introduced in the early 1990s to study spin chains [149, 150]. Vidal later showed how the MPS framework enables efficient classical simulation whenever the system's bipartite entanglement remains sufficiently small [151]. Extensions to higher dimensions include projected entangled pair state (PEPS) in two dimensions [152] and various tree-tensor network (TTN) [153]. Here we focus on MPS.

Historically, the notion of *block decimation* in Wilson's renormalization group [154]—coarse-graining a small cluster of sites into an effective block and discarding its high-energy components—provides a first systematic way to reduce the Hilbert space. However, when applied directly to one-dimensional quantum chains it fails, because it ignores the entanglement between that block and the rest of the system. White's density matrix renormalization group (DMRG) [155] overcomes this by embedding each block in its *environment*, finding the ground state of the combined system, and forming the block's reduced density matrix. By keeping only the eigenvectors with the largest weights—precisely the Schmidt vectors across the block–environment cut—one retains exactly those states that capture the most entanglement. Verstraete, Porras, and Cirac later showed that this entanglement-guided truncation is mathematically equivalent to a variational search over MPS, thus casting DMRG in the modern tensor-network framework [66].

The information necessary to describe the many-body state $|\psi\rangle$, defined in Eq. 4.1, is contained in the rank$-N$ tensor $\Psi_{i_1 i_2 \ldots i_N}$. In Penrose notation, we represent it as

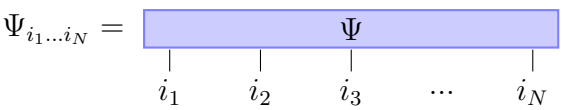

(4.7)

This description is inefficient, as it requires to specify and store in the memory of the computer each of the d^N coefficients needed to specify the state. The complexity of the description can be reduced by breaking the rank$-N$ tensor into smaller rank tensors. MPSs are tensor network states that correspond to one-dimensional arrays of tensors, where each tensor corresponds to a site of the many body system; by replacing the tensor Ψ with the following tensor network:

$$\Psi_{i_1 \ldots i_N} = A_1^{i_1} A_2^{i_2} \ldots A_N^{i_N} =$$

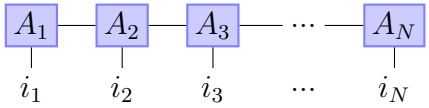

(4.8)

we obtain the MPS representation of the corresponding quantum state $|\psi\rangle$ as:

$$|\psi\rangle = \sum_{i_1 i_2 \ldots i_N} A_1^{i_1} A_2^{i_2} \ldots A_N^{i_N} \, |i_1 i_2 \ldots i_N\rangle \, . \tag{4.9}$$

An MPS is a TN constituted by a one dimensional array of N rank-3 tensors. The tensors A_k are called *sites* of the MPS. Each site has a free leg, called a *physical* leg, that runs over the values of the index i_k. In addition to that, it is connected to the tensors A_{k-1} and A_{k+1} through *virtual* legs, of dimensions χ_{k-1} and χ_k respectively. They are known as *bond dimensions*. The bond dimensions of the first and last dummy virtual legs are set to 1: $\chi_0 = \chi_N = 1$. We refer to the $\max\{\chi_1, \chi_2, ..., \chi_{N-1}\}$ as the *MPS bond dimension*.

Rather than storing all d^N amplitudes explicitly, an MPS encodes them implicitly via a network contraction. To recover a single amplitude $\Psi_{i'_1 i'_2 \ldots i'_N} = \langle i'_1 i'_2 \ldots i_N | \psi \rangle$, one simply fixes each physical index and contracts the one-dimensional chain of matrices of Eq. 4.8

$$\Psi_{i'_1 i'_2 \ldots i'_N} = A_1^{i'_1} A_2^{i'_2} \ldots A_N^{i'_N} =$$

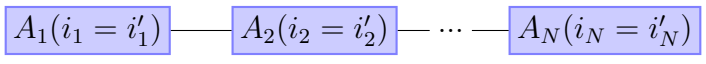

(4.10)

This contraction, which has a cost that increases with the bond dimensions (in the uniform case $\mathcal{O}(N\chi^2)$), yields a single complex amplitude, no lookup table of d^N entries is needed (cf. Eq. 4.7). Moreover, storing the entire MPS requires a total number of complex parameters which scales only linearly, and not exponentially, with N:

$$\#\text{ of complex parameters} = \sum_{k=1}^{N} d_k \, \chi_{k-1} \, \chi_k . \tag{4.11}$$

Assuming that all the local and bond dimensions are the same ($\chi_k = \chi$, $d_k = d$), the number of complex numbers that we need to store is $N\chi^2 d$. If $\chi^2 \propto \exp N$, the gain of the MPS representation is lost. However, the bond dimensions are related to the entanglement present in the system: for quantum states with low entanglement, the MPS representation can be obtained with low values of bond dimensions χ. As a final remark, MPS are dense: they can represent any quantum state of the many-body Hilbert space just by increasing sufficiently the value of the bond dimension. To cover all the states in the Hilbert space, the bond dimension needs to be exponentially large in the system size [145].

Singular value decomposition

To actually extract and normalize the tensors that make up the MPS ansatz, we use the singular value decomposition (SVD). Any matrix $M \in \mathbb{C}^{m\times n}$ can written as:

$$M = USV, \tag{4.12}$$

where $U \in \mathbb{C}^{m\times \min(m,n)}$ is a left unitary matrix ($U^\dagger U = \mathbb{I}$, represented as a triangle pointing to the right), $V \in \mathbb{C}^{\min(m,n)\times n}$ is a right unitary matrix ($VV^\dagger = \mathbb{I}$, represented as a triangle pointing to the left), $S \in \min(m,n) \times \min(m,n)$ is a diagonal matrix with positive real numbers, represented as a diamond, called singular values. In Penrose's notation, with $n > m$ (in the diagram we represent an increase in the dimension as a thicker line):

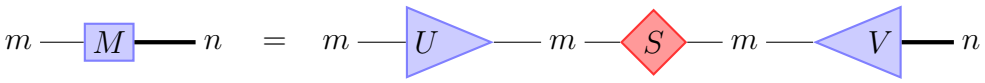

(4.13)

We note that from Eq. 4.7, by performing a sweep SVD, it is possible to obtain, for any state, the MPS representation Eq. 4.8, by factorizing the coefficient tensor A into the site tensors A_k (a step-by-step guide can be found in [72]). Of course, this is not what it is usually done, as the goal of MPS representations is precisely to be able to avoid writing the full tensor A. Crucially, each SVD step produces the two isometric matrices U and V, that one can absorb into neighboring tensors to enforce orthonormality. In other words, the same SVD sweep that builds the MPS chain also fixes its internal gauge in a natural way, laying the groundwork for the canonical gauges of MPS.

Canonical gauges

Because one can always insert the identity $XX^{-1} = \mathbb{I} \in \mathbb{C}^{\chi\times\chi}$ on any bond, an MPS is gauge invariant. The SVD gives a natural choice of X (the singular vector matrices) to define the gauges without any arbitrariness. Putting an MPS in a specific gauge is particularly useful to evaluate operators on MPS sites, as we shall see. The most important canonical gauges are the left canonical, where the matrices corresponding to the sites L_k are left unitary:

$$\Psi_{i_1\ldots i_N} = L_1^{i_1} L_2^{i_2} \ldots L_N^{i_N} =$$

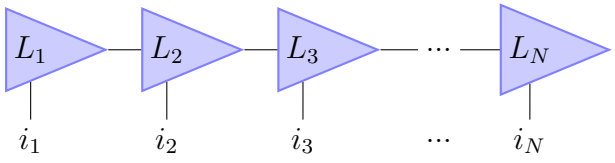

(4.14)

the right canonical, where the matrices corresponding to the sites R_k are right unitary:

$$\Psi_{i_1\ldots i_N} = R_1^{i_1} R_2^{i_2} \ldots R_N^{i_N} =$$

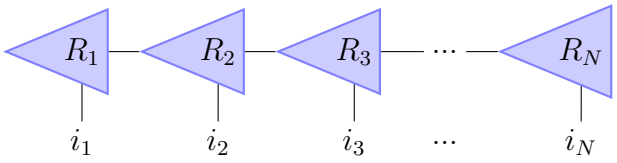

(4.15)

and the canonical gauge, first introduced by Vidal in [151], which is particularly useful to obtain the Schmidt decomposition of an MPS across each bond, where we write the MPS sites as $A_k^{i_k} = \Gamma_k^{i_k} S_k$, with S_k the diagonal matrix of the Schmidt coefficients, so that

$$\Psi_{i_1 \ldots i_N} = L_1^{i_1} S_1^{i_1} \Gamma_2^{i_2} S_2^{i_2} \Gamma_3^{i_3} \ldots S_{N-1}^{i_{N-1}} R_N^{i_N} = \tag{4.16}$$

$=$ 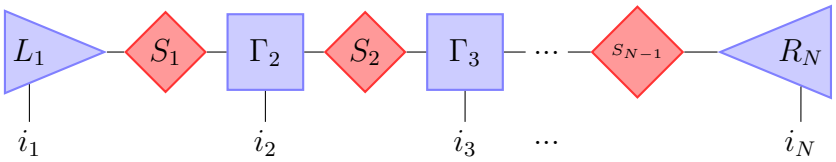

(4.17)

In fact, from the canonical gauge it is straightforward to obtain the so-called mixed canonical gauge: we select the S_k matrix at which we want to divide the MPS in two; we contract the matrices to its left, $L_{k+1} = S_{k+1}\Gamma_{k+1}$, and to its right, $R_k = \Gamma_k S_k$:

$$\Psi_{i_1 \ldots i_N} = L_1^{i_1} S_1^{i_1} \Gamma_2^{i_2} S_2^{i_2} \Gamma_3^{i_3} \ldots S_{N-1}^{i_{N-1}} R_N^{i_N} = \tag{4.18}$$

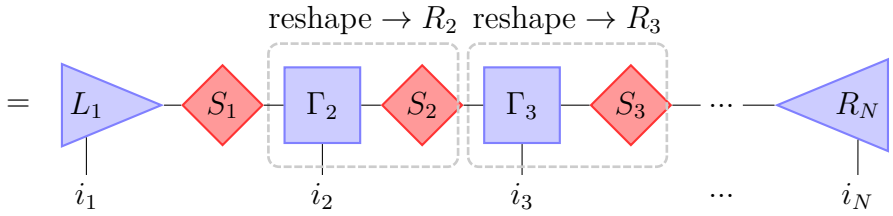

(4.19)

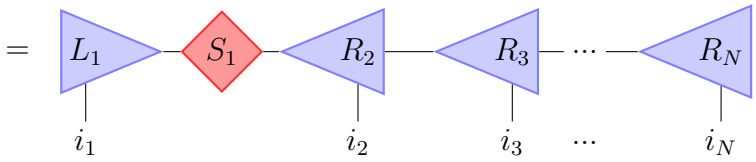

(4.20)

$$= L_1^{i_1} S_1^{i_1} R_2^{i_2} R_3^{i_3} \ldots R_{N-1}^{i_{N-1}} R_N^{i_N} . \tag{4.21}$$

By enforcing local orthonormality, canonical gauges turn any contraction of the MPS with itself (e.g. computing norms, overlaps, or expectation values by contracting the network with its conjugate) into a sequence of identity contractions—thereby stabilizing numerical algorithms, isolating each bond's degrees of freedom, enabling efficient, localized tensor updates. Concretely, in the *left-canonical* gauge each tensor L_k satisfies

$$\sum_{i_k} \left(L_k^{i_k}\right)^\dagger L_k^{i_k} = I_{\chi_k} ,$$

so that contracting all tensors to the left of bond k collapses to the identity on the remaining bond space. Similarly, in the *right-canonical* form each tensor R_k obeys

$$\sum_{i_k} R_k^{i_k} \left(R_k^{i_k}\right)^\dagger = I_{\chi_{k-1}} ,$$

making the contraction of the right side of the MPS trivial. Since only the central singular-value matrix S_k carries nontrivial normalization, any local update or truncation on the corresponding bond does not propagate numerical error elsewhere in the network. This isolation of each bond's degrees of freedom ensures that all norm and overlap calculations remain exact up to machine precision, thus making DMRG sweeps efficient.

Schmidt decomposition and entanglement across bonds

In the mixed canonical form of an MPS, Eq. 4.18, the elements along the diagonals of the S matrix correspond in fact to the Schmidt coefficients λ_i of the bipartition of the system at the point where S is situated. We explicitly write the Schmidt decomposition in the context of an MPS in the mixed canonical form:

$$|\psi\rangle = \sum_{\alpha_k} \lambda_{\alpha_k} \left|\Phi_{\alpha_k}^{[1\ldots k]}\right\rangle \otimes \left|\Phi_{\alpha_k}^{[k\ldots N]}\right\rangle, \tag{4.22}$$

where $\left|\Phi_{\alpha_l}^{[1\ldots k]}\right\rangle$ and $\left|\Phi_{\alpha_l}^{[k+1\ldots N]}\right\rangle$ are the left and right Schmidt vectors describing the subsystems composed of the sites $1,\ldots,k$ and $k+1,\ldots,N$, respectively:

$$\begin{aligned}\left|\Phi_{\alpha_l}^{[1\ldots k]}\right\rangle &= \sum_{i_1\ldots i_k} L_1^{i_1}\ldots L_k^{i_k} \left|i_1\ldots i_k\right\rangle, \\ \left|\Phi_{\alpha_l}^{[k+1\ldots N]}\right\rangle &= \sum_{i_{k+1}\ldots i_N} R_1^{i_{k+1}}\ldots R_k^{i_N} \left|i_{k+1}\ldots i_N\right\rangle.\end{aligned} \tag{4.23}$$

Considering the bipartion at the matrix S_k, the Schmidt coefficients are related to von Neumann entanglement entropy of Eq. 1.6 as:

$$S_k = -\sum_{\alpha_k=1}^{\chi_k} \lambda_{\alpha_k}^2 \log\left(\lambda_{\alpha_k}^2\right). \tag{4.24}$$

The entanglement entropy gives a measure of the correlations between the two partitions of the system. It is possible to obtain a relation between the maximum value of the entanglement entropy and the bond dimension χ: from the positivity of the Schmidt coefficients, $\lambda_{\alpha_k} \geq 0 \quad \forall \alpha_k$, it follows that the Schmidt coefficients must be equal ($\lambda_{\alpha_k} = \lambda \quad \forall \alpha_k$) in order to maximize the entanglement entropy S_k in 1.6; from the normalization condition, $\sum_{\alpha_k=1}^{\chi_k} \lambda_{\alpha_k}^2 = 1$, it follows therefore that $\lambda_{\alpha_k}^2 = \frac{1}{\chi} \quad \forall \alpha_k$. The maximum entanglement between two subsystems linked by a bond of dimension χ_k is:

$$\max(S_k) = \log(\chi_k). \tag{4.25}$$

It follows that to correctly represent the entanglement in an MPS, it must hold that:

$$\chi_k \geq e^{S_k}. \tag{4.26}$$

The minimum bond dimension required to represent a wave function is therefore directly related to the amount of entanglement between the individual sub-systems. It is clear that if two subsystems are strongly entangled, then, to capture in a reliable way the quantum state, the MPS will have exponentially high bond dimensions, and the gain of the MPS representation will be lost. The relation 4.26 in fact, gives us a physical criterion to assess if the MPS representation can efficiently describe a particular wave function. As we have seen in Sec 4.1.3, to keep computationally tractable the number of parameters necessary to the definition of the MPS, we need the bond dimension to scale sub-exponentially with the size of the total system N. If we want the representation to be even more efficient, we can impose the bond dimension to be constant for any size of the total system: $\chi \sim \text{const}, \forall\ N$, a requirement that becomes, because of Eq. 4.26:

$$S_k \sim \text{const}, \tag{4.27}$$

which is the area law for a one-dimensional system, where specifically in one dimension the area of the bipartition is a single site, i.e. independent of the size N of the total system.

4.1.4 Matrix product operators

Another TN structure is matrix product operator (MPO), the operator analogue of an MPS. MPOs are indispensable for evaluating expectation values on MPS-encoded states. Just as any many-body wavefunction can be decomposed into an MPS, any operator $\boldsymbol{O}$ admits an MPO representation:

$$\begin{aligned}\boldsymbol{O} &= \sum_{i_1\ldots i_N, i'_1\ldots i'_N} c_{(i_1\ldots i_N)(i'_1\ldots i'_N)} \left|i_1\ldots i_N\right\rangle \left\langle i'_1\ldots i'_N\right| \\ &= \sum_{i_1\ldots i_N, i'_1\ldots i'_N} c_{(i_1 i'_1)\ldots(i_N i'_N)} \left|i_1\ldots i_N\right\rangle \left\langle i'_1\ldots i'_N\right| \\ &= \sum_{i_1\ldots i_N, i'_1\ldots i'_N} W_1^{i_1 i'_1} W_2^{i_2 i'_2} \ldots W_N^{i_N i'_N} \left|i_1\ldots i_N\right\rangle \left\langle i'_1\ldots i'_N\right|\end{aligned} \tag{4.28}$$

The coefficients $c_{(i_1 i'_1)\ldots(i_N i'_N)}$ therefore define a single rank-N tensor whose kth leg carries the combined index (i_k, i'_k). By decomposing this tensor into a one-dimensional network, as in the last line of Eq. 4.28, one obtains an MPO: a chain of rank-4 site tensors W_k, each with two physical legs (i_k, i'_k) and two virtual legs linking to its neighbors.

$$c_{(i_1 i'_1)\ldots(i_N i'_N)} = W_1^{i_1 i'_1} W_2^{i_2 i'_2} \ldots W_N^{i_N i'_N} =$$

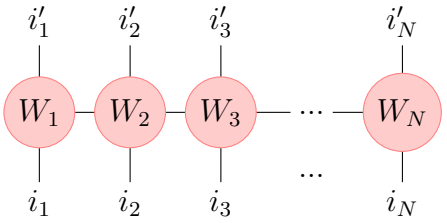

(4.29)

Applying an MPO to an MPS leaves the MPS form invariant, except for an increase in the matrix dimension of the sites: bond dimension on each link is the product of the original MPS and MPO bond dimensions. Concretely, if we consider an MPO of the form of Eq. 4.29, and an MPS of the form of Eq. 4.8, by defining $N_k^{i_k} = \sum_{i'_k} W_k^{i_k i'_k} \otimes A_k^{i'_k}$ we obtain an MPS with site tensors $N_k^{i_k}$ and bond dimensions $d_k \chi_k$:

$$\begin{aligned}\boldsymbol{O}\left|\psi\right\rangle &= \sum_{i_1 i_2\ldots i_N, i'_1 i'_2\ldots i'_N} W_1^{i_1 i'_1} W_2^{i_2 i'_2} \ldots W_N^{i_N i'_N} A_1^{i'_1} A_2^{i'_2} \ldots A_N^{i'_N} \left|i_1 i_2\ldots i_N\right\rangle \\ &= \sum_{i_1 i_2\ldots i_N} N_1^{i_1} N_2^{i_2} \ldots N_N^{i_N} \left|i_1 i_2\ldots i_N\right\rangle \\ &= \sum_{i_1 i_2\ldots i_N} \Phi_{i_1 i_2\ldots i_N} \left|i_1 i_2\ldots i_N\right\rangle = \left|\phi\right\rangle\end{aligned} \tag{4.30}$$

The same operation is depicted below using the diagrammatic notation (enlarged bond dimensions are depicted with thicker lines):

$$\Phi_{i_1 i_2 \ldots i_N} = N_1^{i_1} N_2^{i_2} \ldots N_N^{i_N} =$$

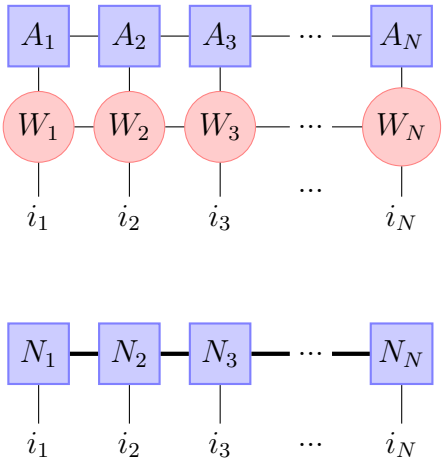

(4.31)

A general procedure based on SVD compression for converting any operator into its MPO form is detailed in [156]. Once in MPO form, operators can be applied to MPS and expectation values computed entirely within the tensor-network framework. For example, the expectation value of a single-site operator O_3,

$$\langle O_3 \rangle \;=\; \langle \psi |\; O_3 \;| \psi \rangle \;,$$

is obtained by contracting the MPS for $|\psi\rangle$, the MPO for O_3, and the conjugate MPS for $\langle\psi|$ into a closed tensor network. In practice this reduces to sweeping an "operator sandwich" over the chain, absorbing the O_3 tensor at site 3 between the corresponding ket and bra tensors and contracting all the identity bonds. Diagrammatically:

$$\langle \psi | \, O_3 \, | \psi \rangle = \textstyle\sum_{i_1 \ldots i_N} (A_1^{i_1})^\dagger A_1^{i_1} (A_2^{i_2})^\dagger A_2 (A_3^{i_3})^\dagger N_3 \ldots (A_N^{i_N})^\dagger A_N^{i_N}$$

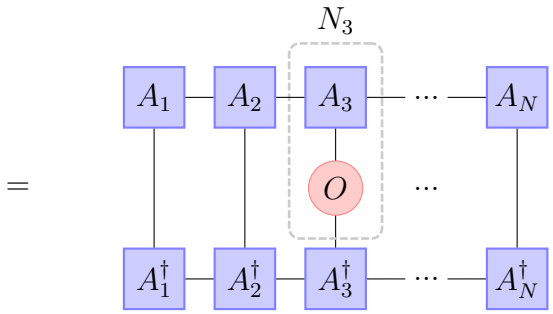

(4.32)

In the mixed-canonical gauge with orthonormalization center at site j (see Eq. 4.1.3), all tensors to the left and right of site j contract to the identity:

$$\sum_{i_k} L_k^{i_k \dagger} L_k^{i_k} = I_{\chi_k}, \qquad \sum_{i_k} R_k^{i_k} R_k^{i_k \dagger} = I_{\chi_{k-1}}.$$

As a result, the full network for

$$\langle \boldsymbol{O}_j \rangle = \langle \psi |\; \boldsymbol{O}_j \;| \psi \rangle$$

collapses to a single three-node contraction at site j:

$$\langle\psi|\, O_j \,|\psi\rangle = \tag{4.33}$$

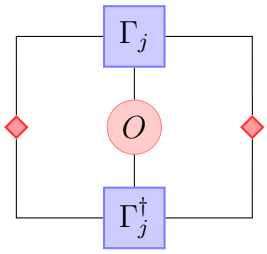

This local contraction can be carried out in $\mathcal{O}(\chi^3 d)$ time, making MPO expectation values both exact (up to machine precision) and efficient when the MPS is in canonical form.

4.1.5 Time evolution with the time dependent variational principle

At the end of Sec. 4.1.3 we have pointed out that any state of $\mathcal{H}$ can be brought to be in a (not unique) MPS representation. In general however, we are interested in constructing MPS of wave functions $|\psi(t)\rangle$ that have evolved in time under a Hamiltonian H, after having started from a known initial state $|\psi(0)\rangle$:

$$|\psi(t)\rangle = U(t)\,|\psi(0)\rangle\,, \tag{4.34}$$

where the time evolution operator is $U(t) = e^{-iHt}$. A simple initial condition is usually given by a product state of the form:

$$|\psi(0)\rangle = |\phi_1\rangle \otimes |\phi_2\rangle \otimes ... \otimes |\phi_N\rangle\,, \tag{4.35}$$

with $|\phi_j\rangle$ as states of the individual subsystems. There are multiple time evolving algorithms that exploit tensor network methods; a complete review is given in [157]. We can divide these methods in two main classes.

Suzuki–Trotter decompositions and TEBD

The algorithms of the first class are based on the approximation of the time evolution operator $U(t)$. Usually the algorithms exploit the Suzuki-Trotter decomposition of $U(t)$, thus breaking the time evolution into a number of finite time-steps:

$$U(t) = e^{-iHt} = e^{-iH\delta}e^{-iH\delta}...e^{-iH\delta} = U(\delta)U(\delta)...U(\delta), \tag{4.36}$$

and finding an MPO reduced expression for $U(\delta)$. Once that is obtained, the MPS at the next temporal step can be computed:

$$|\psi(t+\delta)\rangle = U^{\text{aprx}}(\delta)\,|\psi(t)\rangle\,. \tag{4.37}$$

As we have seen in Eq. 4.31, in applying the MPO, the MPS bond dimension will increase by a factor of the MPO bond dimension, leading to an exponential growth with the number of time steps and thus necessitating a truncation after each step. The most famous algorithm that uses this approach is the time evolving block decimation (TEBD) algorithm [158]. TEBD is particularly effective for short ranged Hamiltonians. The main disadvantage is that the approximation of the time evolution operator introduces a truncation error that breaks unitarity and does not conserve energy during the dynamics.

Dirac–Frenkel TDVP

Central to this work is the time dependent variational principle (TDVP), and its algorithmic implementation. Such an approach falls in the second class of time evolution methods, those that seek to find an approximation of the time-evolved MPS $|\psi(t+dt)\rangle$, therefore preserving unitarity by definition, instead of finding an approximated version of the time evolution MPO U. The TDVP applies the time dependent variational principle to MPS, and efficiently simulates the dynamics of the system [73]. The time dependent variational principle can be exploited to obtain the best possible description of the time-evolved state within the space of MPSs, which is an ansatz for the wave function, using the matrices $A = \{A_i\}_{i=1}^{N}$ that form the MPS as variational parameters [159]. If one fixes the bond dimension of the matrices, the states that the ansatz can describe lie on a manifold $\mathcal{M}$.

To obtain the time evolution of a quantum state, one must solve the time dependent Schroedinger equation:

$$\frac{d}{dt}|\psi(t)\rangle = -i\boldsymbol{H}|\psi(t)\rangle\,. \tag{4.38}$$

The TDVP algorithm [160] is a projector-based method. As we said, the time evolution is constrained to happen on a manifold $\mathcal{M}$, constituted by the states described by MPS with a fixed value of bond dimension. Given the fixed form of the wave function $|\psi(A(t))\rangle$ TDVP seeks to obtain the set of parameters A (the matrices of the MPS) that gives the best approximation to the true wave function $|\psi(t)\rangle$ without leaving the present manifold $\mathcal{M}$, of MPS with fixed bond dimension. The action of the Hamiltonian $\boldsymbol{H}$ on $|\psi(A(t))\rangle$, will in general lead to an increase in the bond dimension value of the time-evolved MPS (as explained in Sec. 4.1.4), potentially taking time evolution outside of the manifold $\mathcal{M}$. The Dirac-Frenkel time dependent variational principle states that the approximate solution of the Schroedinger equation, constrained to happen on the manifold $\mathcal{M}$, is given by:

$$\frac{d}{dt}|\psi(t)\rangle = -i\mathcal{P}_{|\psi(t)\rangle,\mathcal{M}}\boldsymbol{H}|\psi(t)\rangle\,. \tag{4.39}$$

The projector defines an effective Hamiltonian, $\boldsymbol{H}_{\text{eff}} = \mathcal{P}_{|\psi(t)\rangle,\mathcal{M}}\boldsymbol{H}$, under which the dynamics are constrained on $\mathcal{M}$. Constraining the dynamics on a manifold introduces a projection error: the time evolution will obey to an effective Hamiltonian different from the starting one. After the introduction of TDVP as a time evolution method for MPS, in [117] Haegeman *et al.* pointed out that there exists an analytical decomposition for the projector operator $\mathcal{P}$ that simplifies the resolution of Eq. 4.39, turning the problem into one where each matrix A_i can be updated with an effective *on site* Hamiltonian $\boldsymbol{H}_{\text{eff}}$ via a Schroedinger like equation. The effective Hamiltonian $\boldsymbol{H}_{\text{eff}}$ is a contraction of the Hamiltonian MPO and the current state of the other matrices composing the MPS. This allows to do a sequential update. For the details, see [117].

4.2 Mapping the linear system-boson model on a chain

Having introduced how tensor-network ansätze efficiently capture the entanglement structure of many-body states, we now make them practical for open quantum systems

by mapping the Hamiltonian of Eq. 1.45 onto a one-dimensional chain.

4.2.1 TEDOPA chain mapping at zero temperature

Under the Hamiltonian of Eq. 1.45, the system couples *star-wise* to a continuum of bosonic modes. Remarkably, one can show that this star geometry is unitarily equivalent to a semi-infinite tight-binding chain [69, 71], in which the system interacts only with the first site and all bath couplings become nearest-neighbor. In this *chain* picture, entanglement can only spread locally along the chain, making the full system and environment dynamics tractable efficiently with MPS methods—a strategy known as time evolving density matrix using orthogonal polynomials algorithm (TEDOPA) [70].

The TEDOPA chain mapping is implemented by a unitary transformation on the bosonic modes of the environment,

$$\boldsymbol{c}_n^\dagger \;=\; \int_0^\infty d\omega\; U_n(\omega)\, \boldsymbol{b}_\omega^\dagger\,, \qquad U_n(\omega) = \sqrt{J(\omega)}\, \tilde{p}_n(\omega)\,, \tag{4.40}$$

where the functions $\tilde{p}_n(\omega)$ are polynomials orthonormal with respect to the measure $d\mu(\omega) = J(\omega)\, d\omega$, i.e. $\int_0^\infty \tilde{p}_m(\omega)\tilde{p}_n(\omega)\, d\mu(\omega) = \delta_{mn}$, and $\boldsymbol{c}_k$, $\boldsymbol{c}_k^\dagger$ are bosonic modes such that $[\boldsymbol{c}_k, \boldsymbol{c}_l^\dagger] = \delta_{kl}$. Applied to the star-geometry spin–boson Hamiltonian $\boldsymbol{H} = \boldsymbol{H}_S + \boldsymbol{H}_E + \boldsymbol{H}_I$, this transformation yields a semi-infinite, nearest-neighbor chain Hamiltonian [69],

$$\boldsymbol{H}_{\text{chain}} = \boldsymbol{H}_S + \boldsymbol{H}_E^{\text{chain}} + \boldsymbol{H}_I^{\text{chain}}, \tag{4.41}$$

where

$$\boldsymbol{H}_E^{\text{chain}} = \sum_{n=0}^{\infty}\Big(e_n\, \boldsymbol{c}_n^\dagger \boldsymbol{c}_n + t_n\, \boldsymbol{c}_{n+1}^\dagger \boldsymbol{c}_n + t_n\, \boldsymbol{c}_n^\dagger \boldsymbol{c}_{n+1}\Big), \tag{4.42}$$

$$\boldsymbol{H}_I^{\text{chain}} = k_0\, \boldsymbol{A}_S \otimes \Big(\boldsymbol{c}_0^\dagger + \boldsymbol{c}_0\Big). \tag{4.43}$$

Here

$$k_0^2 \;=\; \int_0^\infty d\omega\; J(\omega)\,, \qquad e_1 \;=\; \frac{1}{k_0^2}\int_0^\infty d\omega\; \omega\, J(\omega)\,,$$

while all other on-site energies e_n and hoppings t_n follow directly from a recurrence relation obeyed by the polynomials $\tilde{p}_n$ [161]. The details of this construction can be found in [69], but we make the important remark that the chain coefficients depend on the orthogonal polynomials $\tilde{p}_n(\omega)$ which, in turn, depend on the spectral density $J(\omega)$.

Some properties of the chain coefficients $(k_0,\, e_n,\, t_n)$

- The chain coefficients $(k_0,\, e_n,\, t_n)$ can be analytically computed in some interesting cases, importantly for Ohmic spectral density functions at zero temperature [69]. In all other cases, stable numerical routines, such as ORTHPOL [161], are in general exploited.

- **Wave-like propagation.** If the spectral density $J(\omega)$ is strictly positive on its **finite** support $[\omega_{\min}, \omega_{\max}]$, then the chain parameters e_n and t_n approach constant

values as $n \to \infty$, so that the tail of the chain becomes translationally invariant [70, 71]:

$$\bar{e} = \lim_{n\to+\infty} e_n = \frac{\omega_{\max} + \omega_{\min}}{2} \qquad \bar{t} = \lim_{n\to+\infty} t_n = \frac{\omega_{\max} - \omega_{\min}}{4}. \tag{4.44}$$

Physically, Eq. (4.44) means that, beyond a finite region, excitations launched into the chain propagate as delocalized plane waves—just as in a tight-binding model—and are effectively lost downstream, mimicking irreversible decay. Equivalently, only the first N_{bath} sites (where $\{e_n, t_n\}$ deviate appreciably from $(\bar{e}, \bar{t})$) carry memory effects of the original reservoir, whereas the asymptotic tail behaves like a memoryless Markovian bath. In numerical simulations the chain is truncated to a finite length: this implies that we can define a reflection time t_{refl} after which the excitations reach the end of the chain and bounce back.

- The total excitation number in the chain basis is identical to that in the original mode basis (this follows from the orthogonality of the polynomials):

$$\langle \boldsymbol{N}_{\text{tot}} \rangle = \int_0^{+\infty} \langle \boldsymbol{b}_\omega^\dagger \boldsymbol{b}_\omega \rangle d\omega = \sum_{n=0}^{+\infty} \langle \boldsymbol{c}_n^\dagger \boldsymbol{c}_n \rangle = \langle \boldsymbol{N}_{\text{tot}}^{\text{chain}} \rangle.$$

- The purely quadratic part of the chain Hamiltonian $\boldsymbol{H}_E^{\text{chain}}$ commutes with the total excitation number $\boldsymbol{N}_{\text{tot}}^{\text{chain}}$, so that the system can create or annihilate excitations only at the boundary $n = 0$, after which they propagate along the chain. Studying the transport dynamics on the chain mapped environment can reveal characteristic features (group velocity, dispersion, etc.) of the original continuous environment [162].

Discretization of the environment and spectral density function

During a numerical simulation, a truncation on the number of chain modes (and therefore chain length) is necessarily introduced, in order to work with a chain of finite length, let us say N, instead of a semi-infinite one. The truncation introduces a sampling on the modes in the original star-like environment. We can write the discretized version of the environmental side of the Hamiltonian $\boldsymbol{H}$ of Eq. 1.45 as

$$\boldsymbol{H}_E = \sum_{k=1}^{N} \omega_k \boldsymbol{b}_k^\dagger \boldsymbol{b}_k, \qquad \boldsymbol{H}_I = \boldsymbol{A}_S \otimes \sum_{k=1}^{N} g_k (\boldsymbol{b}_k + \boldsymbol{b}_k^\dagger). \tag{4.45}$$

The discrete parameters $\{\omega_k, g_k\}$ encode a sampling of the continuous spectral density $J(\omega)$ in the sense that

$$J(\omega) \approx \sum_{k=1}^{N} |g_k|^2 \, \delta(\omega - \omega_k), \tag{4.46}$$

with a generally non-uniform grid $\{\omega_k\}$. This finite set fully specifies the bath used in the simulation. Some remarks:

- The discrete star representation is also the usual starting point for microscopic derivations of Markovian (GKSL) master equations under the Born–Markov (secular) approximation [26].

- To recover implicitly sampled frequencies in the orginial star representation, diagonalize the Jacobi (tri-diagonal) Hamiltonian $\boldsymbol{H}^{\text{chain}}$ (on the diagonal the on-site energies $\{e_n\}$, on the upper and lower diagonals the hopping coefficients $\{t_n\}$): its eigenvalues are the sampled frequencies $\{\omega_k\}$, and its eigenoperators form the unitary $\boldsymbol{U}$ that maps between the star and the chain environment.

- Conversely, one can decide to sample the relevant frequencies in the star representation, and apply the inverse transformation to construct the chain Hamiltonian.

- To obtain the picture in the original environment $J(\omega)$, the chain mapping must be reversed. For example, for the occupation number in the environment:

$$\boldsymbol{n}_i^b = \boldsymbol{b}_i^\dagger \boldsymbol{b}_i = \sum_{k,l} U_{ik}^* \boldsymbol{c}_k^\dagger \boldsymbol{c}_l U_{li}. \tag{4.47}$$

- Once the problem is mapped on the chain, the MPO representation of the new Hamiltonian follows straightforwardly.

- At zero temperature, the dynamics dictated by $\boldsymbol{H}^{\text{chain}}$ start from the initial **pure** state

$$|\psi(0)\rangle = |\psi_S(0)\rangle \otimes |\psi_E(0)\rangle\,. \tag{4.48}$$

  In our simulations, $|\psi(0)\rangle$ will be represented as an MPS with the system as the first site(s), followed by N environmental sites.

- **More chain coefficients for finer frequency sampling.** If one starts from the vacuum state of the chain, such that

$$\boldsymbol{c}\,|\text{vac}\rangle = 0, \tag{4.49}$$

  since excitations on the chain propagate as plane waves, only the first $\ell(t)$ sites (set by the asymptotic group velocity $\bar{t}$ of Eq. 4.44) can be populated at time t. We exploit this "finite light–cone" to obtain a finer frequency sampling without adding sites to the MPS of length N. To do so, one has to compute the chain coefficients up to a longer length $M > N$, and embed the measured chain observables ($N \times N$ matrices) into $M \times M$ matrices, by zero–padding the $N - \ell(t)$ unreached sites (still in vacuum). Using the corresponding M–mode star–to–chain isometry (e.g. Eq. 4.47) then yields the observables on a denser frequency mesh $\{\omega_k\}_{k=1}^M$.

To summarize, the TEDOPA mapping provides a representation of the linear system-boson model as a semi-infinite chain with only nearest-neighbor interactions, and therefore local entanglement structure, a key characteristic for an efficient MPS representation and time evolution (see Sec. 4.1). Moreover, for strictly positive $J(\omega)$ the asymptotic coefficients (e_n, t_n) converge (Eq. (4.44)), so excitations injected by the system are transported away and dissipated into the tail of the chain.

4.2.2 T-TEDOPA: chain mapping at finite temperature

At finite temperature, we adopt the standard factorized initial condition

$$\boldsymbol{\rho}(0) = \boldsymbol{\rho}_S(0) \otimes \boldsymbol{\rho}_E^{\beta}(0), \tag{4.50}$$

with the environment in a thermal state at inverse temperature β [163]:

$$\boldsymbol{\rho}_E^{\beta}(0) = \frac{e^{-\beta \boldsymbol{H}_E}}{Z}, \qquad Z = \mathrm{Tr}\left[e^{-\beta \boldsymbol{H}_E}\right]. \tag{4.51}$$

For a discretized bath of bosonic modes (Eq. 4.45) this is equivalently

$$\boldsymbol{\rho}_E^{\beta}(0) \;=\; \bigotimes_i \left(1 - e^{-\beta\omega_i}\right) \sum_{n_i=0}^{\infty} e^{-\beta\omega_i n_i} \; |n_i\rangle\langle n_i| \;, \tag{4.52}$$

i.e. a classical mixture over all occupation configurations $\{n_i\}$ with Boltzmann weights. The support of $\boldsymbol{\rho}_E^{\beta}$ contains an enormous number of configurations even at modest T: Monte-Carlo sampling of initial pure states is prohibitively expensive, while evolving the mixed state directly (as an MPO) typically incurs substantially larger local and bond dimensions than pure-state MPS evolution. This motivates the introduction of the temperature dependent TEDOPA (T-TEDOPA), by Tamascelli *et al.* in [164], an extension of the chain mapping to finite temperature simulations which recasts the finite temperature problem into a zero-temperature pure-state simulation without sacrificing exactness under the usual Gaussian, linear-coupling assumptions.

Equivalence of finite-temperature and extended vacuum baths

Assumptions. Assuming the initial state of the system to be pure $\boldsymbol{\rho}_S(0) = |\psi_S(0)\rangle\langle\psi_S(0)|$, and the initial state of the environment to be the thermal state at inverse temperature $\beta = (k_B T)^{-1}$

$$\boldsymbol{\rho}_E(0) = \bigotimes_\omega \frac{e^{-\beta\omega \boldsymbol{b}_\omega^\dagger \boldsymbol{b}_\omega}}{\mathrm{Tr}_E[e^{-\beta\omega \boldsymbol{b}_\omega^\dagger \boldsymbol{b}_\omega}]} = \bigotimes_\omega \frac{e^{-\beta\omega \boldsymbol{b}_\omega^\dagger \boldsymbol{b}_\omega}}{Z_\omega(\beta)} = \bigotimes_\omega \boldsymbol{\rho}_\omega(\beta), \tag{4.53}$$

by tracing out the environment we recover the reduced state of the time evolving system as

$$\boldsymbol{\rho}_S(t) = \mathrm{Tr}_E\left\{\boldsymbol{U}(t)\boldsymbol{\rho}_S(0) \otimes \boldsymbol{\rho}_E(0)\boldsymbol{U}^\dagger(t)\right\}, \tag{4.54}$$

where the time evolution is dictated by the linear system-boson Hamiltonian of Eq. 1.45.

Equivalence of correlation functions. The bi-linearity of the interaction operator $\boldsymbol{H}_I$ of Eq. 1.46 and the Gaussian character of $\rho_E^{\beta}(0)$ guarantee that reduced state $\rho_S(t)$ of the system at time t is completely determined by the environment's two time correlation function [116]

$$\begin{aligned} C_\beta(t) &= \int_0^\infty d\omega \, \mathrm{Tr}_E\left[\boldsymbol{\rho}_\omega(\beta)\boldsymbol{O}_\omega(t)\boldsymbol{O}_\omega(0)\right] \\ &= \int_0^\infty d\omega J(\omega)\left[e^{-i\omega t}(1 + n_\omega(\beta)) + e^{i\omega t} n_\omega(\beta)\right], \end{aligned} \tag{4.55}$$

where the interaction operator on the bath side $\boldsymbol{O}_\omega = \sqrt{J(\omega)}(\boldsymbol{b}_\omega^\dagger + \boldsymbol{b}_\omega)$ is time evolved in the interaction picture,

$$\boldsymbol{O}_\omega(t) = \sqrt{J(\omega)}(e^{-i\omega t}\boldsymbol{b}_\omega^\dagger(0) + e^{i\omega t}\boldsymbol{b}_\omega(0)), \tag{4.56}$$

and $n_\omega(\beta)$ is the Bose-Einstein occupation number at frequency ω and inverse temperature β:

$$n_\omega(\beta) = \mathrm{Tr}_E\left[\boldsymbol{\rho}_\omega(\beta)\boldsymbol{b}_\omega^\dagger\boldsymbol{b}_\omega\right] = \frac{1}{e^{\beta\omega}-1}. \tag{4.57}$$

As shown in [164], it is possible to replace the finite-temperature bosonic bath E by another bath, with support on an *extended* range of frequencies. The extended bath is characterized by a new spectral density function $J_\beta(\omega)$ such that its pure vacuum state correlation function matches the thermal state correlation function (Eq. 4.59) exactly.

Idea of derivation. We refer the reader to [164] for full detail on the derivation; here we limit ourselves to mention two key points of the T-TEDOPA construction. Firstly, negative frequency modes are added to the environment, by dilating the range of frequencies of the spectral density function's domain. Secondly, the temperature dependence is moved from the thermal distribution of the statistical ensemble $\boldsymbol{\rho}_E^\beta(0)$ to the spectral density function:

$$J_\beta(\omega) \;= \frac{1}{2}\mathrm{sign}(\omega)J(|\omega|)\left[1 + \coth\left(\frac{\beta\omega}{2}\right)\right]. \tag{4.58}$$

A thermally weighted, extended spectral density function with support on the whole real axis is thus defined. The crucial consequence is that $C_\beta(t)$ of the original thermal environment is obtained from the factorized vacuum state of the positive and negative frequency modes which make up the extended environment, i.e.

$$\begin{aligned} C_\beta(t) \;&= \int_{-\infty}^{+\infty} d\omega \,\langle \mathrm{vac}|\, \boldsymbol{O}_\omega^\beta(t)\boldsymbol{O}_\omega^\beta(0)\,|\mathrm{vac}\rangle \\ &= \int_{-\infty}^{+\infty} d\omega J_\beta(\omega)e^{-i\omega t}, \end{aligned} \tag{4.59}$$

with

$$\boldsymbol{O}_\omega^\beta = \sqrt{J_\beta(\omega)}(\boldsymbol{b}_\omega^\dagger + \boldsymbol{b}_\omega), \quad |\mathrm{vac}\rangle = \bigotimes_\omega |0\rangle_\omega, \quad \boldsymbol{b}_\omega|0\rangle_\omega = 0 \quad \forall\omega\in\mathbb{R}, \tag{4.60}$$

so that the system-extended bath interaction Hamiltonian reads:

$$\boldsymbol{H}_I^\beta = \boldsymbol{A}_S \otimes \int_{-\infty}^{+\infty} d\omega\sqrt{J_\beta(\omega)}(\boldsymbol{b}_\omega^\dagger + \boldsymbol{b}_\omega). \tag{4.61}$$

The equivalence result of [164] ensures that the system's reduced dynamics determined by the interaction with the original bath $J(\omega)$, with initial thermal state of the environment, is equivalent to the reduced dynamics determined by the interaction of the system with the extended bath $J_\beta(\omega)$, with initial (pure) vacuum state. T-TEDOPA therefore shifts thermal contributions from the initial state of the environment to the interaction

strength with the harmonic oscillators of the extended environment. Instead of being encoded in the statistics of the initial thermal state, thermal detailed balance is encoded in J_β via

$$\frac{J_\beta(+\omega)}{J_\beta(-\omega)} = \frac{\left\langle \boldsymbol{b}_\omega \boldsymbol{b}_\omega^\dagger \right\rangle_\beta}{\left\langle \boldsymbol{b}_\omega^\dagger \boldsymbol{b}_\omega \right\rangle_\beta} = e^{\beta\omega}. \tag{4.62}$$

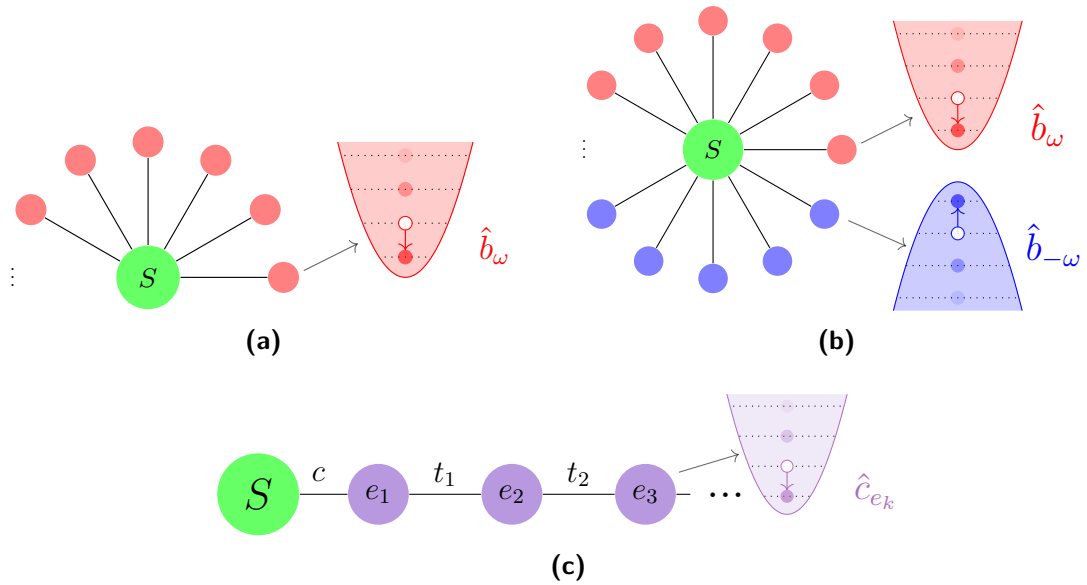

Figure 4.2: A schematic of T-TEDOPA. (a) Star geometry: the system S couples linearly to a continuum of positive frequency bosonic modes ($\omega > 0$). The coupling is encoded by the discretized spectral density $J(\omega)$. (b) Finite-temperature embedding: the mode continuum is extended to negative frequencies ($\omega \in \mathbb{R}$), yielding a temperature-dependent spectral density $J_\beta(\omega)$ that reproduces bath correlations at inverse temperature β. (c) Chain mapping: applying the orthogonal polynomial mapping, now dependent on $J_\beta(\omega)$, maps the problem to a semi-infinite nearest-neighbor chain of harmonic oscillators, whose on-site energies and couplings depend on temperature through $J_\beta(\omega)$. The system couples only to the first site.

The T-TEDOPA chain mapping

Given the equivalence above, the chain mapping proceeds exactly as at zero temperature, with the orthogonality measure replaced by

$$d\mu_\beta(\omega) = J_\beta(\omega)\, d\omega. \tag{4.63}$$

Consequently the chain mapping isometry $\boldsymbol{U}$ and the coefficients (k_0, e_n, t_n) inherit a temperature dependence. This temperature-aware chain is then written as an MPO, and dictates the time evolution of a pure-state MPS, retaining the numerical advantages discussed in Sec. 4.1. A schematic of the procedure is shown in Fig. 4.2. Two practical questions arise: (i) inverting the chain map $\boldsymbol{U}$ (Eq. 4.47) yields mode occupations and correlators in the *extended* bath characterized by $J_\beta(\omega)$, which includes both positive and negative frequencies. How can one consistently recover the same observables for

the original positive-frequency bath $J(\omega)$? (ii) is there any additional computational cost due to finite temperature? We summarize the answers (see [144] for details).

Extended bath with support on negative frequencies. As the temperature increases, the support of $J_\beta(\omega)$ extends to negative frequencies; for a spectral density function $J(\omega)$ supported on $[0, \omega_c]$, the thermalized $J_\beta(\omega)$ approaches a symmetric support $[-\omega_c, +\omega_c]$ in the high-temperature limit $\beta \to 0$. Via Eq. 4.44, this enlarges the asymptotic hopping:

$$\bar{t}(\beta \to 0) = \frac{\omega_c}{2} > \frac{\omega_c}{4} = \bar{t}(\beta \to \infty) \tag{4.64}$$

implying a larger group velocity of bath excitations along the chain at higher temperature, and hence increased computational cost for finite-temperature simulations. Importantly, at any fixed finite time the *local* chain occupations remain bounded, so T-TEDOPA admits controllably accurate simulations for arbitrary times and temperatures.

Unbounded excitation growth in $J_\beta(\omega)$. It is observed that finite-temperature T-TEDOPA simulations require more numerical resources, i.e. higher bond, local Hilbert space dimensions, chain lengths [165, 166]. A contributing factor, observed in [167, 144], is the unbounded growth in the total number of excitations in the extended environment for all finite temperatures. This continuous growth of excitations in the initially empty environment was shown to occur even after the system observables had completely relaxed to their (thermal) steady-state values, raising concerns about the numerical efficiency of T-TEDOPA for long-time simulations, but does not signal physical "heating" of the original thermal reservoir.

The heating cycle instability. A qualitative explanation for the unbounded growth of excitations in the extended bath, referred to as the 'heating cycle' instability, was proposed in Ref. [167] and later confirmed in Ref. [144]. This posits that bath dynamics must continue, even after system relaxation, in order to capture the thermal fluctuations characteristic of the thermal state. For a simple two-level system interacting with a bath in the extended representation, both energetically downhill and uphill system transitions appear as *emissions* into opposite sectors of the extended bath: positive-ω modes for downhill processes and negative-ω modes for uphill ones. Persistent pair creation peaked at $\pm\omega$ (consistent with detailed balance) yields a steady growth of excitations in the extended environment while system observables remain stationary. This picture naturally predicts two-mode correlations between the $\pm\omega$ sectors.

Back to the original environment with the thermofield transformation. A further implication of the heating cycle is that the creation of positive and negative frequency excitations occurs in pairs, so that quantum pair correlations should spontaneously develop during the dynamics. The results presented in Ref. [144], explicitly reveal the existence of such correlations in the extended environment, and relate these back to the thermofield approach of De Vega and Bañuls which is based on the use of two-mode squeezed vacuum states to mimic the effect of a mixed thermal environment [168]. By inverting the thermofield transformation, we are finally able to 'close' the triangle of environment representations shown in Fig. 4.2, allowing the numerical results in the T-TEDOPA chain and the underlying extended environment to be expressed in the *original* (physical) thermal environment. Details on how to invert the thermofield transformation are provided in the Appendix 7.4, following [144].

4.3 Numerical simulations with MPSDynamics.jl

The numerical implementation of the methods here presented can be found in the open-source package `MPSDynamics.jl`. The code performs tensor-network time evolution for open quantum systems in the chain-mapped representation (TEDOPA/T-TEDOPA), using matrix product states MPS and, where appropriate, tree tensor network states. Written in `Julia`, it provides several TDVP schemes—including bond-adaptive one-site variants [166]—together with utilities to (i) construct chain mappings from arbitrary spectral densities $J(\omega)$ at zero and finite temperature, (ii) handle time-dependent Hamiltonians and long-range couplings, and (iii) measure single- and multi-site observables efficiently, including joint system–environment quantities. The package supports bosonic and fermionic environments, and multiple baths.

`MPSDynamics.jl` [74], is distributed under the GPL-3.0 license and publicly available and under development at
`github.com/shareloqs/MPSDynamics.jl`,
with documentation and tutorial examples, including various analytically solvable models for benchmarking. An archived record is provided in [75].

4.3.1 Simulation workflow

We simulate finite-temperature open-system dynamics with T-TEDOPA and MPS, leaving environmental observables open to inspection. For a single bosonic bath, the workflow is:

1. **Microscopic model.** Specify $\boldsymbol{H}_S$, $\boldsymbol{H}_I$, and the temperature-dependent spectral density $J_\beta(\omega)$ (Sec. 4.2.2).

2. **Chain mapping.** Compute the chain coefficients (k_0, e_n, t_n) from $J_\beta(\omega)$ (e.g., `chaincoeffs_finiteT`); use them to build the system+chain MPO.

3. **Initial state.** Prepare the initial state of system-environment as an MPS

$$|\psi_{SE}(t_0)\rangle =$$ 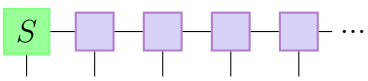

(4.65)

4. **Time evolution.** Evolve with TDVP (one-site, two-site, or bond-adaptive) and log one- and two-point observables on system and chain sites.

5. **Post-processing.** Invert the chain mapping to obtain frequency-resolved bath observables in the extended bath; when using T-TEDOPA, optionally invert the thermofield mapping to recover the original physical bath (Sec. 4.2.1, App.7.4).

4.3.2 Convergence checks

Reliable results require systematic convergence assessments:

- **Spectral cutoff ω_c and chain asymptotics.** A finite high-frequency cutoff ω_c is necessary to ensure that the chain coefficients converge to asymptotic values (Eq. (4.44)).
- **Chain length N.** N should be chosen so the simulation time $t_{\max}$ is shorter than the first reflection time, $t_{\text{refl}} \approx (N - n_0)/v_{\max}$ with $v_{\max} = 2|\bar{t}|$ for a nearest-neighbor chain and n_0 the initially excited region. The utility `findchainlength` provides *a priori* estimates from either $\bar{t}$ or explicit $\{e_n, t_n\}$.
- **Local Hilbert-space truncations.** Local Fock dimension should be chosen so that tail weights of the expected distributions (e.g., coherent-state Poisson tails for driven cavities) are below a set tolerance; monitor commutators (e.g., $\langle [\boldsymbol{a}, \boldsymbol{a}^\dagger] \rangle$) and on-site moments for drift.
- **Bond dimension and truncation error.** Converged observables are insensitive to increasing the maximum bond dimension. The growth of entanglement entropy can be tracked to obtain its max value $S_{\max}$: once converged, we have that $\chi_{\min} \geq e^{S_{\max}}$. For the `DTDVP` algorithm, which adaptively grows bond dimensions at each site and timestep, check convergence for multiple tolerance values on the projection error (or proxy), which the algorithm tries to minimize.
- **Time-step stability.** Check that halving δt leaves observables within tolerance.
- **Sampling resolution.** After inverting the chain mapping, frequency resolution can be increased by zero-padding as described in Sec. 4.2.1.

4.4 Concluding remarks

This Chapter provides a self contained introduction to the chain mapping and MPS methods used throughout this thesis, as implemented in the Julia package MPSDynamics.jl. The package is under active development and is already documented and updated on GitHub. Benchmark tests and tutorial examples are added routinely. The next technical updates to be introduced in the package and broader perspective are discussed in Chap. 6. While the methods here presented are general, we will apply them to a circuit QED setup in Chap. 5.

Chapter 5

Tensor network study of drive-induced relaxation in circuit QED

Contents

Contributions. This chapter contains my original results, which form the basis of an article in preparation. This project is the last part of my thesis, under the supervision of Alexandru Petrescu and Alain Sarlette. From the start, we have had particularly useful discussions with Prakritish Gogoi, Brieuc Le Dé and Alex Chin, all at Sorbonne Université in Paris, and with Serge Florens (Institut Néel in Grenoble) and Nicolas Gheeraert (Krea University in India). I carried out the numerical simulations using the CLEPS infrastructure at Inria Paris, to which I am grateful for providing resources and support.

5.1 The T_1 vs $\bar{n}$ problem in circuit QED

Superconducting circuits are among the leading platforms for quantum technologies [29, 10], leveraging the Josephson effect [169, 170] to endow electrical circuits with the

nonlinearity required to realize quantum bits. As deliberately engineered open quantum systems [3], their practical scalability hinges on balancing two competing demands: suppressing coupling to uncontrolled environmental noise while enabling fast, high-fidelity operations. Engineered control and readout lines deliver the drives that enable state manipulation of qubits with high-fidelity gates [171, 33], reservoir-engineered stabilization of bosonic encodings [44, 43, 42], and qubit state measurement [76, 18, 172, 173].

A persistent obstacle to quantum control is the presence of incoherent errors—energy relaxation and dephasing induced by the electromagnetic environment—which degrade the fidelity of all these tasks [11, 15, 16]. While stronger drive power can, in principle, shorten operation times, and thus reduce the error probability, it also acts a strong perturbation on the dynamics of the system. One widely observed example of such drive-activated effects is T_1-*under-pump* degradation, where the qubit's relaxation time decreases with increasing drive power, as it has been observed in transmon [174, 175] and fluxonium readout [176, 31], single-shot resonator photocounting [35], in cat-qubit lifetime saturation [177, 178], and in single microwave photon detection [179].

5.1.1 The dispersive approximation for QND readout

Although T_1-*under-pump* is generic to driven–dissipative dynamics across gates, active reset, stabilization, and readout, we focus on dispersive readout, which is a minimal but practically relevant case of driven–dissipative dynamics. Reliable qubit measurement is an essential block for fault-tolerant architectures, yet in practice readout errors remain a sizeable fraction of the system error budget [17, 180]; drive-induced T_1 degradation directly undermines measurement fidelity.

Within circuit QED, readout is mediated by a driven resonator dispersively, i.e. off-resonantly and weakly, coupled to the qubit [28]: the cavity frequency shifts depending on the state of the qubit. In the ideal dispersive case the cavity-qubit coupling allows to measure the state of the cavity without disturbing the qubit, as we will detail more precisely in the next paragraph. When considering a non perfectly dispersive coupling, hybridization with the lossy cavity makes the qubit acquire a finite linewidth, and thus dissipation [134]. Minimal dispersive models (two-level system coupled to a driven cavity with a single, frequency-independent loss channel [29, 114], see the next paragraph) capture much of the measurement physics, but they do not account for the often-observed *increase* of the qubit's relaxation with drive; in fact, they can predict the opposite trend (suppression of the relaxation rate with power) [77, 181, 182].

Derivation of the dispersive Hamiltonian. Starting from the Rabi model

$$\boldsymbol{H}_{\text{Rabi}} = \frac{\omega_q}{2}\boldsymbol{\sigma}_z + \omega_a \boldsymbol{a}^\dagger \boldsymbol{a} + g\boldsymbol{\sigma}_x(\boldsymbol{a} + \boldsymbol{a}^\dagger), \tag{5.1}$$

where a qubit described by the Pauli operator $\boldsymbol{\sigma}_z = |e\rangle\langle e| - |g\rangle\langle g|$ is dipolarly coupled to a harmonic oscillator, described by the operators $\boldsymbol{a}$, $\boldsymbol{a}^\dagger$, the RWA (valid for $g \ll \omega_a, \omega_q$) yields the Jaynes-Cummings Hamiltonian

$$\boldsymbol{H}_{\text{JC}} = \frac{\omega_q}{2}\boldsymbol{\sigma}_z + \omega_a \boldsymbol{a}^\dagger \boldsymbol{a} + g(\boldsymbol{a}\boldsymbol{\sigma}_+ + \boldsymbol{a}^\dagger \boldsymbol{\sigma}_-). \tag{5.2}$$

In the dispersive regime $\Delta = \omega_a - \omega_q \gg g$, a Schrieffer-Wolff transformation $\boldsymbol{U} = e^{\boldsymbol{S}}$, where $\boldsymbol{U}^\dagger = e^{\boldsymbol{S}^\dagger} = e^{-\boldsymbol{S}}$, generated by $\boldsymbol{S} = \lambda(\boldsymbol{\sigma}_+\boldsymbol{a} - \boldsymbol{\sigma}_-\boldsymbol{a}^\dagger)$ in $\lambda = g/\Delta$ block-diagonalizes the Hamiltonian up to second order in λ. Namely, using the Baker-Campbell-Hausdorff expansion up to $\mathcal{O}(\lambda^3)$ gives

$$\boldsymbol{H}_{\text{eff}} = e^{\boldsymbol{S}}\boldsymbol{H}e^{-\boldsymbol{S}} = \boldsymbol{H} + [\boldsymbol{S}, \boldsymbol{H}] + \frac{1}{2}[\boldsymbol{S}, [\boldsymbol{S}, \boldsymbol{H}]] + \frac{1}{6}[\boldsymbol{S}, [\boldsymbol{S}, [\boldsymbol{S}, \boldsymbol{H}]]] + ..., \tag{5.3}$$

and writing $\boldsymbol{H} = \boldsymbol{H}_0 + \boldsymbol{H}_{\text{int}}$, with $\boldsymbol{H}_0 = \frac{\omega_q}{2}\boldsymbol{\sigma}_z + \omega_a\boldsymbol{a}^\dagger\boldsymbol{a}$ and $\boldsymbol{H}_{\text{int}} = g(\boldsymbol{a}\boldsymbol{\sigma}_+ + \boldsymbol{a}^\dagger\boldsymbol{\sigma}_-)$, we have that

$$[\boldsymbol{S}, \boldsymbol{H}_0] = -\boldsymbol{H}_{\text{int}}, \quad \text{so that} \quad [\boldsymbol{S}, [\boldsymbol{S}, \boldsymbol{H}_0]] = -[\boldsymbol{S}, \boldsymbol{H}_{\text{int}}] \tag{5.4}$$

and thus

$$\boldsymbol{H}_{\text{eff}} = \boldsymbol{H}_0 + \tfrac{1}{2}[\boldsymbol{S}, \boldsymbol{H}_{\text{int}}] + \mathcal{O}(\lambda^3) \approx \Big(\omega_a + \chi\boldsymbol{\sigma}_z\Big)\boldsymbol{a}^\dagger\boldsymbol{a} + \frac{\omega_q + \chi}{2}\boldsymbol{\sigma}_z, \quad \chi = -\frac{g^2}{\Delta}. \tag{5.5}$$

Since $[\boldsymbol{H}_{\text{eff}}, \boldsymbol{\sigma}_z] = 0$, this enables quantum non-demolition (QND) measurement [183] of $\boldsymbol{\sigma}_z$ via the dispersive shift χ on the cavity frequency [114]. The state of the qubit can be measured by driving the cavity with a microwave pulse at a frequency near its own resonance, and by recording the change in phase or amplitude of the transmitted (or reflected) signal, which depends on the state of the qubit [10]. In this ideal dispersive limit, such a measurement does not disturb the state of the qubit, since the coupling term commutes with the individual Hamiltonians of qubit and cavity (on dispersive readout see e.g. [28, 114, 10]).

Dissipation can be introduced as single-photon loss at rate κ on the cavity, e.g. adding single-photon loss at rate κ to the Jaynes-Cummings Hamiltonian:

$$\frac{d}{dt}\boldsymbol{\rho} = -i[\boldsymbol{H}_{\text{JC}}, \boldsymbol{\rho}] + \kappa\mathcal{D}[\boldsymbol{a}]. \tag{5.6}$$

In the undriven case, adiabatic elimination of the weakly populated cavity gives the standard Purcell rate [134] of relaxation for the qubit

$$\frac{d}{dt}\boldsymbol{\rho}_q = -i\frac{\omega_q}{2}[\boldsymbol{\sigma}_z, \boldsymbol{\rho}_q] + \gamma_P\mathcal{D}[\boldsymbol{\sigma}^-]\boldsymbol{\rho}_q \qquad \gamma_P = |g|^2\frac{\kappa}{\Delta^2 + (\kappa/2)^2}, \tag{5.7}$$

i.e. the qubit's inherited emission is filtered by the cavity Lorentzian at ω_q. In Chaps. 2 and 3 we generalized this by second order adiabatic elimination of the cavity. In particular, in Chap. 2 we treated a cavity–qubit system with both the Jaynes–Cummings $\boldsymbol{H}_{\text{JC}}$ (Example 1) and Rabi $\boldsymbol{H}_{\text{Rabi}}$ (Example 2, covering also the case where cavity and qubit are off-resonant) couplings, in the presence of additional cavity noise channels (thermal noise and dephasing), which induce additional dissipation on the qubit.

Drive-dependence of Purcell rate. A drive acting on the bare cavity mode, such as the readout drive $\boldsymbol{H}_d(t)$ in Eq. 5.10, acts as a perturbation, modifying the spectrum of the coupled system Eq. 5.11, and hence the Purcell rate. In [77], Sete, Gambetta, and Korotkov analyzed the drive dependence of the Purcell relaxation rate for the dynamics governed by

$$\frac{d}{dt}\boldsymbol{\rho} = -i[\boldsymbol{H}_{\text{JC}} + \boldsymbol{H}_d(t), \boldsymbol{\rho}] + \kappa\mathcal{D}[\boldsymbol{a}]\boldsymbol{\rho}. \tag{5.8}$$

Importantly, their analysis is based on the rates computed with respect to *dressed* observables. To define them, one has to associate to each bare factorized state $|i, n\rangle$ ($i \in \{g, e\}$, $n \in \mathbb{N}$) a dressed partner $\left|\overline{i, n}\right\rangle$ belonging to the eigenbasis of the interacting qubit–cavity Hamiltonian ($\boldsymbol{H}_{\mathrm{JC}}$ in the case of [77], $\boldsymbol{H}_{\mathrm{Rabi}}$ in this chapter, see Sec. 5.3.1).

Both the numerical and analytical results presented in [77] show that the Purcell rate should *decrease* as the mean photon number $\bar{n} = \left\langle \boldsymbol{a}^\dagger \boldsymbol{a} \right\rangle$ in the resonator increases, in contradiction with the experimental results mentioned in Sec. 5.1. In fact, for a driven-dissipative cavity ($g = 0$) we have (see e.g. [78, App. B], [63, App. C])

$$\bar{n} = \frac{\epsilon_d^2}{(\omega_a - \omega_d)^2 + \frac{\kappa^2}{4}}, \tag{5.9}$$

so that the average cavity population $\bar{n}$ directly depends on the drive amplitude ϵ_d. The result of Sete *et al.* means that faster readout (stronger drives) should lead to a decrease in the relaxation rate of the qubit, and thus longer lifetimes of the qubit.

5.1.2 Beyond the dispersive approximation

The discrepancy between some of the experimental data (see Sec. 5.1) and the theoretical prediction of Sete *et al.* has motivated a broad effort to model driven-dissipative circuit QED systems more faithfully–especially in the context of readout. Two complementary routes have emerged for explaining the dependence of energy relaxation time T_1 on drive power.

The first explicitly resolves the system beyond the two-level approximation, incorporating its multi-level structure [105] or even the full cosine potential of the Josephson nonlinearity in the superconducting circuit. Dissipation is then modeled as a GKSL master equation. In this vein, several works have identified leakage out of the computational subspace [24, 22, 175] due to drive-activated unwanted state transitions (DUST) and ionization [21, 184] as key contributors of decreased fidelity for a transmon under strong drive, as well as the emergence of chaotic dynamics [23].

A second approach to dissipation consists of including extrinsic degrees of freedom, either as impurities directly coupled to the qubit, and translating into added decay channels [36], quasiparticle excitations [185, 186, 107], or as the inevitably present on-chip components, such as the transmission line, modeled as a bosonic bath of harmonic oscillators [29]. From such linear system-bath models one can, by successive application of perturbation theory and Born-Markov secular approximations [181, 187, 188], derive effective GKSL equations for a transmon [78, 188], for a cat qubit [104], and for a two-level system coupled to a structured bosonic environment [110, 181]. As reviewed in Sec. 1.4, these derivations often rely on time-scale separation assumptions which are not realistic under strong, resonant drives, or in the presence of structured environments with long memory (breakdown of secular/Born–Markov approximations). Periodic drives can be treated with Floquet–Markov approaches [101], but when the drive is resonant with the frequency of the system, numerically finite Hilbert-space truncation produces spurious avoided crossings [102]; analytically, near-resonant denominators make perturbative expansions divergent [78, 104]. Adding weak damping can regularize

these denominators by giving finite linewidths to transitions [106], however these approaches only use a phenomenological dissipator.

5.1.3 A microscopic approach to dissipation

The recent experimental observation in [22] of strong spectral structure of the on-chip impedance network seen by a qubit–marked by resonances due to spurious cavity modes that can mediate inelastic scattering processes at enhanced rates–further motivates the need for microscopic treatment of dissipation during readout, in which the electromagnetic environment is modeled explicitly. Beyond the additional modes of the transmission line, filters and engineered notches are routinely employed during readout [173, 35, 19, 34, 20], with recent examples of metamaterials implemented as cascaded resonators [178, 189, 190], and broadband bandpass filters constituted by multiple harmonic oscillators [191]. Such structure reshapes the spectral function of the environment $J(\omega)$ (introduced in Sec. 1.5 of Chap. 1, and further discussed in Sec. 4.2 of Chap. 4) and, under periodic readout drive, can interact with it in nontrivial ways; indeed, it has been shown that bath-mediated error propagation can compromise dynamical error-suppression protocols even for a qubit coupled to an Ohmic bath [109]. Finally, as detailed in Chap. 1, Sec. 1.4, the dissipation determined from a microscopic model of the environment [192] requires the application of successive approximations, which might not be valid for strongly-driven composite systems, whose eigendecomposition (and thus emission spectrum) is not simply given by factorized states. Predicting the dynamics resulting from the interaction between a driven system, whose resonant frequencies are thereby shifted (AC-Stark shift [29]), and a structured bath is therefore challenging even qualitatively; a quantitative analysis requires a non-perturbative treatment of both the system to environment coupling, under different noise assumptions, and of the time dependence [193, 194, 195].

In this chapter we tackle that interplay microscopically. Starting from a linear system–boson Hamiltonian, we model the transmission line as a structured bosonic bath with spectral density $J(\omega)$ and compute the full unitary dynamics of system *and* environment. This approach allows us to (i) identify when a master equation characterized by single-photon loss dissipator (Eq. 5.6, with the Rabi Hamiltonian of Eq. 5.1), is sufficient to describe the relaxation dynamics of the qubit, (ii) identify additional, drive-enable relaxation pathways that are missed by the approach in the previous item. We find that the readout-power dependence of qubit relaxation rates can be finely dependent on the structure of the bath spectrum, to which we have direct access in our simulations of the microscopic model. In particular, our main finding is that there exist regimes in which T_1 can *decrease* with readout drive $\bar{n}$. This is at odds with previous work, such as [77].

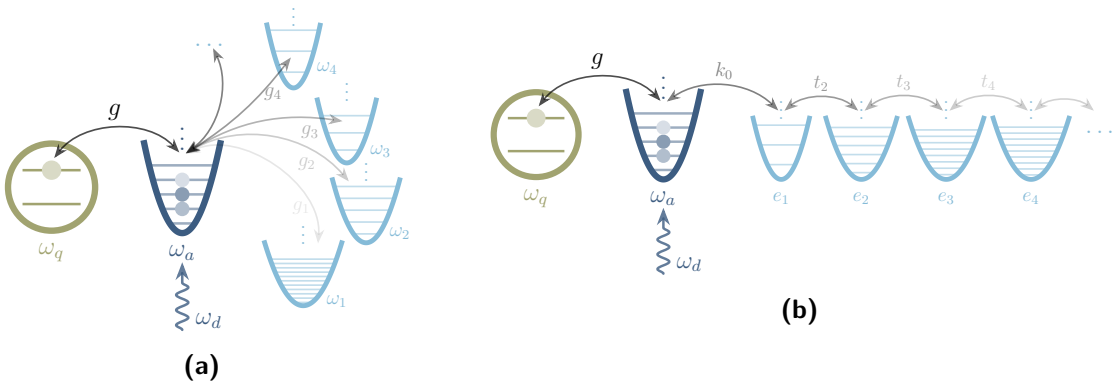

Figure 5.1: Schematic of the model, an abstraction of a readout circuit. (a) A two-level system of transition frequency ω_q is Rabi-coupled, with strength g, to a driven cavity mode of frequency ω_a (drive frequency ω_d). The cavity is coupled to an electromagnetic environment. We model it as a discrete bosonic bath of non-interacting harmonic oscillators with frequencies ω_k and couplings to the two-level system g_k, determined by the spectral density function $J(\omega)$. (b) Chain-mapped representation of the same system: the TLS + driven cavity part is unchanged, while the bosonic bath is mapped onto a semi-infinite chain of harmonic oscillators with onsite energies e_k and nearest-neighbor couplings t_k, the cavity interacting only with the first site via coupling k_0. The dependence of the chain coefficients on $J(\omega)$ is detailed in Sec 4.2.

5.2 Dynamics of the microscopic model

We consider unitary time evolution in the full system-environment Hilbert space $\mathcal{H} = \mathcal{H}_S \otimes \mathcal{H}_E$ under a linear system-boson Hamiltonian

$$\boldsymbol{H}(t) = \boldsymbol{H}_S + \boldsymbol{H}_d(t) + \boldsymbol{H}_E + \boldsymbol{H}_I, \tag{5.10}$$

and set $\hbar = 1$ throughout. The system S is an abstraction of the standard circuit-QED readout subsystem: a two-level system (qubit) Rabi-coupled to a single-mode resonator,

$$\boldsymbol{H}_S = \frac{\omega_q}{2}\boldsymbol{\sigma}_z + \omega_a \boldsymbol{a}^\dagger \boldsymbol{a} + g\boldsymbol{\sigma}_x \otimes (\boldsymbol{a} + \boldsymbol{a}^\dagger), \tag{5.11}$$

where $\boldsymbol{\sigma}_i$ are Pauli operators on the qubit, and $\boldsymbol{a}$, $\boldsymbol{a}^\dagger$ are bosonic ladder operators of the cavity mode, $[\boldsymbol{a}, \boldsymbol{a}^\dagger] = 1$. Modeling the qubit as a two-level system allows to isolate environmental effects from effects related to higher levels which have already been identified as a source of infidelity in dispersive readout, as discussed in Sec. 5.1.2. The cavity is driven coherently by a classical tone at frequency ω_d, which we choose to be resonant with the cavity frequency; provided that the drive amplitude is weak against the drive frequency, $\epsilon_d \ll \omega_d$, a rotating-wave approximation on the drive allows to write

$$\boldsymbol{H}_d(t) = \epsilon_d \left(\boldsymbol{a} e^{+i\omega_d t} + \boldsymbol{a}^\dagger e^{-i\omega_d t} \right), \tag{5.12}$$

with amplitude ϵ_d. The rotating-wave approximation is justified when the drive amplitude is weak relative to the drive frequency. We choose to make it to reduce the

oscillations in the observables for the system, and to make simulations more tractable. We leave a fully ab-initio treatment for future studies.

Dissipation arises from the capacitive coupling of the readout cavity to a transmission-line. Instead of modeling readout of the system as a master equation [114], we choose to model the transmission line microscopically, as a continuum of harmonic modes, as in the Caldeira-Leggett model [68]. Such a model for the transmission line is in fact often used as a starting point to derive master equations on system variables [29, 26]. The environment is thus a continuum of bosonic modes

$$\boldsymbol{H}_E = \int_0^{+\infty} d\omega \omega \boldsymbol{b}_\omega^\dagger \boldsymbol{b}_\omega, \tag{5.13}$$

with $[\boldsymbol{b}_\omega, \boldsymbol{b}_{\omega'}^\dagger] = \delta(\omega - \omega')$, where δ is the Dirac delta. We take a linear, quadrature-quadrature cavity-bath coupling and *do not* apply the secular approximation on this interaction,

$$\boldsymbol{H}_I = (\boldsymbol{a} + \boldsymbol{a}^\dagger) \otimes \int_0^{+\infty} d\omega \sqrt{J(\omega)} \left(\boldsymbol{b}_\omega + \boldsymbol{b}_\omega^\dagger\right), \tag{5.14}$$

where $J(\omega)$ is the spectral density function encoding the coupling strength and bath mode density [26], which has units of frequency given that $\hbar = 1$, the specific form of which we specify below. Following the Caldeira–Leggett construction, the linear quadrature coupling induces a static renormalization of the cavity potential, yielding the reorganization energy term [68]

$$\boldsymbol{H}_S \;\to\; \boldsymbol{H}_S + \lambda_{\text{reorg}} (\boldsymbol{a} + \boldsymbol{a}^\dagger)^2, \qquad \lambda_{\text{reorg}} = \int_0^\infty \frac{J(\omega)}{\omega} d\omega, \tag{5.15}$$

see App. 7.6 for more details.

Chain-mapping and MPS simulation. The spectral density $J(\omega)$ defines the *chain-mapping* [69, 70], introduced in Sec. 4.2 of Chap. 4, an isometry from the linearly coupled system to a bosonic environment Hamiltonian, where the readout mode couples to each bath mode (star-like configuration), to a Hamiltonian where the readout mode only couples to the first mode of a nearest-neighbor, semi-infinite chain of harmonic oscillators. We define new bosonic modes $\boldsymbol{c}_k$, $\boldsymbol{c}_k^\dagger$, with $[\boldsymbol{c}_k, \boldsymbol{c}_l^\dagger] = \delta_{kl}$ by

$$\boldsymbol{c}_n^\dagger = \int_0^\infty d\omega \, U_n(\omega) \, \boldsymbol{b}_\omega^\dagger, \qquad U_n(\omega) = \sqrt{J(\omega)} \, \tilde{p}_n(\omega), \tag{5.16}$$

where $\tilde{p}_n$ are orthonormal polynomials with respect to the measure $d\mu(\omega) = J(\omega)\, d\omega$. The $\boldsymbol{U}$ unitary transformation recasts the linear system-boson Hamiltonian of Eq. 5.14 into a semi-infinite nearest-neighbor chain Hamiltonian

$$\boldsymbol{H}^{\text{chain}} = \boldsymbol{H}_S + \sum_{n=0}^{\infty} \left(e_n \, \boldsymbol{c}_n^\dagger \boldsymbol{c}_n + t_n \, \boldsymbol{c}_{n+1}^\dagger \boldsymbol{c}_n + t_n \, \boldsymbol{c}_n^\dagger \boldsymbol{c}_{n+1} \right) + k_0 \, (\boldsymbol{a} + \boldsymbol{a}^\dagger) \, (\boldsymbol{c}_0 + \boldsymbol{c}_0^\dagger), \tag{5.17}$$

with

$$k_0^2 = \int_0^\infty J(\omega) \, d\omega, \qquad e_1 = \frac{1}{k_0^2} \int_0^\infty \omega \, J(\omega) \, d\omega, \tag{5.18}$$

and the rest of the chain coefficients $\{e_n, t_n\}_{n>0}$ given by the three-term recurrence of $\tilde{p}_n$. While for the flat (Eq. 5.20) and Ohmic (Eq. 5.21) spectral densities the chain coefficients have simple analytical form [69], for the Purcell case (Eq. 5.22) we compute them numerically with the routines available at [75]. The nearest-neighbor coupling structure makes the MPO representation straightforward.

Discretization and sampling. For MPS simulations we truncate the chain to length N. In the original (star) picture this corresponds to replacing the continuum by N effective modes at (generally nonuniform) frequencies ω_k with couplings g_k. The associated spectral density is then, approximately

$$J(\omega) \;\approx\; \sum_{k=1}^{N} |g_k|^2\, \delta(\omega - \omega_k), \tag{5.19}$$

where the frequencies are not equally spaced and '$\approx$' is in the quadrature (weak) sense: for any smooth function f supported on the sampled band, we have that $\int_0^{+\infty} f(\omega) J(\omega) d\omega \;\approx\; \sum_{k=1}^{N} |g_k|^2 f(\omega_k)$, i.e. the discrete measure approximates under integration. The sampled frequencies $\{\omega_i\}$ are the eigenvalues of the $N \times N$ Jacobi (tridiagonal) matrix with diagonal $\{e_0, \ldots, e_{N-1}\}$ and off-diagonal $\{t_0, \ldots, t_{N-2}\}$. The one-dimensional finite chain is well suited to the application of tensor-network time evolution methods, in particular TDVP for MPS [72, 73] (see also Sec. 4.1). A sketch of both representations is given in Fig. 5.1.

Bath models. $J(\omega)$ characterizes the electromagnetic environment to which the cavity is coupled. Throughout this manuscript we consider three bath models:

$$J_{\text{flat}}(\omega) = 2\alpha_{\text{flat}}\theta(\omega_{\max} - \omega)\theta(\omega - \omega_{\min}) \tag{5.20}$$

$$J_{\text{Ohm}}(\omega) = 2\alpha_{\text{Ohm}}\omega\theta(\omega_c - \omega), \tag{5.21}$$

$$J_{\text{PF}}(\omega) = J_{\text{Ohm}}(\omega)\left(1 - De^{-(\omega-\omega_q)^2/(2\sigma)}\right), \tag{5.22}$$

where θ is the Heaviside step function, α is a dimensionless coupling constant, $\omega_{\min}$ and $\omega_{\max}$ define the flat passband, ω_c is a high-frequency cutoff, and $D \in [0, 1]$, σ set the depth and width of a Gaussian Purcell notch centered at the bare qubit frequency ω_q. Despite their simplicity, these choices yield qualitatively distinct relaxation dynamics for the driven qubit–resonator subsystem. While ideal transmission lines are approximately Ohmic [196], real chips see a frequency-dependent impedance due to device geometry, material defects [36], spurious electromagnetic modes [22], and intentional filtering [34], so $J(\omega)$ can have significant features (peaks, notches, band edges) creating non-linear frequency dependence.

GKSL comparison. For a fair comparison with a single-photon GKSL model, we choose parameters so that the cavity linewidth has the same numerical value regardless of which bath spectral function is chosen. According to Fermi's golden rule [11, Eq. E24], we set

$$\kappa = 2\pi J_{\text{Ohm}}(\omega_a) = 2\pi J_{\text{PF}}(\omega_a) = 2\pi J_{\text{flt}}(\omega_a) \tag{5.23}$$

holds in each configuration, with ω_a inside the support of the spectral density. We write

$$\frac{d}{dt}\boldsymbol{\rho} = -i[\boldsymbol{H}_S^{\mathrm{GKSL}} + \boldsymbol{H}_d(t), \boldsymbol{\rho}] + \kappa\mathcal{D}[\boldsymbol{a}]\boldsymbol{\rho}, \tag{5.24}$$

where κ gives the single-photon loss rate of the cavity and implicitly assumes a flat bath (which can be sampled by a single scalar). For a fair comparison with MPS simulations we include a frequency shift proportional to the reorganization energy

$$\boldsymbol{H}_S^{\mathrm{GKSL}} = \frac{\omega_q}{2}\boldsymbol{\sigma}_z + (\omega_a + \lambda_{\mathrm{reorg}})\boldsymbol{a}^\dagger\boldsymbol{a} + g\boldsymbol{\sigma}_x(\boldsymbol{a} + \boldsymbol{a}^\dagger), \tag{5.25}$$

For the drive to be resonant in the GKSL case, the frequency has to be set at

$$\omega_d = \omega_a + \lambda_{\mathrm{reorg}}. \tag{5.26}$$

We label p the proportionality factor

$$\epsilon_d = p\bar{\epsilon}_d, \tag{5.27}$$

where $\bar{\epsilon}_d$ is defined in Table 5.1.

Configurations for simulations. Because the qubit is coupled to the bath through the cavity, which acts as a filter of the electromagnetic environment, another parameter defining the environment perceived by the qubit is the qubit–cavity detuning Δ. In particular, it was shown that the behavior of relaxation rates with respect to drive power can depend on the sign of Δ [105]. We investigate the effect of changing its sign for the Ohmic case. Throughout, we study the following configurations:

- $\Delta > 0$ with flat bath: $J(\omega) = J_{\mathrm{flat}}(\omega)$.
- $\Delta > 0$ with Ohmic bath: $J(\omega) = J_{\mathrm{ohm}}(\omega)$.
- $\Delta < 0$ with Ohmic bath: $J(\omega) = J_{\mathrm{ohm}}(\omega)$.
- $\Delta > 0$ with Purcell-filtered bath: $J(\omega) = J_{\mathrm{PF}}(\omega)$.

5.3 Simulation setup

We investigate the dynamics of the driven qubit–resonator subsystem for the bath models of Sec. 5.2, with the parameters listed in Table 5.2, and system parameters set in Table 5.1. The chain Hamiltonian $\boldsymbol{H}^{\mathrm{chain}}$ (Sec. 5.2) is represented as an MPO and time-evolved exploiting the time-dependent variational principle [73] (see also the discussion in Sec. 4.1.5) on a pure-state MPS, starting from the unentangled system-environment state

$$|\psi(0)\rangle = \left|\overline{i,n}\right\rangle \otimes |\mathrm{vac}\rangle_E\,, \quad |\mathrm{vac}\rangle_E = \bigotimes_{k=1}^{N} |0_k\rangle\,, \tag{5.28}$$

where $\left|\overline{i,n}\right\rangle$ denotes the dressed eigenstates of $\boldsymbol{H}_S$, labeled following [187, 21], by associating to each bare factorized state $|i,n\rangle$ ($i \in \{g,e\}$, $n \in \mathbb{N}$) a dressed eigenstate

Symbol	Meaning	$\Delta > 0$	$\Delta < 0$
ω_q	qubit frequency	5.304	7.500
ω_a	cavity frequency	7.500	5.304
g	qubit–cavity coupling	0.3165	0.3165
κ	cavity linewidth	0.050	0.050
$\bar{\epsilon}_d$	drive amplitude	0.001	0.001
$\Delta = \omega_a - \omega_q$	detuning	$+2.196$	-2.196

Table 5.1: System parameters used throughout, for both the $\Delta > 0$ and $\Delta < 0$ configurations (units: 2π GHz).

Symbol	Meaning	Value
ω_c	cutoff frequency for Eq. 5.21	15
$\omega_{\min}$	low frequency cutoff for Eq. 5.20	3
$\omega_{\max}$	low frequency cutoff for Eq. 5.20	12
D	height of notch filter for Eq. 5.22	0.1
σ	width of notch filter for Eq. 5.22	0.050

Table 5.2: Environmental parameters used throughout (units: 2π GHz).

$\left|\overline{i,n}\right\rangle$ of the interacting qubit–cavity Hamiltonian $\boldsymbol{H}_S$. We report observables in the dressed basis, in particular for the dressed cavity photon number $\boldsymbol{N}_a$ and dressed qubit z Pauli operator $\boldsymbol{\Sigma}_z$, and evaluated as $\boldsymbol{O}_S \otimes \boldsymbol{I}_E$ on the MPS. The construction of dressed states/observables is summarized in Sec. 5.3.1. Crucially, the time evolution of the environment is also left open to inspection, enabling spectroscopy of the qubit-cavity subsystem. To obtain it, one- and two-site observables on chain-modes are also computed at specific timesteps, and related to the original frequency modes by inverting the chain mapping (Sec. 4.2). Additional simulation details are summarized in App. 7.8. MPS simulations use the open-source package MPSDynamics.jl, to which I have contributed [75, 74].

5.3.1 Dressed system observables and initial condition

We define dressed basis observables following the approach outlined in Ref. [187], and adopt the labeling criterion introduced in Eq. (4) of Ref. [21]. Concretely, we associate to each bare factorized state $|i,n\rangle$ ($i \in \{g,e\}$, $n \in \mathbb{N}$) a dressed partner $\left|\overline{i,n}\right\rangle$ belonging to the eigenbasis of the interacting qubit–cavity Hamiltonian $\boldsymbol{H}_S$.

State identification. We diagonalize numerically the Hamiltonian $\boldsymbol{H}_S |\lambda\rangle = E_\lambda |\lambda\rangle$ to obtain its eigenbasis. The dressed ladder is constructed by identifying the ground-state as $|\overline{g,0}\rangle$. Higher rungs are generated by applying the cavity creation operator $\boldsymbol{a}^\dagger$ to the previously identified dressed state, producing a candidate for the next rung. This candidate is projected onto the eigenbasis of $\boldsymbol{H}_S$, and the eigenstate with the highest

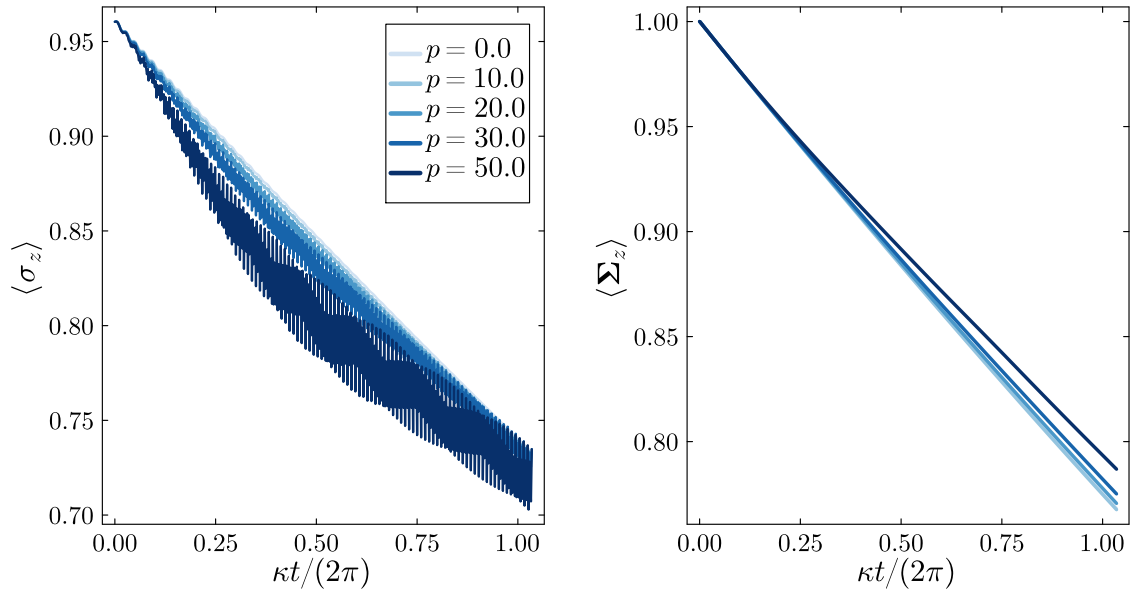

(a) Bare observable $\langle \boldsymbol{\sigma}_z \rangle$.

(b) Dressed observable $\langle \boldsymbol{\Sigma}_z \rangle$.

Figure 5.2: MPS simulation, $\Delta > 0$, $J(\omega) = J_{\text{Ohm}}(\omega)$. Comparison between the bare observable $\langle \boldsymbol{\sigma}_z \rangle$ and the dressed $\langle \boldsymbol{\Sigma}_z \rangle$ of Eq. 5.31 for multiple drive powers $\epsilon_d = p\bar{\epsilon}_d$, the legend is shown in (a).

overlap is selected. We identify the dressed state $|\overline{g, n+1}\rangle$ as the state with index

$$|\overline{g, n+1}\rangle = \text{argmax}_{|\lambda\rangle \text{ eigenvector of } \boldsymbol{H}_S} \left| \frac{\langle \lambda | \, \boldsymbol{a}^\dagger \, |\overline{g, n}\rangle}{\sqrt{\langle \overline{g, n} | \, \boldsymbol{a}\boldsymbol{a}^\dagger \, |\overline{g, n}\rangle}} \right| . \tag{5.29}$$

The excited state ladder is obtained by first applying the qubit's raising operator $\boldsymbol{\sigma}^+$ to the ground state to identify the candidate for $|\overline{e, 0}\rangle$, i.e. the eigenstate with maximum overlap, and subsequently applying the same iterative procedure. Although the procedure does not strictly preclude duplicate selections near quasi-degeneracies, for the parameters used here no duplicates were observed and the dressed ladders are uniquely identified.

System observables. The state-identification procedure provides a systematic way to define observables in the dressed basis. For instance, we define the cavity photon number operator in the dressed basis as

$$\boldsymbol{N}_a = \sum_{i \in \{g,e\}} \sum_{n=0}^{d-1} n \left| \overline{i, n} \right\rangle\!\left\langle \overline{i, n} \right| , \tag{5.30}$$

and similarly the dressed two-level system z Pauli operator (which is equivalent to $\boldsymbol{\sigma}_z$ when $g = 0$) as

$$\boldsymbol{\Sigma}_z = \sum_{n=0}^{d-1} |\overline{e, n}\rangle\langle\overline{e, n}| - |\overline{g, n}\rangle\langle\overline{g, n}| , \tag{5.31}$$

where $\left|\overline{i,n}\right\rangle$ denotes the dressed state corresponding to the bare state $|i,n\rangle$, d is the cutoff in the Fock space of the cavity. The dressed observables allow us to interpret dynamics and decay processes directly in terms of physically meaningful quantities, even in regimes where the bare basis no longer provides a good description due to strong qubit–cavity hybridization.

Observables and dynamics. We evolve a pure state $|\psi(t)\rangle \in \mathcal{H}_S \otimes \mathcal{H}_E$. Placing the MPS in right-canonical form with the orthogonality center on the system block [72] collapses the bath trace, so

$$\langle \boldsymbol{O}_S \rangle(t) = \langle \psi(t)| \, \boldsymbol{O}_S \otimes \boldsymbol{I}_E \, |\psi(t)\rangle = \mathrm{Tr}_S\Big[\boldsymbol{O}_S \, \boldsymbol{\rho}_S(t)\Big], \tag{5.32}$$

with the system reduced state $\boldsymbol{\rho}_S(t) = MM^\dagger$, where $M_{s,\alpha}$ is the center tensor reshaped as a matrix over the composite system index s and the (right-)environment index α. For context, the quality factor of the readout cavity is

$$Q = \frac{\omega_a}{\kappa} = 150, \tag{5.33}$$

and the qubit-cavity coupling is moderately strong compared to the cavity linewidth: $g \sim 6\kappa$, which motivates using dressed system operators.

Bare/dressed comparison Using dressed observables over bare ones is advantageous, as can be seen in Fig. 5.2, where we compare the $\Delta > 0$ case for both GKSL and MPS simulations with $J_{\mathrm{Ohm}}(\omega)$. The GKSL simulations agree well with the MPS results; the small late-time deviations are consistent with the fact that the MPS model retains the full (non-RWA) system–bath coupling, while the microscopic derivation (with $g = 0$) of the single-photon loss dissipator $\mathcal{D}[\boldsymbol{a}]$ implies the secular approximation on the system-bath coupling [26]. The oscillations clearly visible in the bare observables $\boldsymbol{\sigma}_z$ arise primarily from qubit–cavity energy exchange. By switching to dressed observable $\boldsymbol{\Sigma}_z$, expressed in the eigenbasis of the Rabi Hamiltonian, and initializing the simulation in an eigenstate of the Rabi Hamiltonian, we remove these oscillations [77], and obtain a clean decay rate, even at short times–useful because MPS runs are computationally heavy. The oscillations in the bare observables grow in amplitude with the drive power.

5.4 Results

We now present the results of our simulations. In Sec. 5.4.1 we analyze the undriven results, which serve us to calibrate the drive frequencies. In Sec. 5.4.2 we move on to the driven case, comparing both the spectroscopy of the environment and the relaxation rate of the qubit for multiple drive powers.

5.4.1 Undriven spectroscopy of the environment

We first characterize the bath seen by the cavity (and indirectly by the qubit) in the *undriven* setting, with $\epsilon_d = 0$. Details of the calibration scheme can be found in

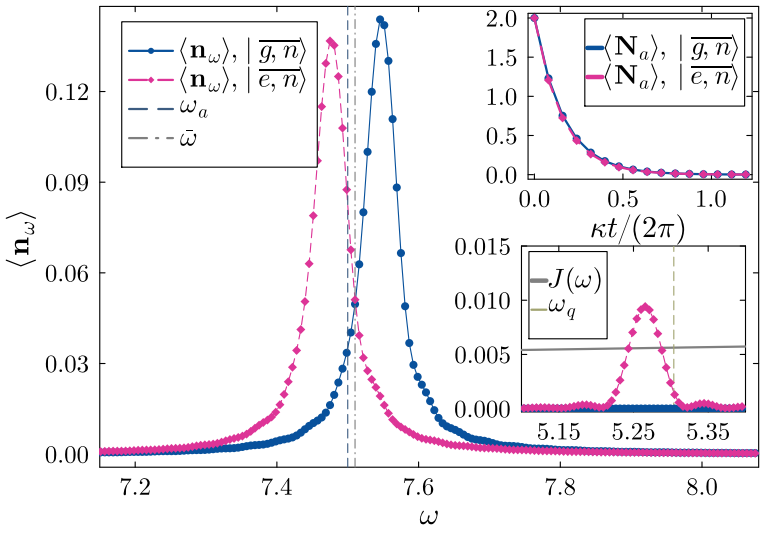

Figure 5.3: Calibration spectroscopy for $\Delta > 0$, $J_{\text{ohm}}(\omega)$. The system is initialized in a dressed Fock state $|\overline{i,n}\rangle$ with $i \in \{g, e\}$ (here $n = 2$) and the bath vacuum $|\text{vac}\rangle_E$. After relaxation of the cavity photon number $\langle \boldsymbol{N}_a \rangle$ to time $\kappa t/(2\pi) = 1$, shown in the upper-right insets, we plot the frequency–resolved bath occupation $\langle \boldsymbol{n}_\omega \rangle$. The cavity–window peak positions define $\omega_{a,e} = \arg\max_\omega \langle \boldsymbol{n}_\omega \rangle = 7.475\,2\pi\text{GHz}$ for the e-like initialization and $\omega_{a,g} = 7.546\,2\pi\text{GHz}$ for the g-like one; the drive is set to the midpoint $\bar{\omega} = (\omega_{a,e} + \omega_{a,g})/2 = 7.51\,2\pi\text{GHz}$. Bottom-right insets around ω_q show the a peak in $\langle \boldsymbol{n}_\omega \rangle$ corresponding to the emission of the qubit and the corresponding spectral density $J(\omega)$.

Appendix 7.7. Starting from dressed Fock states $|\overline{g,n}\rangle$ or $|\overline{e,n}\rangle$ with the environment in $|\text{vac}\rangle_E$, we let the system relax and reconstruct the frequency-resolved bath occupation $\langle \boldsymbol{n}_\omega \rangle$ by inverting the chain mapping. Each resulting spectrum exhibits a peak near the cavity resonance. The frequency of the peak depends on the qubit state, as discussed in Sec. 5.1.1: the cavity frequency acquires a dispersive shift due to the qubit. We plot together the curves resulting from the two initial conditions, and from the maximum of the peaks we obtain the g-like and e-like cavity frequencies; we take their midpoint as the frequency for the drive,

$$\omega_d \equiv \bar{\omega} = \tfrac{1}{2}(\omega_{a,g} + \omega_{a,e}). \tag{5.34}$$

In Fig. 5.3 we report the calibration results for the Ohmic case. The initial state is a dressed eigenstate of the Rabi Hamiltonian, factorized with the vacuum of the chain as in Eq. 5.28 with $n = 2$. The cavity starts from a two photon-like states, as it can be clearly seen by the inset representing the time evolution of $\langle \boldsymbol{N}_a(t) \rangle$, which starts at $\langle \boldsymbol{N}_a(0) \rangle = 2$, while the qubit is initialized respectively in a $e-$like and $g-$like state. We note that the peak corresponding to the $e-$like initial condition, shifted to lower frequencies, is slightly lower than the $g-$like peak, due to the Ohmic dependence of the spectral density function. A smaller peak close to the bare qubit frequency is also clearly visible in the $e-$like case, while it is absent in the $g-$like state, as the qubit has no energy to relax into the environment. We report in Appendix 7.7 the results for the other environmental models considered.

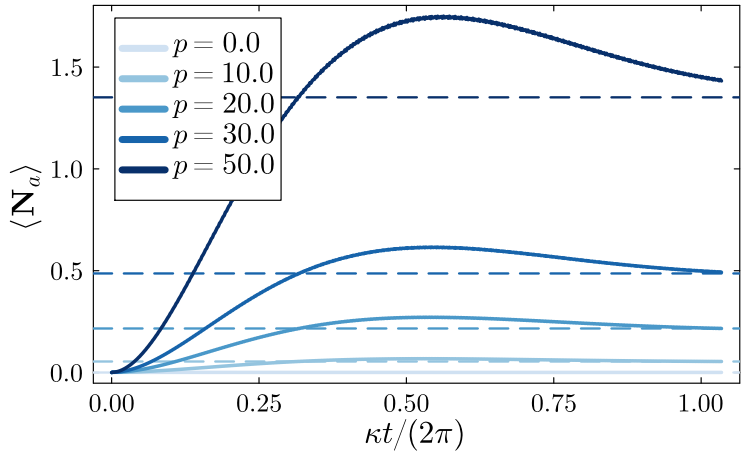

(a) MPS $\Delta > 0$, $J(\omega) = J_{\mathrm{Ohm}}(\omega)$.

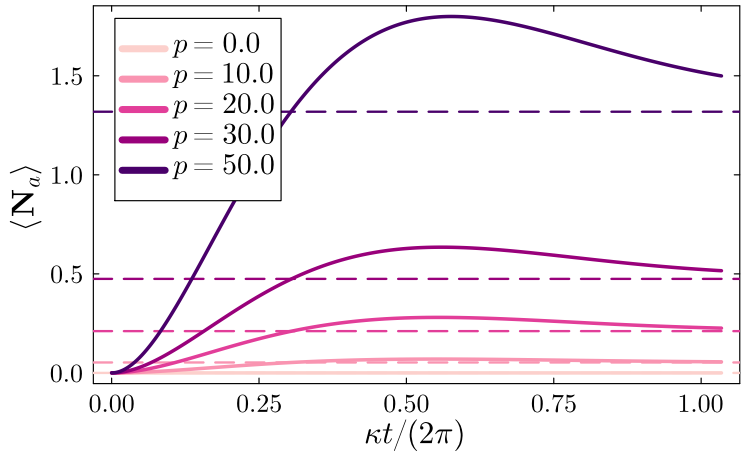

(b) GKSL, $\Delta > 0$.

Figure 5.4: Dressed cavity population dynamics $\langle \boldsymbol{N}_a(t) \rangle$ for both MPS and GKSL simulations, for multiple drive power values $\epsilon_d = p\bar{\epsilon}_d$. The dashed lines represent the steady state population of the cavity $\bar{n}(p)$ of Eq. 5.9.

5.4.2 Computing the relaxation rate at varying drive power

In this section we report the results for the driven simulations, at varying drive power. The initial condition is

$$|\overline{e,n}\rangle_S \otimes |\mathrm{vac}\rangle_E\,, \qquad n = 0. \tag{5.35}$$

The drive frequencies are taken from the calibration results of Sec. 5.4.1, with ω_d defined in Eq. 5.34.

Comparison of the Ohmic/GKSL long-time dynamics

We start this section by comparing GKSL and MPS results for the Ohmic case $J_{\mathrm{Ohm}}(\omega)$, $\Delta > 0$ for long-time simulations, reaching $\kappa t/(2\pi) = 1$. In Fig. 5.4 we report the time evolution for the dressed cavity population $\langle \boldsymbol{N}_a(t) \rangle$. As expected, both GKSL and MPS show an initial transient from the dressed vacuum of the cavity, $\langle \boldsymbol{N}_a(0) \rangle = 0$,

followed by saturation to the steady-state population $\bar{n}(p)$, that increases with p. To estimate the steady-state cavity population $\bar{n}(p)$ for the MPS simulations, we insert the frequency $\omega_{a,e}$ of the peak corresponding to the $e-$like initialization, obtained from the calibration scheme (see Fig. 5.3), in Eq. 5.9. By $\kappa t/(2\pi) = 1$, $\langle \boldsymbol{N}_a(t) \rangle$ reaches the estimated value at lower drive powers, while the transient lasts longer as the drive amplitude is increased. For GKSL, we estimate the qubit-dependent shifted cavity frequency by numerical diagonalization of the Rabi Hamiltonian. With the labeling criterion detailed in Sec. 5.3.1, we write

$$\omega_{a,e}^{\mathrm{GKSL}} = \omega_{e,1} - \omega_{e,0}, \quad \text{where} \quad \boldsymbol{H}_{\mathrm{Rabi}} \left|\overline{e,1}\right\rangle = \omega_{e,1} \left|\overline{e,1}\right\rangle, \quad \boldsymbol{H}_{\mathrm{Rabi}} \left|\overline{e,0}\right\rangle = \omega_{e,0} \left|\overline{e,0}\right\rangle, \tag{5.36}$$

and input it in Eq. 5.9 to estimate $\bar{n}(p)$ for GKSL.

As shown in Fig. 5.2, the long-time dynamics of the dressed qubit observable $\langle \Sigma_z(t) \rangle$, defined in Eq. 5.31, exhibits the beginning of an approximately single exponential decay, and the extracted rates $\Gamma_{eg}(p)$ decrease with drive power (the qubit relaxation rate $T_1 = \Gamma_{eg}^{-1}$ increases). The trend is already visible from early times. The Ohmic MPS and GKSL simulations show good qualitative agreement, confirming that, for this choice of parameters, which we chose according to dispersive readout circuit QED setups, the single-photon loss GKSL of Eq. 5.24 models well the dissipation induced by an environment characterized by an Ohmic spectrum (e.g. a transmission line [29]).

Relaxation rate of the qubit at varying drive power

In this thesis we deliberately retain the minimal model of qubit Rabi-coupled to a cavity in the dispersive readout circuit QED parameter regime, but we introduce structure in the environmental spectral density function $J(\omega)$. This alone suffices to produce qualitatively different trends for $\Gamma_{eg}(p)$ at varying drive amplitude. As noted in [36], qualitatively different trends of $\Gamma_{eg}(p)$ reflect how drive-induced AC-Stark shifts and power broadening sweep the system frequencies through features of the spectral density function $J(\omega)$, motivating a frequency resolved description of dissipation. While [36] demonstrated how $\Gamma_{eg}(p)$ increases with p due to spurious two-level systems becoming resonant with the AC-Stark shifted/power broadened qubit, here we show that engineered spectral features, specifically Purcell notches, produce the same effect.

To test this hypothesis, we compare the spectroscopy results and the $\langle \boldsymbol{\Sigma}_z(t) \rangle$ dynamics for the configurations specified in Sec. 5.2. Convergence tests and a discussion of the details of the numerics can be found in Appendix 7.8. Given the dispersive Hamiltonian of Eq. 5.5, we can estimate the AC-Stark shifted frequency of the qubit as [29]

$$\omega_q^{\mathrm{AC-Stark}}(p) = \omega_q \; + \; 2\chi\, \bar{n}(p), \qquad \chi = -\frac{g^2}{\Delta}. \tag{5.37}$$

with $\bar{n}(p)$ the steady-state cavity population at drive amplitude $\epsilon_d = p\,\bar{\epsilon}_d$ of Eq. 5.9. Thus the sign of the shift is fixed by the detuning: for $\Delta > 0$ we have $\chi < 0$ and $\omega_q(p)$ moves downward with power; for $\Delta < 0$ we have $\chi > 0$ and $\omega_q(p)$ moves upward with power. This is directly visible in the bath spectroscopy of Fig. 5.5, which depicts the bath occupation numbers as a function of frequency $\langle \boldsymbol{n}_\omega \rangle$ at final time $\kappa t/(2\pi) = 0.5$.

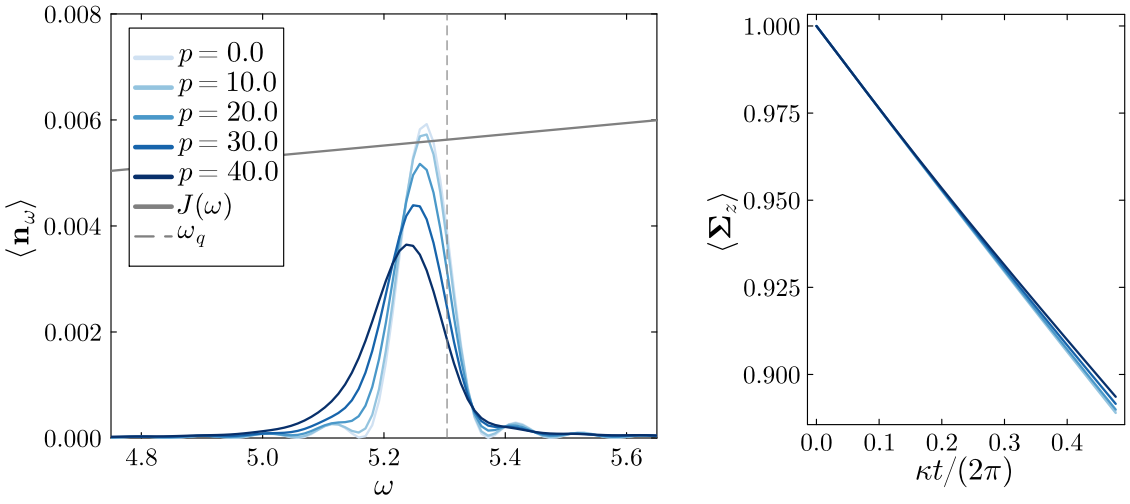

(a) $\Delta > 0$.

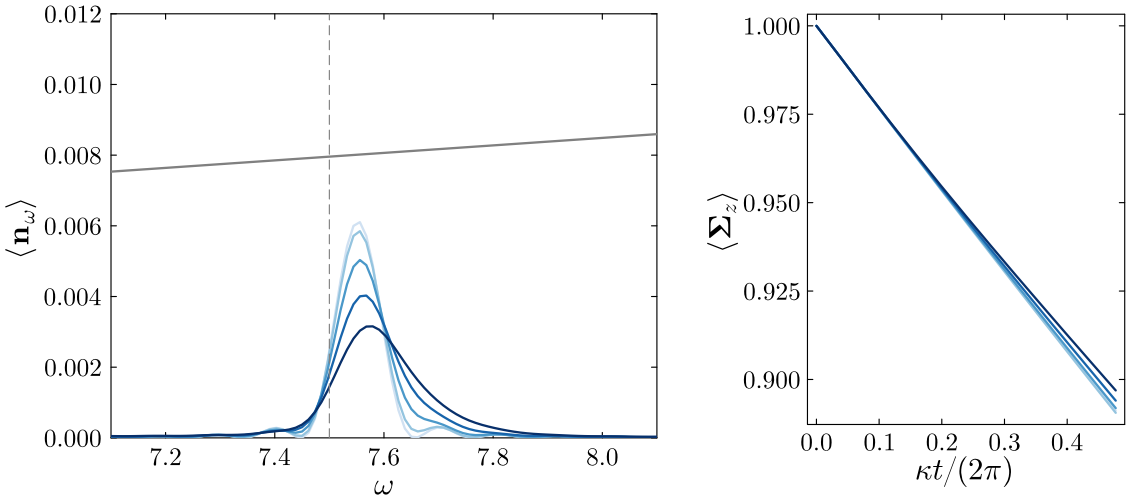

(b) $\Delta < 0$.

Figure 5.5: MPS simulation results for the spectroscopy of the qubit, for the Ohmic case $J(\omega) = J_{\mathrm{Ohm}}(\omega)$. The plots on the left show the bath mode occupations $\langle \boldsymbol{n}_\omega \rangle$ at final time. On the right, the time evolution of $\langle \mathbf{\Sigma}_z \rangle$, for multiple drive powers $\epsilon_d = p\bar{\epsilon}_d$. The legend is common for Fig. **(a)**, where $\Delta > 0$, and **(b)**, $\Delta < 0$.

The qubit-emission peak, initially near the bare ω_q, drifts to lower frequencies as p increases when $\Delta > 0$, and to higher frequencies when $\Delta < 0$, as predicted by Eq. 5.37.

We now relate such a sampling of the environmental spectrum $J(\omega)$ to the relaxation rate of the qubit itself. We therefore analyze the time-dependence of $\langle \mathbf{\Sigma}_z(t) \rangle$, and extract Γ_{eg} by single–exponential fits. For the Ohmic case $J_{\mathrm{Ohm}}(\omega)$ we observe in Fig. 5.5 a *decrease* of the decay rate of the qubit Γ_{eg} with increasing drive power for both detuning signs, $\Delta > 0$ and $\Delta < 0$, in qualitative agreement with the GKSL benchmark. By contrast, in presence of a Purcell notch in the spectral density $J_{\mathrm{PF}}(\omega)$ case, we observe the opposite behavior: Γ_{eg} *increases with drive power*. The decay rates Γ_{eg} of $\langle \mathbf{\Sigma}_z(t) \rangle$

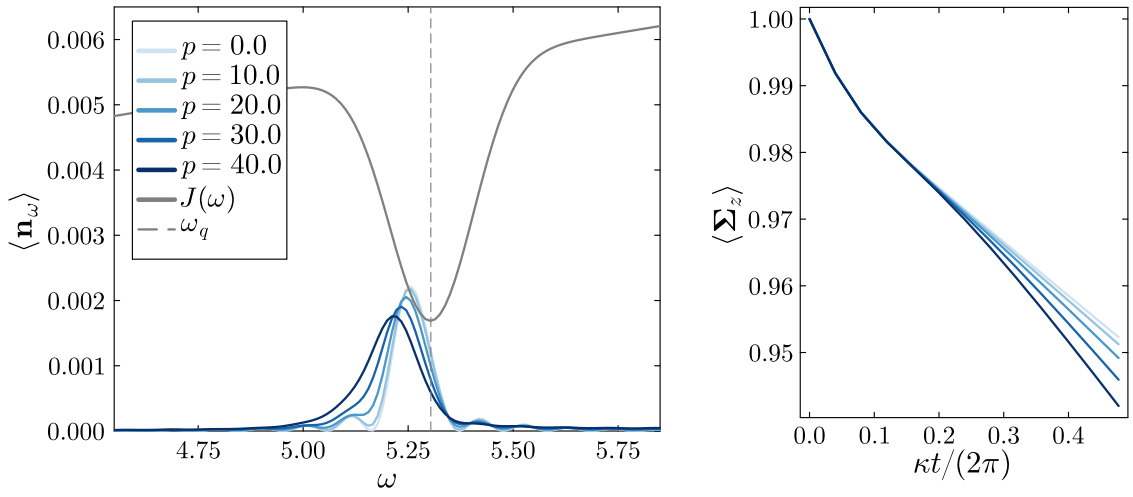

Figure 5.6: MPS simulation results for the spectroscopy of the qubit, for the Purcell filter case $J(\omega) = J_{\mathrm{PF}}(\omega)$. The plots on the left show the bath mode occupations $\langle \boldsymbol{n}_\omega \rangle$ at final time. On the right, the time evolution of $\langle \mathbf{\Sigma}_z \rangle$, for multiple drive powers $\epsilon_d = p\bar{\epsilon}_d$.

are summarized in Fig. 5.7 as a function of $\bar{n}$ (and thus of ϵ_d). This shows what we advertised in the beginning of this chapter: that the behavior of the qubit energy relaxation rate with increasing readout drive power depends sensitively on the details of the bath spectrum.

Such qualitative behavior should be related to the effective environment seen by the qubit. In fact, in a weak-coupling, single-photon loss picture one expects the relaxation rate of the qubit to be proportional to the effective spectral density of the environment filtered by the cavity,

$$\Gamma_{eg}(p) \;\propto\; J^{\mathrm{eff}}\Big(\,\omega_{ge}(p)\,\Big), \tag{5.38}$$

Here $J^{\mathrm{eff}}(\omega)$ denotes the external $J(\omega)$ filtered by the cavity response (a Lorentzian of width κ centered at ω_a as we saw in Sec. 5.1.1). This explains why, in the Ohmic case with $\Delta < 0$, Γ_{eg} still decreases with power even though $J_{\mathrm{Ohm}}(\omega)$ grows with ω: the upward Stark shift moves the transition further away from the cavity center ω_a, and the cavity filter dominates, reducing $J^{\mathrm{eff}}(\omega)$. Similarly, for $\Delta > 0$ the transition shifts downward, both lowering $J_{\mathrm{Ohm}}(\omega)$ and moving off the cavity peak, again decreasing $J^{\mathrm{eff}}(\omega)$. In the Purcell–filter case, however, $J^{\mathrm{eff}}_{\mathrm{PF}}(\omega)$ has a notch centered near ω_q; any Stark shift away from the notch minimum samples the *shoulders* where the effective density is larger, so $J^{\mathrm{eff}}_{\mathrm{PF}}\big(\omega_{ge}(p)\big)$—and hence Γ_{eg}—increases with drive.

$J^{\mathrm{eff}}(\omega)$ can be computed using the chain-mapping. In general, given a set of chain coefficients $\{e_i,\, t_i,\, k_0\}$, by inverting the chain mapping it is always possible to reconstruct the spectral density function of the corresponding environment, as described in Appendix 7.5. Since the cavity is just another harmonic oscillator, we can consider it as part of a chain defined by the following chain coefficients

$$[\omega_a, e_0, e_1, \ldots], \quad [k_0, t_0, t_1, \ldots], \quad g, \tag{5.39}$$

and reconstruct the corresponding spectral density, which we denote as $J^{\mathrm{eff}}_{\mathrm{PF}}(\omega)$. We

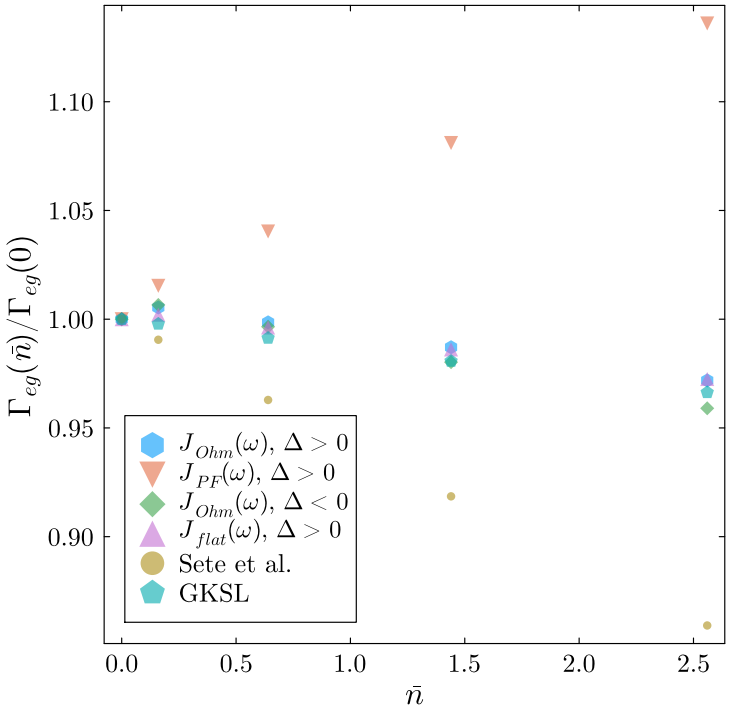

Figure 5.7: T_1 vs. $\bar{n}$, given by Eq. 5.9 with $\omega_d = \omega_a$. We show the relative change in relaxation rate $\Gamma_{eg}(\bar{n})/\Gamma_{eg}(0)$ for all the configurations here, with a comparison to GKSL and to the theoretical prediction of Sete *et al.* in [77, Eq. 33]. Different spectral densities give rise to distinct relaxation dependence of the qubit on drive power, with a change in qualitative behavior at increasing drive power for the Purcell filter case, the only case among the ones here considered where T_1 decreases with $\bar{n}$.

stress that this is not exact, as the coupling between chain modes is assumed to be Jaynes-Cummings like, while in general the cavity-chain coupling is dipolar.

The plot of $J^{\text{eff}}_{\text{PF}}(\omega_q(p))$ in Fig. 5.8 makes the qualitative trends in Fig. 5.7 immediate: for a Purcell notch any Stark drift off the minimum samples the notch shoulders and *increases* Γ_{eg}. The same inversion of the chain mapping can be used to compute the effective environment $J^{\text{eff}}(\omega)$ produced by multiple harmonic modes concatenated in series, and to arbitrary spectral density functions. We note that similar analytical computations can be found in [197, 198, 36]. An effective master equation for the qubit could also be derived microscopically, assuming a bath described by $J^{\text{eff}}(\omega)$. Still, the definition of the dressed observables of Sec. 5.3.1 would be more complicated.

5.5 Concluding remarks

In this Chapter, we studied drive-induced degradation of the relaxation time of a qubit in the dispersive readout of circuit QED. Our analysis relied on the tensor network and chain mapping methods presented in Chap. 4 to numerically simulate the full unitary dynamics generated by a microscopic Hamiltonian describing the transmission line used

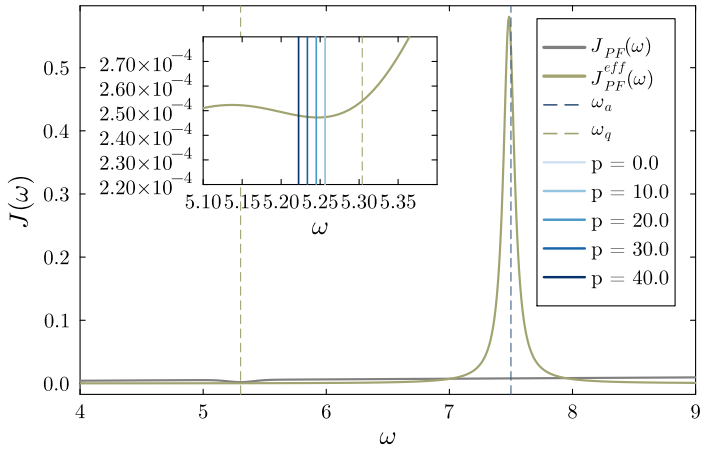

Figure 5.8: Effective spectral density function $J^{\text{eff}}_{\text{PF}}(\omega)$ for the qubit. The environmental spectral density is given by Eq. 5.22, and the Lorentzian centered close to the cavity frequency ω_a is due to the effective environment produced by the cavity. The inset shows $J^{\text{eff}}_{\text{PF}}(\omega)$ around the bare frequency of the qubit ω_q: a small dip due to the notch filter is visible.

for reading out the state of a qubit in superconducting circuits. We considered multiple profiles for the spectral density defining the system-bath coupling.

For the Ohmic $J_{\text{Ohm}}(\omega)$ and flat $J_{\text{flat}}(\omega)$ spectral densities, we obtained converged results qualitatively agreeing with the single-photon loss dissipator GKSL model of Eq. 5.24: the relaxation rate of the qubit decreases with drive power, in agreement with previous analytical results [77]. When a Purcell notch is introduced, $J_{\text{PF}}(\omega)$, the relaxation rate dependence on the drive power reverses: the AC-Stark–shifted qubit samples steep spectral features and its relaxation rate increases with drive power. Our environmental spectroscopy results confirm this picture, showing a drive-dependent emission spectrum of the system in the environment. Analyzing the emission spectrum of the driven system in particular might provide design and mitigation strategies for realistic setups. We postpone a more detailed discussion of future research directions to Chap. 6.

Chapter 6

Conclusion and prospects

In this thesis we developed complementary analytical and numerical tools to efficiently model the time evolution of bipartite open quantum systems, motivated by and applied to quantum-hardware settings.

Analytically, we extended the geometric approach to adiabatic elimination to Liouvillians that may exhibit fast unitary dynamics, deriving compact reduced generators and reconstruction maps from the Sylvester equation integral solution (Chap. 2). From a formal viewpoint, this provides a unified treatment of spectral block-decomposition for generators with a real-axis spectral gap, assuming only a time-scale separation in the real parts of the spectrum (fast-decaying versus long-lived modes) while allowing for modes associated to eigenvalues with large imaginary parts. This corresponds to the linear version of a center manifold with non-trivial motion in general systems theory. From a practical viewpoint, we have illustrated how our results eliminate the need of the preliminary transformation to the interaction picture and the use of averaging approximations prior to model reduction. In Chap. 3 we established the time-convolutionless master equation approach to adiabatic elimination, and demonstrated its equivalence with the geometric approach considered in Chap. 2. We demonstrated how the time-convolutionless approach enables treatment of cases where rapid unitary dynamics persist on the target system. We also showed that within this formalism it is possible to retain the explicit time dependence of the reduced model, thus capturing the initial transient dynamics that the geometric approach to adiabatic elimination neglects.

On the numerical side, we contributed to the open source Julia package MPSDynamics.jl, the chain mapping and tensor network toolkit presented in Chap. 4 and used throughout Chap. 5, enabling simulations of driven systems coupled to structured environments. We focused on the dispersive readout setting in circuit QED: a two-level system dipolarly coupled to a driven, lossy cavity. In Chap. 5, we analyzed the dependence of the relaxation time of the qubit on the drive strength. As discussed in Sec. 5.1, experiments report a decrease of the relaxation time of the qubit T_1 with increasing drive amplitude, in contradiction with predictions from standard GKSL master-equation models. With a Purcell notch filter at the qubit frequency, our simulations predict T_1 decreases with drive power, consistent with the experimental trend, indicating that filtering can mediate the observed T_1 degradation. These results indicate that precise modeling of filters is required for quantitative descriptions of driven-dissipative circuit

QED dynamics.

We conclude with perspectives for future work.

Adiabatic elimination of the fast decaying degrees of freedom

Future work building on Chap. 2 should allow us to determine if alternative gauge choices restore complete positivity of the reduced dynamics in Example 2, as it was the case in [61], in our generalized setting too. It should also be possible to generalize Proposition 1 beyond the bipartite system case, to settings where $\mathcal{L} = \mathcal{L}_0 + \epsilon\mathcal{L}_1$, with the spectrum of $\mathcal{L}_0$ containing eigenvalues with large imaginary part. We also note that the GKSL form is not required for Proposition 1 to hold. Finally, as already mentioned, the Heisenberg evolution trick of Proposition 2 may be applied iteratively to simplify the computation of higher orders without explicitly computing the map $\mathcal{K}$. The treatment of this case is work in progress.

Additionally, the formulas here derived, although valid for a more general class of problems, could be directly applicable to any linear quantum system [133]. In this case, the Heisenberg equations for the operators $\boldsymbol{B}_l(t)$ are closed, so that the kernel in Proposition 2 can be explicitly written in terms of all the system parameters (frequencies, dissipation rates and couplings), providing insights on how the system's various tunings can be integrated into quantum dissipation engineering.

We would also use this tool to further explore corrections to averaging approximations, also called rotating-wave approximation (RWA), and ubiquitous in quantum engineering, where the frequencies are set to be on/off-resonant in order to enhance/suppress terms contributing to the dynamics. Indeed, while averaging expansions can in principle be carried out at higher order, they are a priori not converging, unlike the block-spectral decomposition here considered.

The formulation presented in Chap. 3 opens the possibility of applying techniques already developed for the time-convolutionless master equation to adiabatic elimination problems. For instance, diagrammatic techniques that simplify the evaluation of higher-order contributions, such as those developed for computing the generator of the dynamics [199] and for steady states [200, 201], might now be employed. It would also be interesting to exploit the explicit formulas of higher orders corrections to develop numerical schemes for reduced model computation, as done in [128] for the geometric approach.

An immediate application of the TCL formalism could be to obtain reduced models of many-body systems, which thus have a multipartite structure, a setting naturally handled in this framework. One such example could be to compute the reduced polarization dynamics for spin systems in nuclear magnetic resonance, as done in [122] by Karabanov *et al.*.

Finally, it would be interesting to check if it is possible to exploit the Heisenberg formulation employed in Chapter 2 to compute the reduced evolution also in the time-convolutionless formulation. This would allow to easily obtain symbolic expressions, as in Proposition 2 of Chap. 2.

Unitary dynamics compression applied to the readout problem in circuit QED

A first objective of future work on the numerical methods presented in Chap. 4 would be to update the Julia package MPSDynamics.jl to allow for multithreading, which is currently not supported. This would allow to add GPU backends enabling parallel computing. A second objective is to include in the package the implementation of the Markovian closure introduced in [202, 203] for bosonic environments, and in [204] for fermionic ones, which proved the equivalence between the multi-time expectation values of an open quantum system interacting with either a unitarily evolving environment or a discrete set of damped modes obeying a GKSL master equation.

If the timescale separation conditions which allow for adiabatic elimination are respected, the Markovian closure of [202, 203] might also allow for model reduction of the GKSL dynamics through adiabatic elimination. Such possibility could be investigated in future work, which would connect the two approaches to model reduction of open quantum systems pursued in this thesis.

The results presented in Chap. 5 motivate a microscopic treatment of frequency-dependent system-environment coupling in circuit QED settings. Such structure can be introduced by filters. Our setup can model multipole filters [191], metamaterials [178, 189, 190] and spurious harmonic modes in the electromagnetic environment [22]. Future work should thus consider realistic spectral density functions, to compare quantitatively experimental [35] and numerical results of the relaxation time of the qubit T_1 dependence on the population in the cavity $\bar{n}$, in the presence of a notch filter at the frequency of the qubit. This could lead to engineering alternative designs for filters, mitigating the drive-induced T_1 relaxation. Future work might also extend our model to incorporate $1/f$ noise [205, 206, 207], possibly using tree tensor networks to include multiple environments with different couplings to the open quantum system, inducing relaxation and dephasing [208, 209], and repeat the analysis here presented to assess the impact of low frequency noise on the drive dependence of T_1.

Another important question is how the relaxation time dependence on drive power would change for a superconducting qubit modeled as an anharmonic oscillator, and thus as a multi-level system, instead of as a two-level system. Our setup could be extended to treat such a case, and provide non-perturbative benchmarks for the results presented in [78] for a transmon and in [104] for a cat qubit, obtained by deriving effective master equations from a microscopic model, and predicting a degradation of the relaxation time T_1 at increasing drive power, even in the absence of a frequency dependent spectral density function.

We expect that finite temperature effects should be included when applying the methods of Chap. 4 to low frequency superconducting qubits, such as fluxonium [63], whose transition frequencies can be only a few megahertz, leading to non-negligible thermal occupation. In addition, a system constituted of a voltage-biased Josephson junction directly coupled to a high-impedance transmission line has been shown [210] to exhibit drive-induced overheating of the photonic modes, with qualitative impact on the observables of the junction, motivating a non-perturbative study within the framework of Chap. 4 as future work. Since these methods allow for treatment of general driven-dissipative systems, they could be applied to model multi-mode quantum hardware setups not limited to circuit QED.

Chapter 7

Appendix

Contents

7.1 [Chap. 3] Perturbative solution to the invariance condition

In this appendix, we present a way to obtain a perturbative solution to the invariance condition Eq. 3.7. For this purpose, we expand the maps $\mathcal{K}^{(\epsilon)}$ and $\mathcal{F}^{(\epsilon)}$ with respect to ϵ as $\mathcal{K}^{(\epsilon)} = \sum_{n=0}^{\infty} \epsilon^n \mathcal{K}_n$ and $\mathcal{F}^{(\epsilon)} = \sum_{n=0}^{\infty} \epsilon^n \mathcal{F}_n$, respectively, where $\mathcal{K}_n$ and $\mathcal{F}_n$ are independent of ϵ. Inserting these into the invariance condition Eq. 3.7, the zeroth-order of ϵ reads

$$\mathcal{K}_0 \mathcal{F}_0 = \mathcal{L}_0 \mathcal{K}_0.$$

Note that $\mathcal{K}_0 = \mathcal{K}^{(\epsilon=0)}$. From Eq. 3.6, we find $\mathcal{K}_0 = \chi_R$ with χ_R defined in Eq. 3.22. Using $\chi_L^\dagger \chi_R = 1$, the above equation yields $\mathcal{F}^{(\epsilon=0)} = \mathcal{F}_0 = \chi_L^\dagger \mathcal{L}_0 \chi_R$.

For $n \geq 1$, the invariance condition at the order of ϵ^n is given by

$$\mathcal{K}_0 \mathcal{F}_n + \mathcal{K}_n \mathcal{F}_0 + \sum_{m=1}^{n-1} \mathcal{K}_m \mathcal{F}_{n-m} = \mathcal{L}_0 \mathcal{K}_n + \mathcal{L}_1 \mathcal{K}_{n-1}. \tag{7.1}$$

This can be solved for $\mathcal{K}_n$ and $\mathcal{F}_n$ straightforwardly when $\mathcal{F}_0 = 0$ or, equivalently, when $\lambda_s = 0$ for any surviving modes s [118]. In this case, Eq. 7.1 reads

$$\mathcal{K}_0 \mathcal{F}_n + \sum_{m=1}^{n-1} \mathcal{K}_m \mathcal{F}_{n-m} = \mathcal{L}_0 \mathcal{K}_n + \mathcal{L}_1 \mathcal{K}_{n-1}. \tag{7.2}$$

Applying $\chi_L^\dagger$ from the left yields

$$\mathcal{F}_n = \chi_L^\dagger \Big[\mathcal{L}_1 \mathcal{K}_{n-1} - \sum_{m=1}^{n-1} \mathcal{K}_m \mathcal{F}_{n-m} \Big],$$

where we have used $\chi_L^\dagger \mathcal{L}_0 = 0$, which is true when $\lambda_s = 0$. Eq. 7.2 can be rearranged as

$$\mathcal{L}_0 \mathcal{K}_n = \mathcal{K}_0 \mathcal{F}_n + \sum_{m=1}^{n-1} \mathcal{K}_m \mathcal{F}_{n-m} - \mathcal{L}_1 \mathcal{K}_{n-1}.$$

By inverting $\mathcal{L}_0$, thus, we obtain $\mathcal{K}_n$. Since $\mathcal{L}_0$ is singular, the solution to this linear equation is not unique. This leads to the gauge degree of freedom discussed in Sec. 3.2 (see Ref. [83] for details).

When $\lambda_s \neq 0$, Eq. 7.2 similarly yields

$$\mathcal{F}_n = \chi_L^\dagger \Big[\mathcal{L}_0 \mathcal{K}_n + \mathcal{L}_1 \mathcal{K}_{n-1} - \sum_{m=1}^{n-1} \mathcal{K}_m \mathcal{F}_{n-m} \Big], \tag{7.3}$$

which depends on $\mathcal{K}_n$ that has not yet been determined. To find $\mathcal{K}_n$ and $\mathcal{F}_n$ in this case, the authors of Ref. [60] guessed the form of $\mathcal{K}_n$ with an unknown quantity. By determining the unknown quantity so that the resulting $\mathcal{K}_n$ is consistent with Eq. 7.1, they successfully obtained $\mathcal{K}_n$ and $\mathcal{F}_n$. However, they calculated only up to the second order of ϵ and the analysis was limited to bipartite systems. A systematic method for solving Eq. 7.1 with $\lambda_s \neq 0$ was developed in Chap. 2 in the case of bipartite systems.

7.2 [Chap. 3] Perturbation expansion of $\mathcal{P}_{\rm inv}^{(\epsilon)}(t)$

In this appendix, we provide several formulas that are useful in a perturbation calculation of $\mathcal{P}_{\rm inv}^{(\epsilon)}(t)$. By considering $\mathcal{P}_{\rm inv}^{(\epsilon)} = \lim_{t\to\infty} \mathcal{P}_{\rm inv}^{(\epsilon)}(t)$, one can evaluate $\mathcal{K}_{\rm TCL}^{(\epsilon)}$ and $\mathcal{F}_{\rm TCL}^{(\epsilon)}$ defined in Eqs. (3.29). With finite t, the dynamics including the transient regime can be discussed (see Appendix 7.3.2).

In what follows, we use the expression (3.20), that is, $\mathcal{P}_{\rm inv}^{(\epsilon)}(t) = [\mathcal{I} - \Sigma_{\rm inv}^{(\epsilon)}(t)]^{-1} \mathcal{P}_{\rm inv}$ with

$$\Sigma_{\rm inv}^{(\epsilon)}(t) = \epsilon \int_0^t d\tau \, e^{\mathcal{Q}_{\rm inv}\mathcal{L}\mathcal{Q}_{\rm inv}\tau} \mathcal{Q}_{\rm inv} \mathcal{L}_1 \mathcal{P}_{\rm inv} e^{-\mathcal{L}\tau}.$$

To expand $\Sigma^{(\epsilon)}_{\rm inv}(t)$ with respect to ϵ, we note the following identities;

$$e^{(\mathcal{A}+\epsilon\mathcal{B})(t-s)}$$
$$= e^{\mathcal{A}t}\,\mathrm{T}_{\leftarrow}\Big\{\exp\Big[\epsilon\int_s^t d\tau\,\tilde{\mathcal{B}}(\tau)\Big]\Big\}\,e^{-\mathcal{A}s},$$

and

$$e^{(\mathcal{A}+\epsilon\mathcal{B})(s-t)}$$
$$= e^{\mathcal{A}s}\,\mathrm{T}_{\rightarrow}\Big\{\exp\Big[-\epsilon\int_s^t d\tau\,\tilde{\mathcal{B}}(\tau)\Big]\Big\}\,e^{-\mathcal{A}t},$$

with $\mathrm{T}_{\leftarrow}$ and $\mathrm{T}_{\rightarrow}$ denoting the chronological and the antichronological time-orderings, respectively, and $\tilde{\mathcal{B}}(\tau) = \exp(-\mathcal{A}\tau)\,\mathcal{B}\,\exp(\mathcal{A}\tau)$. These identities can be verified by considering the differential equations with respect to t and s. Using these, the above expression of $\Sigma^{(\epsilon)}_{\rm inv}(t)$ can be recast into the following form,

$$\Sigma^{(\epsilon)}_{\rm inv}(t) = \epsilon\int_0^t d\tau\,\mathcal{G}(\tau)\mathcal{Q}_{\rm inv}\mathcal{L}_1\mathcal{P}_{\rm inv}G(\tau), \tag{7.4}$$

where we have introduced $(t \geq s)$,

$$\mathcal{G}(t-s=\tau_0) = e^{\mathcal{Q}_{\rm inv}\mathcal{L}\mathcal{Q}_{\rm inv}\tau_0}$$
$$= e^{\mathcal{L}_0\tau_0}\mathcal{Q}_{\rm inv} + \sum_{n=1}^{\infty}\epsilon^n\int_0^{\tau_0}d\tau_1\cdots\int_0^{\tau_{n-1}}d\tau_n$$
$$e^{\mathcal{L}_0(\tau_0-\tau_1)}\mathcal{Q}_{\rm inv}\mathcal{L}_1\ldots e^{\mathcal{L}_0(\tau_{n-1}-\tau_n)}\mathcal{Q}_{\rm inv}\mathcal{L}_1 e^{\mathcal{L}_0\tau_n}\mathcal{Q}_{\rm inv},$$

and

$$G(t-s=\tau_0) = e^{-\mathcal{L}\tau_0}$$
$$= e^{\mathcal{L}_0 s}\,\mathrm{T}_{\rightarrow}\Big\{\exp\Big[-\epsilon\int_s^t d\tau\,\tilde{\mathcal{L}}_1(\tau)\Big]\Big\}\,e^{-\mathcal{L}_0 t}$$
$$e^{-\mathcal{L}_0\tau_n}\mathcal{L}_1 e^{-\mathcal{L}_0(\tau_{n-1}-\tau_n)}\ldots\mathcal{L}_1 e^{-\mathcal{L}_0(\tau_0-\tau_1)}.$$

Let us expand $\Sigma^{(\epsilon)}_{\rm inv}(t)$ as $\Sigma^{(\epsilon)}_{\rm inv}(t) = \sum_{n=1}^{\infty}\epsilon^n\Sigma_n(t)$. Inserting $\mathcal{G}(\tau)$ and $G(\tau)$ into Eq. (7.4), we obtain, up to the order of ϵ^3,

$$\Sigma_1(t) = \int_0^t d\tau e^{\mathcal{L}_0\tau}\mathcal{Q}_{\rm inv}\mathcal{L}_1\mathcal{P}_{\rm inv}e^{-\mathcal{L}_0\tau},$$

$$\Sigma_2(t) = \int_0^t d\tau_1\int_0^{\tau_1}d\tau_2$$
$$\Big\{e^{\mathcal{L}_0(\tau_1-\tau_2)}\mathcal{Q}_{\rm inv}\mathcal{L}_1 e^{\mathcal{L}_0\tau_2}\mathcal{Q}_{\rm inv}\mathcal{L}_1\mathcal{P}_{\rm inv}e^{-\mathcal{L}_0\tau_1} \tag{7.5}$$
$$-e^{\mathcal{L}_0\tau_1}\mathcal{Q}_{\rm inv}\mathcal{L}_1\mathcal{P}_{\rm inv}e^{-\mathcal{L}_0\tau_2}\mathcal{L}_1 e^{-\mathcal{L}_0(\tau_1-\tau_2)}\Big\},$$

and

$$\Sigma_3(t) = \int_0^t d\tau_1 \int_0^{\tau_1} d\tau_2 \int_0^{\tau_2} d\tau_3 \Big\{ e^{\mathcal{L}_0(\tau_1-\tau_2)} \mathcal{Q}_{\rm inv}\mathcal{L}_1 e^{\mathcal{L}_0(\tau_2-\tau_3)} \mathcal{Q}_{\rm inv}\mathcal{L}_1 e^{\mathcal{L}_0\tau_3} \times \mathcal{Q}_{\rm inv}\mathcal{L}_1\mathcal{P}_{\rm inv} e^{-\mathcal{L}_0\tau_1} + e^{\mathcal{L}_0\tau_1}\mathcal{Q}_{\rm inv}\mathcal{L}_1\mathcal{P}_{\rm inv} e^{-\mathcal{L}_0\tau_3} \times \mathcal{L}_1 e^{-\mathcal{L}_0(\tau_2-\tau_3)}\mathcal{L}_1 e^{-\mathcal{L}_0(\tau_1-\tau_2)} \Big\} - \int_0^t d\tau_1 \int_0^{\tau_1} d\tau_2 \int_0^{\tau_1} d\tau_3\, e^{\mathcal{L}_0(\tau_1-\tau_2)} \mathcal{Q}_{\rm inv}\mathcal{L}_1 e^{\mathcal{L}_0\tau_2} \times \mathcal{Q}_{\rm inv}\mathcal{L}_1\mathcal{P}_{\rm inv} e^{-\mathcal{L}_0\tau_3}\mathcal{L}_1 e^{-\mathcal{L}_0(\tau_1-\tau_3)}.$$

Up to the order of ϵ^3, $[\mathcal{I} - \Sigma^{(\epsilon)}_{\rm inv}(t)]^{-1}$ can be expanded as

$$[\mathcal{I} - \Sigma^{(\epsilon)}_{\rm inv}(t)]^{-1} = \mathcal{I} + \epsilon\Sigma_1(t) + \epsilon^2\Sigma_2(t) + \epsilon^3\Big[\Sigma_3(t) + \Sigma_2(t)\Sigma_1(t)\Big] + O(\epsilon^4).$$

From this, we can evaluate $\mathcal{P}^{(\epsilon)}_{\rm inv}(t)$ perturbatively. Expanding as $\mathcal{P}^{(\epsilon)}_{\rm inv}(t) = \mathcal{P}_{\rm inv} + \sum_{n=1}^{\infty}\epsilon^n\mathcal{P}_n(t)$, we find

$$\begin{aligned} \mathcal{P}_1(t) &= \Sigma_1(t)\mathcal{P}_{\rm inv}, \\ \mathcal{P}_2(t) &= \Sigma_2(t)\mathcal{P}_{\rm inv}, \\ \mathcal{P}_3(t) &= \Big[\Sigma_3(t) + \Sigma_2(t)\Sigma_1(t)\Big]\mathcal{P}_{\rm inv}, \\ &\vdots \end{aligned} \tag{7.6}$$

When the limit $t \to \infty$ is taken, a simpler expression of $\mathcal{P}^{(\epsilon)}_{\rm inv}$ can be found as follows. Note first that $\mathcal{P}_1(t)$ reads

$$\mathcal{P}_1(t) = \int_0^t d\tau\, e^{\mathcal{L}_0\tau}\mathcal{Q}_{\rm inv}\mathcal{L}_1 e^{-\mathcal{L}_0\tau}\mathcal{P}_{\rm inv}. \tag{7.7}$$

Let $\mathcal{P}_n = \lim_{t\to\infty}\mathcal{P}_n(t)$. For $\{\mathcal{P}_n\}$, we can find relatively compact expressions by using the fact that

$$\hat{\mathcal{P}}_{\rm inv} = \sum_s |r_s\rangle\!\rangle\langle\!\langle l_s| \equiv \sum_s \hat{\Pi}_s \quad \text{and} \quad \hat{\mathcal{Q}}_{\rm inv} = \sum_f |r_f\rangle\!\rangle\langle\!\langle l_f| \equiv \sum_f \hat{\Pi}_f \tag{7.8}$$

are projections onto the eigenspaces of $\mathcal{L}_0$. For instance, $\mathcal{P}_1$ reads from Eq. (7.7) as

$$\begin{aligned} \mathcal{P}_1 &= \int_0^\infty d\tau\, e^{\mathcal{L}_0\tau}\mathcal{Q}_{\rm inv}\mathcal{L}_1\mathcal{P}_{\rm inv}e^{-\mathcal{L}_0\tau}\mathcal{P}_{\rm inv} \\ &= \sum_{sf}\left(\int_0^\infty d\tau e^{(\lambda_f-\lambda_s)\tau}\right)\Pi_f\mathcal{L}_1\Pi_s \\ &= \sum_{sf}\frac{1}{\Delta_{sf}}\Pi_f\mathcal{L}_1\Pi_s, \end{aligned}$$

where we have introduced $\Delta_{sf} = \lambda_s - \lambda_f$, which has the positive real part as $\mathrm{Re}\Delta_{sf} \geq \Delta > 0$. Similar calculations yield higher-order contributions as

$$\mathcal{P}_{\mathrm{inv}}^{(\epsilon)} = \mathcal{P}_{\mathrm{inv}} + \sum_{sf} \frac{1}{\Delta_{sf}} \Pi_f \left[\epsilon \mathcal{L}_1 + \sum_{n=2}^{\infty} \epsilon^n \Gamma_{n,fs} \right] \Pi_s, \tag{7.9}$$

with

$$\Gamma_{2,fs} = \mathcal{L}_1 \frac{\mathcal{Q}_{\mathrm{inv}}}{\lambda_s - \mathcal{L}_0} \mathcal{L}_1 - \mathcal{L}_1 \frac{\mathcal{P}_{\mathrm{inv}}}{\mathcal{L}_0 - \lambda_f} \mathcal{L}_1, \tag{7.10}$$

and

$$\begin{aligned} \Gamma_{3,fs} = & \mathcal{L}_1 \frac{\mathcal{Q}_{\mathrm{inv}}}{\lambda_s - \mathcal{L}_0} \mathcal{L}_1 \frac{\mathcal{Q}_{\mathrm{inv}}}{\lambda_s - \mathcal{L}_0} \mathcal{L}_1 \\ & + \mathcal{L}_1 \frac{\mathcal{P}_{\mathrm{inv}}}{\mathcal{L}_0 - \lambda_f} \mathcal{L}_1 \frac{\mathcal{P}_{\mathrm{inv}}}{\mathcal{L}_0 - \lambda_f} \mathcal{L}_1 \\ & - \mathcal{L}_1 \frac{\mathcal{Q}_{\mathrm{inv}}}{\lambda_s - \mathcal{L}_0} \mathcal{L}_1 \frac{\mathcal{P}_{\mathrm{inv}}}{\mathcal{L}_0 - \lambda_f} \mathcal{L}_1 \\ & - \mathcal{L}_1 \frac{\mathcal{P}_{\mathrm{inv}}}{\mathcal{L}_0 - \lambda_f} \mathcal{L}_1 \frac{\mathcal{Q}_{\mathrm{inv}}}{\lambda_s - \mathcal{L}_0} \mathcal{L}_1 \\ & - \sum_{s'f'} \frac{\Delta_{sf}}{\Delta_{s'f'}} \mathcal{L}_1 \frac{\Pi_{f'}}{\Delta_{sf'}} \mathcal{L}_1 \frac{\Pi_{s'}}{\Delta_{s'f}} \mathcal{L}_1. \end{aligned} \tag{7.11}$$

7.3 [Chap. 3] Adiabatic elimination for the Rabi model including a lossy photon mode

In this appendix, we present details of the second-order adiabatic elimination calculation for the Rabi model considered in Sec. 3.4. The computation is similar to the one presented in Example 2 of Chap. 2, so we put it in appendix. The generator reads $\mathcal{L} = \mathcal{L}_0 + \epsilon \mathcal{L}_1$ with $\mathcal{L}_0 = \mathcal{L}_A \otimes \mathcal{I}_B + \mathcal{I}_A \otimes \mathcal{L}_B$ and $\epsilon \mathcal{L}_1 = \mathcal{L}_{\mathrm{int}}$. The generators $\mathcal{L}_A$, $\mathcal{L}_B$, and $\mathcal{L}_{\mathrm{int}}$ are respectively defined in Eqs. 3.38, 3.39, and 3.40. In this case, the eigenvalue problem of $\mathcal{L}_A$ can be solved analytically as (see Appendix C of Ref. [83])

$$(\hat{\mathcal{L}}_A - \lambda_{A,mn} \hat{\mathcal{I}}) \, |r_{A,mn}\rangle\!\rangle = 0, \quad \langle\!\langle l_{A,mn}| \, (\hat{\mathcal{L}}_A - \lambda_{A,mn} \hat{\mathcal{I}}) = 0,$$

for $m, n \in \mathbb{Z}_{\geq 0}$, where the eigenvalues are given by $\lambda_{A,mn} = -(\bar{\kappa} m + \bar{\kappa}^* n)/2$, with $\bar{\kappa} = \kappa + 2i\omega_{\mathrm{ph}}$, and the right and left eigenvectors are given by $|r_{A,mn}\rangle\!\rangle = \exp\left(-\hat{\mathcal{A}}\right) ||m\rangle\langle n|\rangle\!\rangle$, $\langle\!\langle l_{A,mn}| = \langle\!\langle |m\rangle\langle n|| \exp\left(\hat{\mathcal{A}}\right)$, respectively, with $\{|n\rangle\}_{n \in \mathbb{Z}_{\geq 0}}$ the Fock states of the photon mode and $\mathcal{A}\boldsymbol{\rho} = \boldsymbol{a}\boldsymbol{\rho}\boldsymbol{a}^\dagger$. The mode $m = n = 0$ is the only mode with the eigenvalue of 0. Hence, the steady state $\bar{\boldsymbol{\rho}}_A$ is unique and is given by

$$\bar{\boldsymbol{\rho}}_A = \boldsymbol{r}_{A,00} = |0\rangle\langle 0| \, .$$

As we mentioned in Chap. 2, solving the eigenvalue problem for $\mathcal{L}_0$ is usually the bottleneck of the computation.

As shown in Eq. 3.35, the projection $\mathcal{P}_{\rm inv}$ in the current example reads

$$\hat{\mathcal{P}}_{\rm inv} = |\bar{\rho}_A\rangle\!\rangle\langle\!\langle I_A| \otimes \hat{\mathcal{I}}_B = ||0\rangle\langle 0|\rangle\!\rangle\langle\!\langle I_A| \otimes \hat{\mathcal{I}}_B.$$

From this, we can show

$$\mathcal{P}_{\rm inv}\mathcal{L}_1\mathcal{P}_{\rm inv} = 0, \tag{7.12}$$

as $\mathcal{L}_1$ is in the odd power of a and $a^\dagger$. In addition, we find the expression of $\mathcal{Q}_{\rm inv} = \mathcal{I} - \mathcal{P}_{\rm inv}$ as

$$\hat{\mathcal{Q}}_{\rm inv} = \sum_{\substack{m,n=0 \\ m+n>0}}^{\infty} |r_{A,mn}\rangle\!\rangle\langle\!\langle l_{A,mn}| \otimes \hat{\mathcal{I}}_B.$$

Since $|r_{A,mn}\rangle\!\rangle$ are the right eigenvectors of $\mathcal{L}_A$, this yields, for an arbitrary qubit operator $\boldsymbol{X}$,

$$\begin{aligned} &e^{\mathcal{L}_0 t}\mathcal{Q}_{\rm inv}(|m\rangle\langle n| \otimes \boldsymbol{X} + (H.c.)) \\ &= \sum_{\substack{k,q=0 \\ k+q>0}}^{\infty} e^{-(\bar{\kappa}k+\bar{\kappa}^* q)t/2}\, \langle k|e^{\mathcal{A}}(|m\rangle\langle n|)|q\rangle\, e^{-\mathcal{A}}(|k\rangle\langle q|) \otimes e^{\mathcal{L}_B t}(\boldsymbol{X}) + (H.c.), \end{aligned} \tag{7.13}$$

where $H.c.$ denotes the Hermitian conjugate of the preceding terms. We remark that expressing the propagator $e^{\mathcal{L}_0}$ is usually hard, and avoiding such computation motivated the Heisenberg formulation presented in Chap. 2.

Our goal is to evaluate $\mathcal{P}^{(\epsilon)}_{\rm inv}(t)$ up to the second-order of ϵ. The perturbation expansion of $\mathcal{P}^{(\epsilon)}_{\rm inv}(t)$, $\mathcal{P}^{(\epsilon)}_{\rm inv}(t) = \mathcal{P}_{\rm inv} + \sum_{n=1}^{\infty}\epsilon^n\mathcal{P}_n(t)$, is performed in Appendix 7.2. The second-order contribution, $\mathcal{P}_2(t)$, is given by Eq. 7.6 with $\Sigma_2(t)$ defined in Eq. 7.5. Using Eq. 7.12, it reads

$$\epsilon^2\mathcal{P}_2(t)\rho = \epsilon^2 \int_0^t d\tau_1 \int_0^{\tau_1} d\tau_2\, e^{\mathcal{L}_0(\tau_1-\tau_2)}\mathcal{Q}_{\rm inv}\mathcal{L}_1 e^{\mathcal{L}_0\tau_2}\mathcal{Q}_{\rm inv}\mathcal{L}_1\mathcal{P}_{\rm inv}e^{-\mathcal{L}_0\tau_1}\boldsymbol{\rho}. \tag{7.14}$$

The expression of the integrand can be simplified using Eq. 7.13. For later use, we calculate it sequentially as

$$\epsilon e^{\mathcal{L}_0\tau_2}\mathcal{Q}_{\rm inv}\mathcal{L}_1\mathcal{P}_{\rm inv}e^{-\mathcal{L}_0\tau_1}\rho = -ige^{-\bar{\kappa}\tau_2/2}\,|1\rangle\langle 0| \otimes e^{\mathcal{L}_B\tau_2}(\sigma_x e^{-\mathcal{L}_B\tau_1}(\boldsymbol{\rho}_B)) + (H.c.), \tag{7.15}$$

and

$$\begin{aligned} &\epsilon^2 e^{\mathcal{L}_0(\tau_1-\tau_2)}\mathcal{Q}_{\rm inv}\mathcal{L}_1 e^{\mathcal{L}_0\tau_2}\mathcal{Q}_{\rm inv}\mathcal{L}_1\mathcal{P}_{\rm inv}e^{-\mathcal{L}_0\tau_1}\rho \\ &= g^2 e^{-\bar{\kappa}\tau_2/2}\Big\{e^{-(\bar{\kappa}+\bar{\kappa}^*)(\tau_1-\tau_2)/2}(|1\rangle\langle 1| - |0\rangle\langle 0|) \otimes e^{\mathcal{L}_B(\tau_1-\tau_2)}(e^{\mathcal{L}_B\tau_2}(\boldsymbol{\sigma}_x e^{-\mathcal{L}_B\tau_1}(\boldsymbol{\rho}_B))\sigma_x) \\ &\quad + \sqrt{2}e^{-\bar{\kappa}(\tau_1-\tau_2)}\,|2\rangle\langle 0| \otimes e^{\mathcal{L}_B(\tau_1-\tau_2)}(\boldsymbol{\sigma}_x e^{\mathcal{L}_B\tau_2}(\sigma_x e^{-\mathcal{L}_B\tau_1}(\boldsymbol{\rho}_B)))\Big\} + (H.c.). \end{aligned} \tag{7.16}$$

It follows from $\mathcal{L}_B\rho = -i(\omega_{\rm eg}/2)[\boldsymbol{\sigma}_z, \boldsymbol{\rho}]$ that the operation of $\exp(\mathcal{L}_B t)$ is given by

$$e^{\mathcal{L}_B t}(\boldsymbol{\rho}) = \boldsymbol{U}_B(t)\boldsymbol{\rho}\boldsymbol{U}_B^\dagger(t),$$

with $\boldsymbol{U}_B(t) = \exp(-i(\omega_{\rm eg}t/2)\boldsymbol{\sigma}_z)$ being the unitary operator $\boldsymbol{U}_B^\dagger(t) = \boldsymbol{U}_B(-t) = \boldsymbol{U}_B(t)^{-1}$. By unitary transformation, σ_x is transformed as

$$\boldsymbol{U}_B(t)\boldsymbol{\sigma}_x\boldsymbol{U}_B^\dagger(t) = \boldsymbol{\sigma}_- e^{i\omega_{\rm eg}t} + \boldsymbol{\sigma}_+ e^{-i\omega_{\rm eg}t}.$$

Using these relations, we can evaluate the parts involving $\boldsymbol{\rho}_B$ in Eqs. 7.15 and 7.16.

7.3.1 Second-order expansion of $\mathcal{F}^{(\epsilon)}_{\rm TCL}$ and $\mathcal{K}^{(\epsilon)}_{\rm TCL}$

We now evaluate the maps $\mathcal{F}^{(\epsilon)}_{\rm TCL}$ and $\mathcal{K}^{(\epsilon)}_{\rm TCL}$ up to the second-order of ϵ. As a parametrization, we consider $\boldsymbol{\rho}_B = {\rm Tr}_A(\boldsymbol{\rho})$ [see Eq. 3.37 for its validity]. It then follows that the operations of χ_R and $\chi_L^\dagger$ defined in Eq. 3.22 are given by $\chi_R\boldsymbol{\rho}_B = |0\rangle\langle 0| \otimes \boldsymbol{\rho}_B$ and $\chi_L^\dagger\boldsymbol{\rho} = {\rm Tr}_A(\boldsymbol{\rho})$, respectively. Inserting these into the definition of the maps $\mathcal{F}^{(\epsilon)}_{\rm TCL}$ and $\mathcal{K}^{(\epsilon)}_{\rm TCL}$, Eqs. 3.29, we find, up to the second-order of ϵ,

$$\mathcal{F}^{(\epsilon)}_{\rm TCL}\boldsymbol{\rho}_B = {\rm Tr}_A(\mathcal{L}\mathcal{P}^{(\epsilon)}_{\rm inv}\boldsymbol{\rho}) = \mathcal{L}_B\boldsymbol{\rho}_B + \epsilon^2{\rm Tr}_A(\mathcal{L}_1\mathcal{P}_1\boldsymbol{\rho}), \tag{7.17}$$

and

$$\mathcal{K}^{(\epsilon)}_{\rm TCL}\boldsymbol{\rho}_B = \mathcal{P}^{(\epsilon)}_{\rm inv}\boldsymbol{\rho} = (\mathcal{P}_{\rm inv} + \epsilon\mathcal{P}_1 + \epsilon^2\mathcal{P}_2)\boldsymbol{\rho}, \tag{7.18}$$

with $\mathcal{P}_n = \lim_{t\to\infty}\mathcal{P}_n(t)$ $(n = 1, 2)$. Note that we have used Eq. 7.12 to derive Eq. 7.17.

The first-order contribution $\mathcal{P}_1(t)$ is given by Eq. 7.7, the integrand of which is given by Eq. 7.15 with $\tau_1 = \tau_2 = \tau$. Accordingly, we obtain

$$\epsilon\mathcal{P}_1(t) = -ig\,|0\rangle\langle 0| \otimes \boldsymbol{\sigma}_\gamma(t)\boldsymbol{\rho}_B + (H.c.), \tag{7.19}$$

where we have introduced

$$\boldsymbol{\sigma}_\gamma(t) = c_-(t)\boldsymbol{\sigma}_- + c_+(t)\boldsymbol{\sigma}_+,$$

with $c_\pm(t) = [1 - \exp(-\gamma_\pm t)]/\gamma_\pm$ and $\gamma_\pm = \bar{\kappa}/2 \pm i\omega_{\rm eg}$. This then leads to

$$\begin{aligned}
&\epsilon^2{\rm tr}_A(\mathcal{L}_1\mathcal{P}_1(t)\boldsymbol{\rho}) \\
&= -g^2\Big\{\boldsymbol{\sigma}_x\boldsymbol{\sigma}_\gamma(t)\boldsymbol{\rho}_B - \boldsymbol{\sigma}_\gamma(t)\boldsymbol{\rho}_B\boldsymbol{\sigma}_x\Big\} + (H.c.) \\
&= -\frac{ig^2}{2}{\rm Im}(c_+(t) - c_-(t))[\boldsymbol{\sigma}_z, \boldsymbol{\rho}_B] \\
&+g^2\sum_{j,k=\pm} K_{jk}(t)\left[\boldsymbol{\sigma}_j\boldsymbol{\rho}_B\sigma_k^\dagger - \frac{\boldsymbol{\sigma}_k^\dagger\boldsymbol{\sigma}_j\boldsymbol{\rho}_B + \boldsymbol{\rho}_B\boldsymbol{\sigma}_k^\dagger\boldsymbol{\sigma}_j}{2}\right],
\end{aligned} \tag{7.20}$$

with $K_{jk}(t) = c_j(t) + c_k^*(t)$. We thus obtain from Eq. 7.17 the second-order reduced dynamics $(d/dt)\rho_B(t) = \mathcal{F}^{(\epsilon)}_{\rm TCL}\rho_B(t)$ with

$$\begin{aligned}
\mathcal{F}^{(\epsilon)}_{\rm TCL}\rho_B &= -\frac{i}{2}\Big\{\omega_{\rm eg} + g^2{\rm Im}(c_+ - c_-)\Big\}[\boldsymbol{\sigma}_z, \boldsymbol{\rho}_B] \\
&+g^2\sum_{j,k=\pm} K_{jk}\left[\boldsymbol{\sigma}_j\boldsymbol{\rho}_B\boldsymbol{\sigma}_k^\dagger - \frac{\sigma_k^\dagger\boldsymbol{\sigma}_j\boldsymbol{\rho}_B + \boldsymbol{\rho}_B\boldsymbol{\sigma}_k^\dagger\boldsymbol{\sigma}_j}{2}\right],
\end{aligned} \tag{7.21}$$

where $c_\pm = \lim_{t\to\infty} c_\pm(t) = 1/\gamma_\pm$ and $K_{jk} = \lim_{t\to\infty} K_{jk}(t) = c_j + c_k^*$. We note that $\mathcal{F}^{(\epsilon)}$ at second order is obtained from the first order $\mathcal{P}_1$. We need $\mathcal{P}_2$ to obtain $\mathcal{K}^{(\epsilon)}$ at order two. This is the same complexity as in the projective approach to adiabatic elimination of Chap. 2, where we only need $k-1$ inversions of $\mathcal{L}_0$ to obtain the reduced dynamics $\mathcal{L}_{f,\|}$ at order k, but we need k inversions of $\mathcal{L}_0$ to compute $\mathcal{K}$.

The second-order contribution $\mathcal{P}_2$ can be evaluated by inserting Eq. 7.16 into Eq. 7.14. As a result, we obtain

$$\epsilon^2\mathcal{P}_2\boldsymbol{\rho} = \mathcal{X}\boldsymbol{\rho}_B - g^2\left[\sqrt{2}\,|2\rangle\langle 0| \otimes \left(\frac{\sigma_-\sigma_+}{\bar{\kappa}\gamma_+} + \frac{\sigma_+\sigma_-}{\bar{\kappa}\gamma_-}\right)\boldsymbol{\rho}_B + (H.c.)\right],$$

with

$$\begin{aligned}\mathcal{X}\rho_B = g^2(|1\rangle\langle 1| - |0\rangle\langle 0|) \otimes \Bigg(&\frac{\boldsymbol{\sigma}_-\boldsymbol{\rho}_B\boldsymbol{\sigma}_-}{\gamma_-(\gamma_- + \gamma_+^*)} + \frac{\boldsymbol{\sigma}_+\boldsymbol{\rho}_B\boldsymbol{\sigma}_+}{\gamma_+(\gamma_+ + \gamma_-^*)} \\ &+ \frac{\boldsymbol{\sigma}_-\boldsymbol{\rho}_B\boldsymbol{\sigma}_+}{\gamma_-(\gamma_- + \gamma_-^*)} + \frac{\boldsymbol{\sigma}_+\boldsymbol{\rho}_B\boldsymbol{\sigma}_-}{\gamma_+(\gamma_+ + \gamma_+^*)}\Bigg) + (H.c.) \\ = g^2(|1\rangle\langle 1| - |0\rangle\langle 0|) &\otimes \boldsymbol{\sigma}_\gamma\boldsymbol{\rho}_B\boldsymbol{\sigma}_\gamma^\dagger,\end{aligned}$$

with $\boldsymbol{\sigma}_\gamma = \lim_{t\to\infty}\boldsymbol{\sigma}_\gamma(t) = c_-\sigma_- + c_+\boldsymbol{\sigma}_+$. Inserting this and Eq. 7.19 in the limit $t \to \infty$ into Eq. 7.18, we find

$$\mathcal{K}_{\mathrm{TCL}}^{(\epsilon)}\boldsymbol{\rho}_B = |0\rangle\langle 0| \otimes \boldsymbol{\rho}_B + \boldsymbol{W}(|0\rangle\langle 0| \otimes \boldsymbol{\rho}_B) + (|0\rangle\langle 0| \otimes \boldsymbol{\rho}_B)\boldsymbol{W}^\dagger + \mathcal{X}\boldsymbol{\rho}_B,$$

with

$$W = -ig\boldsymbol{a}^\dagger \otimes \boldsymbol{\sigma}_\gamma - g^2(\boldsymbol{a}^\dagger)^2 \otimes \left(\frac{\boldsymbol{\sigma}_-\boldsymbol{\sigma}_+}{\bar{\kappa}\gamma_+} + \frac{\boldsymbol{\sigma}_+\boldsymbol{\sigma}_-}{\bar{\kappa}\gamma_-}\right).$$

Note that

$$\mathcal{K}_{\mathrm{TCL}}^{(\epsilon)}\boldsymbol{\rho}_B = (\boldsymbol{I} + \boldsymbol{W})(|0\rangle\langle 0| \otimes \boldsymbol{\rho}_B)(\boldsymbol{I} + \boldsymbol{W})^\dagger\mathcal{X}\boldsymbol{\rho}_B - \boldsymbol{W}(|0\rangle\langle 0| \otimes \boldsymbol{\rho}_B)\boldsymbol{W}^\dagger,$$

where $\boldsymbol{I}$ is the identity operator on the total space and

$$\mathcal{X}\boldsymbol{\rho}_B - \boldsymbol{W}(|0\rangle\langle 0| \otimes \boldsymbol{\rho}_B)\boldsymbol{W}^\dagger = -g^2\,|0\rangle\langle 0| \otimes \boldsymbol{\sigma}_\gamma\boldsymbol{\rho}_B\boldsymbol{\sigma}_\gamma^\dagger + O(g^3).$$

Therefore, within the accuracy of the second-order expansion, we obtain $\boldsymbol{\rho}(t) = \mathcal{K}_{\mathrm{TCL}}^{(\epsilon)}\boldsymbol{\rho}_B(t)$ with

$$\begin{aligned}\mathcal{K}_{\mathrm{TCL}}^{(\epsilon)}\boldsymbol{\rho}_B = (\boldsymbol{I} + \boldsymbol{W})(|0\rangle\langle 0| \otimes \boldsymbol{\rho}_B)(\boldsymbol{I} + \boldsymbol{W})^\dagger \\ -g^2(\boldsymbol{I}_A \otimes \boldsymbol{\sigma}_\gamma)(|0\rangle\langle 0| \otimes \boldsymbol{\rho}_B)(\boldsymbol{I}_A \otimes \boldsymbol{\sigma}_\gamma)^\dagger.\end{aligned} \tag{7.22}$$

7.3.2 Recovering complete positivity by incorporating the time-dependence

As discussed with Eq. (3.41), the generator $\mathcal{F}_{\mathrm{TCL}}^{(\epsilon)}$ given by Eq. (7.21) is not in the GKSL form and the evolution is not completely positive. Here we numerically show that the evolution generated by the time-dependent counterpart $\mathcal{F}_{\mathrm{TCL}}^{(\epsilon)}(t)$ defined by Eq. (3.42) is completely positive.

As the second-order contribution is given by Eq. (7.20), $\mathcal{F}_{\mathrm{TCL}}^{(\epsilon)}(t)$ can be obtained by replacing $c_\pm$ and K_{jk} in Eq. (7.21) by $c_\pm(t)$ and $K_{jk}(t)$, respectively. Since

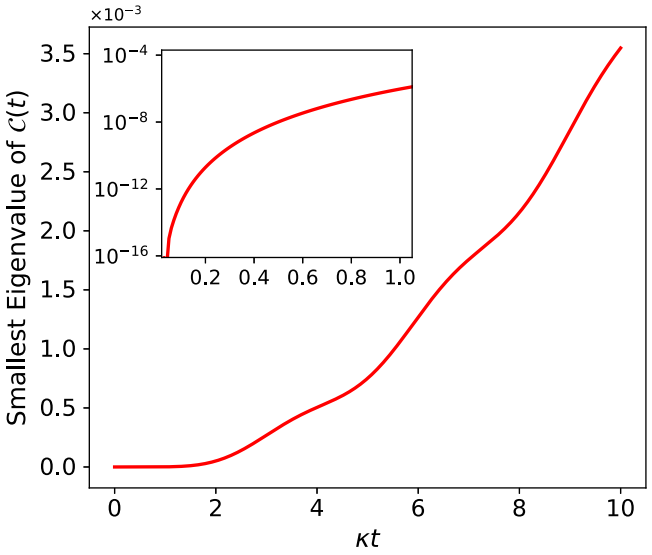

Figure 7.1: Nonnegativity of the smallest eigenvalue of the Choi matrix $\mathcal{C}(t)$ [see Eq. (7.23)]. The inset is a zoom in on the region $0 \leq \kappa t \leq 1.05$.

$[\mathcal{F}^{(\epsilon)}_{\mathrm{TCL}}(t_1), \mathcal{F}^{(\epsilon)}_{\mathrm{TCL}}(t_2)] \neq 0$ $(t_1 \neq t_2)$ in general, the propagator from 0 to t is given with the chronological time-ordering $T_{\leftarrow}$ as

$$T_{\leftarrow}\left\{e^{\int_0^t d\tau \mathcal{F}^{(\epsilon)}_{\mathrm{TCL}}(\tau)}\right\},$$

which approximates the exact reduced propagator.

To confirm its complete positivity, we consider the Choi matrix representation

$$\mathcal{C}(t) = \sum_{p,q=e,g} |p\rangle\langle q| \otimes T_{\leftarrow}\left\{e^{\int_0^t d\tau \mathcal{F}^{(\epsilon)}_{\mathrm{TCL}}(\tau)}\right\}(|p\rangle\langle q|), \tag{7.23}$$

which is positive semidefinite if and only if the propagator is completely positive [79]. The Choi matrix $\mathcal{C}(t)$ can be evaluated by solving $(d/dt)\rho_B(t) = \mathcal{F}^{(\epsilon)}_{\mathrm{TCL}}(t)\rho_B(t)$ with different initial states $\rho_B(t=0) = |p\rangle\langle q|$ $(p, q = e, g)$. For numerical computations, we arbitrarily set $\omega_{\mathrm{ph}} = \omega_{\mathrm{eg}} = \kappa$ and $g = 0.1\kappa$. The differential equation was solved using the fourth-order Runge-Kutta method with the time step size $10^{-3}\kappa^{-1}$.

Figure 7.1 shows the smallest eigenvalue of $\mathcal{C}(t)$ as a function of time. Except for the infinitesimal time region, the smallest eigenvalue is positive. In the infinitesimal time region, note that

$$K(dt) = 2dt \begin{pmatrix} 1 & 1 \\ 1 & 1 \end{pmatrix} + O(dt^2).$$

Accordingly, the matrix K is positive semidefinite to the leading order, ensuring complete positivity of the infinitesimal evolution. For the parameter set considered we observe numerically that the Choi matrix remains positive over the simulated time interval. We do not claim CP for all parameters or all times.

7.4 [Chap. 4] Inverse thermofield transformation to recover original bath results from T-TEDOPA simulations

In [168], De Vega and Bañuls present the thermofield transformation approach to obtain finite-temperature simulations from pure states. The idea is to double the environmental degrees of freedom and then to apply a Bogoliubov transformation: the real environment in a thermal state is transformed into two virtual environments in the vacuum state, defined as the thermofield vacuum. For any operator of the real environment, the expectation values in the thermal state are equivalent to those calculated in the thermofield vacuum. Behind the thermofield approach there is the concept of purification: the initial mixed state of the environment can be represented as the partial trace of a pure state (the thermofield vacuum) defined on the larger Hilbert space of the modes of the two virtual environments at zero temperature. The interaction of the system and each one of the two environments is then mapped on two separate chains, using the TEDOPA chain mapping to define a unitary transformation that can be applied to the bath modes, in order to define new modes for the environment, mapping it from a star-like to a one-dimensional chain-like configuration.

7.4.1 Thermofield for finite temperature simulation with pure initial states

In [168], the first step is to introduce an auxiliary environment of non-interacting bosonic modes of negative frequencies:

$$\boldsymbol{H}^{\text{aux}} = \boldsymbol{H} - \sum_{k=1}^{N} \omega_k \boldsymbol{c}_k^\dagger \boldsymbol{c}_k, \tag{7.24}$$

where the Hamiltonian $\boldsymbol{H}$ is the bosonic Hamiltonian:

$$\boldsymbol{H} = \boldsymbol{H}_S + \sum_{k=1}^{N} \omega_k \boldsymbol{b}_k^\dagger \boldsymbol{b}_k + \frac{\boldsymbol{\sigma}_x}{2} \otimes \sum_{k=1}^{N} g_k (\boldsymbol{b}_k^\dagger + \boldsymbol{b}_k). \tag{7.25}$$

The two environments, of positive and negative frequencies, are assumed to be in a thermal environment at inverse temperature β; the second step is to apply a thermal Bogoliubov transformation to change the basis. The applied transformation produces two-modes squeezed states:

$$\begin{aligned} \boldsymbol{a}_{1k} &= e^{-iG} \boldsymbol{b}_k e^{iG} = \cosh(\theta_k) \boldsymbol{b}_k - \sinh(\theta_k) \boldsymbol{c}_k^\dagger \\ \boldsymbol{a}_{2k} &= e^{-iG} \boldsymbol{c}_k e^{iG} = \cosh(\theta_k) \boldsymbol{c}_k - \sinh(\theta_k) \boldsymbol{b}_k^\dagger, \end{aligned} \tag{7.26}$$

where the exponent of the squeezing operator is $G = i \sum_k \theta_k (\boldsymbol{b}_k^\dagger \boldsymbol{c}_k^\dagger - \boldsymbol{c}_k \boldsymbol{b}_k)$, and θ_k is dependent on the temperature as in the following relations, where the average number

of excitations in the k-th mode is $\langle \boldsymbol{n}_k \rangle = 1/(e^{\beta\omega_k} - 1)$:

$$\begin{aligned} \cosh(\theta_k) &= \sqrt{1 + \langle \boldsymbol{n}_k \rangle} = \sqrt{\frac{1}{1 - e^{-\beta\omega_k}}} \\ \sinh(\theta_k) &= \sqrt{\langle \boldsymbol{n}_k \rangle} = \sqrt{\frac{1}{e^{+\beta\omega_k} - 1}}. \end{aligned} \tag{7.27}$$

The Bogoliubov transformation defines a new squeezed vacuum state, which we write in terms of the vacuum state $|\Omega_0\rangle$ of the bosonic modes (original and auxiliary) of the operators $\boldsymbol{b}_k$, $\boldsymbol{c}_k$:

$$|\Omega\rangle = e^{iG} |\Omega_0\rangle , \quad \boldsymbol{a}_{1k} |\Omega\rangle = 0, \boldsymbol{a}_{2k} |\Omega\rangle = 0. \tag{7.28}$$

From the vacuum state, we can obtain the thermal state of the original environment:

$$\boldsymbol{\rho}_E = \mathrm{Tr}_{\mathrm{aux}}\{|\Omega\rangle \langle\Omega|\}, \tag{7.29}$$

and it can be now used as pure an initial state for both of the environments.

7.4.2 From the extended to the physical environment

As shown in [144], the matrix M defining the transformation of Eq. 7.26 is invertible: it is therefore possible to obtain the modes of the original ($\boldsymbol{b}_k$) and auxiliary ($\boldsymbol{c}_k$) environments as linear combination of the Bogoliubov-transformed modes $\boldsymbol{a}_{1k}$ and $\boldsymbol{a}_{2k}$. We explicitly write the transformation:

$$\begin{bmatrix} \boldsymbol{a}_{1k} \\ \boldsymbol{a}_{2k} \\ \boldsymbol{a}_{1k}^\dagger \\ \boldsymbol{a}_{2k}^\dagger \end{bmatrix} = \begin{bmatrix} \cosh\theta_k & 0 & 0 & -\sinh\theta_k \\ 0 & \cosh\theta_k & -\sinh\theta_k & 0 \\ 0 & -\sinh\theta_k & \cosh\theta_k & 0 \\ -\sinh\theta_k & 0 & 0 & \cosh\theta_k \end{bmatrix} \begin{bmatrix} \boldsymbol{b}_k \\ \boldsymbol{c}_k \\ \boldsymbol{b}_k^\dagger \\ \boldsymbol{c}_k^\dagger \end{bmatrix}, \tag{7.30}$$

and its inverse:

$$\begin{bmatrix} \boldsymbol{b}_k \\ \boldsymbol{c}_k \\ \boldsymbol{b}_k^\dagger \\ \boldsymbol{c}_k^\dagger \end{bmatrix} = \begin{bmatrix} \cosh\theta_k & 0 & 0 & \sinh\theta_k \\ 0 & \cosh\theta_k & \sinh\theta_k & 0 \\ 0 & \sinh\theta_k & \cosh\theta_k & 0 \\ \sinh\theta_k & 0 & 0 & \cosh\theta_k \end{bmatrix} \begin{bmatrix} \boldsymbol{a}_{1k} \\ \boldsymbol{a}_{2k} \\ \boldsymbol{a}_{1k}^\dagger \\ \boldsymbol{a}_{2k}^\dagger \end{bmatrix}. \tag{7.31}$$

It is now possible to obtain the mean value of the number operator for the physical modes as a function of mean values that we already have evaluated:

$$\begin{aligned} \langle \boldsymbol{b}_k^\dagger \boldsymbol{b}_k \rangle = &\cosh\theta_k \sinh\theta_k \Big(\langle \boldsymbol{a}_{2k} \boldsymbol{a}_{1k} \rangle + \langle \boldsymbol{a}_{1k}^\dagger \boldsymbol{a}_{2k}^\dagger \rangle \Big) + \\ &+ \sinh^2\theta_k \Big(1 + \langle \boldsymbol{a}_{2k}^\dagger \boldsymbol{a}_{2k} \rangle \Big) + \cosh^2\theta_k \langle \boldsymbol{a}_{1k}^\dagger \boldsymbol{a}_{1k} \rangle, \end{aligned} \tag{7.32}$$

where we exploited the bosonic commutation relations to obtain: $\boldsymbol{a}_{1k}\boldsymbol{a}_{1k}^\dagger = 1 + \boldsymbol{a}_{1k}^\dagger \boldsymbol{a}_{1k}$. In the thermofield case, a negative frequency ω_{2k} is associated to each positive frequency ω_{1k}. The sampling is therefore symmetric around zero. This marks a difference with

T-TEDOPA, where the sampling of frequencies is obtained through the thermalized measure $d\mu(\beta) = \sqrt{J(\omega,\beta)}d\omega$, and is not symmetric. To recover the results for the physical bath of frequencies starting from the results of T-TEDOPA simulations, we need to do an extrapolation for all of the mean values appearing in Eq. 7.32, in order to have their values for each ω at $-\omega$ as well. Given this need, the enlarged grid of frequencies of the remark 4.2.1 is particularly useful.

7.5 [Chap. 5] Reconstructing the spectral density from chain coefficients

Given a set of arbitrary chain coefficients $\{e_k, t_k, k_0\}$, it is possible to reconstruct the corresponding spectral density function. We remark that the $N \times N$ Jacobi matrix of the chain coefficients implies a tight-binding (nearest-neighbors) structure of interaction.

1. Diagonalize the $N \times N$ Jacobi matrix of the chain coefficients, obtaining the eigenvalues $\{\omega_k\}$ and corresponding eigenvectors $\{v^{(k)}\}$

2. Given k_0^2 defined in Eq. 5.18, we compute the weights (with $g_k \equiv \sqrt{w_k}$) as

$$w_k = k_0^2 \left| v_1^{(k)} \right|^2, \tag{7.33}$$

   where $v_1^{(k)}$ is the first element of the $k-$th eigenvector.

3. To obtain a smoother function, we convolve the discretized spectral density of Eq 5.19 with a Gaussian or Lorentzian kernel f_η, where η gives the broadening

$$J_{\text{smooth}}(\omega) = (J * f_\eta)(\omega) = \sum_k w_k f_\eta(\omega - \omega_k). \tag{7.34}$$

7.6 [Chap. 5] Reorganisation energy term from Caldeira-Leggett

We derive the reorganisation energy term from the microscopic Caldeira-Leggett Hamiltonian. Following [211], we suppose that the cavity quadrature $\boldsymbol{x} = (\boldsymbol{a} + \boldsymbol{a}^\dagger)/\sqrt{2m\omega_a}$ couples linearly to a bath of harmonic oscillators of coordinates $\{\boldsymbol{q}_k, \boldsymbol{p}_k\}$, masses m_k, frequencies ω_k and couplings c_k:

$$\boldsymbol{H}_I + \boldsymbol{H}_E = \sum_k \left(\frac{\boldsymbol{p}_k}{2m_k} + \frac{1}{2} m\omega_k^2 (\boldsymbol{q}_k - c_k \boldsymbol{x})^2 \right). \tag{7.35}$$

We express the same Hamiltonian with the second quantization ladder operators $\boldsymbol{b}_k$, $\boldsymbol{b}_k^\dagger$ by setting

$$\boldsymbol{q}_k = \frac{1}{\sqrt{2m_k\omega_k}} \left(\boldsymbol{b}_k + \boldsymbol{b}_k^\dagger \right), \quad \boldsymbol{p}_k = i\sqrt{\frac{m_k\omega_k}{2}} \left(\boldsymbol{b}_k + \boldsymbol{b}_k^\dagger \right), \tag{7.36}$$

and we obtain the discretized version of the interaction Hamiltonian by setting

$$g_k = \frac{c_k \omega_k}{2} \sqrt{\frac{m_k \omega_k}{m\omega}}, \tag{7.37}$$

plus the additional term

$$\sum_k \frac{g_k^2}{4} \left(\boldsymbol{a} + \boldsymbol{a}^\dagger\right)^2, \tag{7.38}$$

which, exploiting the definition of Eq. 5.19 to go from the discrete to the continuum, can be rewritten as

$$\lambda_{\text{reorg}} \left(\boldsymbol{a} + \boldsymbol{a}^\dagger\right)^2, \tag{7.39}$$

with

$$\lambda_{\text{reorg}} = \int_0^{+\infty} d\omega \, \frac{J(\omega)}{\omega}. \tag{7.40}$$

The coupling of the system to environmental modes introduces a static renormalization of the cavity potential. In the Caldeira–Leggett formulation this appears as the quadratic "counterterm"

$$\lambda_{\text{reorg}} \left(\boldsymbol{a} + \boldsymbol{a}^\dagger\right)^2, \qquad \lambda_{\text{reorg}} = \int_0^{\infty} \frac{J(\omega)}{\omega} \, d\omega, \tag{7.41}$$

which we must include in the system Hamiltonian so that the resonance of the cavity is kept fixed

$$\boldsymbol{H}_S \;\rightarrow\; \boldsymbol{H}_S + \lambda_{\text{reorg}} \left(\boldsymbol{a} + \boldsymbol{a}^\dagger\right)^2. \tag{7.42}$$

Using $(\boldsymbol{a} + \boldsymbol{a}^\dagger)^2 = 2\,\boldsymbol{a}^\dagger \boldsymbol{a} + I + \boldsymbol{a}^2 + \boldsymbol{a}^{\dagger 2}$, one sees that the counterterm both corrects the number-conserving dispersive shift (via $2\lambda_{\text{reorg}}\,\boldsymbol{a}^\dagger \boldsymbol{a}$) and balances residual quadratic (squeezing–like) contributions proportional to $\boldsymbol{a}$, $\boldsymbol{a}^\dagger$. We remark that this term is not included in the textbook spin-boson model [26], because in that case it is just proportional to the identity ($\boldsymbol{\sigma}_i^2 = \boldsymbol{I}$). In this case, our boson to bosons coupling imposes us to keep it.

7.7 [Chap. 5] Calibration scheme to select the drive frequency

Calibration scheme. To select the drive frequency ω_d for each configuration, the protocol goes as follows:

1. Set the drive to zero $\epsilon_d = 0$.
2. Prepare the qubit-cavity system in a $e-$like dressed Fock state, and the environmental vacuum: $|\overline{e, n}\rangle \otimes |\text{vac}\rangle_E$, here $n = 2$.
3. Let such a state relax into the environment so that the population of the cavity $\boldsymbol{N}_a$ converges to near zero.
4. Compute the two-sites observable $\langle \boldsymbol{c}_n^\dagger \boldsymbol{c}_m \rangle$ at final time.

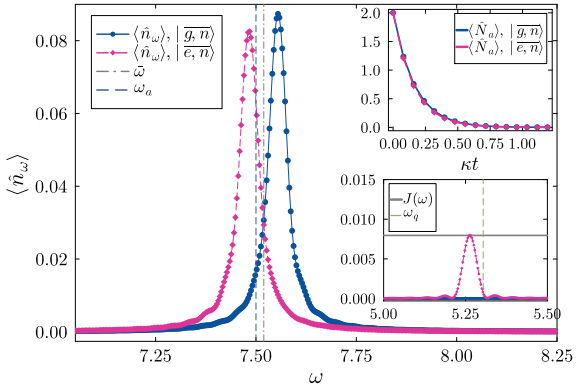

(a) $\Delta > 0$, $J(\omega) = J_{\text{flat}}(\omega)$. $\omega_{a,e} = 7.484\,2\pi\text{GHz}$, $\omega_{a,g} = 7.555\,2\pi\text{GHz}$, $\bar{\omega} = 7.519\,2\pi\text{GHz}$. $\omega_{q,e} = 5.263\,2\pi\text{GHz}$.

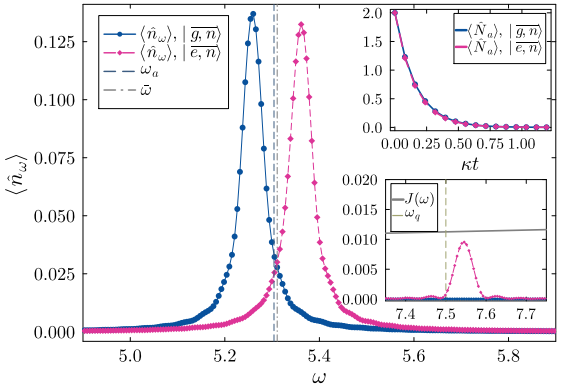

(b) $\Delta < 0$, $J(\omega) = J_{\text{ohm}}(\omega)$. $\omega_{a,e} = 5.361\,2\pi\text{GHz}$, $\omega_{a,g} = 5.26\,2\pi\text{GHz}$, $\bar{\omega} = 5.311\,2\pi\text{GHz}$. $\omega_{q,e} = 7.551\,2\pi\text{GHz}$.

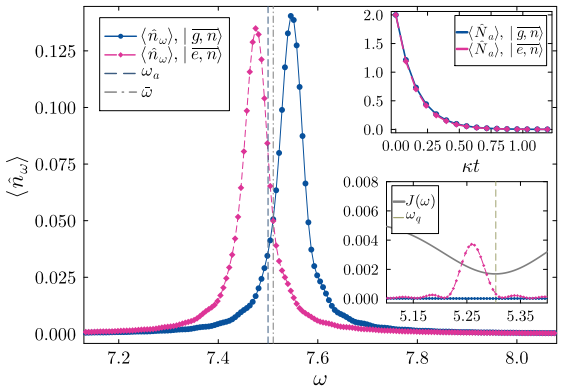

(c) $\Delta > 0$, $J(\omega) = J_{\text{PF}}(\omega)$. $\omega_{a,e} = 7.475\,2\pi\text{GHz}$, $\omega_{a,g} = 7.546\,2\pi\text{GHz}$, $\bar{\omega} = 7.51\,2\pi\text{GHz}$. $\omega_{q,e} = 5.259\,2\pi\text{GHz}$.

Figure 7.2: Calibration of the cavity drive frequency by undriven relaxation ($\epsilon_d = 0$). In each panel the system is initialized in a dressed Fock state $|\overline{i,n}\rangle$ with $i \in \{g, e\}$ (here $n = 2$) and the bath vacuum $|\text{vac}\rangle_E$. After relaxation of the cavity photon number $\langle \boldsymbol{N}_a \rangle$, computed up to time $\kappa t/(2\pi) = 1$, shown in the upper-right insets, we plot the frequency–resolved bath occupation $\langle \boldsymbol{n}_\omega \rangle$. The cavity–window peak positions define $\omega_{a,e} = \arg\max_\omega \langle \boldsymbol{n}_\omega \rangle$ for the e-like initialization and $\omega_{a,g}$ for the g-like one; the drive is set to the midpoint $\bar{\omega} = (\omega_{a,e} + \omega_{a,g})/2$. Bottom-right insets around ω_q show the qubit peak and the corresponding spectral density $J(\omega)$. A displacement of $\bar{\omega}$ from ω_a reflects a Lamb shift induced by the environmental modes.

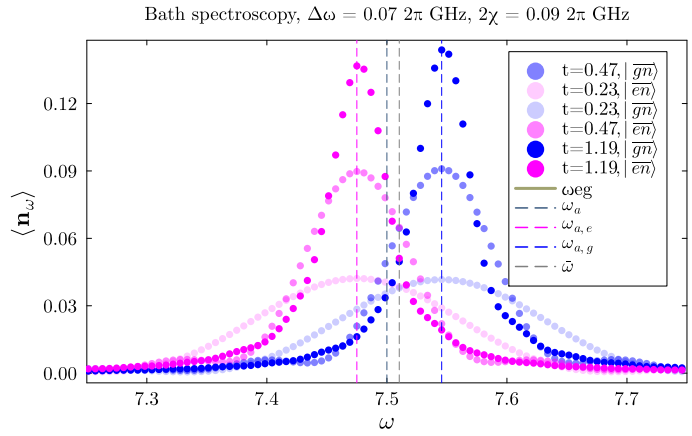

Figure 7.3: $\Delta > 0$, $J(\omega) = J_{\text{Ohm}}(\omega)$. Multiple timestamps showing the frequency–resolved bath occupation $\langle \boldsymbol{n}_\omega \rangle$, for the two initial conditions $|\overline{e,2}\rangle$ (magenta) and $|\overline{g,2}\rangle$ (blue). The frequency of the peaks does not depend on the simulation time.

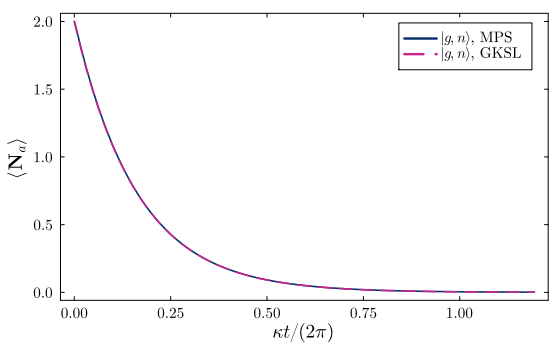

(a) GKSL vs $J_{\text{Ohm}}(\omega)$, $\Delta > 0$.

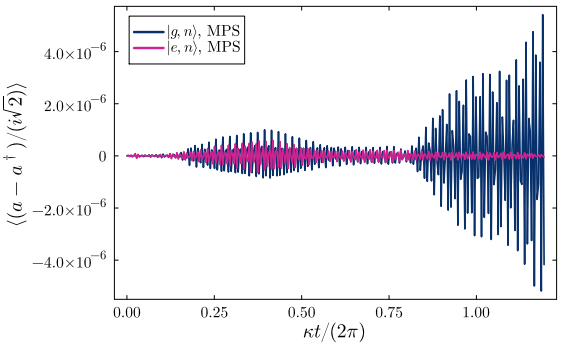

(b) $J_{\text{Ohm}}(\omega)$, $\Delta > 0$.

Figure 7.4: $J_{\text{Ohm}}(\omega)$, $\Delta > 0$. Checks on the cavity observables. In the left panel we show a comparison between the evolution of $\langle \boldsymbol{N}_a \rangle$ for both GKSL and MPS, which for this undriven case perfectly agree. In the right panel, we show some small ($\sim 10^{-6}$), high frequency fluctuations of the $\langle \boldsymbol{p} \rangle$ quadrature of the cavity.

5. Invert the chain mapping as in Sec. 4.2 to obtain the bath occupation number $\langle \boldsymbol{n}_\omega \rangle$ and extract from the cavity peaks

$$\omega_{a,e} = \arg\max_{\omega} \langle n_\omega \rangle \tag{7.43}$$

6. Repeat steps 2-4 for the $g-$like initial state $|\overline{g,n}\rangle \otimes |\text{vac}\rangle_E$, obtaining $\omega_{a,g}$.

7. Set the drive to the midpoint

$$\omega_d \equiv \bar{\omega} = \frac{\omega_{a,e} + \omega_{a,g}}{2}. \tag{7.44}$$

Calibration results. Calibration results for the flat, Ohmic-inverted, and Purcell configurations are shown in Fig 7.2, where we plot the bath spectroscopy in each case, with an inset showing the relaxation dynamics of $\boldsymbol{N}_a$ and another inset centered around the qubit peak. The frequency of the cavity peaks is shifted depending on the state of the qubit, but does not depend on the simulation time, as it is shown in Fig. 7.3. In Fig. 7.4.a we compare cavity dressed population $\boldsymbol{N}_a$ for both the Ohmic case $J_{\text{Ohm}}(\omega)$, $\Delta > 0$, and GKSL simulations. We find good agreement. In Fig. 7.4.b, we report an example of small ($\sim 10^{-6}$), high frequency fluctuations of the $\langle \boldsymbol{p} \rangle$ quadrature of the cavity, which is equal to zero for the GKSL simulations. We note that it should hold exactly that $\langle \boldsymbol{p} \rangle = 0$, as the undriven Hamiltonian of Eq. 5.17 commutes with the global parity operator

$$\boldsymbol{\Pi} = \boldsymbol{\sigma}_z \otimes (-1)^{\boldsymbol{a}^\dagger \boldsymbol{a}} \otimes \prod_k (-1)^{c_k^\dagger c_k}, \tag{7.45}$$

since $\boldsymbol{\Pi}\boldsymbol{\sigma}_x\boldsymbol{\Pi} = -\boldsymbol{\sigma}_x$, and our initial state is an eigenstate of $\boldsymbol{\Pi}$. We conclude that such small oscillations are due to numerical truncation errors. We also note that adding the drive Hamiltonian breaks the parity conservation.

7.8 [Chap. 5] Numerical simulations details

Units. All Hamiltonian parameters as well as the spectral density function $J(\omega)$ are defined in 2πGHz (rad/ns). The decay rate is computed using

$$\kappa = 2\pi J(\omega),$$

which yields κ in radians/ns (angular frequency units). MPS and Lindblad simulations remain consistent because both treat κ numerically, without enforcing unit semantics. As a result, simulation outputs agree. When plotting, the time is rescaled as

$$\kappa_{\text{GHz}} t = \frac{\kappa t}{2\pi},$$

to express dynamics in a-dimensional units of cavity linewidths (Hz).

Computing the dynamics. The simulation workflow is detailed in Sec. 4.3.1. The MPS simulations are conducted using the 1TDVP algorithm (see Sec. 4.1.5), which constrains the evolution on a manifold in the Hilbert space characterized by those states that can be represented as matrix product states of a fixed bond dimension χ, set at the beginning of the simulation. We choose the 1TDVP algorithm because of its advantageous scaling with respect to the local dimensions d of the MPS sites: 1TDVP $\sim d^2$ while 2TDVP $\sim d^3$.

Since the same χ is set at the beginning of the simulation, and for every bond of the MPS, such strategy is non-optimal. To improve efficiency, future simulations might rely instead on DTDVP [212], that adapts bond dimensions at each time-step and chain site following entanglement growth. The adaptive TDVP (DTDVP) has been introduced in [212, 167]. DTDVP is advantageous in comparison to both the one-site (1TDVP) and two-site (two-sites TDVP (2TDVP)) version of TDVP. The main advantage of the

one-site 1TDVP algorithm is that it preserves the unitarity of the MPS during the time evolution. Its main problem, conversely, is that the time evolution is constrained to happen on a manifold constituted by tensors of fixed bond dimension, a quantity closely related to the amount of entanglement in the MPS, and such a bond dimension has therefore to be fixed before the beginning of the time evolution. The scaling of 1TDVP is $\mathcal{O}(\chi^2 d^2 w^2 + \chi^3 dw + \chi^3 d^2)$, where w is the MPO bond dimension. This strategy will necessarily be non optimal: the growth of the bond dimensions required to describe the quantum state should ideally mirror the entanglement growth induced by the time evolution. 2TDVP allows for such a dynamical growth of the bond dimensions, and therefore better describes the entanglement in the MPS. It suffers however of other drawbacks: first of all, a truncation error is introduced (by the means of an SVD decomposition), which entails a loss of unitarity of the time-evolved MPS. Moreover, 2TDVP has bad scaling properties with the size of the local dimensions of the MPS, $\mathcal{O}(\chi^2 d^3 w^2 + \chi^3 d^2 w + \chi^3 d^3)$: this is a major issue when dealing with bosons, as it is the case in this work. The DTDVP algorithm combines the best features of 1TDVP and 2TDVP: it preserves unitarity, it has the same scaling properties of 1TDVP, and it adapts the bond dimensions to the entanglement evolution at each site and at each time-step. DTDVP does not suffer from a truncation error, but introduces a projection error.

7.8.1 Checking convergence

A big part of running simulations is to make systematic convergence tests. It is hard to distinguish between an ill-converged result and a qualitative change in the behavior of $\mathbf{\Sigma}_z(t)$. It is thus essential to make extensive tests. Beyond being a necessary sanity check on our numerics, a global view of the requirements for convergence can be a useful guideline for allocating a correct amount of resources for future simulations (e.g. longer-time simulations). In this section we report some of the tests we made to validate the results presented in Chap. 5. We focus on the sanity checks detailed in Sec. 4.3.2 of Chap. 4, where we detail how to choose the chain length N, local dimension of the MPS site, cutoff frequency ω_c, and sampling resolution for spectroscopy. The chain length depends on the chain coefficients and on the simulation time. For the simulations at $\kappa t/(2\pi) = 0.5$ we have:

- $J_{\mathrm{Ohm}}(\omega)$: chain length of $N = 471$
- $J_{\mathrm{flat}}(\omega)$: chain length of $N = 289$
- $J_{\mathrm{PF}}(\omega)$: chain length of $N = 472$.

We choose to only report the convergence tests made for the simulations at strongest drive amplitude, as this is the most unfavorable case. We can provide the same plots showing convergence for all other drive amplitudes as well.

Saturation of local dimensions d

In driven simulations with bosonic sites, we size the local Hilbert spaces from an analytic estimate of the steady-state photon number and add some margin for Poisson tails and

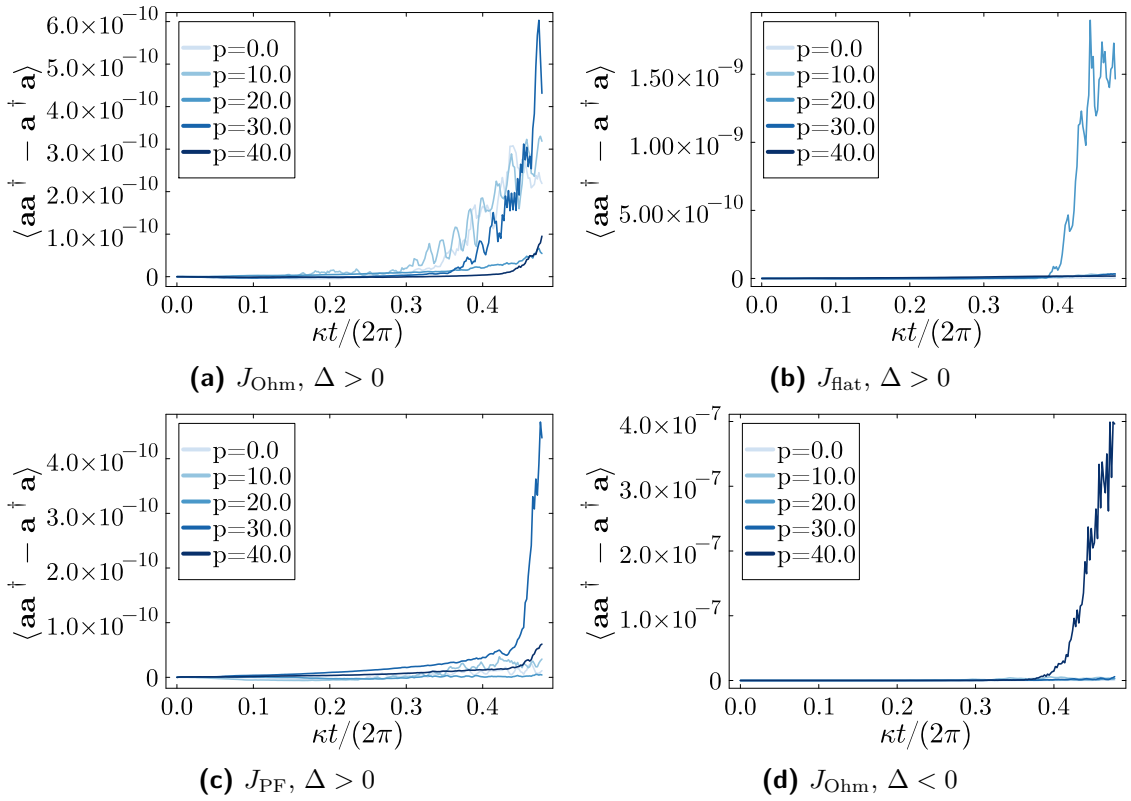

(a) J_{Ohm}, $\Delta > 0$ **(b)** J_{flat}, $\Delta > 0$

(c) J_{PF}, $\Delta > 0$ **(d)** J_{Ohm}, $\Delta < 0$

Figure 7.5: The error $\delta_{\mathrm{sat}}(t)$ of Eq. 7.49 as a function of time for multiple drive powers $\epsilon_d = p\bar{\epsilon}_d$. In the worst case (Ohmic with $\Delta < 0$), the error is of the order 10^{-7}.

transients. For the cavity, resonantly driven at amplitude $\epsilon_d = p\,\bar{\epsilon}_d$, we set the local dimension as

$$d_a \;=\; \left\lceil\, 10 \;+\; 7\sqrt{\bar{n}_a} \;+\; \bar{n}_a \,\right\rceil, \qquad \bar{n}_a = \frac{4\,\epsilon_d^2}{\kappa^2} = \frac{4\,(p\,\bar{\epsilon}_d)^2}{\kappa^2} \tag{7.46}$$

i.e. mean $+7\sigma$ for Poisson-like fluctuations ($\sigma \simeq \sqrt{\bar{n}}$) plus some constant. For the bosonic chain sites, which are not directly driven, we estimate the average occupation of the first site from the chain coefficients of Eq. 5.18

$$\bar{n}_{\text{chain}} \;=\; \frac{t_0}{k_0}\,\bar{n}_a, \tag{7.47}$$

where k_0 is the cavity–chain coupling and t_0 the hopping between the first and second chain sites. We then choose a uniform Fock cutoff for all chain sites

$$d_{\text{chain}} \;=\; \left\lceil\, 2 \;+\; 5\,\bar{n}_{\text{chain}} \,\right\rceil, \tag{7.48}$$

where the constants where chosen after some convergence tests.

To check that the simulations are not saturating the Hilbert space, a useful quantity to monitor is

$$\delta_{\text{sat}}(t) = 1 - \left\langle [\boldsymbol{a},\, \boldsymbol{a}^\dagger](t) \right\rangle, \tag{7.49}$$

which could deviate from zero due to the finite truncation d_a of the Hilbert space, so that the creation and annihilation operators are now projected $\boldsymbol{a} = \boldsymbol{P}_{d_a}\boldsymbol{a}\boldsymbol{P}_{d_a}$. Figure 7.5 confirms that the cavity Hilbert-space truncation does not bias our results: $\delta_{\text{sat}}(t)$ stays essentially zero for all $J(\omega)$ and both detunings at the highest drive, so neither the transient filling nor the steady-state plateau pushes probability mass against the cutoff.

Convergence with varying bond dimension χ

We report in this section convergence tests for varying bond dimensions χ. The drive amplitude is set to be $\epsilon_d = p\bar{\epsilon}_d$, with $p = 40.0$. In Fig. 7.6 the Ohmic spectral density with $\Delta > 0$, in Fig. 7.7 the Purcell filter spectral density, in Fig. 7.8 the Ohmic spectral density with $\Delta < 0$, in Fig. 7.9 the flat spectral density results. Top panels show the entanglement entropy, from which we estimate the minimum value of bond dimension required to capture the entanglement in the MPS as $\chi_{\text{min}} = e^{S_{\text{max}}}$. Center-row panels show the dynamics of $\langle \boldsymbol{\Sigma}_z(t) \rangle$, bottom-row panels show the dynamics of $\langle \boldsymbol{N}_a(t) \rangle$. Different columns represent different time discretization steps, specified on top of each column.

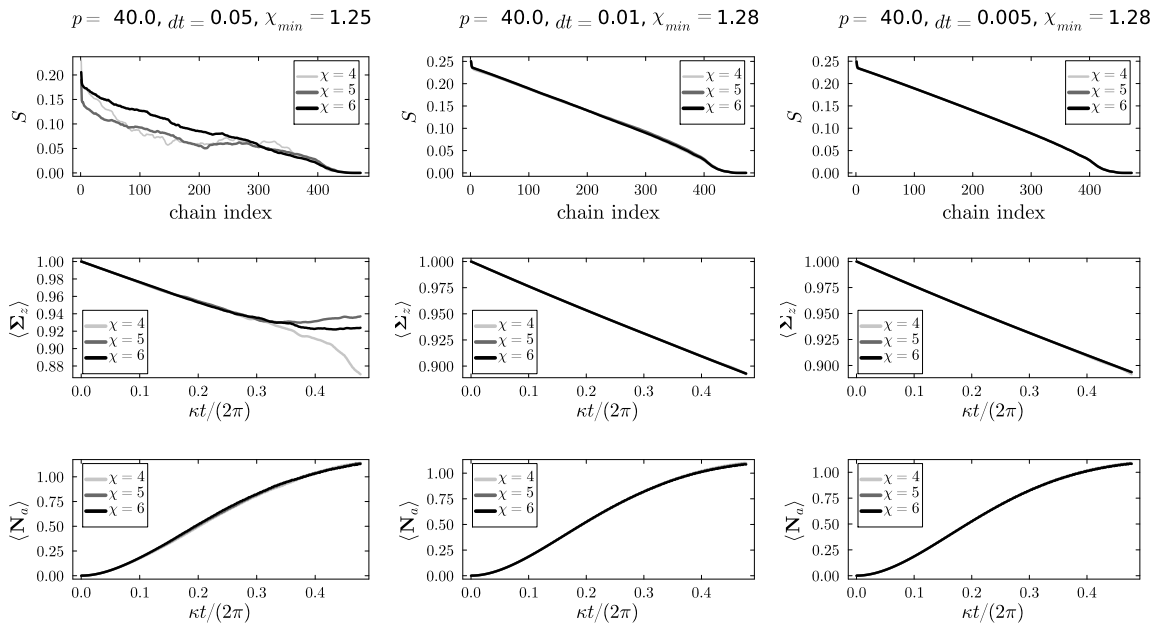

Figure 7.6: Ohmic case, $J_{\mathrm{Ohm}}(\omega)$, $\Delta > 0$.

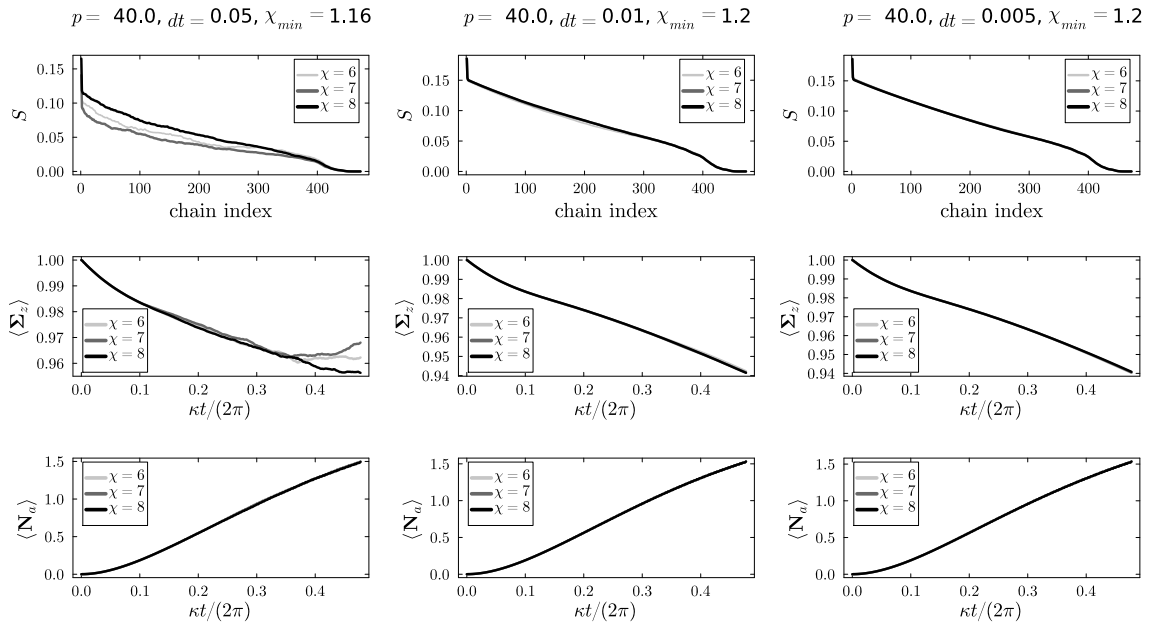

Figure 7.7: Purcell filter case, $J_{\mathrm{PF}}(\omega)$, $\Delta > 0$.

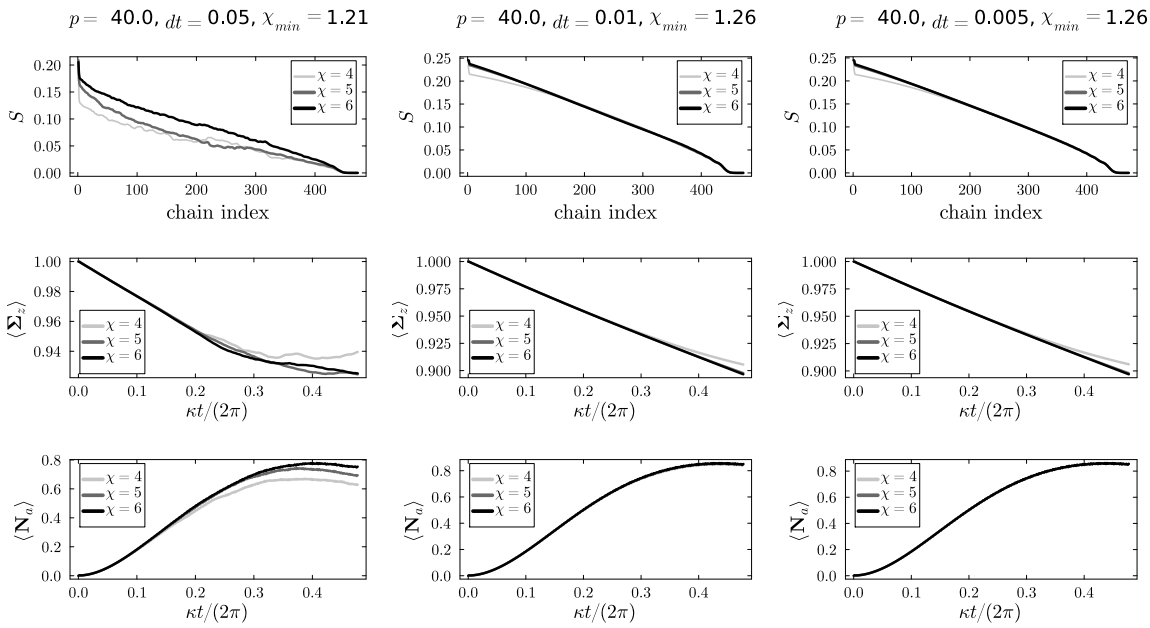

Figure 7.8: Ohmic case, inverted frequencies, $J_{\text{Ohm}}(\omega)$, $\Delta < 0$.

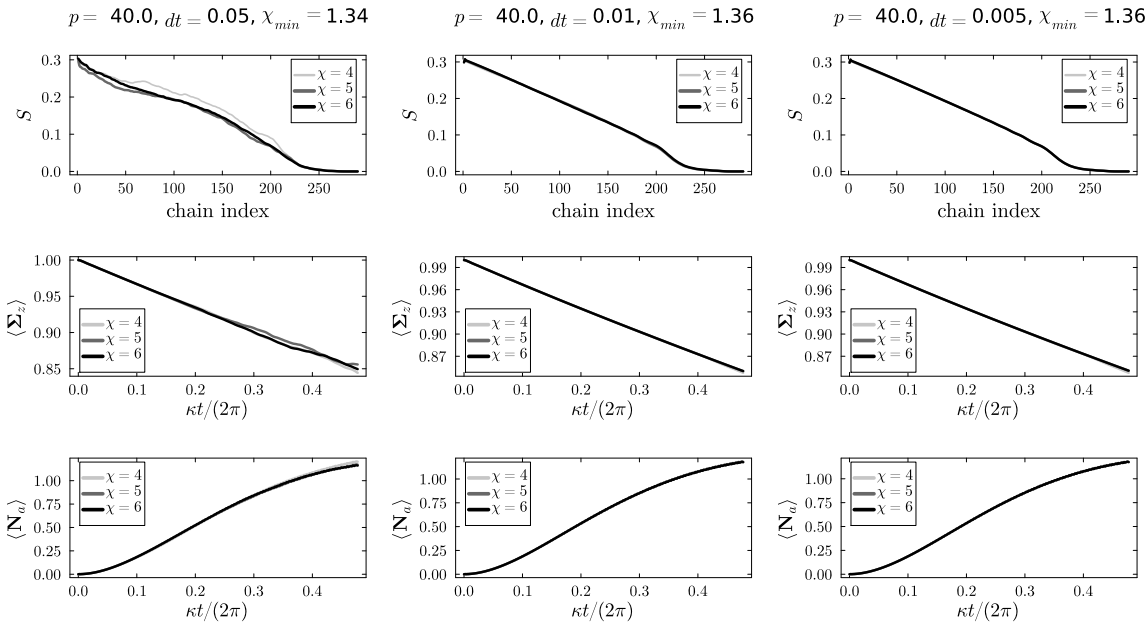

Figure 7.9: Flat case, $J_{\text{flat}}(\omega)$, $\Delta > 0$.

Bibliography

[1] J. I. Cirac and P. Zoller. "Quantum Computations with Cold Trapped Ions". In: *Phys. Rev. Lett.* 74 (20 May 1995), pp. 4091–4094. DOI: 10.1103/PhysRevLett.74.4091. URL: https://link.aps.org/doi/10.1103/PhysRevLett.74.4091.

[2] Dolev Bluvstein et al. "Logical quantum processor based on reconfigurable atom arrays". In: *Nature* 626.7997 (Feb. 2024), pp. 58–65. ISSN: 1476-4687. DOI: 10.1038/s41586-023-06927-3.

[3] David P. DiVincenzo. "The Physical Implementation of Quantum Computation". In: *Fortschritte der Physik* 48.9-11 (2000), pp. 771–783. DOI: https://doi.org/10.1002/1521-3978(200009)48:9/11<771::AID-PROP771>3.0.CO;2-E. eprint: https://onlinelibrary.wiley.com/doi/pdf/10.1002/1521-3978%28200009%2948%3A9/11%3C771%3A%3AAID-PROP771%3E3.0.CO%3B2-E. URL: https://onlinelibrary.wiley.com/doi/abs/10.1002/1521-3978%28200009%2948%3A9/11%3C771%3A%3AAID-PROP771%3E3.0.CO%3B2-E.

[4] Guido Burkard et al. "Semiconductor spin qubits". In: *Rev. Mod. Phys.* 95 (2 June 2023), p. 025003. DOI: 10.1103/RevModPhys.95.025003. URL: https://link.aps.org/doi/10.1103/RevModPhys.95.025003.

[5] M. H. Devoret and R. J. Schoelkopf. "Superconducting Circuits for Quantum Information: An Outlook". In: *Science* 339.6124 (2013), pp. 1169–1174. DOI: 10.1126/science.1231930. eprint: https://www.science.org/doi/pdf/10.1126/science.1231930. URL: https://www.science.org/doi/abs/10.1126/science.1231930.

[6] Antonio Acín et al. "The quantum technologies roadmap: a European community view". In: *New Journal of Physics* 20.8 (Aug. 2018), p. 080201. DOI: 10.1088/1367-2630/aad1ea.

[7] Jonathan Dowling and Gerard Milburn. "Quantum Technology: The Second Quantum Revolution". In: *Philosophical transactions. Series A, Mathematical, physical, and engineering sciences* 361 (Sept. 2003), pp. 1655–74. DOI: 10.1098/rsta.2003.1227.

[8] John Preskill. "Reliable quantum computers". In: *Proceedings of the Royal Society of London. Series A: Mathematical, Physical and Engineering Sciences* 454.1969 (1998), pp. 385–410. DOI: 10.1098/rspa.1998.0167. eprint: https://royalsocietypublishing.org/doi/pdf/10.1098/rspa.1998.0167. URL: https://royalsocietypublishing.org/doi/abs/10.1098/rspa.1998.0167.

[9] C. W. Gardiner and P. Zoller. *Quantum Noise*. Ed. by H. Haken. second. Springer, 2000.

[10] P. Krantz et al. "A quantum engineer's guide to superconducting qubits". In: *Applied Physics Reviews* 6.2 (June 2019). ISSN: 1931-9401. DOI: 10.1063/1.5089550. URL: http://dx.doi.org/10.1063/1.5089550.

[11] A. A. Clerk et al. "Introduction to quantum noise, measurement, and amplification". In: *Rev. Mod. Phys.* 82 (2 Apr. 2010), pp. 1155–1208. DOI: 10.1103/RevModPhys.82.1155. URL: https://link.aps.org/doi/10.1103/RevModPhys.82.1155.

[12] Jonas Bylander et al. "Noise spectroscopy through dynamical decoupling with a superconducting flux qubit". In: *Nature Physics* 7.7 (2011), pp. 565–570. ISSN: 1745-2481. DOI: 10.1038/nphys1994.

[13] C. M. Quintana et al. "Observation of Classical-Quantum Crossover of $1/f$ Flux Noise and Its Paramagnetic Temperature Dependence". In: *Phys. Rev. Lett.* 118 (5 Jan. 2017), p. 057702. DOI: 10.1103/PhysRevLett.118.057702. URL: https://link.aps.org/doi/10.1103/PhysRevLett.118.057702.

[14] P. Kumar et al. "Origin and Reduction of $1/f$ Magnetic Flux Noise in Superconducting Devices". In: *Phys. Rev. Appl.* 6 (4 Oct. 2016), p. 041001. DOI: 10.1103/PhysRevApplied.6.041001. URL: https://link.aps.org/doi/10.1103/PhysRevApplied.6.041001.

[15] Christian Kraglund Andersen et al. "Repeated quantum error detection in a surface code". In: *Nature Physics* 16.8 (Aug. 2020), pp. 875–880. ISSN: 1745-2481. DOI: 10.1038/s41567-020-0920-y.

[16] Sebastian Krinner et al. "Realizing repeated quantum error correction in a distance-three surface code". In: *Nature* 605.7911 (May 2022), pp. 669–674. ISSN: 1476-4687. DOI: 10.1038/s41586-022-04566-8.

[17] Rajeev Acharya et al. "Quantum error correction below the surface code threshold". In: *Nature* 638.8052 (Dec. 2024), pp. 920–926. ISSN: 1476-4687. DOI: 10.1038/s41586-024-08449-y. URL: http://dx.doi.org/10.1038/s41586-024-08449-y.

[18] Nicolas Didier, Jérôme Bourassa, and Alexandre Blais. "Fast Quantum Nondemolition Readout by Parametric Modulation of Longitudinal Qubit-Oscillator Interaction". In: *Phys. Rev. Lett.* 115 (20 Nov. 2015), p. 203601. DOI: 10.1103/PhysRevLett.115.203601. URL: https://link.aps.org/doi/10.1103/PhysRevLett.115.203601.

[19] Y. Sunada et al. "Fast Readout and Reset of a Superconducting Qubit Coupled to a Resonator with an Intrinsic Purcell Filter". In: *Phys. Rev. Appl.* 17 (4 Apr. 2022), p. 044016. DOI: 10.1103/PhysRevApplied.17.044016. URL: https://link.aps.org/doi/10.1103/PhysRevApplied.17.044016.

[20] M. D. Reed et al. “Fast reset and suppressing spontaneous emission of a superconducting qubit”. In: *Applied Physics Letters* 96.20 (May 2010). ISSN: 1077-3118. DOI: 10.1063/1.3435463. URL: http://dx.doi.org/10.1063/1.3435463.

[21] Ross Shillito et al. “Dynamics of Transmon Ionization”. en. In: *Physical Review Applied* 18.3 (Sept. 2022). arXiv:2203.11235 [quant-ph], p. 034031. ISSN: 2331-7019. DOI: 10.1103/PhysRevApplied.18.034031.

[22] W. Dai et al. *Spectroscopy of drive-induced unwanted state transitions in superconducting circuits*. 2025. arXiv: 2506.24070 [quant-ph]. URL: https://arxiv.org/abs/2506.24070.

[23] Joachim Cohen et al. “Reminiscence of Classical Chaos in Driven Transmons”. In: *PRX Quantum* 4 (2 Apr. 2023), p. 020312. DOI: 10.1103/PRXQuantum.4.020312. URL: https://link.aps.org/doi/10.1103/PRXQuantum.4.020312.

[24] Lucas Verney et al. “Structural Instability of Driven Josephson Circuits Prevented by an Inductive Shunt”. In: *Physical Review Applied* 11.2 (Feb. 2019). ISSN: 2331-7019. DOI: 10.1103/physrevapplied.11.024003. URL: http://dx.doi.org/10.1103/PhysRevApplied.11.024003.

[25] Lorenza Viola, Emanuel Knill, and Seth Lloyd. “Dynamical Decoupling of Open Quantum Systems”. In: *Phys. Rev. Lett.* 82 (12 Mar. 1999), pp. 2417–2421. DOI: 10.1103/PhysRevLett.82.2417. URL: https://link.aps.org/doi/10.1103/PhysRevLett.82.2417.

[26] H. P. Breuer and F. Petruccione. *The theory of open quantum systems*. Great Clarendon Street: Oxford University Press, Aug. 2002.

[27] Bassano Vacchini. *Open Quantum Systems: Foundations and Theory*. 1st ed. Graduate Texts in Physics. Cham: Springer, 2024, pp. xxiv+420. ISBN: 978-3-031-58217-2. DOI: 10.1007/978-3-031-58218-9. URL: https://link.springer.com/book/10.1007/978-3-031-58218-9.

[28] Alexandre Blais et al. “Cavity quantum electrodynamics for superconducting electrical circuits: An architecture for quantum computation”. In: *Phys. Rev. A* 69 (6 June 2004), p. 062320. DOI: 10.1103/PhysRevA.69.062320. URL: https://link.aps.org/doi/10.1103/PhysRevA.69.062320.

[29] Alexandre Blais et al. “Circuit quantum electrodynamics”. In: *Rev. Mod. Phys.* 93 (2 May 2021), p. 025005. DOI: 10.1103/RevModPhys.93.025005. URL: https://link.aps.org/doi/10.1103/RevModPhys.93.025005.

[30] John Clarke and Frank K. Wilhelm. “Superconducting quantum bits”. In: *Nature* 453.7198 (2008), pp. 1031–1042. ISSN: 1476-4687. DOI: 10.1038/nature07128.

[31] Daria Gusenkova et al. “Quantum Nondemolition Dispersive Readout of a Superconducting Artificial Atom Using Large Photon Numbers”. In: *Physical Review Applied* 15.6 (June 2021). ISSN: 2331-7019. DOI: 10.1103/physrevapplied.15.064030. URL: http://dx.doi.org/10.1103/PhysRevApplied.15.064030.

[32] Fran çois Swiadek et al. “Enhancing Dispersive Readout of Superconducting Qubits through Dynamic Control of the Dispersive Shift: Experiment and Theory”. In: *PRX Quantum* 5 (4 Nov. 2024), p. 040326. DOI: 10.1103/PRXQuantum.5.040326. URL: https://link.aps.org/doi/10.1103/PRXQuantum.5.040326.

[33] Rui Li et al. “Realization of High-Fidelity CZ Gate Based on a Double-Transmon Coupler”. In: *Phys. Rev. X* 14 (4 Nov. 2024), p. 041050. DOI: 10.1103/PhysRevX.14.041050. URL: https://link.aps.org/doi/10.1103/PhysRevX.14.041050.

[34] Yong-Xi Xiao et al. *Flexible Readout and Unconditional Reset for Superconducting Multi-Qubit Processors with Tunable Purcell Filters*. 2025. arXiv: 2507.06988 [quant-ph]. URL: https://arxiv.org/abs/2507.06988.

[35] H. Hutin et al. “Monitoring the Energy of a Cavity by Observing the Emission of a Repeatedly Excited Qubit”. In: *Physical Review Letters* 133.15 (Oct. 2024). ISSN: 1079-7114. DOI: 10.1103/physrevlett.133.153602. URL: http://dx.doi.org/10.1103/PhysRevLett.133.153602.

[36] Ted Thorbeck et al. “Readout-Induced Suppression and Enhancement of Superconducting Qubit Lifetimes”. In: *Phys. Rev. Lett.* 132 (9 Feb. 2024), p. 090602. DOI: 10.1103/PhysRevLett.132.090602. URL: https://link.aps.org/doi/10.1103/PhysRevLett.132.090602.

[37] Seth Lloyd. “Universal Quantum Simulators”. In: *Science* 273.5278 (1996), pp. 1073–1078. DOI: 10.1126/science.273.5278.1073. eprint: https://www.science.org/doi/pdf/10.1126/science.273.5278.1073. URL: https://www.science.org/doi/abs/10.1126/science.273.5278.1073.

[38] Richard P. Feynman. “Simulating physics with computers”. In: *International Journal of Theoretical Physics* 21.6 (1982), pp. 467–488. ISSN: 1572-9575. DOI: 10.1007/BF02650179.

[39] JF Poyatos, J Ignacio Cirac, and P Zoller. “Quantum reservoir engineering with laser cooled trapped ions”. In: *Phys.Rev.Letters* 77.23 (1996).

[40] Anja Metelmann and Aashish A Clerk. “Nonreciprocal photon transmission and amplification via reservoir engineering”. In: *Phys.Rev.X* 5.2 (2015).

[41] Mazyar Mirrahimi et al. “Dynamically protected cat-qubits: a new paradigm for universal quantum computation”. In: *New J.Physics* 16.4 (2014).

[42] Nissim Ofek et al. “Extending the lifetime of a quantum bit with error correction in superconducting circuits”. In: *Nature* 536.7617 (Aug. 2016), pp. 441–445. ISSN: 1476-4687. DOI: 10.1038/nature18949.

[43] Z. Leghtas et al. “Confining the state of light to a quantum manifold by engineered two-photon loss”. In: *Science* 347.6224 (2015), pp. 853–857. DOI: 10.1126/science.aaa2085. eprint: https://www.science.org/doi/pdf/10.1126/science.aaa2085. URL: https://www.science.org/doi/abs/10.1126/science.aaa2085.

[44] P. Campagne-Ibarcq et al. “Quantum error correction of a qubit encoded in grid states of an oscillator”. In: *Nature* 584.7821 (Aug. 2020), pp. 368–372. ISSN: 1476-4687. DOI: 10.1038/s41586-020-2603-3.

[45] Raphaël Lescanne et al. “Irreversible Qubit-Photon Coupling for the Detection of Itinerant Microwave Photons”. In: *Phys. Rev. X* 10 (2 May 2020), p. 021038. DOI: 10.1103/PhysRevX.10.021038. URL: https://link.aps.org/doi/10.1103/PhysRevX.10.021038.

[46] Eric S. Cooper et al. “Graph states of atomic ensembles engineered by photon-mediated entanglement”. In: *Nature Physics* 20.5 (May 2024), pp. 770–775. ISSN: 1745-2481. DOI: 10.1038/s41567-024-02407-1.

[47] Brandon Grinkemeyer et al. “Error-detected quantum operations with neutral atoms mediated by an optical cavity”. In: *Science* 387.6740 (2025), pp. 1301–1305. DOI: 10.1126/science.adr7075. eprint: https://www.science.org/doi/pdf/10.1126/science.adr7075. URL: https://www.science.org/doi/abs/10.1126/science.adr7075.

[48] A. Bienfait et al. “Controlling spin relaxation with a cavity”. In: *Nature* 531.7592 (Mar. 2016), pp. 74–77. ISSN: 1476-4687. DOI: 10.1038/nature16944.

[49] M. Wolinsky and H. J. Carmichael. “Quantum noise in the parametric oscillator: From squeezed states to coherent-state superpositions”. In: *Phys. Rev. Lett.* 60 (18 May 1988), pp. 1836–1839. DOI: 10.1103/PhysRevLett.60.1836. URL: https://link.aps.org/doi/10.1103/PhysRevLett.60.1836.

[50] Tommaso Grigoletto et al. “Exact Model Reduction for Continuous-Time Open Quantum Dynamics”. In: *Quantum* 9 (July 2025), p. 1814. ISSN: 2521-327X. DOI: 10.22331/q-2025-07-29-1814. URL: https://doi.org/10.22331/q-2025-07-29-1814.

[51] Yuriel Núñez-Fernández, Maxime Debertolis, and Serge Florens. *Resolving space-time structures of quantum impurities with a numerically exact few-body algorithm*. 2025. arXiv: 2503.13706 [cond-mat.str-el]. URL: https://arxiv.org/abs/2503.13706.

[52] Nicolas Gheeraert et al. “Particle production in ultrastrong-coupling waveguide QED”. In: *Physical Review A* 98.4 (Oct. 2018). ISSN: 2469-9934. DOI: 10.1103/physreva.98.043816. URL: http://dx.doi.org/10.1103/PhysRevA.98.043816.

[53] Soumya Bera et al. “Generalized multipolaron expansion for the spin-boson model: Environmental entanglement and the biased two-state system”. In: *Phys. Rev. B* 90 (7 Aug. 2014), p. 075110. DOI: 10.1103/PhysRevB.90.075110. URL: https://link.aps.org/doi/10.1103/PhysRevB.90.075110.

[54] Howard M. Wiseman and Gerard J. Milburn. *Quantum Measurement and Control*. Cambridge University Press, 2009.

[55] Tameem Albash et al. “Corrigendum: Quantum adiabatic Markovian master equations (2012 New J. Phys. 14 123016)”. In: *New Journal of Physics* 17.12 (Dec. 2015), p. 129501. DOI: 10.1088/1367-2630/17/12/129501.

[56] Daniel Finkelstein-Shapiro et al. “Adiabatic elimination and subspace evolution of open quantum systems”. In: *Phys.Rev.A* 101.4 (2020). DOI: https://doi.org/10.1103/PhysRevA.101.042102.

[57] Florentin Reiter and Anders S Sørensen. “Effective operator formalism for open quantum systems”. In: *Phys.Rev.A* 85.3 (2012).

[58] Rémi Azouit, Alain Sarlette, and Pierre Rouchon. “Adiabatic elimination for open quantum systems with effective Lindblad master equations”. In: *IEEE 55th Conference on Decision and Control (CDC)*. 2016.

[59] Rémi Azouit et al. “Towards generic adiabatic elimination for bipartite open quantum systems”. In: *Quantum Science and Technology* 2.4 (2017).

[60] Paolo Forni et al. “Adiabatic elimination for multi-partite open quantum systems with non-trivial zero-order dynamics”. In: *IEEE 57th Conference on Decision and Control (CDC)*. 2018.

[61] Paolo Forni et al. “A palette of approaches for adiabatic elimination in bipartite open quantum systems with Hamiltonian dynamics on target”. In: *IEEE 58th Conference on Decision and Control (CDC)*. 2019.

[62] Angela Riva, Alain Sarlette, and Pierre Rouchon. “Explicit formulas for adiabatic elimination with fast unitary dynamics”. In: *2024 IEEE 63rd Conference on Decision and Control (CDC)*. 2024, pp. 755–760. DOI: 10.1109/CDC56724.2024.10886784.

[63] B.-L. Najera-Santos *et al.* “High-Sensitivity ac-Charge Detection with a MHz-Frequency Fluxonium Qubit”. In: *Phys. Rev. X* 14 (1 2024). DOI: 10.1103/PhysRevX.14.011007. URL: https://link.aps.org/doi/10.1103/PhysRevX.14.011007.

[64] Masaaki Tokieda and Angela Riva. “Time-convolutionless master equation applied to adiabatic elimination”. In: *Physical Review A* 111.5 (May 2025). ISSN: 2469-9934. DOI: 10.1103/physreva.111.052206. URL: http://dx.doi.org/10.1103/PhysRevA.111.052206.

[65] J. Ignacio Cirac et al. “Matrix product states and projected entangled pair states: Concepts, symmetries, theorems”. In: *Rev. Mod. Phys.* 93 (4 Dec. 2021), p. 045003. DOI: 10.1103/RevModPhys.93.045003. URL: https://link.aps.org/doi/10.1103/RevModPhys.93.045003.

[66] F. Verstraete, D. Porras, and J. I. Cirac. “Density Matrix Renormalization Group and Periodic Boundary Conditions: A Quantum Information Perspective”. In: *Phys. Rev. Lett.* 93 (22 Nov. 2004), p. 227205. DOI: 10.1103/PhysRevLett.93.227205. URL: https://link.aps.org/doi/10.1103/PhysRevLett.93.227205.

[67] J. Eisert, M. Cramer, and M. B. Plenio. “Colloquium: Area laws for the entanglement entropy”. In: *Rev. Mod. Phys.* 82 (1 Feb. 2010), pp. 277–306. DOI: 10.1103/RevModPhys.82.277.

[68] A.O Caldeira and A.J Leggett. “Quantum tunnelling in a dissipative system”. In: *Annals of Physics* 149.2 (1983), pp. 374–456. ISSN: 0003-4916. DOI: https://doi.org/10.1016/0003-4916(83)90202-6. URL: https://www.sciencedirect.com/science/article/pii/0003491683902026.

[69] A. W. Chin et al. “Exact mapping between system-reservoir quantum models and semi-infinite discrete chains using orthogonal polynomials”. In: *Journal of Mathematical Physics* 51.9 (Sept. 2010), p. 092109. DOI: 10.1063/1.3490188. eprint: https://doi.org/10.1063/1.3490188. URL: https://doi.org/10.1063/1.3490188.

[70] J. Prior et al. “Efficient Simulation of Strong System-Environment Interactions”. In: *Physical Review Letters* 105.5 (July 2010), p. 050404. DOI: 10.1103/PhysRevLett.105.050404. URL: https://link.aps.org/doi/10.1103/PhysRevLett.105.050404.

[71] M. P. Woods et al. “Mappings of open quantum systems onto chain representations and Markovian embeddings”. In: *Journal of Mathematical Physics* 55.3 (Mar. 2014), p. 032101. ISSN: 1089-7658. DOI: 10.1063/1.4866769. URL: http://dx.doi.org/10.1063/1.4866769.

[72] Ulrich Schollwöck. “The density-matrix renormalization group in the age of matrix product states”. In: *Annals of Physics* 326.1 (2011). January 2011 Special Issue, pp. 96–192. ISSN: 0003-4916. DOI: https://doi.org/10.1016/j.aop.2010.09.012. URL: https://www.sciencedirect.com/science/article/pii/S0003491610001752.

[73] Jutho Haegeman et al. “Time-dependent variational principle for quantum lattices”. en. In: *Physical Review Letters* 107.7 (Aug. 2011). arXiv: 1103.0936, p. 070601. ISSN: 0031-9007, 1079-7114. DOI: 10.1103/PhysRevLett.107.070601. URL: http://arxiv.org/abs/1103.0936.

[74] Thibaut Lacroix et al. “MPSDynamics.jl: Tensor network simulations for finite-temperature (non-Markovian) open quantum system dynamics”. In: *The Journal of Chemical Physics* 161.8 (Aug. 2024), p. 084116. ISSN: 0021-9606. DOI: 10.1063/5.0223107. URL: https://doi.org/10.1063/5.0223107.

[75] Angus Dunnett et al. *shareloqs/MPSDynamics*. 2021. DOI: 10.5281/zenodo.5106435. URL: https://zenodo.org/record/5106435.

[76] A. Wallraff et al. “Strong coupling of a single photon to a superconducting qubit using circuit quantum electrodynamics”. In: *Nature* 431.7005 (2004), pp. 162–167. ISSN: 1476-4687. DOI: 10.1038/nature02851.

[77] Eyob A. Sete, Jay M. Gambetta, and Alexander N. Korotkov. “Purcell effect with microwave drive: Suppression of qubit relaxation rate”. In: *Phys. Rev. B* 89 (10 Mar. 2014), p. 104516. DOI: 10.1103/PhysRevB.89.104516. URL: https://link.aps.org/doi/10.1103/PhysRevB.89.104516.

[78] Alexandru Petrescu, Moein Malekakhlagh, and Hakan E. Türeci. "Lifetime renormalization of driven weakly anharmonic superconducting qubits. II. The readout problem". In: *Phys. Rev. B* 101 (13 Apr. 2020), p. 134510. DOI: 10.1103/PhysRevB.101.134510. URL: https://link.aps.org/doi/10.1103/PhysRevB.101.134510.

[79] Michael A. Nielsen and Isaac L. Chuang. *Quantum Computation and Quantum Information*. Cambridge University Press, 2000.

[80] M. G. A. Paris. "The modern tools of quantum mechanics". In: *The European Physical Journal Special Topics* 203.1 (Apr. 2012), pp. 61–86. ISSN: 1951-6401. DOI: 10.1140/epjst/e2012-01535-1.

[81] Fabrizio Minganti and Alberto Biella. *Open quantum systems – A brief introduction*. 2024. arXiv: 2407.16855 [quant-ph]. URL: https://arxiv.org/abs/2407.16855.

[82] M. M. Wolf et al. "Assessing Non-Markovian Quantum Dynamics". In: *Phys. Rev. Lett.* 101 (15 Oct. 2008), p. 150402. DOI: 10.1103/PhysRevLett.101.150402. URL: https://link.aps.org/doi/10.1103/PhysRevLett.101.150402.

[83] Masaaki Tokieda et al. "Complete positivity violation of the reduced dynamics in higher-order quantum adiabatic elimination". In: *Phys. Rev. A* 109 (6 June 2024). DOI: 10.1103/PhysRevA.109.062206. URL: https://link.aps.org/doi/10.1103/PhysRevA.109.062206.

[84] Dariusz Chruściński and Saverio Pascazio. "A Brief History of the GKLS Equation". In: *Open Systems & Information Dynamics* 24.03 (2017), p. 1740001. DOI: 10.1142/S1230161217400017. eprint: https://doi.org/10.1142/S1230161217400017. URL: https://doi.org/10.1142/S1230161217400017.

[85] Sadao Nakajima. "On Quantum Theory of Transport Phenomena: Steady Diffusion". In: *Progress of Theoretical Physics* 20.6 (Dec. 1958), pp. 948–959. ISSN: 0033-068X. DOI: 10.1143/PTP.20.948.

[86] Robert Zwanzig. "Ensemble Method in the Theory of Irreversibility". In: *The Journal of Chemical Physics, Volume 33, Issue 5* 33.5 (Nov. 1960), pp. 1338–1341. DOI: 10.1063/1.1731409.

[87] E. B. Davies. "Markovian master equations". In: *Communications in Mathematical Physics* 39.2 (1974), pp. 91–110. ISSN: 1432-0916. DOI: 10.1007/BF01608389.

[88] Fumiaki Shibata, Yoshinori Takahashi, and Natsuki Hashitsume. "A generalized stochastic liouville equation. Non-Markovian versus memoryless master equations". In: *Journal of Statistical Physics* 17.4 (Oct. 1977), pp. 171–187. ISSN: 1572-9613. DOI: 10.1007/BF01040100.

[89] Ryogo Kubo. "Statistical-Mechanical Theory of Irreversible Processes. I. General Theory and Simple Applications to Magnetic and Conduction Problems". In: *Journal of the Physical Society of Japan* 12.6 (1957), pp. 570–586. DOI: 10.1143/JPSJ.12.570. eprint: https://doi.org/10.1143/JPSJ.12.570. URL: https://doi.org/10.1143/JPSJ.12.570.

[90] Robert S Whitney. "Staying positive: going beyond Lindblad with perturbative master equations". In: *Journal of Physics A: Mathematical and Theoretical* 41.17 (Apr. 2008), p. 175304. DOI: 10.1088/1751-8113/41/17/175304.

[91] Dragomir Davidović. "Completely Positive, Simple, and Possibly Highly Accurate Approximation of the Redfield Equation". In: *Quantum* 4 (Sept. 2020), p. 326. ISSN: 2521-327X. DOI: 10.22331/q-2020-09-21-326. URL: https://doi.org/10.22331/q-2020-09-21-326.

[92] Evgeny Mozgunov and Daniel Lidar. "Completely positive master equation for arbitrary driving and small level spacing". In: *Quantum* 4 (Feb. 2020), p. 227. ISSN: 2521-327X. DOI: 10.22331/q-2020-02-06-227. URL: https://doi.org/10.22331/q-2020-02-06-227.

[93] Anton Trushechkin. "Unified Gorini-Kossakowski-Lindblad-Sudarshan quantum master equation beyond the secular approximation". In: *Phys. Rev. A* 103 (6 June 2021), p. 062226. DOI: 10.1103/PhysRevA.103.062226. URL: https://link.aps.org/doi/10.1103/PhysRevA.103.062226.

[94] S. Gasparinetti et al. "Environment-Governed Dynamics in Driven Quantum Systems". In: *Phys. Rev. Lett.* 110 (15 Apr. 2013), p. 150403. DOI: 10.1103/PhysRevLett.110.150403. URL: https://link.aps.org/doi/10.1103/PhysRevLett.110.150403.

[95] Donato Farina and Vittorio Giovannetti. "Open-quantum-system dynamics: Recovering positivity of the Redfield equation via the partial secular approximation". In: *Phys. Rev. A* 100 (1 July 2019), p. 012107. DOI: 10.1103/PhysRevA.100.012107. URL: https://link.aps.org/doi/10.1103/PhysRevA.100.012107.

[96] Giovanni Di Meglio, Martin B. Plenio, and Susana F. Huelga. "Time dependent Markovian master equation beyond the adiabatic limit". In: *Quantum* 8 (Nov. 2024), p. 1534. ISSN: 2521-327X. DOI: 10.22331/q-2024-11-21-1534. URL: https://doi.org/10.22331/q-2024-11-21-1534.

[97] Roie Dann, Amikam Levy, and Ronnie Kosloff. "Time-dependent Markovian quantum master equation". In: *Phys. Rev. A* 98 (5 Nov. 2018), p. 052129. DOI: 10.1103/PhysRevA.98.052129. URL: https://link.aps.org/doi/10.1103/PhysRevA.98.052129.

[98] Ziwen Huang et al. "Completely Positive Map for Noisy Driven Quantum Systems Derived by Keldysh Expansion". In: *Quantum* 7 (Nov. 2023), p. 1158. ISSN: 2521-327X. DOI: 10.22331/q-2023-11-03-1158. URL: https://doi.org/10.22331/q-2023-11-03-1158.

[99] Takashi Mori. *Floquet States in Open Quantum Systems*. 2023. DOI: https://doi.org/10.1146/annurev-conmatphys-040721-015537.

[100] R. Blümel et al. "Dynamical localization in the microwave interaction of Rydberg atoms: The influence of noise". In: *Phys. Rev. A* 44 (7 Oct. 1991), pp. 4521–4540. DOI: 10.1103/PhysRevA.44.4521. URL: https://link.aps.org/doi/10.1103/PhysRevA.44.4521.

[101] Milena Grifoni and Peter Hänggi. "Driven quantum tunneling". In: *Physics Reports* 304.5 (1998), pp. 229–354. ISSN: 0370-1573. DOI: https://doi.org/10.1016/S0370-1573(98)00022-2.

[102] H. P. Breuer and M. Holthaus. "Adiabatic processes in the ionization of highly excited hydrogen atoms". In: *Zeitschrift für Physik D Atoms, Molecules and Clusters* 11.1 (Mar. 1989), pp. 1–14. ISSN: 1431-5866. DOI: 10.1007/BF01436579.

[103] P. Hänggi et al. *Driven Quantum Systems*. Universität Augsburg, 2018. URL: https://books.google.fr/books?id=pRXLzQEACAAJ.

[104] Léon Carde et al. "Flux-pump-induced degradation of T_1 for dissipative cat qubits". In: *Phys. Rev. Appl.* 23 (2 Feb. 2025), p. 024073. DOI: 10.1103/PhysRevApplied.23.024073. URL: https://link.aps.org/doi/10.1103/PhysRevApplied.23.024073.

[105] Ryo Hanai, Alexander McDonald, and Aashish Clerk. "Intrinsic mechanisms for drive-dependent Purcell decay in superconducting quantum circuits". In: *Physical Review Research* 3.4 (Dec. 2021). ISSN: 2643-1564. DOI: 10.1103/physrevresearch.3.043228. URL: http://dx.doi.org/10.1103/PhysRevResearch.3.043228.

[106] Moein Malekakhlagh, Easwar Magesan, and Luke C. G. Govia. "Time-dependent Schrieffer-Wolff-Lindblad perturbation theory: Measurement-induced dephasing and second-order Stark shift in dispersive readout". In: *Physical Review A* 106.5 (Nov. 2022). ISSN: 2469-9934. DOI: 10.1103/physreva.106.052601. URL: http://dx.doi.org/10.1103/PhysRevA.106.052601.

[107] Kirill S. Dubovitskii et al. "Theory of quasiparticle-induced errors in driven-dissipative Schrödinger cat qubits". In: *Phys. Rev. B* 110 (2 July 2024), p. 024505. DOI: 10.1103/PhysRevB.110.024505. URL: https://link.aps.org/doi/10.1103/PhysRevB.110.024505.

[108] Kirill S. Dubovitskii. "Bit-flip errors in dissipative cat qubits: Second-order perturbation theory". In: *Phys. Rev. A* 111 (1 Jan. 2025), p. 012617. DOI: 10.1103/PhysRevA.111.012617. URL: https://link.aps.org/doi/10.1103/PhysRevA.111.012617.

[109] Michiel Burgelman et al. "Limitations to Dynamical Error Suppression and Gate-Error Virtualization from Temporally Correlated Nonclassical Noise". In: *PRX Quantum* 6.1 (Feb. 2025). ISSN: 2691-3399. DOI: 10.1103/prxquantum.6.010323. URL: http://dx.doi.org/10.1103/PRXQuantum.6.010323.

[110] M. C. Goorden, M. Thorwart, and M. Grifoni. "Spectroscopy of a driven solid-state qubit coupled to a structuredenvironment". In: *The European Physical Journal B - Condensed Matter and Complex Systems* 45.3 (2005), pp. 405–417. ISSN: 1434-6036. DOI: 10.1140/epjb/e2005-00192-5.

[111] Inés de Vega and Daniel Alonso. "Dynamics of non-Markovian open quantum systems". In: *Rev. Mod. Phys.* 89 (1 Jan. 2017), p. 015001. DOI: 10.1103/RevModPhys.89.015001. URL: https://link.aps.org/doi/10.1103/RevModPhys.89.015001.

[112] Jonathan Keeling et al. *Process Tensor Approaches to Non-Markovian Quantum Dynamics*. 2025. arXiv: 2509.07661 [quant-ph]. URL: https://arxiv.org/abs/2509.07661.

[113] Valentin Link, Hong-Hao Tu, and Walter T. Strunz. "Open Quantum System Dynamics from Infinite Tensor Network Contraction". In: *Physical Review Letters* 132.20 (May 2024). ISSN: 1079-7114. DOI: 10.1103/physrevlett.132.200403. URL: http://dx.doi.org/10.1103/PhysRevLett.132.200403.

[114] S. Girvin. "Circuit QED: superconducting qubits coupled to microwave photons". In: June 2014, pp. 113–256. ISBN: 9780199681181. DOI: 10.1093/acprof:oso/9780199681181.003.0003.

[115] Jan Dereziński. "Bosonic quadratic Hamiltonians". In: *Journal of Mathematical Physics* 58.12 (Dec. 2017). ISSN: 1089-7658. DOI: 10.1063/1.5017931. URL: http://dx.doi.org/10.1063/1.5017931.

[116] R.P Feynman and F.L Vernon. "The theory of a general quantum system interacting with a linear dissipative system". In: *Annals of Physics* 24 (Oct. 1963), pp. 118–173. ISSN: 0003-4916. DOI: https://doi.org/10.1016/0003-4916(63)90068-X. URL: https://www.sciencedirect.com/science/article/pii/000349166390068X.

[117] Jutho Haegeman et al. "Unifying time evolution and optimization with matrix product states". In: *Phys. Rev. B* 94 (16 Oct. 2016), p. 165116. DOI: 10.1103/PhysRevB.94.165116. URL: https://link.aps.org/doi/10.1103/PhysRevB.94.165116.

[118] Francois-Marie Le Régent and Pierre Rouchon. "Heisenberg formulation of adiabatic elimination for open quantum systems with two timescales". In: *IEEE 62nd Conference on Decision and Control (CDC)*. 2023.

[119] J J García-Ripoll et al. "Dissipation-induced hard-core boson gas in an optical lattice". In: *New Journal of Physics* 11.1 (Jan. 2009), p. 013053. DOI: 10.1088/1367-2630/11/1/013053.

[120] J. I. Cirac. "Interaction of a two-level atom with a cavity mode in the bad-cavity limit". In: *Phys. Rev. A* 46 (7 Oct. 1992), pp. 4354–4362. DOI: 10.1103/PhysRevA.46.4354. URL: https://link.aps.org/doi/10.1103/PhysRevA.46.4354.

[121] H. M. Wiseman and G. J. Milburn. "Quantum theory of field-quadrature measurements". In: *Phys. Rev. A* 47 (1 Jan. 1993), pp. 642–662. DOI: 10.1103/PhysRevA.47.642. URL: https://link.aps.org/doi/10.1103/PhysRevA.47.642.

[122] A. Karabanov et al. "Dynamic Nuclear Polarization as Kinetically Constrained Diffusion". In: *Phys. Rev. Lett.* 115 (2 July 2015), p. 020404. DOI: 10.1103/PhysRevLett.115.020404. URL: https://link.aps.org/doi/10.1103/PhysRevLett.115.020404.

[123] E. M. Kessler. "Generalized Schrieffer-Wolff formalism for dissipative systems". In: *Phys. Rev. A* 86 (1 July 2012), p. 012126. DOI: 10.1103/PhysRevA.86.012126. URL: https://link.aps.org/doi/10.1103/PhysRevA.86.012126.

[124] Simon B. Jäger et al. "Lindblad Master Equations for Quantum Systems Coupled to Dissipative Bosonic Modes". In: *Phys. Rev. Lett.* 129 (6 Aug. 2022), p. 063601. DOI: 10.1103/PhysRevLett.129.063601. URL: https://link.aps.org/doi/10.1103/PhysRevLett.129.063601.

[125] Paolo Zanardi, Jeffrey Marshall, and Lorenzo Campos Venuti. "Dissipative universal Lindbladian simulation". In: *Phys. Rev. A* 93 (2 Feb. 2016), p. 022312. DOI: 10.1103/PhysRevA.93.022312. URL: https://link.aps.org/doi/10.1103/PhysRevA.93.022312.

[126] Katarzyna Macieszczak et al. "Towards a Theory of Metastability in Open Quantum Dynamics". In: *Phys. Rev. Lett.* 116 (24 June 2016), p. 240404. DOI: 10.1103/PhysRevLett.116.240404. URL: https://link.aps.org/doi/10.1103/PhysRevLett.116.240404.

[127] Neil Fenichel. "Geometric singular perturbation theory for ordinary differential equations". In: *Journal of Differential Equations* 31.1 (1979), pp. 53–98. ISSN: 0022-0396. DOI: https://doi.org/10.1016/0022-0396(79)90152-9.

[128] Francois-Marie Le Régent and Pierre Rouchon. "Adiabatic elimination for composite open quantum systems: Reduced-model formulation and numerical simulations". In: *Phys.Rev.A* 109 (3 Mar. 2024). DOI: 10.1103/PhysRevA.109.032603. URL: https://link.aps.org/doi/10.1103/PhysRevA.109.032603.

[129] J. Carr. *Applications of Centre Manifold Theory*. Applied Mathematical Sciences. Springer New York, 1981. ISBN: 978-0-387-90577-8. URL: https://books.google.fr/books?id=93BdN7btysoC.

[130] Maximilian Behr, Peter Benner, and Jan Heiland. *Solution Formulas for Differential Sylvester and Lyapunov Equations*. 2018. arXiv: 1811.08327 [math.NA]. URL: https://arxiv.org/abs/1811.08327.

[131] Mazyar Mirrahimi and Pierre Rouchon. "Dynamics and control of open quantum systems". In: *Lecture notes* (2015).

[132] Jérémie Guillaud. "Thermal adiabatic elimination with adjoint Lindbladian". inria Technical Note. 2020.

[133] Hendra Nurdin and Naoki Yamamoto. *Linear Dynamical Quantum Systems: Analysis, Synthesis, and Control*. May 2017. ISBN: 978-3-319-55201-9. DOI: 10.1007/978-3-319-55201-9.

[134] Serge Haroche and J-M Raimond. *Exploring the quantum: atoms, cavities, and photons*. Oxford university press, 2006.

[135] Jan A Sanders, Ferdinand Verhulst, and James Murdock. *Averaging methods in nonlinear dynamical systems*. Vol. 59. Springer, 2007.

[136] Michio Tokuyama and Hazime Mori. "Statistical-Mechanical Theory of Random Frequency Modulations and Generalized Brownian Motions*)". In: *Progress of Theoretical Physics* 55.2 (Feb. 1976), pp. 411–429. ISSN: 0033-068X. DOI: 10.1143/PTP.55.411.

[137] Natsuki Hashitsumae, Fumiaki Shibata, and Mayumi Shing¯u. "Quantal master equation valid for any time scale". In: *Journal of Statistical Physics* 17.4 (Oct. 1977), pp. 155–169. ISSN: 1572-9613. DOI: 10.1007/BF01040099.

[138] P. Hänggi and H. Thomas. "Time evolution, correlations, and linear response of non-Markov processes". In: *Zeitschrift für Physik B Condensed Matter* 26.1 (Mar. 1977), pp. 85–92. ISSN: 1431-584X. DOI: 10.1007/BF01313376.

[139] Michiel Burgelman, Paolo Forni, and Alain Sarlette. *Quantum dynamical decoupling by shaking the close environment*. 2022. arXiv: 2201.09849 [quant-ph]. URL: https://arxiv.org/abs/2201.09849.

[140] Alain Sarlette et al. "Quantum adiabatic elimination at arbitrary order for photon number measurement**This work has been supported by ANR grant HAMROQS. Part of this work was made possible through the support of Fondation Del Duca and IDEX Lyon (Contract No. ANR-16-IDEX-0005)." In: *IFAC-PapersOnLine* 53.2 (2020), pp. 250–256. ISSN: 2405-8963. DOI: https://doi.org/10.1016/j.ifacol.2020.12.131.

[141] Fran çois Damanet, Andrew J. Daley, and Jonathan Keeling. "Atom-only descriptions of the driven-dissipative Dicke model". In: *Phys. Rev. A* 99 (3 Mar. 2019), p. 033845. DOI: 10.1103/PhysRevA.99.033845. URL: https://link.aps.org/doi/10.1103/PhysRevA.99.033845.

[142] Simon B. Jäger et al. "Lindblad Master Equations for Quantum Systems Coupled to Dissipative Bosonic Modes". In: *Phys. Rev. Lett.* 129 (6 Aug. 2022), p. 063601. DOI: 10.1103/PhysRevLett.129.063601. URL: https://link.aps.org/doi/10.1103/PhysRevLett.129.063601.

[143] Richard Hartmann and Walter T. Strunz. "Accuracy assessment of perturbative master equations: Embracing nonpositivity". In: *Phys. Rev. A* 101 (1 Jan. 2020), p. 012103. DOI: 10.1103/PhysRevA.101.012103. URL: https://link.aps.org/doi/10.1103/PhysRevA.101.012103.

[144] Angela Riva et al. "Thermal cycle and polaron formation in structured bosonic environments". In: *Physical Review B* 108.19 (2023), p. 195138.

[145] Román Orús. "A practical introduction to tensor networks: Matrix product states and projected entangled pair states". In: *Annals of Physics* 349 (2014), pp. 117–158. ISSN: 0003-4916. DOI: https://doi.org/10.1016/j.aop.2014.06.013. URL: https://www.sciencedirect.com/science/article/pii/S0003491614001596.

[146] J. Biamonte. *Lectures on Quantum Tensor Networks*. 2019. DOI: 10.48550/ARXIV.1912.10049. URL: https://arxiv.org/abs/1912.10049.

[147] Alexander Altland and Ben D. Simons. *Condensed Matter Field Theory*. 2nd ed. Cambridge University Press, 2010.

[148] Or Sharir, Amnon Shashua, and Giuseppe Carleo. "Neural tensor contractions and the expressive power of deep neural quantum states". In: *Phys. Rev. B* 106 (20 Nov. 2022), p. 205136. DOI: 10.1103/PhysRevB.106.205136. URL: https://link.aps.org/doi/10.1103/PhysRevB.106.205136.

[149] M. Fannes, B. Nachtergaele, and R. F. Werner. "Finitely correlated states on quantum spin chains". In: *Communications in Mathematical Physics* 144.3 (Mar. 1992), pp. 443–490. ISSN: 1432-0916. DOI: 10.1007/BF02099178.

[150] A. Klümper, A. Schadschneider, and J. Zittartz. "Groundstate properties of a generalized VBS-model". In: *Zeitschrift für Physik B Condensed Matter* 87.3 (Oct. 1992), pp. 281–287. ISSN: 1431-584X. DOI: 10.1007/BF01309281.

[151] Guifré Vidal. "Efficient Classical Simulation of Slightly Entangled Quantum Computations". In: *Phys. Rev. Lett.* 91 (14 Oct. 2003), p. 147902. DOI: 10.1103/PhysRevLett.91.147902. URL: https://link.aps.org/doi/10.1103/PhysRevLett.91.147902.

[152] F. Verstraete and J. I. Cirac. "Valence-bond states for quantum computation". In: *Phys. Rev. A* 70 (6 Dec. 2004), p. 060302. DOI: 10.1103/PhysRevA.70.060302. URL: https://link.aps.org/doi/10.1103/PhysRevA.70.060302.

[153] M. Gerster et al. "Unconstrained tree tensor network: An adaptive gauge picture for enhanced performance". In: *Phys. Rev. B* 90 (12 Sept. 2014), p. 125154. DOI: 10.1103/PhysRevB.90.125154. URL: https://link.aps.org/doi/10.1103/PhysRevB.90.125154.

[154] Kenneth G. Wilson. "The renormalization group: Critical phenomena and the Kondo problem". In: *Rev. Mod. Phys.* 47 (4 Oct. 1975), pp. 773–840. DOI: 10.1103/RevModPhys.47.773. URL: https://link.aps.org/doi/10.1103/RevModPhys.47.773.

[155] Steven R. White. "Density matrix formulation for quantum renormalization groups". In: *Phys. Rev. Lett.* 69 (19 Nov. 1992), pp. 2863–2866. DOI: 10.1103/PhysRevLett.69.2863. URL: https://link.aps.org/doi/10.1103/PhysRevLett.69.2863.

[156] C. Hubig, I. P. McCulloch, and U. Schollwöck. "Generic construction of efficient matrix product operators". In: *Physical Review B* 95.3 (Jan. 2017), p. 035129. DOI: 10.1103/PhysRevB.95.035129. URL: https://link.aps.org/doi/10.1103/PhysRevB.95.035129.

[157] S. Paeckel et al. “Time-evolution methods for matrix-product states”. In: *Annals of Physics* 411 (Dec. 2019), p. 167998. ISSN: 0003-4916. DOI: https://doi.org/10.1016/j.aop.2019.167998. URL: https://www.sciencedirect.com/science/article/pii/S0003491619302532.

[158] Guifré Vidal. “Efficient Simulation of One-Dimensional Quantum Many-Body Systems”. In: *Phys. Rev. Lett.* 93 (4 July 2004), p. 040502. DOI: 10.1103/PhysRevLett.93.040502. URL: https://link.aps.org/doi/10.1103/PhysRevLett.93.040502.

[159] F. Verstraete, J. I. Cirac, and V. Murg. “Matrix Product States, Projected Entangled Pair States, and variational renormalization group methods for quantum spin systems”. en. In: *Advances in Physics* 57.2 (Mar. 2008). arXiv: 0907.2796, pp. 143–224. ISSN: 0001-8732, 1460-6976. DOI: 10.1080/14789940801912366. URL: http://arxiv.org/abs/0907.2796.

[160] Christian Lubich, Ivan V. Oseledets, and Bart Vandereycken. “Time Integration of Tensor Trains”. en. In: *SIAM Journal on Numerical Analysis* 53.2 (Jan. 2015), pp. 917–941. ISSN: 0036-1429, 1095-7170. DOI: 10.1137/140976546. URL: http://epubs.siam.org/doi/10.1137/140976546.

[161] W. Gautschi. “Algorithm 726: ORTHPOL–a Package of Routines for Generating Orthogonal Polynomials and Gauss-Type Quadrature Rules”. In: *ACM Trans. Math. Softw.* 20.1 (Mar. 1994), pp. 21–62. ISSN: 0098-3500. DOI: 10.1145/174603.174605. URL: https://doi.org/10.1145/174603.174605.

[162] D. Tamascelli. “Excitation Dynamics in Chain-Mapped Environments”. In: *Entropy* 22.11 (Nov. 2020), p. 1320. ISSN: 1099-4300. DOI: 10.3390/e22111320. URL: http://dx.doi.org/10.3390/e22111320.

[163] H. P. Breuer et al. “Colloquium: Non-Markovian dynamics in open quantum systems”. In: *Reviews of Modern Physics* 88.2 (Apr. 2016). ISSN: 1539-0756. DOI: 10.1103/revmodphys.88.021002. URL: http://dx.doi.org/10.1103/RevModPhys.88.021002.

[164] D. Tamascelli et al. “Efficient Simulation of Finite-Temperature Open Quantum Systems”. In: *Phys. Rev. Lett.* 123 (9 Aug. 2019), p. 090402. DOI: 10.1103/PhysRevLett.123.090402. URL: https://link.aps.org/doi/10.1103/PhysRevLett.123.090402.

[165] A. J. Dunnett and A. W. Chin. “Simulating Quantum Vibronic Dynamics at Finite Temperatures With Many Body Wave Functions at 0 K”. In: *Frontiers in Chemistry* 8 (2021), p. 1195. ISSN: 2296-2646. DOI: 10.3389/fchem.2020.600731. URL: https://www.frontiersin.org/article/10.3389/fchem.2020.600731.

[166] Angus J. Dunnett and Alex W. Chin. “Efficient bond-adaptive approach for finite-temperature open quantum dynamics using the one-site time-dependent variational principle for matrix product states”. In: *Physical Review B* 104.21 (Dec. 2021), p. 214302. ISSN: 2469-9950, 2469-9969. DOI: 10.1103/PhysRevB.104.214302. URL: https://link.aps.org/doi/10.1103/PhysRevB.104.214302.

[167] Angus J. Dunnett and Alex W. Chin. "Efficient bond-adaptive approach for finite-temperature open quantum dynamics using the one-site time-dependent variational principle for matrix product states". In: *Physical Review B* 104.21 (Dec. 2021), p. 214302. ISSN: 2469-9950, 2469-9969. DOI: 10.1103/PhysRevB.104.214302. URL: https://link.aps.org/doi/10.1103/PhysRevB.104.214302.

[168] I. de Vega and M. C. Bañuls. "Thermofield-based chain-mapping approach for open quantum systems". In: *Physical Review A* 92.5 (Nov. 2015). ISSN: 1094-1622. DOI: 10.1103/physreva.92.052116. URL: http://dx.doi.org/10.1103/PhysRevA.92.052116.

[169] P. W. Anderson and J. M. Rowell. "Probable Observation of the Josephson Superconducting Tunneling Effect". In: *Phys. Rev. Lett.* 10 (6 Mar. 1963), pp. 230–232. DOI: 10.1103/PhysRevLett.10.230. URL: https://link.aps.org/doi/10.1103/PhysRevLett.10.230.

[170] B. D. Josephson. "Possible new effects in superconductive tunnelling". In: *Physics Letters* 1.7 (1962), pp. 251–253. ISSN: 0031-9163. DOI: https://doi.org/10.1016/0031-9163(62)91369-0.

[171] A. Kandala et al. "Demonstration of a High-Fidelity cnot Gate for Fixed-Frequency Transmons with Engineered ZZ Suppression". In: *Phys. Rev. Lett.* 127 (13 Sept. 2021), p. 130501. DOI: 10.1103/PhysRevLett.127.130501. URL: https://link.aps.org/doi/10.1103/PhysRevLett.127.130501.

[172] Cristóbal Lledó et al. "Cloaking a qubit in a cavity". In: *Nature Communications* 14.1 (Oct. 2023), p. 6313. ISSN: 2041-1723. DOI: 10.1038/s41467-023-42060-5.

[173] T. Walter et al. "Rapid High-Fidelity Single-Shot Dispersive Readout of Superconducting Qubits". In: *Physical Review Applied* 7.5 (May 2017). ISSN: 2331-7019. DOI: 10.1103/physrevapplied.7.054020. URL: http://dx.doi.org/10.1103/PhysRevApplied.7.054020.

[174] Z. K. Minev et al. "To catch and reverse a quantum jump mid-flight". In: *Nature* 570.7760 (2019), pp. 200–204. ISSN: 1476-4687. DOI: 10.1038/s41586-019-1287-z.

[175] D. H. Slichter et al. "Measurement-Induced Qubit State Mixing in Circuit QED from Up-Converted Dephasing Noise". In: *Phys. Rev. Lett.* 109 (15 Oct. 2012), p. 153601. DOI: 10.1103/PhysRevLett.109.153601. URL: https://link.aps.org/doi/10.1103/PhysRevLett.109.153601.

[176] Aayam Bista et al. *Readout-induced leakage of the fluxonium qubit*. 2025. arXiv: 2501.17807 [quant-ph]. URL: https://arxiv.org/abs/2501.17807.

[177] U. Réglade et al. "Quantum control of a cat qubit with bit-flip times exceeding ten seconds". In: *Nature* 629.8013 (May 2024), pp. 778–783. ISSN: 1476-4687. DOI: 10.1038/s41586-024-07294-3. URL: http://dx.doi.org/10.1038/s41586-024-07294-3.

[178] Harald Putterman et al. “Preserving Phase Coherence and Linearity in Cat Qubits with Exponential Bit-Flip Suppression”. In: *Physical Review X* 15.1 (Mar. 2025). ISSN: 2160-3308. DOI: 10.1103/physrevx.15.011070. URL: http://dx.doi.org/10.1103/PhysRevX.15.011070.

[179] Alexandre S. May et al. *Noise Mitigation in Single Microwave Photon Counting by Cascaded Quantum Measurements*. 2025. arXiv: 2502.14804 [quant-ph]. URL: https://arxiv.org/abs/2502.14804.

[180] Harald Putterman et al. “Hardware-efficient quantum error correction via concatenated bosonic qubits”. In: *Nature* 638.8052 (Feb. 2025), pp. 927–934. ISSN: 1476-4687. DOI: 10.1038/s41586-025-08642-7.

[181] Maxime Boissonneault, J. M. Gambetta, and Alexandre Blais. “Dispersive regime of circuit QED: Photon-dependent qubit dephasing and relaxation rates”. In: *Physical Review A* 79.1 (Jan. 2009). ISSN: 1094-1622. DOI: 10.1103/physreva.79.013819. URL: http://dx.doi.org/10.1103/PhysRevA.79.013819.

[182] D H Slichter et al. “Quantum Zeno effect in the strong measurement regime of circuit quantum electrodynamics”. In: *New Journal of Physics* 18.5 (May 2016), p. 053031. DOI: 10.1088/1367-2630/18/5/053031.

[183] Vladimir B. Braginsky, Yuri I. Vorontsov, and Kip S. Thorne. “Quantum Nondemolition Measurements”. In: *Science* 209.4456 (1980), pp. 547–557. DOI: 10.1126/science.209.4456.547. eprint: https://www.science.org/doi/pdf/10.1126/science.209.4456.547. URL: https://www.science.org/doi/abs/10.1126/science.209.4456.547.

[184] Marie Frédérique Dumas et al. “Measurement-Induced Transmon Ionization”. In: *Phys. Rev. X* 14 (4 Oct. 2024), p. 041023. DOI: 10.1103/PhysRevX.14.041023. URL: https://link.aps.org/doi/10.1103/PhysRevX.14.041023.

[185] U. Vool et al. “Non-Poissonian Quantum Jumps of a Fluxonium Qubit due to Quasiparticle Excitations”. In: *Physical Review Letters* 113.24 (Dec. 2014). ISSN: 1079-7114. DOI: 10.1103/physrevlett.113.247001. URL: http://dx.doi.org/10.1103/PhysRevLett.113.247001.

[186] G. Catelani et al. “Quasiparticle Relaxation of Superconducting Qubits in the Presence of Flux”. In: *Physical Review Letters* 106.7 (Feb. 2011). ISSN: 1079-7114. DOI: 10.1103/physrevlett.106.077002. URL: http://dx.doi.org/10.1103/PhysRevLett.106.077002.

[187] Maxime Boissonneault, J. M. Gambetta, and Alexandre Blais. “Nonlinear dispersive regime of cavity QED: The dressed dephasing model”. In: *Phys. Rev. A* 77 (6 June 2008), p. 060305. DOI: 10.1103/PhysRevA.77.060305. URL: https://link.aps.org/doi/10.1103/PhysRevA.77.060305.

[188] Xu Xiao et al. *A diagrammatic method to compute the effective Hamiltonian of driven nonlinear oscillators*. 2024. arXiv: 2304.13656 [quant-ph]. URL: https://arxiv.org/abs/2304.13656.

[189] B Foxen et al. “Qubit compatible superconducting interconnects”. In: *Quantum Science and Technology* 3.1 (Nov. 2017), p. 014005. DOI: 10.1088/2058-9565/aa94fc.

[190] Mohammad Mirhosseini et al. “Superconducting metamaterials for waveguide quantum electrodynamics”. In: *Nature Communications* 9.1 (2018), p. 3706. ISSN: 2041-1723. DOI: 10.1038/s41467-018-06142-z.

[191] Haoxiong Yan et al. “Broadband bandpass Purcell filter for circuit quantum electrodynamics”. In: *Applied Physics Letters* 123.13 (Sept. 2023). ISSN: 1077-3118. DOI: 10.1063/5.0161893. URL: http://dx.doi.org/10.1063/5.0161893.

[192] Félix Beaudoin, Jay M. Gambetta, and A. Blais. “Dissipation and ultrastrong coupling in circuit QED”. In: *Physical Review A* 84.4 (Oct. 2011). ISSN: 1094-1622. DOI: 10.1103/physreva.84.043832. URL: http://dx.doi.org/10.1103/PhysRevA.84.043832.

[193] Kiyoto Nakamura and Joachim Ankerhold. *Entanglement dynamics and performance of two-qubit gates for superconducting qubits under non-Markovian effects*. 2025. arXiv: 2510.05872 [quant-ph]. URL: https://arxiv.org/abs/2510.05872.

[194] Kiyoto Nakamura and Joachim Ankerhold. “Impact of time-retarded noise on dynamical decoupling schemes for qubits”. In: *Physical Review B* 111.6 (Feb. 2025). ISSN: 2469-9969. DOI: 10.1103/physrevb.111.064503. URL: http://dx.doi.org/10.1103/PhysRevB.111.064503.

[195] Kiyoto Nakamura and Joachim Ankerhold. “Gate operations for superconducting qubits and non-Markovianity”. In: *Physical Review Research* 6.3 (Aug. 2024). ISSN: 2643-1564. DOI: 10.1103/physrevresearch.6.033215. URL: http://dx.doi.org/10.1103/PhysRevResearch.6.033215.

[196] Marco Cattaneo and Gheorghe Sorin Paraoanu. “Engineering Dissipation with Resistive Elements in Circuit Quantum Electrodynamics”. In: *Advanced Quantum Technologies* 4.11 (2021), p. 2100054. DOI: https://doi.org/10.1002/qute.202100054. eprint: https://advanced.onlinelibrary.wiley.com/doi/pdf/10.1002/qute.202100054. URL: https://advanced.onlinelibrary.wiley.com/doi/abs/10.1002/qute.202100054.

[197] Lin Tian, Seth Lloyd, and T. P. Orlando. “Decoherence and relaxation of a superconducting quantum bit during measurement”. In: *Phys. Rev. B* 65 (14 Apr. 2002), p. 144516. DOI: 10.1103/PhysRevB.65.144516. URL: https://link.aps.org/doi/10.1103/PhysRevB.65.144516.

[198] M. Thorwart et al. “Controlling decoherence of a two-level atom in a lossy cavity”. In: *Journal of Modern Optics* 47.14–15 (Nov. 2000), pp. 2905–2919. ISSN: 1362-3044. DOI: 10.1080/09500340008232205. URL: http://dx.doi.org/10.1080/09500340008232205.

[199] G. Gasbarri and L. Ferialdi. “Recursive approach for non-Markovian time-convolutionless master equations”. In: *Physical Review A* 97.2 (Feb. 2018). ISSN: 2469-9934. DOI: 10.1103/physreva.97.022114. URL: http://dx.doi.org/10.1103/PhysRevA.97.022114.

[200] Luca Magazzù and Milena Grifoni. “Feynman-Vernon influence functional approach to quantum transport in interacting nanojunctions: An analytical hierarchical study”. In: *Phys. Rev. B* 105 (12 Mar. 2022), p. 125417. DOI: 10.1103/PhysRevB.105.125417. URL: https://link.aps.org/doi/10.1103/PhysRevB.105.125417.

[201] Michael Sven Ferguson, Oded Zilberberg, and Gianni Blatter. “Open quantum systems beyond Fermi’s golden rule: Diagrammatic expansion of the steady-state time-convolutionless master equations”. In: *Phys. Rev. Res.* 3 (2 May 2021), p. 023127. DOI: 10.1103/PhysRevResearch.3.023127. URL: https://link.aps.org/doi/10.1103/PhysRevResearch.3.023127.

[202] Andrea Smirne et al. “Non-Perturbative Treatment of Open-System Multi-Time Expectation Values in Gaussian Bosonic Environments”. In: *Open Systems & Information Dynamics* 29.04 (Dec. 2022). ISSN: 1793-7191. DOI: 10.1142/s1230161222500196. URL: http://dx.doi.org/10.1142/S1230161222500196.

[203] Alexander Nüßeler et al. “Fingerprint and Universal Markovian Closure of Structured Bosonic Environments”. In: *Physical Review Letters* 129.14 (Sept. 2022). ISSN: 1079-7114. DOI: 10.1103/physrevlett.129.140604. URL: http://dx.doi.org/10.1103/PhysRevLett.129.140604.

[204] Davide Ferracin et al. “Spectral density modulation and universal Markovian closure of fermionic environments”. In: *The Journal of Chemical Physics* 161.17 (Nov. 2024). ISSN: 1089-7690. DOI: 10.1063/5.0226723. URL: http://dx.doi.org/10.1063/5.0226723.

[205] E. Paladino et al. “1/f noise: Implications for solid-state quantum informationImplications for solid-state quantum information”. In: *Reviews of Modern Physics* 86.2 (Apr. 2014), pp. 361–418. ISSN: 1539-0756. DOI: 10.1103/revmodphys.86.361. URL: http://dx.doi.org/10.1103/RevModPhys.86.361.

[206] Vinay Tripathi et al. “Modeling Low- and High-Frequency Noise in Transmon Qubits with Resource-Efficient Measurement”. In: *PRX Quantum* 5 (1 Feb. 2024), p. 010320. DOI: 10.1103/PRXQuantum.5.010320. URL: https://link.aps.org/doi/10.1103/PRXQuantum.5.010320.

[207] David A. Rower et al. “Evolution of 1/f Flux Noise in Superconducting Qubits with Weak Magnetic Fields”. In: *Physical Review Letters* 130.22 (May 2023). ISSN: 1079-7114. DOI: 10.1103/physrevlett.130.220602. URL: http://dx.doi.org/10.1103/PhysRevLett.130.220602.

[208] Nora Reinić et al. *The Augmented Tree Tensor Network Cookbook*. 2025. arXiv: 2507.21236 [quant-ph]. URL: https://arxiv.org/abs/2507.21236.

[209] Brieuc Le Dé et al. “Extending Non-Perturbative Simulation Techniques for Open-Quantum Systems to Excited-State Proton Transfer and Ultrafast Non-Adiabatic Dynamics”. In: *Journal of Chemical Theory and Computation* 20.20 (Oct. 2024), pp. 8749–8766. ISSN: 1549-9626. DOI: 10.1021/acs.jctc.4c00666. URL: http://dx.doi.org/10.1021/acs.jctc.4c00666.

[210] Samuel Cailleaux et al. “Theory of the Photonic Joule Effect in Superconducting Circuits”. In: *Physical Review Letters* 134.22 (June 2025). ISSN: 1079-7114. DOI: 10.1103/b9hw-b6y6. URL: http://dx.doi.org/10.1103/b9hw-b6y6.

[211] Brieuc Le Dé et al. “Extending Non-Perturbative Simulation Techniques for Open-Quantum Systems to Excited-State Proton Transfer and Ultrafast Non-Adiabatic Dynamics”. In: *Journal of Chemical Theory and Computation* 20.20 (2024). PMID: 39388593, pp. 8749–8766. DOI: 10.1021/acs.jctc.4c00666. eprint: https://doi.org/10.1021/acs.jctc.4c00666. URL: https://doi.org/10.1021/acs.jctc.4c00666.

[212] A. J. Dunnett and A. W. Chin. *Dynamically Evolving Bond-Dimensions within the one-site Time-Dependent-Variational-Principle method for Matrix Product States: Towards efficient simulation of non-equilibrium open quantum dynamics*. 2020. arXiv: 2007.13528 [quant-ph].